

Peptide Nanofibres for Drug Delivery



MARIAROSA MAZZA

A THESIS SUBMITTED IN FULFILMENT OF THE REQUIREMENTS FOR THE
DEGREE OF DOCTOR OF PHILOSOPHY

THE SCHOOL OF PHARMACY
UNIVERSITY OF LONDON

ProQuest Number: 10104758

All rights reserved

INFORMATION TO ALL USERS

The quality of this reproduction is dependent upon the quality of the copy submitted.

In the unlikely event that the author did not send a complete manuscript and there are missing pages, these will be noted. Also, if material had to be removed, a note will indicate the deletion.



ProQuest 10104758

Published by ProQuest LLC(2016). Copyright of the Dissertation is held by the Author.

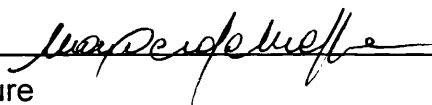
All rights reserved.

This work is protected against unauthorized copying under Title 17, United States Code.
Microform Edition © ProQuest LLC.

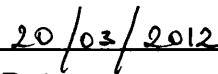
ProQuest LLC
789 East Eisenhower Parkway
P.O. Box 1346
Ann Arbor, MI 48106-1346

This thesis describes research conducted in the School of Pharmacy, University of London between October 2007 and July 2011 under the supervision of Prof. Ijeoma F. Uchegbu. I certify that the research described is original and that any parts of the work that have been conducted by collaboration are clearly indicated. I also certify that I have written all the text herein and have clearly indicated by suitable citation any part of this dissertation that has already appeared in publication.

Signature

A handwritten signature in black ink, appearing to read 'Ijeoma F. Uchegbu', written over a horizontal line.

Date

A handwritten date '20/03/2012' in black ink, written over a horizontal line.

ABSTRACT

Peptide and proteins are involved in a wide range of brain disease but they don't cross the blood brain barrier because of their hydrophilic nature and size. Nanofibrous systems are attracting increasing interest in the field of drug delivery and regenerative medicine. The aim of this work is to investigate the therapeutic applicability of peptide nanofibres as new drug delivery system to the Central Nervous System. Our working hypothesis was to choose a model hydrophilic peptide unable to enter the brain, make a lipophilic derivative from which monodomain nanofibres were constructed, in order to test them as a peptide carrier to the brain.

Dalargin, a hexapeptide analogue of Leu-enkephalin, which is unable to cross the blood brain barrier was chosen as a model drug. On direct injection into the brain, Dalargin acts on brain opioid receptors, resulting in analgesia. An amphipatic derivative of dalargin, palmitoyl Dalargin (pDal) was synthesized resulting in a surfactant like peptide able to form high-axial-ratio nanostructures in aqueous environments. The self-assembly of the peptide amphiphile has been assessed experimentally and in silico. Intravenous injection of formulation of nanofibres resulted in analgesic response in mice. Brain peptide delivery was assessed with Raman microscopy as well as by measuring analgesia and peptide nanofibres pharmacokinetic profiles in biological matrices.

While Dalargin was not detected in any of the tissue samples, palmitoyl Dalargin was measured in the brain tissue confirming the ability of peptide palmitoyl dalargin nanofibres to deliver the peptide across the blood brain barrier. Furthermore Raman microscopy revealed the presence of palmitoyl dalargin in the brain parenchyma.

We conclude that peptide nanofibres offer a unique method for delivering hydrophilic peptides across the blood brain barrier.

Peptide Nanofibres for Drug Delivery

Chapter 1

Introduction to Blood-Brain Barrier and new nanotechnologies for drug delivery to CNS

1.1	Introduction to Blood Brain Barrier	1
1.1.1	Physiological Anatomy of the Blood Brain Barrier	1
1.1.2	Role of the Tight Junctions in the BBB Functions	3
1.1.3	Factors Influencing the Drug Delivery to the Central Nervous System	5
1.1.4	Endocytosis at the Level of the BBB	11
1.1.5	Nanomedicine: a Solution to Brain Delivery?	13
1.1.6	Carriers Used in Drug Delivery to the Brain	15
1.2	Introduction to Nanofibres and their Potential in Drug Delivery	24
1.2.1	Peptides as Therapeutics for CNS Disorders	24
1.2.2	Nanofibrous Systems	24
1.2.3	Self-Assembling Peptide Nanofibres	27
1.2.4	Mechanism of Self-Assembly	32
1.2.5	Gelation of Peptide Nanofibres	33
1.2.6	Current Technologies Based on Peptide Nanofibres	34
1.2.7	Biom mineralization and High-Tech Applications	34
1.2.8	Peptide Nanofibres as Stabilizer Agents and a Bioactive Surfactant in Cosmetics	35
1.2.9	Drug Delivery (Antimicrobial, Drug and Gene)	35
1.3	Aims and Objectives	36

Chapter 2

Self-Assembling Amphiphiles Synthesis and Structural Characterization

2.1	Introduction	37
2.1.1	Gel Permeation Chromatography - Multi-Angle Laser Light Scattering (GPC-MALLS)	40
2.1.2	Solid Phase Peptide Synthesis (SPPS)	41

2.1.3	Coupling Agents	44
2.1.4	Drawbacks of SPPS and Strategies to Overcome these Limitations	47
2.1.5	HPLC Peptide Purification and Analysis	48
2.1.6	Mass Spectrometry	49
2.1.7	Electrospray Ionization /Mass Spectrometry	49
2.1.8	Matrix Assisted Laser Desorption/Ionization - Time of Flight (MALDI-TOF)	50
2.1.9	Fragmentation in Sequencing of Peptides and Spectra Interpretation	51
2.2	Materials	54
2.3	Methods	55
2.3.1	Synthesis of GCPQA	55
2.3.2	GCPQA NMR Analysis	56
2.3.3	Gel Permeation Chromatography - Multi-Angle Liser Scattering (GPC-MALLS)	56
2.3.4	Synthesis of Dalargin	57
2.3.5	Synthesis of Palmitoyl Dalargin	58
2.3.6	Peptide Purification	59
2.3.7	Mass Spectrometry	59
2.3.8	Nuclear Magnetic Resonance	60
2.3.9	Fourier Transformed Infrared Reflectance	60
2.3.10	X-Ray Diffraction	60
2.3.11	Polarizing Microscopy Analysis	60
2.4	Results	61
2.4.1	GCPQA Synthesis	61
2.4.2	Peptide Synthesis	67
2.5	Discussion	77

Chapter 3

pDal Nanofibres Preparation and Characterization

3.1	Introduction: Non-Spherical Shape Nanostructures	84
3.1.2	Encapsulation of Pyrene within Self-Assembled pDal Amphiphile Nanofibers	88

3.1.3	Z-Potential	89
3.1.4	Fibre X-ray Diffraction	90
3.1.5	Circular and Linear Dichroism Spectroscopy	92
3.2	Methods	93
3.2.1	Preparation of Nanofibres	93
3.2.2	Pyrene	93
3.2.3	Z-Potential	94
3.2.4	Electron Microscopy Fragmentation	94
3.2.5	X-ray Diffraction (XRD)	94
3.2.6	Congo Red UV-Absorbance	95
3.2.7	Thioflavin-T Fluorescence	95
3.2.8	Dichroism Spectroscopy	95
3.3	Results	97
3.4	Discussion	110

Chapter 4

Coarse-grained Simulation Study of pDal Nanofibres Self-Assembly

4.1	Introduction	119
4.1.1	Coarse-grained Molecular Modelling	119
4.2	Methods	122
4.2.1	Computational Details	122
4.3	Results	126
4.4	Discussion	136

Chapter 5

pDal Nanofibre Gels

5.1	Introduction	144
5.1.1	Thermal Analysis by Differential Scanning Calorimetry	146
5.1.2	Thermal Microscopy and Polarized Light Microscopy	148
5.1.3	Fourier Transform-Infra Red Attenuated Total Reflectance Spectroscopy (TFIR-ATR)	149
5.2	Methods	151
5.2.1	Differential Scanning Calorimetry	151
5.2.2	X-ray Diffraction	151
5.2.3	Microwave Sample Preparation	151
5.2.4	FTIR-ATR	152
5.2.5	Optical Microscopy Analyses	152
5.2.6	Congo Red Staining	152
5.2.7	Electron Microscopy	153
5.2.8	Pilot Study: Peptide Release in Simulated Gastric (SGF) and Intestinal Fluids (SIF)	153
5.2.9	Pilot Study: Pharmacokinetics of pDal Gels Following Oral Administration	154
5.3	Results	155
5.4	Discussion	167

Chapter 6

Biological Evaluation of Peptide Nanofibres as Carrier for Brain Delivery

6.1	Introduction	173
6.1.1	Cell Viability Assay	176
6.1.2	Cell Uptake of pDal Nanofibres Studied by Electron Microscopy	177
6.1.3	Measuring Compound Permeation into the Brain	178
6.1.4	Liquid Chromatography-Mass Spectrometry (LC-MS) in Pharmacokinetics Studies	179
6.1.5	Coherent Raman Scattering (CRS) Imaging: Label Free Detection Imaging	182
6.1.6	Pharmacodynamics: Pain Relief Studies in Animal Models	185
6.2	Methods	187

6.2.1	MTT Assay	187
6.2.2	TEM Studies of Nanofibres Endocytosis	188
6.2.3	Pharmacokinetics Study	189
6.2.4	Extraction and Sample Preparation for LC-MS Analysis	190
6.2.5	LC-MS Analysis	190
6.2.6	Spontaneous Raman Spectroscopy Imaging	193
6.2.7	Warm Water Bioassay	195
6.2.8	Statistical Analysis	196
6.3	Results	197
6.3.1	MTT Assay	197
6.3.2	Transmission Electron Microscopy Cell Uptake Studies	198
6.3.3	Pharmacokinetics Studies: LC-MS Analyses	201
6.3.4	SRS Imaging	209
6.3.5	Pharmacodynamics Studies: Warm Water Bioassay	210
6.4	Discussion	212

Chapter 7

<i>Conclusion and Future Perspectives</i>	219
-------------------------------------------	-----

Appendix	226
-----------------	-----

References	228
-------------------	-----

Acknowledgments

Thank you to my supervisors Prof Ijeoma Uchegbu and Dr Andreas Schatzlein and my lab mates for the time spent together at the School of Pharmacy.

Thank you to the University of London for funding.

Thank you to all the member of staff that have supported me and my work, it has been a pleasure to work with you all.

A special thanks to Dr Malkinson and his students for sharing with me their knowledge. To Dr Rebecca Notman and Dr Matthew Hicks for supervising my work at the University of Warwick, to Tania Mead for supervising my work at GSK, to Dr Julian Moger for the CRS imaging at the University of Exeter and Dr Larisa Mihoreanu for the TEM imaging at the London King's College.

My deepest gratitude goes to Dr Simon Gaisford for the introduction to calorimetry and the use of the calorimeters and to Dave McCarthy for the training in Electron Microscopy.

Thank you to my family and my friends.

And thank you to my love. Even if it is over....next week is still going to be "the most important week!", because I will spend it with you.

CHAPTER 1

Introduction to Blood-Brain Barrier and new nanotechnologies for drug delivery to CNS

1.1 Introduction to the Blood Brain Barrier

The blood-brain barrier's (BBB) primary function is to maintain the homeostasis of the brain (Pardridge, 1998). The complex regulation of the properties of the blood-brain barrier is not entirely understood and this lack of knowledge is a hurdle in the development of strategies for the delivery of many potentially therapeutic and diagnostic compounds to the Central Nervous System (CNS).

1.1.1 Physiological Anatomy of the Blood-Brain Barrier

In the brain, three barriers contribute to limit drug transport to the parenchyma (de Boer and Gaillard, 2007)

- The *Blood-Brain barrier*, localized in the capillaries in the brain.
- The *Blood-Cerebrospinal-Fluid barrier*, formed by the choroid plexus epithelium in the ventricles.
- The *Ependyma*, an epithelial layer of cells covering the brain tissue in the ventricles limiting the transport from the cerebrospinal fluid to the brain tissue.

Among this three elements, the BBB offers the biggest surface area and, thus, represents the major hurdle to successful drug delivery to the brain (Abbott et al., 2010).

The BBB protects the brain from exposure to both endogenous and exogenous substrates; it acts as a physical, metabolic and immunological barrier that prevents unwanted compounds from crossing from the circulation into the brain parenchyma

(de Boer and Gaillard, 2007). In contrast to the peripheral capillaries, brain endothelial cells are characterized by continuous tight junctions, the absence of fenestrations and very low pinocytotic activity. Furthermore, cells are surrounded by a basal membrane and extracellular matrix, as well as pericytes and astrocytes feet processes, which further form and help strengthen the BBB (Figure 1.1), and mediate its permeability (Dermietzel et al., 2006, Pardridge, 1998).

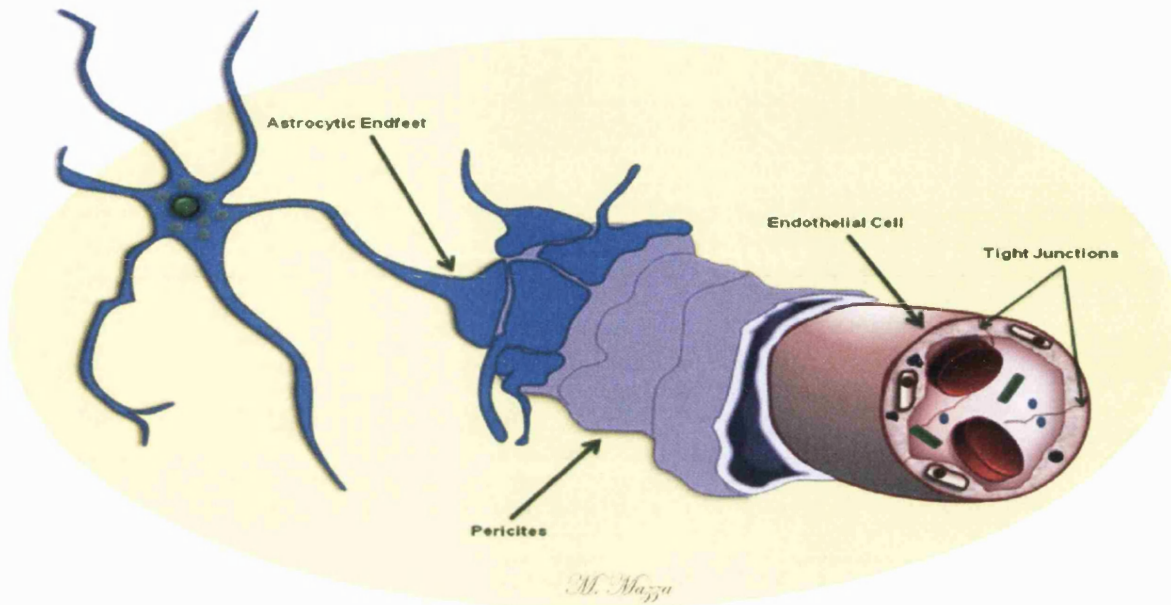


Figure 1.1: Schematic depiction of the BBB and its components.

In addition to these physical barriers, brain capillary cells are highly polarized, expressing various integral membrane proteins at the luminal and abluminal surfaces. These include various receptors, enzymes and transporters that support the functions of this cellular barrier within the neurovascular unit (Neuwelt et al., 2011).

The movement of solutes across the capillary endothelial barrier is a process of movement through two membranes in series, the luminal and the abluminal membranes of the capillary endothelial cell. These two membranes are separated only by 200-300 nm of endothelial cytoplasm (Pardridge, 2007, Cornford et al., 1994).

However these membranes are not iron gates that indiscriminately prevent the passage of solutes and other molecules. Permeability through the BBB remains a dynamic process controlled by intra- and intercellular signaling events among endothelial cells,

astrocytes and neurons in the BBB, as well as the presence of close tight junctions that restrict the passage of molecules via the paracellular route by sealing the space between adjacent endothelial cells.

Several endogenous transporters and receptors also contribute to maintain the brain homeostasis (de Boer and Gaillard, 2007).

1.1.2 Role of the Tight Junctions in the BBB Function

In a transverse section, the tight junctions appear as a system of fusion points, each of which represents a sectioned strand (Pardridge, 2007). These strands form the real obstacle guarding the intercellular pathway, and are under strict control of the brain microenvironment, in particular the astrocytes. At a molecular level, several proteins with differing structures and functions have been identified:

- *Membrane Proteins*, comprise occludin, members of the claudin family, members of the Ig-superfamily (junction adhesion molecules and endothelial cell selective adhesion molecules) (Cardoso et al., 2010);
- *Adaptor proteins*, consisting of two classes. First-order adaptors are based on their direct association with the integral tight junction proteins via PDZ domains. PDZ domains are formed by the proteins postsynaptic density protein 95 (PSD-95), discs large (Dlg) protein, and zonula occludens-1 protein (ZO-1). Second-order adaptors are based on their indirect association with the integral tight junction proteins and include cingulin and the cingulin-related junction-associated coiled-coil protein (Dermietzel et al., 2006, Kohler and Zahraoui, 2005);
- *Other proteins* involved in signaling cascades, such as G-proteins, regulators of G-protein signaling, small GTPase (Hopkins et al., 2000).

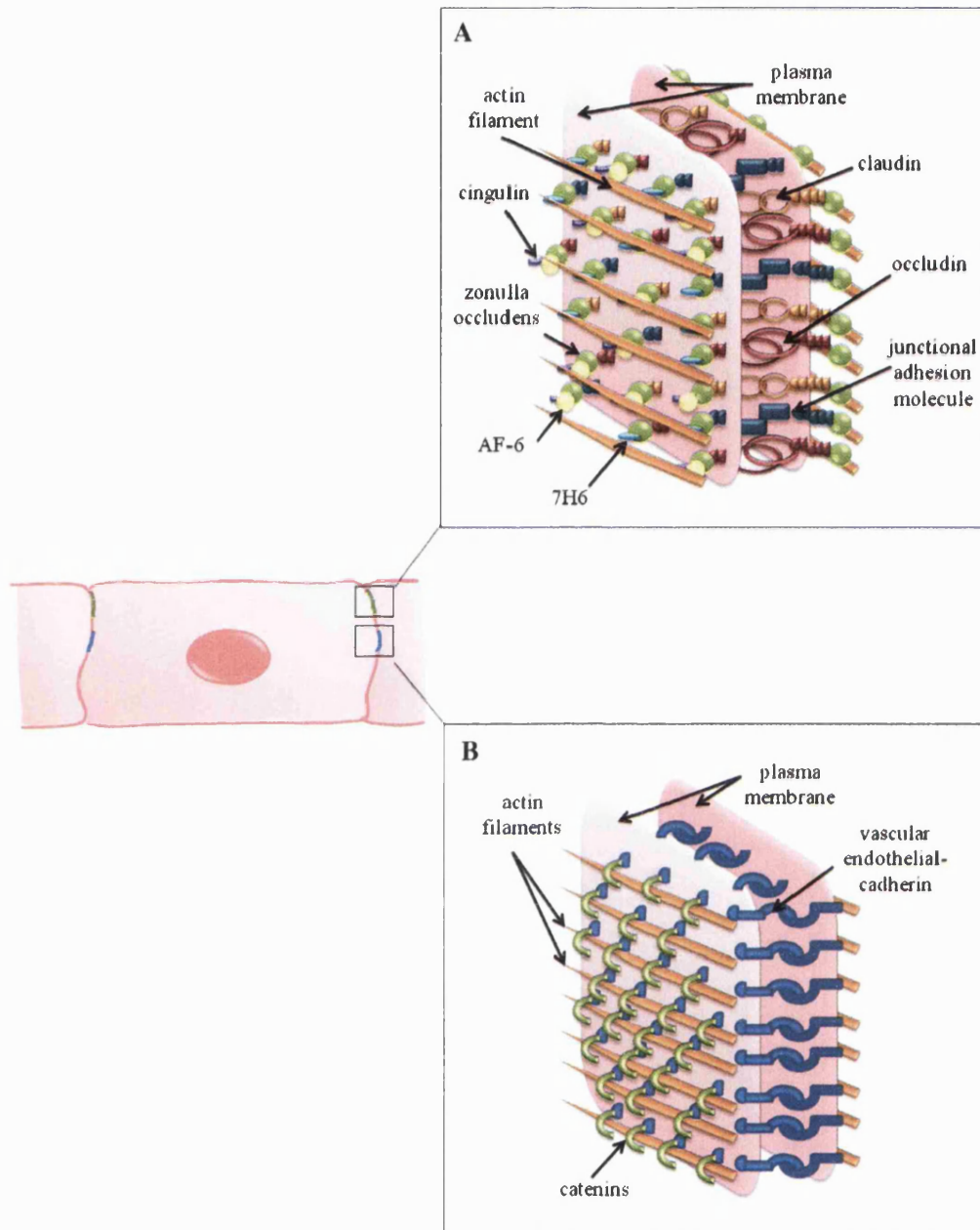


Figure 1.2: Endothelial cells at the blood–brain barrier present an elaborated junctional complex formed by tight junctions and adherens junctions. A) Tight junctions are located on the apical region of endothelial cells and form an intricate complex of parallel, interconnected, transmembrane and cytoplasmatic strands of proteins arranged as a series of multiple barriers. B) Adherens junctions are located below the tight junctions and are composed of transmembrane glycoproteins linked to the cytoskeleton by cytoplasmatic proteins, giving place to an adhesion belt. Adapted from (Cardoso et al., 2010).

Although there is now a better knowledge of the subcellular structures that take part in the formation of the junctions, their exact role in the regulation of the barrier function is not fully understood, due to insufficient understanding of the mechanisms by which these proteins act together to create these highly regulated and effective sealed points.

For example, Claudin-5 has been shown to be an essential component in preventing the passage of small molecules to the brain parenchyma. However, at the same time, it has been shown to be present in all endothelial cells and thus is not specific for the brain endothelial cells (Nitta et al., 2003). Occludin, another essential brain tight-junction membrane protein, has been shown to be cell-specific for the brain endothelial cells but, on the other side, its presence does not seem to be required to maintain the normal function of the BBB (Saitou et al., 2000).

In conclusion, even if the underlying molecular events giving rise to the tight junctions remains poorly understood, it is certain that these tight junctions clearly represent a major obstacle for the passage of hydrophilic molecules, including drugs with potential therapeutic effects, to the CNS.

1.1.3 Factors Influencing the Drug Delivery to the Central Nervous System

Transport across the BBB

There are various transport processes that may occur at the blood-brain barrier, as graphically summarized in Figure 1.3

- *adsorptive mediated endocytosis*
- *carrier mediated endocytosis*
- *receptor mediated endocytosis*
- *active efflux transport (i.e. Pgp)*
- *transcellular lipophilic diffusion*
- *paracellular hydrophilic diffusion*

Adsorptive mediated transcytosis is initiated by the binding of polycationic substances (such as most cell-penetrating peptides) to negative charges on the plasma membrane (Bickel, 1995). This process does not involve specific receptors. Upon binding of the cationic compound to the plasma membrane, endocytosis occurs, followed by the formation of endosomes (Herve et al., 2008). However, vesicular transport is actively down regulated in the BBB to protect the brain from non specific exposure to polycationic compounds. Moreover, according to some authors, forcing drugs to enter the brain by adsorptive mediated transcytosis goes against the neuroprotective barrier function, as it has been shown for anionic and cationic nanoparticles that disrupted the BBB (Lockman et al., 2004, Jallouli et al., 2007).

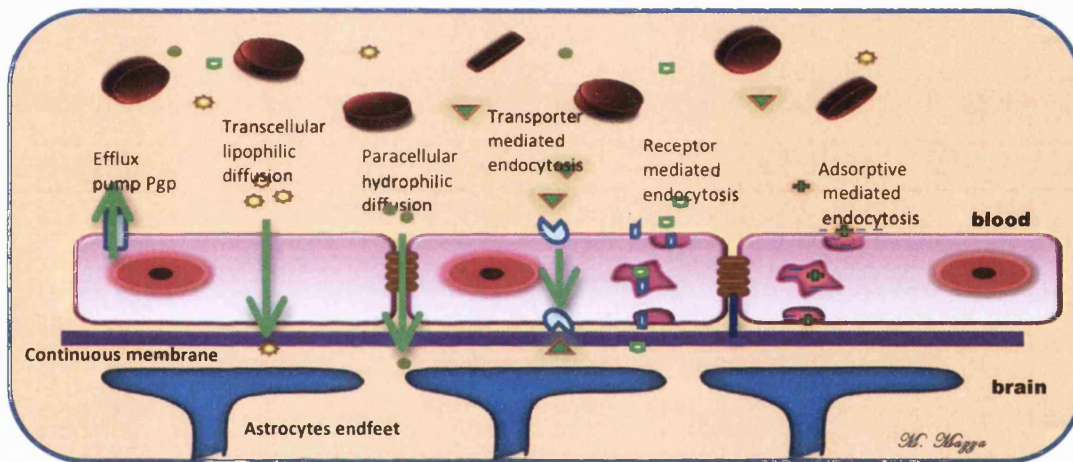


Figure 1.3: Graphical representation of the mechanisms of transport occurring at the level of the brain endothelial cells.

Carrier-mediated transcytosis is used for the delivery of nutrients, such as glucose, amino acids, and purine bases, to the brain. At least eight different nutrient transport systems have been identified, with each transporting a group of nutrients of comparable structure. Carrier-mediated transcytosis is substrate selective and only the drugs that closely mimic the endogenous carrier substrates will be taken up and transported into the brain (Tamai and Tsuji, 2000).

Receptor-mediated transcytosis enables larger molecules, such as peptides, proteins, and genes, to specifically enter the brain. Classic examples of receptors involved include (Pardridge, 2007):

- insulin receptor
- transferrin receptor
- insulin-like growth factor receptors (IGF1R, IGF2R)
- leptin receptor
- Fc fragment of IgG receptor (neonatal Fc receptor FCRN or FCGRT)
- scavenger receptor, class B, member 1 (SCARB1)

In addition, transporters are present at the BBB, such as the organic anion transporter (influx and efflux), the organic cation transport system (influx) and the nucleoside transporter system (influx) (Pardridge, 2007).

Drug Efflux Transporters in the blood-brain barrier

Almost 100% of large neuroactive agents and less than 2% of small therapeutics molecules are prevented from accessing their site of action in the CNS by the BBB (Pardridge, 2005).

The efflux transporter P-glycoprotein (P-gp) exerts a major role in the control of the passage of exogenous substance to the brain. There are an increasing number of studies showing that the activity of the efflux transporter (P-gp) at the BBB prevents significant accumulation of many hydrophobic molecules or drugs in the CNS (Loscher and Potschka, 2005). P-gp is a phosphorylated glycoprotein with a molecular weight of ~170Da. P-gp is part of the ATP-binding cassette transporters family, and most of these ATP-binding cassette transporters are also members of the superfamily of the multidrug resistance proteins (Loscher and Potschka, 2005).

There are two types of human P-gp: Type I encoded by the MDR1 Gene, which confers the drug resistance phenotype and drug efflux at the BBB, and a Type II encoded by the MRD2 gene, present in the canalicular membrane of hepatocytes and functioning as a phosphatidylcholine translocase enzyme (Schinkel, 1997).

Multidrug transporters such as P-gp are located on the luminal cell membrane of capillary endothelial cells and act as outwardly directed active efflux pumps, transferring part of the drug, which manages to enter the endothelial cell by diffusion, back into blood, thus limiting penetration (Schinkel, 1997) of many lipophilic drugs into the brain parenchyma. Furthermore, by lowering the drug concentration in the endothelial cells, these proteins indirectly may promote flux from the brain extracellular space into endothelial cells, followed by extrusion into the blood (Fromm, 2004).

P-gp may serve as a general defense mechanism in the BBB of vertebrates, protecting the brain from intoxication by potentially harmful lipophilic compounds from natural sources and other lipophilic xenobiotics, that could otherwise penetrate the BBB by simple diffusion without any limitation. However, the standard pathway for removal of intracellular peptides or proteins is still degradation rather than efflux (Fromm, 2004).

Physicochemical factors affecting the brain uptake: the rule of two

The majority of small-molecule drug candidates do not cross the BBB because the drugs are water-soluble and/or have a molecular weight (MW) of more than ~500 Da. In addition to small molecules, macromolecular drugs (e.g. recombinant proteins, monoclonal antibodies, gene medicines, antisense drugs) could act as potential neuropharmaceuticals, but essentially do not cross the BBB (Pardridge, 2002). These drugs are thus eliminated early-on from entering CNS drug development programmes because they do not cross the BBB and because no suitable brain drug (or gene) targeting technology is available (Pardridge, 2002).

There is a clear relationship between the lipid solubility of a drug and its CNS penetration (Levin, 1980). Consequently, the logP (octanol/water partition coefficient), a standard and convenient measure for lipophilicity, became a very useful physicochemical parameter used in pharmaceutical and medicinal chemistry. *In vivo* log cerebrovascular permeability data tend to correlate well with logP. In agreement with the structural aspects of the BBB there is a good correlation over a wide range of molecules of about eight log units between logP and *in vivo* log

permeability data of rat brain capillaries $\log P_{\text{BBB}}$ for compounds that are not subject to active transport, as depicted in Figure 1.4 (Bodor and Buchwald, 1999).

Yet, some lipophilic compounds, showed an unexpectedly low apparent transfer rate. This has been hypothesized to result from high binding to plasma proteins and/or a MW cut-off for transfer through BBB (Levin, 1980). Furthermore, active efflux by P-glycoprotein may also account for this behavior.

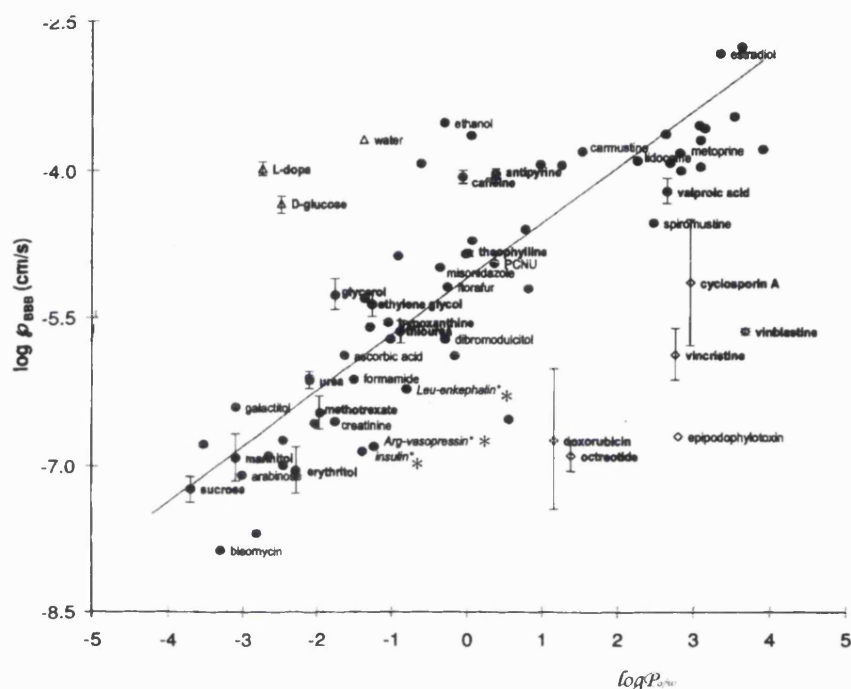


Figure 1.4: Graph showing the in vivo log permeability coefficient of rat brain capillaries ($\log P_{\text{BBB}}$) as function of log octanol /water partition coefficient ($\log P_{\text{o/w}}$). Names are shown for a few well known compounds; values denoted with a star are for guinea pig, and values denoted in italics are for cases where the log distribution coefficient measured at physiological pH was used ($\log D_{\text{o/w}}$). Strong deviants below the line, shown as diamonds, are known substrates for P-gp (Bodor and Buchwald, 1999).

Despite lipophilicity being a desirable property, increasing lipophilic character with the intent to improve membrane permeability might make chemical handling difficult.

It is difficult to formulate general rules, but Hansch suggested that, when designing prospective new CNS drugs, the likelihood of success is better if one starts

with an apparent calculated logP around 2. Alternatively, if CNS-related side effects are to be avoided it is probably better to avoid the $1 < \log P < 3$ region. This has been referred as the “rule of two”.

However, this linear relationship is only applicable if the MW of the molecule is below 400-600Da. If the MW of the drug exceeds this threshold, the BBB permeability is decreased by one to three log orders of magnitude from the value predicted solely on the basis of the lipid solubility of the compound.

Passive diffusion depends on lipophilicity and MW; furthermore, the ability of a compound to form hydrogen bonds will limit its diffusion through the BBB. As a general rule, the BBB permeability of a drug decreases 1 order of magnitude for each pair of H-bonds added to the molecule in the form of polar functional groups (Pavan et al., 2008). Apart from MW and H-bonding, drug levels achieved in the brain will also depend on its pharmacokinetics and the plasma area under the concentration curve (AUC) (Pavan et al., 2008). Increasing lipophilicity tends to increase the volume of distribution as well as other pharmacokinetic parameters, such as the rate of oxidative metabolism by cytochromes P450 and the ABC efflux transporters (Lewis et al., 2004, Lin and Lu, 1997, Smith et al., 2002, Abbott et al., 2010).

In addition to this, lipidization of the molecule will increase the uptake in all organs of the body, resulting in a decrease in plasma AUC; thus, the brain uptake of the drug, expressed as percentage of injected dose (ID/g) decreases in proportion to the decrease in plasma AUC caused by lipidization. In general, Lipinsky’s rule-of-five, as well as the Abraham’s Equation can be used to predict the passive transport of a drug molecule across the BBB (Abraham and Platts, 2000). The Abraham’s equation first correlated in vitro data sets of blood-brain distribution coefficients ($\log BB$) with in vivo data sets by means of hydrogen bonds descriptors. The general equation states

$$\log BB = -0.038 + 0.198R_2 - 0.687 \pi_2^H - 0.715 \Sigma\alpha_2^H + 0.995 V_x$$

where R_2 is an excess molar refraction, is the π_2^H dipolarity/polarizability, $\Sigma\alpha_2^H$ is the hydrogen bond descriptor and V_x is the solute McGowan volume in units of cubic centimeters per mole divided by 100.

Transport of hydrophilic compounds via the paracellular route is limited due to the presence of the tight junctions, whereas lipophilic drugs smaller than 400-600 Da may freely enter the brain via the transcellular route (Partridge, 2007). Peptides and

proteins are hydrophilic and, generally, are excluded from passive transport because of their hydrophilicity and large MW. Yet, some molecules may overcome these limitations using as alternative route endocytosis.

1.1.4 Endocytosis at the Level of the BBB

In all cells endocytosis can occur through at least four mechanisms: clathrin mediated endocytosis, caveolae mediated endocytosis, clathrin and caveolae independent endocytosis (still poorly understood), macropinocytosis.

At the level of the BBB there are some limitations associated with the caveolae mediated transport of substances from the luminal to the abluminal side of the endothelial cells. This transport process is limited by the low occurrence of caveolae in the brain capillaries (Tuma and Hubbard, 2003).

In contrast to the limited transcytosis activity determined by the low occurrence of caveolae, the brain capillary endothelial cells are characterized by a high density of negatively charged clathrin-coated pits/vesicles. In fact, brain capillaries endothelial cells present a luminal electrostatic barrier at physiologic pH (Vorbrodt, 1989). The negative electrostatic charge is created by surface expression and adhesion of the glycocalyx residues (Figure 1.5): proteoglycans, sulphated mucopolysaccharides and sulphated and sialic acid-containing glycoproteins and glycolipids that constitute the glycocalix (Vorbrodt, 1989).

These anionic sites are found both on the luminal and abluminal side, but in different distribution. On the luminal side, they are constituted of carboxylic acid groups present on glycoproteins containing sialic acid as their sugar moiety and there is a small percentage of sulfate groups belonging to heparan sulfate proteoglycans (Herve et al., 2008). The anionic sites on the abluminal side are mainly constituted of mixed proteoglycans (Herve et al., 2008). Heparan sulphates are the main glycosaminoglycans (GAGs) found on the glycocalix of the endothelial cells. On the cell surface, the heparansulphate proteoglycans are more abundant than the syndecans ($-\text{SO}_3^-$) and the glypicans ($-\text{COO}^-$). The basal membrane contiguous to the basolateral surface of the brain endothelial cells is also negatively charged, because of its glycosaminoglycans enriched in chondroitine and heparansulphate (the perlecan, the less common of the heparansulphate proteoglycans, is localized on the basal membrane). All three of these electrostatic barriers in series (luminal and abluminal

sides of the brain capillaries endothelial cells and basal membrane) create a selective anionic boundary to the positively charged substrates (Herve et al., 2008).

This anionic boundary repels anionic molecules except those targeted to specific transporters/receptors and lies at the bottom of the mechanism of Adsorptive Mediated Transcytosis (AMT).

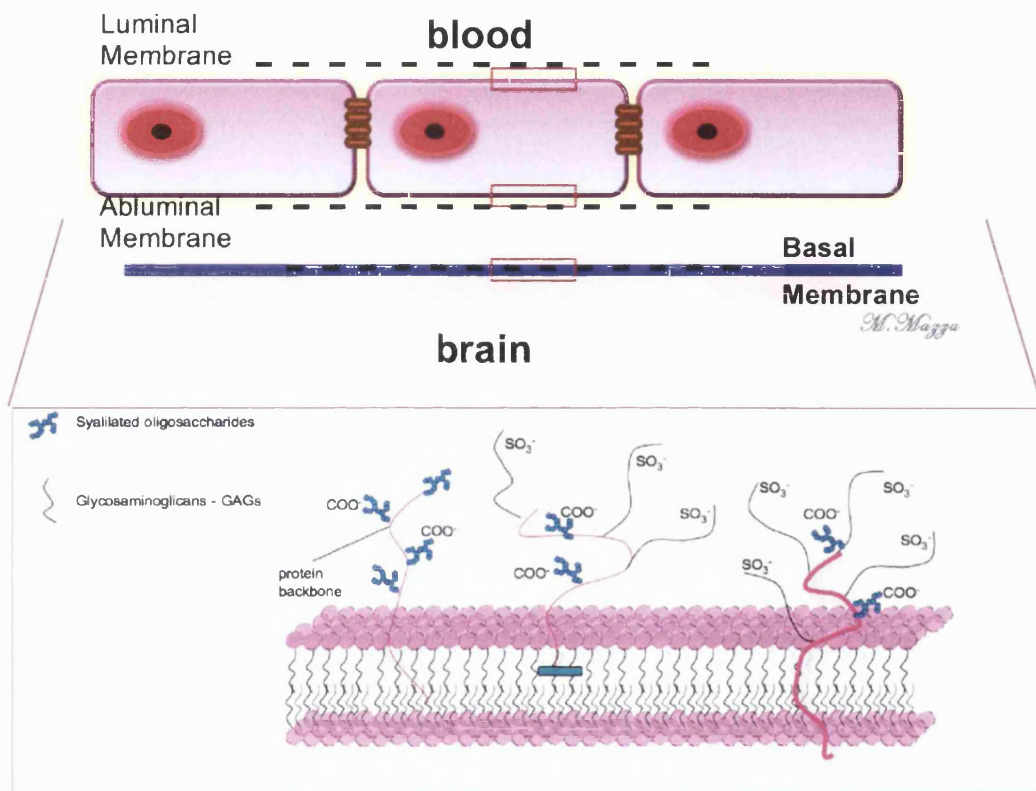


Figure 1.5: (A) electrostatic negative barrier in series creating a selective anionic ambient for positive substrates; (B) Schematic illustration of major membrane-surface glycan-containing components.

AMT through the blood brain barrier was originally observed when polycationic proteins, such as protamine, were able to not only bind to the brain endothelial cell surface, but also to penetrate the BBB in rats dosed with albumin bound to protamine (Pardridge et al., 1993), thus the cationic charge has been considered as an important factor for the uptake of molecules at the level of cerebral capillaries.

1.1.5 Nanomedicine: a Solution to Brain Delivery?

For CNS drug discovery programs brain penetration of new compounds is a key property to be addressed (Reichel, 2009b), as many factors influence the penetration of a drug into the brain, the distribution in the parenchyma and the clearance from the tissue, as summarized in Figure 1.6:

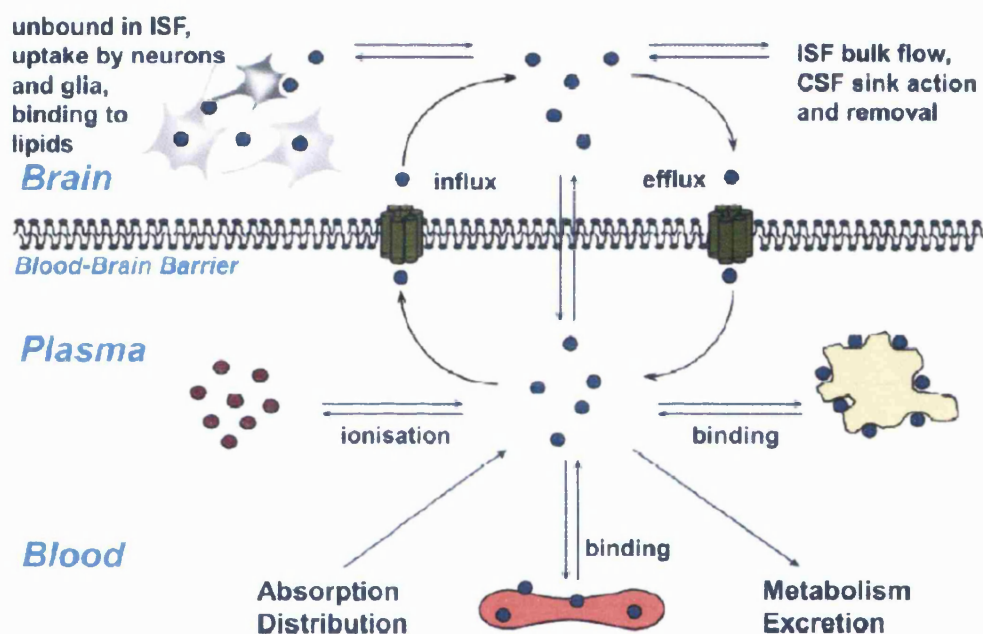


Figure 1.6: Drug penetration in the CNS. Summary of the processes that contribute to the drug penetration, distribution and clearance of drugs. (ISF= interstitial fluid; CSF= cerebrospinal fluid). Adapted from (Reichel, 2009b).

The BBB transport controls the rate of transport from blood to brain, and vice versa, via passive diffusion, active uptake, or efflux transport processes.

As a rule of thumb for CNS penetration it is known that as the molecular weight of a molecule increases the CNS penetration on average decreases, furthermore molecular weight influences also binding of molecules to plasma proteins: molecules with a MW of <300Da are 72% bound to plasma proteins while those with a MW between 300 - 500 are 54% bound and those with MW between 500

- 700 are 98.2% bound. Basic molecules are in average more likely to enter the CNS compared to neutral, zwitterions and acidic molecules (less likely). The binding to plasma protein is higher for acids, followed by neutral species and zwitterions, with basic drugs being the least protein bound. Lipophilicity also leads to a direct increase in protein binding. Drugs which are highly protein bound: acidic drugs and drugs of high molecular weight are thus less likely to cross the BBB (Gleeson, 2008).

Another factor to be taken into account when considering brain penetration of a drug is the molecule tissue binding, as it is the unbound drug fraction that elicits the pharmacological action, rather than the total amount in brain (Reichel, 2009b, Gleeson, 2008).

Considering the complexity of the morphological structures of the CNS and the complexity of the processes that regulate drug penetration in the brain, it is easy to understand why most biopharmaceuticals based on antibody fragments, proteins and peptides are prevented from entering the brain because of their high molecular weight, the charges at physiological pH and their hydrophilicity. Thus, nanomedicines could bring a solution to this hurdles, protecting the molecules from enzymatic degradation and protein binding in the blood and facilitating the overcoming of the BBB without the need to use invasive methods such as intrathecal administration (Hayek et al., 2011), brain implantation (e.g. Gliadel® wafer for the treatment of glioblastoma) (Attenello et al., 2008), or temporary BBB disruption (McDannold et al., 2007).

The global market value for therapeutic drugs for CNS disorders was an estimated \$79 billion in 2010, but is expected to increase to nearly \$82 billion in 2015 (bbcresearch.com, 2010), however at the present time 98% of the drugs are excluded from entering the brain (Pardridge, 2005).

The need of strategies enabling therapeutic molecules to cross the BBB has seen a boost in publications in the recent years as a consequence of an enormous increase in investments also from the public sector, promoting the collaboration of researchers working in different scientific areas (neuroscience, materials, pharmaceutics, biophysics) on the discovery of nanomedicine based systems for drug delivery to the brain (Europe CORDIS FP7 NMP.2011.1.2-2; New targeted therapy using nanotechnology for transport of molecules across the biological blood-brain barrier - EPSRC Nanotechnology Grand Challenges Healthcare (EPSRC, 2009)).

1.1.6 Carriers Used in Drug Delivery to the Brain

Nanocarriers injected by the systemic route and used for drug delivery should ideally possess some essential characteristics. They need to be

- biodegradable
- biocompatible
- non-immunogenic
- physically stable in the blood

In the recent years many new strategies have been investigated as potential technology platforms for brain delivery.

Nanoparticles are solid colloidal particles ranging in size from 1 to 1000 nm (1 μ m) consisting of macromolecular materials in which the active principle (drug or biologically active material) is dissolved, entrapped, or encapsulated, or to which the active principle is adsorbed or attached (Kreuter, 2006b).

Early studies with poly-(butyl cyanoacrylate) nanoparticles were conducted using the model drug dalargin and overcoating these particles with polysorbate 80: after i.v. injection a dose-dependent analgesic effect was observed using the tail flick test and the hot-plate test; the observed analgesia was attributed to central action of the Leu-enkephalin derivative (Ramage et al., 1999). Up to 3-fold higher concentrations in brain homogenates were found with the polysorbate 80-coated nanoparticles (0.01% coating) than with dalargin solution in a study where mice were dosed intravenously with formulations containing radiolabelled Dalargin bound to the nanoparticles (Schroeder et al., 2000, Kreuter, 2006a).

In other studies, polybutylcyanoacrylate nanoparticles loaded with doxorubicin and coated with polysorbate 80 were tested on mice after tail vein injection. 35% of these animals survived for over 180 days (termination of the experiments) (Ambruosi et al., 2006).

In light of these findings, nanoparticle surfactant coating was considered as a new potential approach to improve brain drug uptake. Other surfactants, such as poloxamers 184, 188, 338, 407, poloxamine 908, Cremophor EZ, Cremophor RH40, and Brij 35 were totally or almost inactive (Troster et al., 1990). Furthermore, other drugs that normally do not penetrate the blood brain barrier, such as tubocurarine, loperamide, 8-chloro-4-hydroxy-1-oxol, MRZ 2/576 (a novel NMDA receptor

antagonist) and doxorubicin showed higher brain concentrations when associated with P80-coated NPs (Blasi et al., 2007).

However, *in vitro* studies showed that the polysorbate 80 coating was causing increased non-specific permeabilization of the blood-brain barrier, which could be imputable to the toxicity of the carrier (Olivier et al., 1999).

The major limiting factor for the systemic use of nanoparticles is their rapid clearance by the reticuloendothelial system (RES). Nevertheless, nanoparticle-surface-bound PEG chains can prevent the opsonisation and rapid capture by the RES of these carriers and thus prolong the blood circulation time. Couvreur and co-workers showed that polymeric nanoparticles made of poly (hexadecyl cyanoacrylate), PHDA, and conjugated to PEG penetrated into the brain, as established by radioactivity counting after intravenous administration in mice and rats of the radiolabelled ¹⁴C-PHDA nanoparticles (Calvo et al., 2001).

When an exogenous particulate material is exposed to serum or plasma, proteins readily adsorb on its surface influencing its fate in the body, thus a differential adsorption targeting concept was developed to postulate that an adsorption of the Apo proteins on nanoparticles could be responsible for the interaction with the BBB and the subsequent endocytosis (LDL receptor mediated) (Muller and Keck, 2004).

Accordingly, Kreuter *et al.* (Kreuter et al., 2007) have shown that the covalent attachment of ApolipoproteinE3, Apolipoprotein A-I as well as Apolipoprotein B-100 to human serum albumin nanoparticles via the NHS-PEG-Mal 3400 linker enables the transport of drugs across the blood brain barrier. Loperamide was used as a model drug, and it was bound to these nanoparticles; the antinociceptive reaction of these preparations was recorded after intravenous injection in mice by the tail-flick test. The maximal possible effect (MPE) of the antinociceptive response of mice was then recorded. Nanoparticles with ApolipoproteinE3 showed the highest antinociceptive effects of almost 100% after 15 min. The antinociceptive effect with apolipoprotein A-I was around 65% and those of nanoparticles with Apolipoprotein B100 below 50%. The loperamide-loaded unmodified nanoparticles, and loperamide solution produced no considerable effect (MPE below 20%).

Nanoparticles have also been studied as carriers for Paclitaxel (Kozziara et al., 2004), an antineoplastic drug with very low solubility in water and many pharmaceutically acceptable solvents. The commercially available Paclitaxel (Taxol®) is dissolved in a mixture 50:50 of Cremophor EL and dehydrated ethanol. Cremophor EL causes acute hypersensitivity reactions, one of the most severe side effects associated with administration of Taxol (Singla et al., 2002). Paclitaxel is also a substrate of the Pgp efflux pump (Gallo et al., 2003), and so virtually unable to cross the BBB. Paclitaxel promotes assembly of microtubules from tubule dimers and prevents them from depolarizing leading to loss of normal microtubule dynamics necessary for cell division and other vital processes, and consequently causes cell death (Kozziara et al., 2004). The ability of paclitaxel to stabilize the microtubules makes it an effective agent against various types of cancers, and the loading of Paclitaxel in nanoparticles significantly increases the drug brain uptake (Kozziara et al., 2004).

Polymeric nanoparticles for drug delivery to the CNS have also been prepared with hydrophilic polymers such as chitosan (Aktas et al., 2005). Chitosan is a cationic polysaccharide in neutral conditions and contains free amino groups which can undergo protonation, thus making chitosan soluble in acid pH. Chitosan-PEG nanoparticles have been functionalized with the monoclonal antibody OX26, which shows high affinity for the transferrin receptor and facilitates the translocation into the brain tissue after i.v. administration of the nanocarriers (Aktas et al., 2005). The authors confirm the translocation of the nanoparticles from the blood vessel to the brain interstitial fluid by observing the tissue samples taken from the dosed mice under TEM. However, from the control picture this is not easy to say, as the control picture seems to belong to a different brain area.

Recently, nanoparticles made of methoxy poly(ethylene glycol) (MPEG)/poly(ϵ -caprolactone) (PCL) amphiphilic block copolymers have been modified by attachment of a TAT analog cell penetrating sequence through an ester bond. The nanoparticles were loaded with coumarin and both the nasal and IV routes of administration were investigated. The nanoparticles were able to deliver the coumarin to the brain and the amount of coumarin in the tissue was assessed quantifying the coumarin fluorescence. After intranasal administration the amount of

coumarin detected was significantly higher than that after intravenous administration (Kanazawa et al., 2011).

Similar strategies to the use of polymeric nanoparticles have been adopted for the investigation of Solid Lipid Nanoparticles (SLN) for drug delivery to the brain.

SLNs are composed of a solid lipid matrix stabilized by surfactants. The lipids used (triglycerides, complex glyceride mixtures and waxes) have the peculiarity of remaining in solid form at both room and physiological temperatures (Blasi *et al.*, 2007). The physical stability of SLNs, the use of bioacceptable and biodegradable lipids, the size in the nanometer range and the protection of the encapsulated drug are promising features for parenteral administration of SLNs. However, the drug loading capacity is limited by the weak solubility of drugs in the lipid melt and drug expulsion after polymorphic transition (Freitas and Muller, 1999).

The phagocytosis of SLNs can be controlled by modifying their surface properties, as has been done for liposomes and polymeric micro- and nanoparticles, in this way, it is possible to target molecules to the brain by limiting RES uptake (Owens and Peppas, 2006).

Clozapine loaded tripalmitin SLN with and without stearylamine were able to significantly increase drug brain concentration after intravenous administration in mice when compared to clozapine suspension (Manjunath and Venkateswarlu, 2005). Unfortunately, the strategy of using surface charged SLN, or NPs in general, to cross the BBB has shown some important drawbacks (Lockman et al., 2004). Neutral, negatively and positively charged SLN were loaded with tobramycin in a study by Bargoni *et al.* (Bargoni et al., 2001) and their rat BBB permeability was studied using *in situ* brain perfusion. Neutral SLNs or low amounts of negatively charged SLN showed no effect on the cortical cerebrovascular volume, indicating a good BBB integrity. Higher amounts of negatively charged SLN or positively charged SLN significantly increased the cortical cerebrovascular volume pointing to a BBB disruption.

Dendrimers, having a hydrophobic core and hydrophilic surface layer, have been termed unimolecular micelles, they present a high drug-loading capacity, and they can solubilise poorly soluble drugs by encapsulating them within the dendritic structure (D'Emanuele and Attwood, 2005). As explained by Najlah *et al* (Najlah et

al., 2006), transport studies of PAMAM dendrimers across Caco-2 cell monolayers revealed that cationic dendrimers decrease transepithelial electrical resistance and increase the permeability of the paracellular marker mannitol at concentrations that were shown to be non-toxic to cells, suggesting that PAMAM dendrimers modulate the tight junction between Caco-2 cells, although no evidence of tight junction modulation was presented in the study.

Transferrin-conjugated polyethyleneglycol-modified polyamidoamine dendrimer have also been evaluated as gene delivery system to the brain. The brain gene expression in mice dosed with the dendrimer formulatio of the PAMAM-PEG-Tf/DNA complex was examined and found to be $3.08 \pm 0.38 \times 10^3$ units/mg protein, ~2-fold higher than that of the PAMAM/DNA complex ($1.46 \pm 0.41 \times 10^3$ units/mg protein) and PAMAM-PEG/DNA complex ($1.35 \pm 0.20 \times 10^3$ units/mg protein) (Huang et al., 2007).

Actually, several new nanotechnology platforms have been investigated as potential carriers for drug delivery into the brain.

Water-soluble nanoformulations of fullerene (C(60)) have been prepared using poly(N-vinyl pyrrolidone) (PVP) or poly(2-alkyl-2-oxazoline)s (POx) homopolymer and random copolymer to form nano-complexes with fullerene. Cellular uptake and intracellular distribution of the selected formulations in catecholaminergic (CATH.a) neurons was then examined (Tonga et al., 2011). Surprisingly the authors claim that C(60)-POx complexes are not only neuronal cell permeable and superoxide scavenging antioxidants, but are also non-toxic, however *in vivo* toxicology has not been evaluated.

Polyelectrolyte multilayer-coated gold nanoparticles incorporating human serum albumin were injected into the tail vein of healthy mice and the biodistribution was characterized in detail (Sousa et al., 2010). Microscopy of brain slices verified that the nanoparticles were localized to specific brain regions.

Many ligands have been successful in delivering nanomedicines across the BBB, however recently to compare which targeting ligand is the best a study employing liposome was carried out (van Rooy et al., 2011b). Liposomes were targeted with transferrin, the monoclonal antibody RI7217, the apo-E mimetic peptide COG133, angiopep-2, and the mutated form of diphtheria toxin CRM197. Only the RI7217 was

able to significantly enhance brain uptake *in vivo* at all time points. Uptake in the brain capillaries was up to 10 times higher compared to untargeted liposomes (van Rooy et al., 2011b).

The report from van Rooy et al. is of particular interest, also because many spin off companies from universities have come up in recent years each one proposing different solutions to the BBB challenge. For example, Angiochem in Canada, has just recently published a new report on the use of their vector technology Angiopep for the delivery of doxorubicine and etoposide to the brain (Che et al., 2010). A further example is the company *toBBB* in the Netherlands, which first optimized the use of CRM197 for targeted delivery to the brain purposes (Gaillard and de Boer, 2006). *toBBB* has also intensive industrial collaborations for the development of their new liposome based technology for brain delivery, G-Technology®, consisting of liposomes coated with glutathione-conjugated polyethylene glycol (PEG) (*toBBB.com*, 2011).

An interesting approach to brain delivery is the use of phagocytic cells of the innate immune system; neutrophils and monocytes, may then be exploited as transporters of drugs to the brain (Afergan et al., 2008). Negatively-charged nano-sized liposomes were formulated encapsulating serotonin, a BBB impermeable neuroactive drug. These liposomes were targeted by the circulating mononuclear phagocytic cells, uptaken and carried to the for brain parenchyma (Afergan et al., 2008).

The low-density lipoprotein (LDL) receptor has also been identified as a target for brain delivery. A synthetic Nano-LDL containing paclitaxel oleate (nLDL-PO) was constructed by combining a synthetic peptide containing a lipid binding motif and the LDL receptor (LDLR) binding domain of apolipoprotein B-100 with a lipid emulsion consisting of phosphatidyl choline, triolein, and paclitaxel oleate for targeted delivery to glioblastoma multiforme (Nikanjarn et al., 2007).

Considering that the LRP receptor for LDL is one of those receptor expressed on the BBB luminal side it is possible that further studies could demonstrate the brain permeability to this nanoparticles.

Sialic acid and glycopeptide conjugated PLGA nanoparticles loaded with loperamide have been also explored as carriers for brain delivery: the IV administration to mice of the formulation resulted in a pronounced analgesic effect, thus demonstrating that the carrier was enabling the drug to reach the opioid receptor centrally expressed, while loperamide on its own is unable to get across the BBB (Tosi et al., 2010).

Engineered fusion protein, also known as molecular Trojan Horses, have been investigated as drug carriers for the delivery of peptide and proteins to the brain. The principle of delivering peptide and proteins to the CNS utilizing a Trojan Horse is depicted in Figure 1.7.

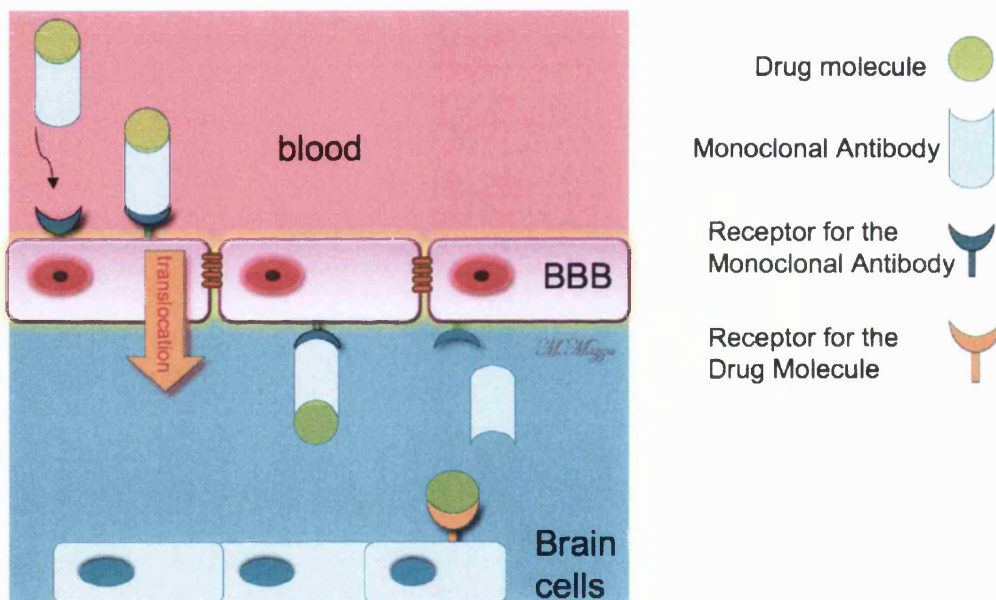


Figure 1.7: Delivery of biopharmaceuticals by means of Trojan Horses. The molecule of interest is conjugated to a monoclonal antibody that targets a receptor expressed on the luminal side of the brain endothelial cells. The binding to the receptor determines the formation of a complex that is released in the interstitial fluid. The molecule is cleaved from the monoclonal antibody and exerts its pharmacological action on the brain receptors.

This chimeric (or fusion peptide) technology can be used to deliver recombinant proteins and monoclonal antibody-based therapeutics. In the avidin-biotin technology, a fusion protein of the molecular Trojan horse and avidin is

produced parallel with monobiotinylation of the therapeutic, which might be an oligopeptide, an antisense agent, or an siRNA. Non-viral plasmid DNA can be delivered across the BBB by formulating liposomes with MTHs and production of Trojan horse liposomes (Pardridge, 2007).

Pharmacokinetics studies in mice showed that the fusion protein was rapidly cleared from blood with a median residence time of 175 +/- 32 min. The fusion protein was avidly taken up by brain with a % injected dose (ID)/g of 3.5 +/- 0.7, as compared to a MAb with no receptor specificity, which was 0.06 +/- 0.01% ID/g (Boado et al., 2010).

The “fusion protein technology” has also been used in combination with liposomes, and Trojan Horse Liposomes have been used for non-viral gene delivery (Boado, 2007).

Despite these promising findings, it has always to be remembered for this chimeric technologies that the Trojan horse not only has to cross the BBB but also has to elicit a pharmacological response on the central receptors. One problem can be that once engineered with the monoclonal antibody the therapeutic peptide or protein might not retain its pharmacological activity. Moreover, exerting the pharmacological activity may require cleavage from the transport vector, in which case the action of enzymes would be involved. Thus, the choice of the vector, the linker and the retention of activity are very important and might limit the development of these technologies in the real life.

The general overview undertaken in this section is symptomatic of the fact that despite enormous efforts, achieving in a safe and efficacious manner delivery of therapeutics in the brain remains still an open challenge.

Not all the technologies that aim at the delivery across the blood-brain barrier are successful in vivo. A summary of the technologies that have aimed to show in vivo achievements are reported in Table 1.

Table 1.1 – Summary of several nanotechnology platforms tested *in vivo* for drug delivery to the brain. Adapted from (van Rooy et al., 2011a, Costantino et al., 2009)

<i>Particle</i>	<i>Drug/molecule</i>	<i>Dose</i>	<i>Test</i>	<i>% ID brain</i>	<i>Reference</i>
Liposome + RMP7	Evans blue	1g/kg	Formamide extracting–ultraviolet-spectrophotometric method	Non-targ 0.002% Targ 0.012%	(Zhang et al., 2004)
Liposome + RMP7	¹²⁵ I-NGF	200 µg/kg	gamma counting	Non-targ 0.11% Targ 0.32%	(Xie et al., 2005)
Liposome + OX26	³ H-daunomycin	20 m Ci/kg	liquid beta scintillation counting	Non-targ 0.005% Targ 0.01%	(Schnyder et al., 2005)
SLN	Prodrug DO-FUDR	20mg/kg	Biodistribution using HPLC	Released drug 2.08% SLN drug 2.66%	(Wang et al., 2002a)
SLN+thiamine	³ H-hexadecanol and ³ H-thiamine	5mg/kg	Radioactivity by gamma counting	Both 0.5 %	(Lockman et al., 2003)
BSA nanoparticles + Transferrin	Compound AZT	54.4mg/kg	Biodistribution using HPLC	Non-targ 9.3% Targ 21.1%	(Mishra et al., 2006)
PMMA nanoparticles + Poloxamer 407,908 ot tween 80	Methyl ¹⁴ C-methacrylate	0.01mL/g 1.128 mg/mL	Liquid scintillation counting	Non-targ 0.088% Targ 0.99%	(Lode et al., 2001)
PAMAM nanoparticles + Angiopep-2	p-EGFP	50 µg/mouse	(¹²⁵ I) Radioactivity by gamma counting	Non-targ 0.03% Targ 0.25%	(Ke et al., 2009)
nanogel	³ H-ODN	50µM/mouse	Liquid scintillation counting	2.67%	(Vinogradov et al., 2004)
PLGA nanoparticles + TAT peptide	³ H-ritonavir	45mg/kg	Liquid scintillation counting	Non-targ 1.08% Targ 7.1%	(Rao et al., 2008)
PLGA nanoparticles + g7 peptide	loperamide	68 µg/kg of Rh-123	Biodistribution by HPLC (detection of rodamine not of loperamide)	Non-targ low % Targ 15%	(Vergoni et al., 2009)
PLGA nanoparticles + g7 peptide	loperamide	68 µg/kg of Rh-123	Biodistribution by HPLC (detection of rodamine not of loperamide)	Non-targ low % Targ 14.3%	(Tosi et al., 2010, Rao et al., 2008)

In particular, for peptide and proteins technological challenges relating to the crossing of the blood-brain barrier, the instability in vivo and the short half-life of these molecules are not a trivial problem (Brasnjevic et al., 2009). The goals to be addressed should involve the development of pharmacological strategies able to increase the permeability of the blood-brain barrier, to facilitate the transport of drugs over the BBB and to realize innovative drug formulations that increase stability and half-life of peptide and proteins (Huang et al., 2007) .

For these reasons peptide delivery to the brain is one of the most promising and challenging areas in the CNS pharmaceuticals sector.

1.2 Introduction to Nanofibres and their Potential in Drug Delivery

1.2.1 Peptides as Therapeutics for CNS Disorders

There is no full agreement among researchers in making a net distinction between what can be defined peptide and what is instead a protein. For example, insulin has a sequence of 51 amino acids and is referred to as a peptide by some authors and as a protein by others. However, in general can be said that amino acids up to 50 residues constitute a peptide, while longer sequences form a protein. This limit is set by what is achievable in normal solid phase peptide synthesis as a maximum sequence length (van der Walle CF and O, 2011).

Peptides and proteins are involved in a wide range of roles at level of the Central Nervous System, acting as transmitters and signaling molecules for the regulation of numerous biological actions, maintenance of the homeostasis of the brain, modulation of intake and release of nutrients, neurotransmitters and neuromodulators at the level of the blood-brain barrier, modulation of the immune system and the hormonal regulation as well as many other brain controlled biological activities in our body (Krieger, 1983). For this reason, peptide and proteins have been identified as promising pharmaceuticals in the treatment of a variety of brain pathologies, including cancer, Alzheimer's Disease, Parkinson's Disease and cerebrovascular stroke (Brasnjevic et al., 2009, Dufes, 2011).

This thesis introduces the use of peptide nanofibres made of short amphiphilic peptides as a means of delivering such peptides to the brain following intravenous injection. In this section, self-assembly and current applications of peptide nanofibres will be reviewed.

1.2.2 Nanofibrous Systems

Nanofibrous systems are able to mimic the architecture of naturally occurring cellular structures (i.e tethers and extracellular matrix components), present a high surface to volume ratio, and are constituted of biocompatible materials. For these reasons nanofibrous materials are being applied in the fields of regenerative medicine as cell signaling carriers and drug delivery systems. The nature of the biocompatible materials employed for the construction of nanofibrous systems can be of two kinds, polymer based or peptide based.

This distinction is necessary because the techniques and the chemical conditions involved in the preparation of such systems are completely different.

Polymer based nanofibres are prepared through an electrostatic spinning process or *electrospinning*: a high voltage current is applied on a molten polymeric material or on a polymer solution in order to form a charged polymer jet. As the jet flies in air, the repulsive forces in the solution and the attractive forces between the liquid and the collector exert a tensile force on the solution or the molten polymer causing an acceleration of the jet that leads to elongation and formation of fibres in the nanoscale range (Formhals, 1938). Electrospun nanofibres are prepared starting from a molten polymeric material or from a polymeric solution that involves the use of organic solvents such as Dichloromethane (DCM), Dimethylformamide (DMF), Hexafluoroisopropanol (HFP), Tetrahydrofuran (THF), and the diameter of the ejected nanofibre is influenced by many factors. Firstly, the fibres generating from the apex of the droplet have a diameter significantly smaller compare to the diameter of the ejecting capillary needle or pipette; this is due, as observed by Taylor (Taylor, 1969), to the formation of the Taylor cone developing from the droplet when electrostatic forces are balanced by surface tension. The solution viscosity also influences the diameter of the electrospun nanofibres, increasing the viscosity of the

medium will increase the diameter of the fibre, as observed by Baumgarten in 1971 (Baumgarten, 1971), but this is always ranging from $>100\text{nm}$ up to μm .

Electrospun polymer nanofibres are currently employed as drug delivery carrier as well as materials for tissue engineering.

A wide number of therapeutic agents have been physically or chemically loaded in the hollow of the polymeric nanofibres or on the surface for the controlled release formulation of anti-cancer drugs (Lv et al., 2008), antibiotics (Lochman et al., 2010, Bolgen et al., 2007), genes (Cao et al., 2009), proteins (Choi and Yoo, 2010, Gelain et al., 2010) and growth factors (Sahoo et al., 2010).

Electrospun Nanofibrous meshes are excellent candidates for tissue engineering, indeed they have been employed for bone tissue regeneration (Jang et al., 2009), stem cell engineering (Lim and Mao, 2009), neural (Cao et al., 2009) and cardiovascular tissue engineering (Sell et al., 2009).

The peptide based nanofibre fabrication process is mediated by the formation of non-covalent H-bonds that accomplish the spontaneous organization of molecules into ordered structures. Therefore, the formation of peptide nanofibres is a *self-assembling process* that occurs in aqueous media and gives rise to the formation of regular micellar aggregates with diameters ranging from 5-8 to 20nm, being then at least one order of magnitude smaller than polymer nanofibres (Hamley, 2011).

Similarly to their polymeric nanofibres, peptide nanofibres find a wide range of application in tissue engineering.

Peptide nanofibres have been investigated for tissue and nerve regeneration, as cell scaffolds and as delivery carrier for anticancer therapy. In a mouse spinal cord injury model peptide nanofibres promoted the regeneration of descending motor neurons and ascending sensory neurons (Tysseling-Mattiace et al., 2008).

Hydrogels formed by the entanglement of peptide nanofibres provide a stiff network mimicking the extracellular matrix which promotes the adhesion of fibroblasts and cell proliferation, suggesting the possible employment of these gels as material for cell anchorage (Zhou et al., 2009).

Nanofibres including a peptide sequence known to activate a mechanism that culminates in membrane disruption have been internalized by breast cancer cells inducing their death (Standley et al., 2010).

In this work we have investigated the ability of peptide nanofibres to deliver peptides across the BBB and we are the first to do so.

1.2.3 Self-Assembling Peptide Nanofibres

Molecular self-assembly is a process in which molecules spontaneously form ordered aggregates and involves no human intervention (Whitesides and Boncheva, 2002) and is governed by non-covalent interactions and structural compatibility among the individual molecule monomers taking part in the aggregation process.

Self-assembling of peptide nanostructures mimics this natural process ubiquitous among many class of natural compounds, from lipids to complex viral structures.

Peptides adopt specific configurations depending on which amino acids are near one another in a peptide chain. As a consequence there is a relationship between amino acid sequence and structure and considering that there are 20 natural amino acids the supramolecular architectures that can arise are more than one (Figure 1.8). In peptide based nanomaterials, the structure formed by a single peptide can interact with another complementary peptide via non-covalent interactions: ionic, hydrophobic, hydrogen bonding and π - π stacking (Ulijn and Smith, 2008).

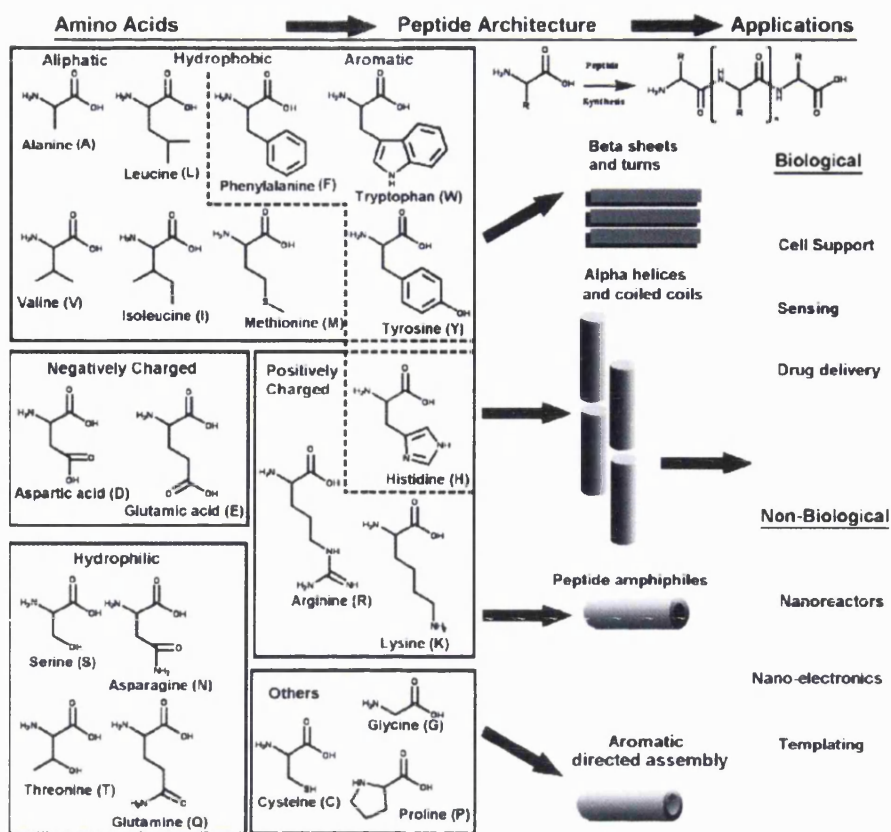
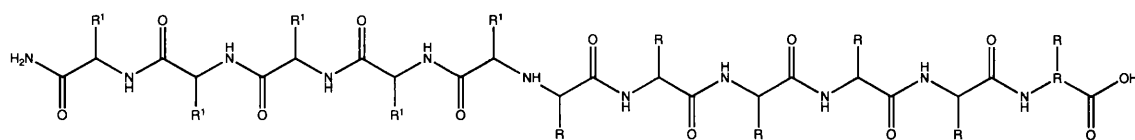


Figure 1.8: Amino acid structures are shown with their common name and the one-letter abbreviations that are commonly used in peptide sequences. The four main classes of possible architecture that peptides can adopt are shown with potential applications for these architectures. Adapted from (Ulijn and Smith, 2008)

The chemical structure of self-assembling peptides resembles the architecture of surfactants thus there is a hydrophilic region, often made of charged amino acids, and a hydrophobic part, this last can be tailored by introducing a sequence of lipophilic amino acids or by attaching an alkyl chain at the terminus of the peptidic sequence, as schematized in Figure 1.9.

The peptide sequence of the self-assembling peptide can include different epitopes in order to obtain the biological effect of interest.

(a)



R= hydrophilic side chain

R¹= lipophilic side chain

(b)

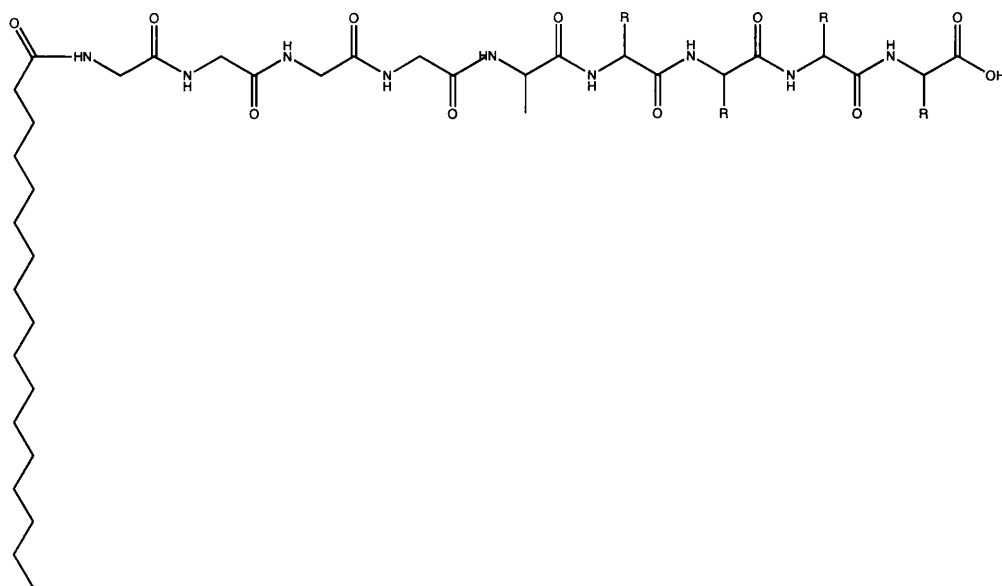


Figure 1.9: (a) A self-assembling peptide composed of hydrophilic and hydrophobic amino acids; (b) A peptide amphiphile formed by the attachment of an alkyl chain at the one of the sequence termini.

The self-assembly of peptides can involve the formation of aggregates of different shape, depending on the equilibrium among all the weak forces that play a key role in the aggregation process. In fact, although the interactions involved are weak *per se*, all together they are able to form strongly organized structures, ranging from small spherical like micelles to high axial ratio nanostructures Figure 1.10.

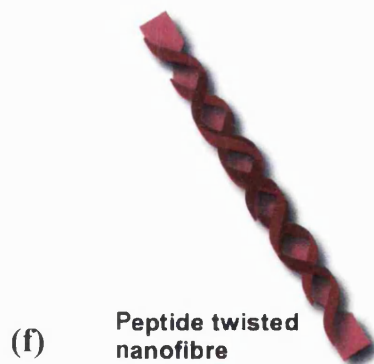
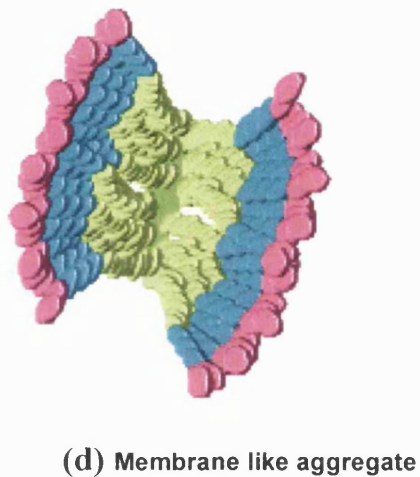
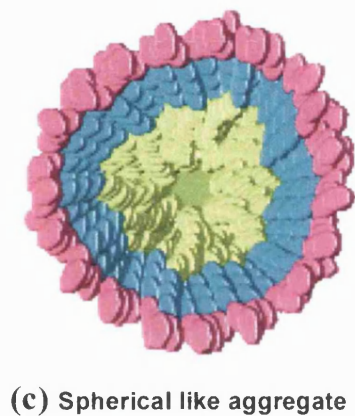
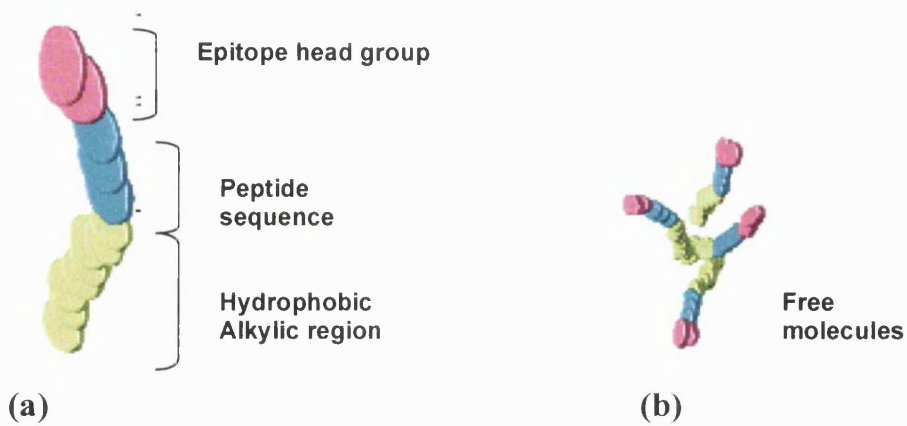


Fig 1 Self-assembly of a peptide molecule suitable for self-assembly; (b) micellization is started by the non polar region of free molecules moving toward each other in order to escape the surrounding aqueous environment; (c) the close association of single molecules can lead to the formation of spherical like micellar aggregates; the formation of β -sheets can lead to formation of membrane like aggregate (d) or nanofibres (e, f).

Spherical like micelles often represent an intermediate structure later evolving into fibrillar aggregates. Nanovesicles were observed in the earlier studies on amphiphilic peptides conducted by Zhang (Zhang et al., 2002) on a V₆D peptide (peptide sequence containing 6 hydrophobic valines and an aspartic acid residue resulting in two negative charges, one from the C-terminus and one from the side chain), the peptide was aggregating in nanovesicles. Also spherical nanovesicles can be the dominant aggregation form for a defined surfactant like peptide depending on solution conditions, pH and salinity, as observed by Tsonchev (Tsonchev et al., 2008).

Morphology can also be influenced by the concentration of the peptide in the solution; Aulisa observed that for the same peptide the shape was a function of its concentration in solution; at low concentration the peptide amphiphile studied (a peptide containing an inhibitory sequence for HOX proteins, the so called sequence *penetratin*, that helps the transport of molecules across the cell membrane, and a palmitic acyl chain) was organized into spherical micelles, while at higher concentrations the peptide amphiphile formed nanofibres (Aulisa et al., 2009b).

Baumann also observed that increasing concentrations of peptide could give rise to the sheet like formations (Baumann et al., 2008). Deng has observed that nanoribbons can be constructed as the peptide backbones form intermolecular hydrogen bonds perpendicular to the ribbon's long axis in a small twisting angle as a result of the steric hindrance of the amino acid side chains, which cause the ribbon to twist (Deng et al., 2009b). Alternating tetrapeptide sequences with hydrophobic and negatively charged residues (V and E) and alkyl segments with 16 carbons have been shown to self-assemble into 1D nanostructures that grow laterally to create nanobelts (Cui et al., 2009).

Some authors report the presence of helical nanofibres as intermediate structures in the formation of fibres (Marini et al., 2002, Cui et al., 2009).

In general one can say that peptide amphiphiles can form metastable micellar aggregates of various morphologies, but these initial structure evolve into cylindrical nanofibres (through the formation of β -sheet interactions).

1.2.4 Mechanism of Self-Assembly

The self-assembly of small amphiphilic polymers has been widely investigated. Amphiphilic polymers contain hydrophobic regions and separate hydrophilic regions, and they will self assemble in aqueous media into micelles, vesicles or tubules due to an hydrophobic effect that drives the non polar region of each polymer molecule away from water and towards one another.

Self-assembly of surfactant like peptides is governed by hydrophobic interactions between alkyl tails and a network of hydrogen bonding between the amino acids of the peptidic sequence (Zhang et al., 2002). The dimension and shape of the supramolecular structures formed from such assemblies will then depend on different factors, such as the geometry of the polar head group and the shape of each molecule (Zhang et al., 2002).

According to some simulations studies on the interaction of self-assembling peptide amphiphiles (Velichko et al., 2008a), “pure” hydrophobic interaction result in the formation of monodisperse finite-size micelles. Micellization follows a closed association scenario that involves a critical micelle temperature. The nucleation is the dominant mechanism of aggregation when the H-bonding is equal to zero. On the other hand, “pure” hydrogen bonding leads to step-by-step aggregation of molecules into one-dimensional β -sheets. It follows an open association scenario that is characterized by a wide aggregate size distribution. However this simulation study is unable to show the formation of a fibrillar micelle as a result of self-assembly of peptide amphiphiles.

Some authors suggest that the formation of long planar β -sheets in the spherical layer of the micellar corona applies additional geometric constraints. The curvature of the micellar surface induces geometric frustration in the ordering of β -sheets. With further increase in hydrogen bonding energy, this results in instability and breaking of the spherical symmetry of the micelle. This instability results in the formation of one-dimensional long cylindrical fibres where β -sheets are aligned in parallel along the fibre (Paramonov et al., 2006).

Encoding hydrophilic domains, choosing the primary structure, adding amino acids with charged side chains, can influence the assembly preferences of the monomers to favour β -sheets or α -helices (Baumann et al., 2008).

Considering the stiffness of a long alkyl chain or of a long sequence of hydrophobic amino acids the micelle aggregate might not be very favourable because when the number of molecules increase it becomes very difficult to fill up the space and hide the hydrophobic chain to the water molecules into a hydrophobic core.

In a membrane like geometry the molecules would be adjacent occupying a very little space, thus if they are electrostatically charged, positively or negatively, they would repulse each other.

In a twisted conformation the curvature would give a little extra space that would solve some of the entropy issues. In Pashuk's work is pointed out the difference in the geometry for twisted and untwisted β -sheets: in a perfectly planar untwisted β -sheet each peptide lines up perfectly with the one next to it down the long axis of is fibre. In this model the hydrogen bond length should remain constant throughout the length of two adjacent amphiphilic molecules. Twisting of the β -sheet causes a small rotation between each peptide amphiphile molecule in the β -sheet down the long axis of the fibre, which will increase the hydrogen bond length between amino acids closer to the periphery of the fibre and likely increase disorder as shown with Circular Dichroism experiments. The more twisted a β -sheet is, the weaker the bonds are between adjacent peptide amphiphiles on the periphery of the fibre. In addition the amino acids at the periphery of the fibre can adopt secondary structures other than β -sheets, which would further weaker bonding among peptide amphiphile molecules (Pashuck et al., 2010).

1.2.5 Gelation of Peptide Nanofibres

A characteristic of many peptide nanofibrous system is the ability to form gels at very low concentration.

If we consider gelation of micellar and polyelectrolyte systems a couple of % weight in the system are necessary before gelation is achieved, because the micelles have to be tightly packed, while these fibrillar nanostructures are more effective in filling up the space than micelles so it is possible to reach a network at much lower concentration (~1%), while water absorption by the mesh-like network formed by these nanofibres results in gel structure (Stendahl et al., 2006).

Peptide nanofibre gels find application in cell scaffolding and regenerative medicine, some of these applications will be reviewed in the Chapter 5 of this thesis.

1.2.6 Current Technologies Based on Peptide Nanofibres

Tissue Engineering

The demonstrated biocompatibility makes of peptide nanofibres excellent candidates for cell culture matrices in tissue engineering (Ellis-Behnke and Schneider, 2011). Examples of the use of self-assembling peptide nanofibres for tissue engineering include: Fmoc-RGD mimicking the extracellular matrix, which has been tested on 3D cultured adult dermal fibroblast cells (Zhou et al., 2009). Furthermore a peptide amphiphile system presenting RGDS has also been developed and optimized for biological adhesion as a matrix for the therapeutic delivery bone marrow mononuclear cells (Webber et al., 2010b). A laminin-derived IKVAV sequence has been incorporated into peptide amphiphiles in order to enhance neural attachment, migration, and neurite outgrowth. Silva et al. showed that neural progenitor cells cultured within IKVAV peptide amphiphiles nanofibres networks was quickly undergoing selective and rapid differentiation into neurons while the formation of astrocytes was largely suppressed (Silva et al., 2004). Peptide amphiphiles bearing the IKVAV epitope have also been found to reduce cell death at the injury site and decrease astrogliosis when applied as a nanofibre gel in a spinal cord injury mouse model (Tysseling-Mattiace et al., 2008).

Heparin, a biopolymer that binds to angiogenic growth factors, was used to design a peptide amphiphile, that resulted in the self-assembly of nanostructures able to form gels (Rajangam et al., 2006).

1.2.7 Biomineralization and High-Tech Applications

Mineralization around a bond implant hybrid between peptide nanofibres and titanium has been observed *in vivo*. These templates are built by immobilizing a peptide-capping agent on the surface of synthetic self-assembled helical or nonhelical nanofibres and CdS nanocrystals were allowed to grow on them (Bose and Banerjee, 2010).

Vascularization and the absence of cytotoxic response indicate that nanofibres may be used to initiate mineralization and direct a cellular response from the host tissue into

porous implants to form new bone and thereby improve fixation, osteointegration, and long term stability of implants (Sargeant et al., 2008).

1.2.8 Peptide Nanofibres as Stabilizing Agents and a Bioactive Surfactant in Cosmetics

The activity of proteins is closely related to their native conformation. Membrane proteins exert a wide range of roles in cells, however it is difficult to extract, purify and stabilize them. In this context, it has been demonstrated that peptide amphiphiles A6K were able to stabilize PS-I complex, a membrane protein associated with the transport of electrons, in its dried form (Kiley et al., 2005).

The palmitoyl pentapeptide 3 and 4 (Matrixyl ® Sederma SA, France) is used in cosmetics with function of anti-wrinkle agent and its sequence is a fragment of type I collagen. Matrixyl has been structurally characterized and it has been shown to organize into giant fibrillar nanotapes with lengths extending to at least 10-100nm (Castelletto et al., 2010a). Clinical trials on Caucasian female subjects (n = 93, aged 35-55) have demonstrated that in 12 weeks fine line/wrinkles improvements were noticed in the subjects that were topically applying the matrixyl cream compared to the controls (Robinson et al., 2005)

1.2.9 Drug Delivery (Antimicrobial, Drug and Gene)

A number of cationic peptide amphiphiles forming micellar nanostructures have been reported to act as drug delivery system. Cationic antimicrobial peptides can kill microbes by disrupting their bacterial membrane (Makovitzki et al., 2008, Chu-Kung et al., 2004).

Recently shell-core nanoparticles made of peptide amphiphiles based on the Tat sequence were prepared and their antimicrobial activity successfully proven against a range of bacteria, yeasts and fungi. The TAT (YGRKKRRQRRR) peptide is the minimal amino-acid sequence required for membrane translocation, and was found in the transcriptional activator TAT protein of the human immunodeficiency virus type-1 (HIV-1) (Lihong Liu et al., 2009). TAT was conjugated to a cholesterol lipidic chain via a spacer of three glycines and a sequence positively charged of six arginines. In vivo these nanostructures showed a high therapeutic index against

Staphylococcus aureus infection in mice and were more potent than their unassembled peptide counterparts. Using Staphylococcus aureus infected meningitis rabbits, nanoparticles were shown to cross the blood– brain barrier and suppress bacterial growth in infected brains (Lihong Liu et al., 2009).

Self-assembled cholesterol oilgopeptides containing three blocks of amino acids, Ac-(AF)6-H5-K15-NH₂, (FA32), were evaluated as carriers for co-delivery of drug (doxorubicin) and genes (luciferase reporter gene and p53 gene). The self-assembling peptides were able to form core-shell nanostructures able to incorporate the drug and the gene. The co-delivery of the p53 encoding gene and doxorubicin suppressed the proliferation of HepG2 cells. These core-shell nanostructures showed a great potential in delivering hydrophobic anticancer drugs and genes simultaneously in vitro for improved cancer therapy (Wiradharma et al., 2009).

1.3 Aims and Objectives

In this work for the first time peptide nanofibres are investigated as CNS drug delivery systems. The synthesis of two amphiphiles molecules will be attempted in order to study their application for peptide delivery to the brain.

A lipophilic peptide will be synthesized by attachment of a palmitoyl moiety. High axial ratio nanostructures will be formulated by using a peptide amphiphile.

Self-assembly of nanofibres will be evaluated experimentally and in silico.

Cytotoxicity on in vitro cells will be assessed and interaction with BBB in vitro model investigated to evaluate the mechanistic pathways undertaken.

The ability of these assemblies to act as carrier for brain delivery will be finally assessed in vivo by administering IV formulation based on peptide nanofibres.

Pharmacodynamics and pharmacokinetics profiles of the nanotechnology cargo will be assessed in order to obtain a full description of the capabilities of the carrier to be employed as a new delivery system for peptide delivery to the brain.

CHAPTER 2

Self-assembling Amphiphiles Synthesis and Structural Characterization

2.1 Introduction

The working hypothesis states that the lipidization of peptides enables the delivery of peptides to the brain.

The polymeric amphiphile quaternary ammonium palmitoyl glycol chitosan (GCPQ) enhances the delivery of propofol (Qu et al., 2006) and hydrophilic peptides such as Leu-enkephalin via the intravenous route (Lalatsa, 2009). The amphiphile also enables the delivery of the peptide to the brain via the oral route (Lalatsa, 2009).

The use of chitosan and chitosan derivatives is also reported in literature for the delivery of peptides via the oral route (Senel et al., 2000, Prego et al., 2006).

Chitosan is a natural polysaccharide comprising copolymers of glucosamine and N-acetylglucosamine and it represents an interesting material for pharmaceutical applications due to its biodegradability, biocompatibility, and low toxicity (Gao et al., 2003, Hejazi and Amiji, 2003, Illum, 1998, Thanou et al., 2001b). However, chitosan is insoluble at physiological pH (7.4), as it requires acid to be protonated, indeed its aqueous solubility is increased at pH lower than 6.5 (Gao et al., 2003, Hyung Park et al., 2006). Therefore, a derivative of chitosan with hydrophilic glycol moieties, glycol chitosan, has received a rising interest as a drug carrier, as the pendant glycol branches on the polymer increase the aqueous solubility of the native chitosan (Uchegbu et al., 2001, Trapani et al., 2009).

Knight *et al.* suggest that low molecular weight glycol chitosan could be desirable for as its lower viscosity would favor the manufacturing process and it would be cleared from the blood circulation more efficiently after intravenous administration (Knight et al., 2007). However in vivo studies on the effect of the

molecular weight of glycol chitosan nanoparticles for tumor targeting suggest that high molecular weight glycol chitosan nanoparticles remain for longer periods in the blood circulation, leading to increased accumulation at the tumor site (Park et al., 2007). The study shows that glycol chitosan nanoparticles display a prolonged blood circulation time, decreased time-dependent excretion from the body, and elevated tumor accumulation with increasing polymer molecular weight (Park et al., 2007).

Studies have shown that quaternary ammonium charges increase the solubility and safety of amphiphiles (Cheng et al., 2006). Other studies have also demonstrated that increasing the hydrophobic levels will favor the loading capacity of poorly soluble drugs (Siew, 2009, Cheng et al., 2006, Anton. P and Laschewsky. A, 1994). In this study, a second-generation GCPQ polymer was synthesized by attachment of palmitoyl (C₁₆) and acetyl (C₃) pendant branches on the glycol chitosan backbone in order to achieve a polymer with higher hydrophobic levels.

The palmitoyl chain was chosen because this medium chain amphiphile is believed to form effective aggregates for the accommodation of hydrophobic drugs and to exhibit prime penetration into the lipid epithelial membrane (Francis et al., 2003, Venkatesan et al., 2006). The acetyl groups were also added to minimize the packing jam due to the palmitoyl chains and allow bigger hydrophobic voids available for drug loading within the micelles as schematized in Figure 2.1.

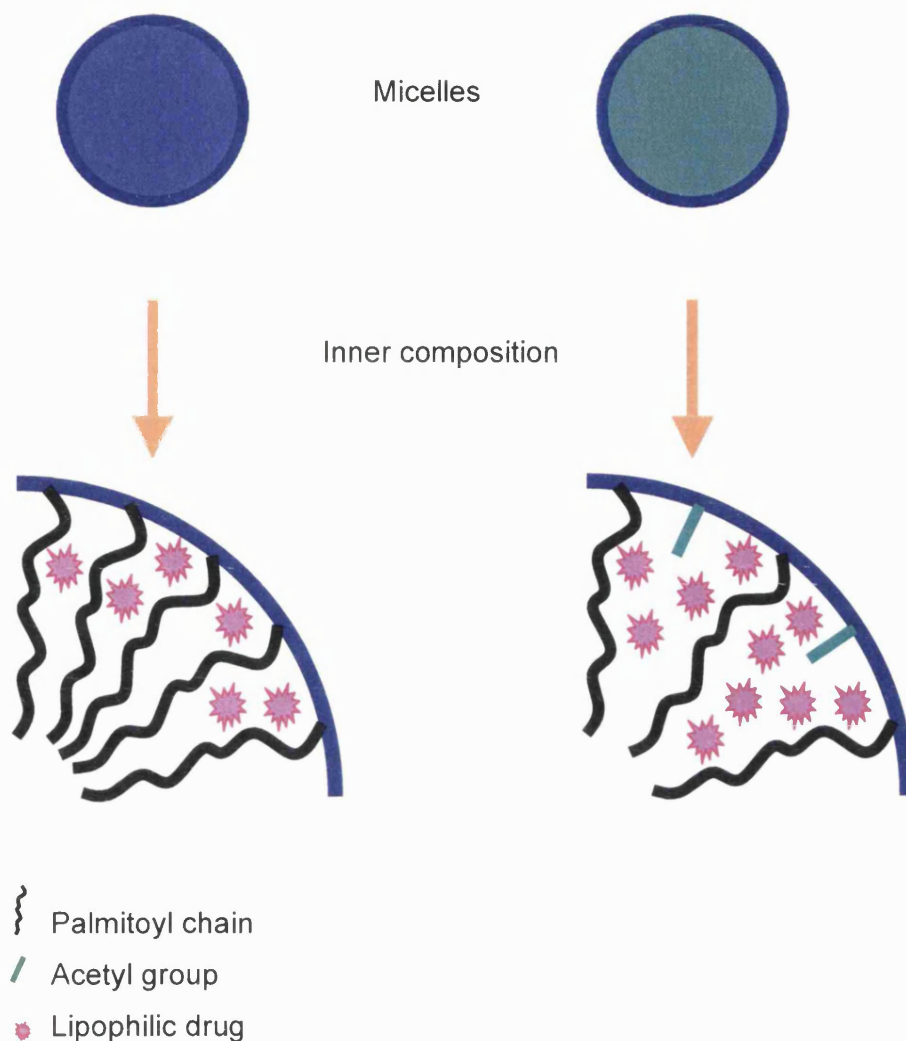


Figure 2.1: Schematic depiction of the drug loading ability of polymeric micelles.

In this chapter the synthesis and characterization of dalargin, the pDal peptide amphiphile, and the second-generation acetyl ammonium palmitoyl glycol chitosan amphiphile are described.

The hydrophilic hexapeptide dalargin and its amphiphilic derivative palmitoyl dalargin (pDal) were synthesized by solid phase peptide synthesis approach. The covalent linkage of the C_{16} chain was designed to achieve a change in the physical properties of the peptide, enabling its self-assembly into high axial ratio

nanostructures, as it was reported in the literature by several authors (Hartgerink et al., 2001, Santoso et al., 2002, Yang and Zhang, 2006).

GCPQA polymer was synthesized and its structural characterization studied using proton nuclear magnetic resonance; the molecular weight of the polymer was determined using gel permeation chromatography.

2.1.1. Gel Permeation Chromatography – Multi-Angle Laser Light Scattering (GPC- MALLS)

The GPC-MALLS method is widely used for a rapid and reliable characterization of polymer molecular weight and molecular weight distribution. Gel permeation chromatography (GPC), also known as size exclusion chromatography (SEC), is a chromatographic approach used to separate macromolecules according to their hydrodynamic volume, which is dependent on both molecular weight and molecular conformation of a compound in solution (Uchegbu and Schätzlein, 2006).

Polymer solutions are passed through a column packed with a polymeric gel medium. Gel filtration media are made of porous inert materials which are chemically and physically stable, such as dextran, e.g Sephadex (Determann, 1964). During elution a fractionation of the polymer solution takes place as the larger molecules elute first, while smaller molecules are delayed due to their diffusion inside the porous media; thus, a fractionation is achieved according to their size (Hunt and Holding, 1989).

The eluting compound is characterized for molecular weight by an interferometric refractometer which measures changes in the refractive index (RI) of the sample with changes in concentration (dn/dc) and a multi-angle laser light scattering (MALLS) detector which measures the intensity of light scattered by the polymers eluting from the column.

Incident light scatters in different directions with intensity directly dependent on the molecular weight of the polymer in the sample. However not all the particles in a sample have the same molecular weight, thus light scattering will depend on weight average (Mw). In a GPC/MALLS system, the signal from the light- scattering detector is proportional to molecular mass of the eluted polymer, multiplied by its concentration. Therefore, the molecular mass of the eluted polymer can be calculated by combining the signal from light scattering detector with signal from the concentration detector (refractive index) (Wyatt, 1998).

The quantity refractive index increment (dn/dc) describes the change in refractive index of a polymer solution in terms of polymer concentration. The dn/dc value is essential for the characterization of the molar mass. To measure dn/dc value of a solute, a series of dilutions of the sample are prepared. These dilutions are then injected into the RI detector and data collection is automatically performed using the DNDC software. The software (ASTRA) then calculates the dn/dc value based on the signal strength from the RI (dn) and the concentrations of the samples (dc) (Wyatt, 1998).

2.1.2. Solid Phase Peptide Synthesis (SPPS)

The principle of solid phase peptide synthesis is based on the construction of a peptide chain on a resin support of polymeric nature (Merrifield and Nord, 1969).

The synthesis of a peptidic sequence involves the formation of an amide bond between a carboxyl group and an amino group (Figure 2.2).

The synthesis is normally driven from C-terminus towards N-terminus, thus the C-terminal amino acid residue of the peptide of interest is attached to the resin via its carboxyl group. The protecting group strategy is orthogonal, i.e. the protecting groups on the side chain functionalities of the amino acids are chosen such that they are resistant to conditions for cleavage of the N-terminal protecting group of the growing peptide chain. In addition, the N-terminal protecting group must be cleaved under conditions that will not affect the anchorage to the resin. The great benefit of SPPS consists of the potential to remove all solvents and excess reagents from each coupling and deprotection step simply by filtration and washing. This allows large excesses of reagents to be used resulting in short reaction times. Coupling can also be repeated as many times as required in order to achieve reaction completion, before subsequent N-terminal deprotection. On completion of the sequence and cleavage from the resin, the product can be obtained after a single purification step, in much less time than if a standard solution phase peptide synthesis methodology was used (Chan W.C, 2000).

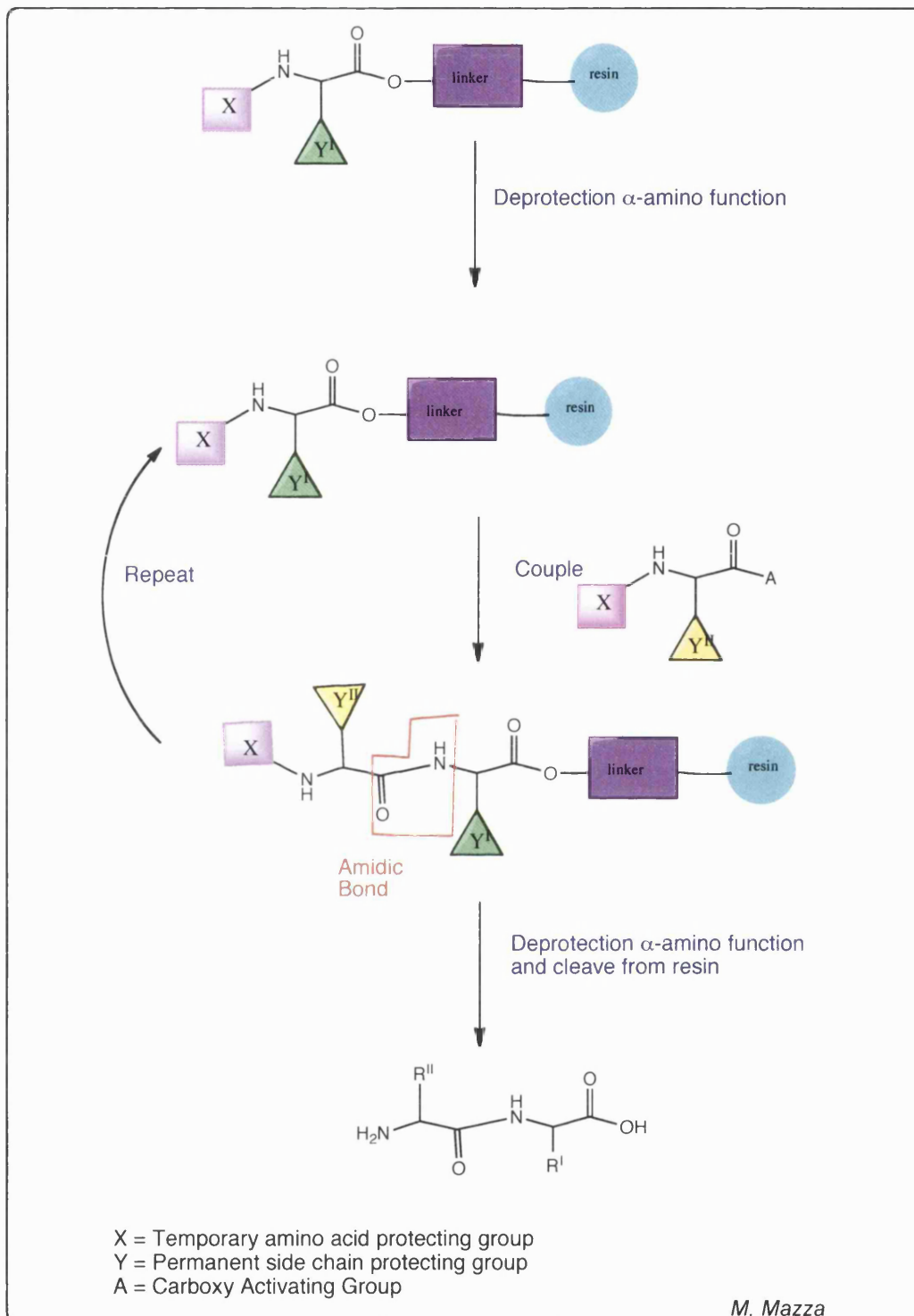


Figure 2.2: Schematic summary of the SPPS synthesis method. The functional groups on the side chain of the amino acids are masked with “permanent” protecting groups that are not affected by the conditions of the overall peptide synthesis reaction. The “temporary” protecting groups on the α -amino group is removed from the N-terminus.

There are two main strategies that have been used in the last forty years for SPPS, both based on the use of a temporary protecting group on the α -amino group of the growing chain, and of a permanent protecting group on the side chains as schematized in Figure 2.2:

- the Boc strategy, where the Boc group is an acid-labile temporary protecting group (figure 2.3A)
- the Fmoc strategy, where the Fmoc group is a base-labile temporary protecting group. (Figure 2.3 B)

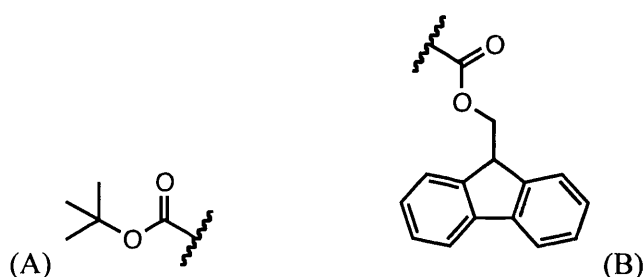


Figure 2.3: (A) *tert*-butyloxycarbonyl (Boc)-group; (B) Fluorenylmethyloxycarbonyl (Fmoc)-group.

Boc strategy SPPS involves graduated acidolysis to obtain removal of the temporary protecting group first, and subsequently of the permanent protecting groups (Barlos et al., 1989).

The Fmoc strategy is based instead on an orthogonal protection, where the Fmoc group is cleaved under weakly basic conditions (i.e. 20-50% v/v piperidine). The overall milder conditions of the N-terminal deprotection and the orthogonality of the remaining protecting groups have resulted in the Fmoc strategy gaining much more application in SPPS synthesis; this was therefore the approach chosen to synthesize the peptides in the present thesis.

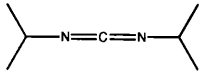
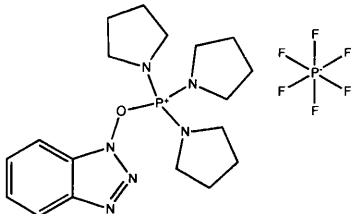
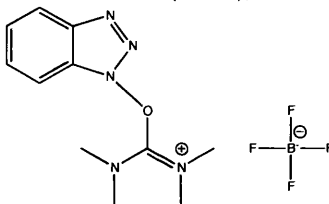
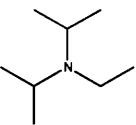
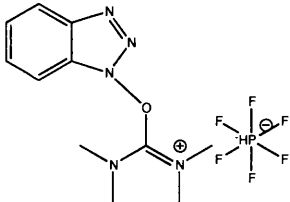
The Fmoc strategy often utilizes acid-labile (e.g. *t*-butyl and trytil based) side-chain protecting groups, furthermore the nature of the linker between the resin and the first attached amino acid is also acid-labile, thus removal of the permanent protecting groups and cleavage from the resin in most of the cases can be obtained by treatment

with trifluoroacetic acid (TFA), which is highly volatile and can be easily removed by evaporation (Chan W.C, 2000).

2.1.3 Coupling Agents

The formation of an amide bond during peptide chain synthesis involves the *in situ* activation of the carboxyl component of the amino acid that is going to be added to the sequence. The activating agents for coupling reactions give rise to the formation of active esters, as summarized in Table 2.1. The mechanisms of activation involved during the coupling reaction are schematized in Figure 2.4 and 2.5.

Table 2.1 Coupling method used in Fmoc SPPS; *adapted from* (Chan W.C, 2000); (DIPEA = diisopropylethylamine).

Coupling Reagent	Additive	Active Species	Conditions
Diisopropylcarbodiimide(DIC)  or dicycloesylcarbodiimide (DCC) Figure 2.4		Symmetrical Anhydride	Fmoc-amino acid/DIC (2:1) in DCM
Diisopropylcarbodiimide(DIC) or dicycloesylcarbodiimide (DCC)	1-hydroxybenzo triazolo (HOBT)	Benzotriazolyl ester	Fmoc-aminoacid/DIC/HOBT(1:1:1) in DMF
Benzotriazol-1-yloxytris(pyrrolidino)posphonium hexafluorophosphate (PyBOP) ,  or N-[(1H-benzotriazol-1-yl)(dimethylamino)methylene]-N-methylmethanamino tetrafluoroborate(TBTU),  or N-[(1H-benzotriazol-1-yl)(dimethylamino)methylene]-N-methylmethanamino hexafluorophosphate(HBTU), Figure 2.5	1-hydroxybenzo triazolo (HOBT)	Benzotriazolyl ester	Fmoc-aminoacid/ PyBOP/HOBT/DIPEA(1:1:1:2) in DMF DIPEA structure 
N-[(dimethylamino)-1H-1,2,3-triazolo[4,5-b]pyridin-1-ylmethylene]-N-methylmethanamino hexafluorophosphate N-oxide (HATU) 		9-azabenzotriazolyl ester	Fmoc-aminoacid/HATU/DIPEA(1:1:2) in DMF

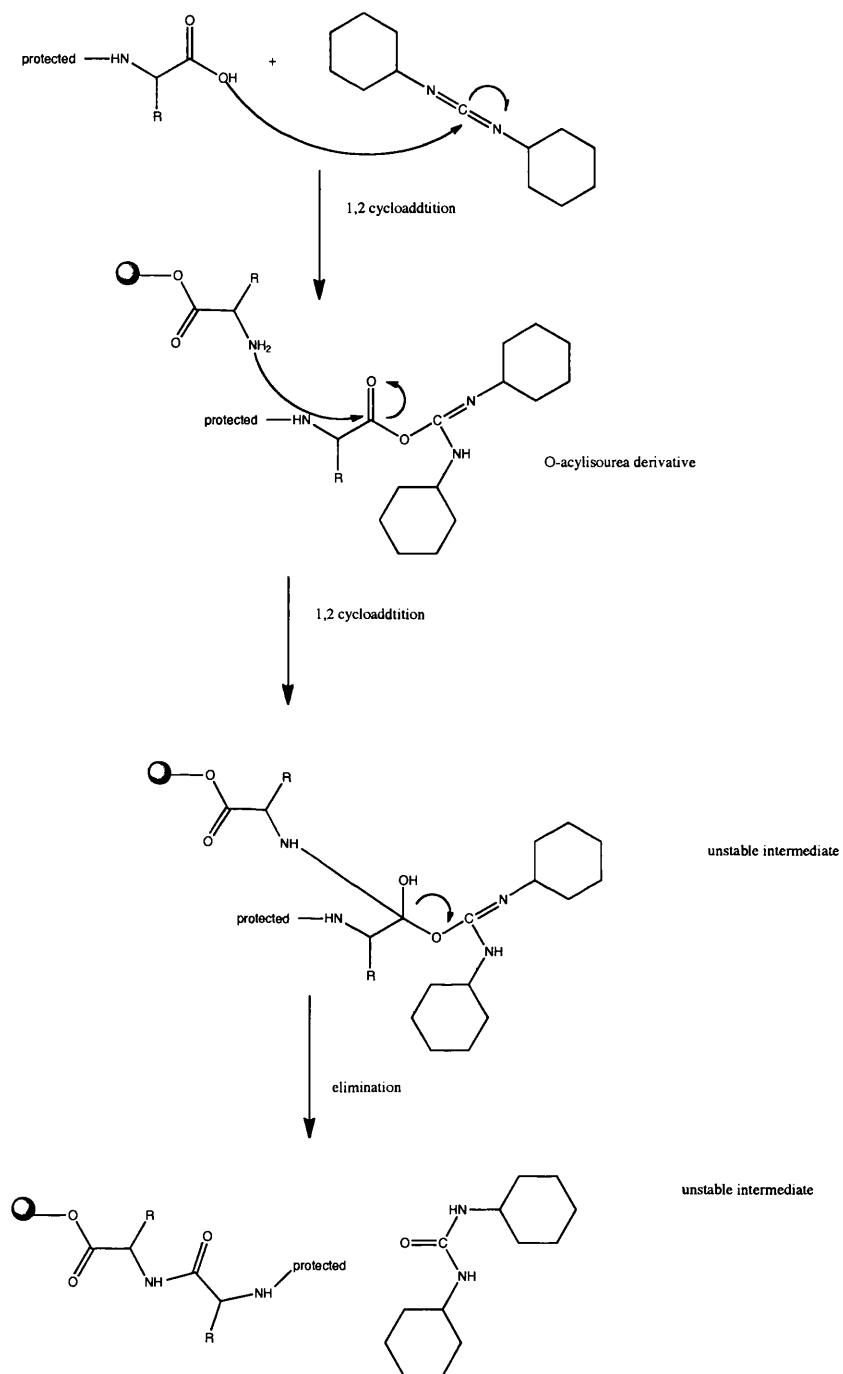


Figure 2.4 : Amino Acid coupling mediated by DCC.

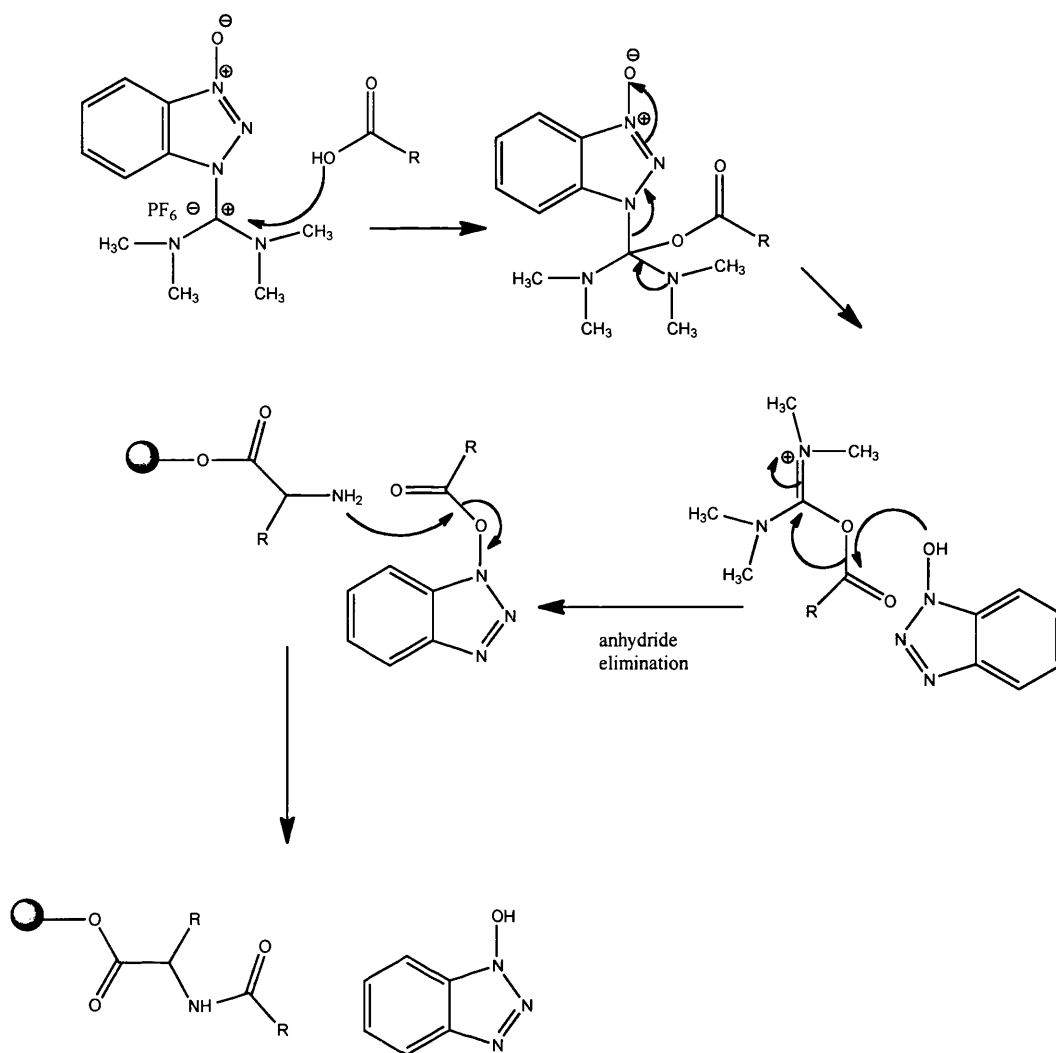


Figure 2.5: Coupling reaction in presence of HBTU. The same mechanism of reaction applies for HATU, PyBOP and TBTU.

2.1.4 Drawbacks of SPPS and Strategies to Overcome these Limitations

Monitoring peptide synthesis is one of the major drawbacks of SPPS. Incomplete removal of protecting groups and partially completed coupling steps cause the formation of truncated sequences or ‘deletion’ sequences on the resin, sequences in which one or more of the residues is missing. This results in the formation of side-products after resin cleavage, and thus decreases the overall yield of the synthesis (Fields, 1997). Furthermore, these side-products are difficult to remove during the purification process, since they have similar composition to the desired cleavage

product. The principles of using excess of reagents, using multiple couplings and/or extending the coupling times are useful when necessary to obtain reasonably pure peptides. Monitoring the coupling reactions to avoid the formation of deletion sequences can be performed qualitatively with the Kaiser Test (Figure 2.6), an assay based on the classical ninhydrin test for primary amines. The test gives a dark blue color with free primary amino groups (Kaiser et al., 1970). Couplings are repeated until a negative test is obtained which ensures complete coupling. One disadvantage of this method is that can only be used for the detection of primary amines, as secondary amines (as well as tertiary and aromatic amines) cannot form the highly conjugated dimer, thus affording an apparently negative result (Fields, 1997).

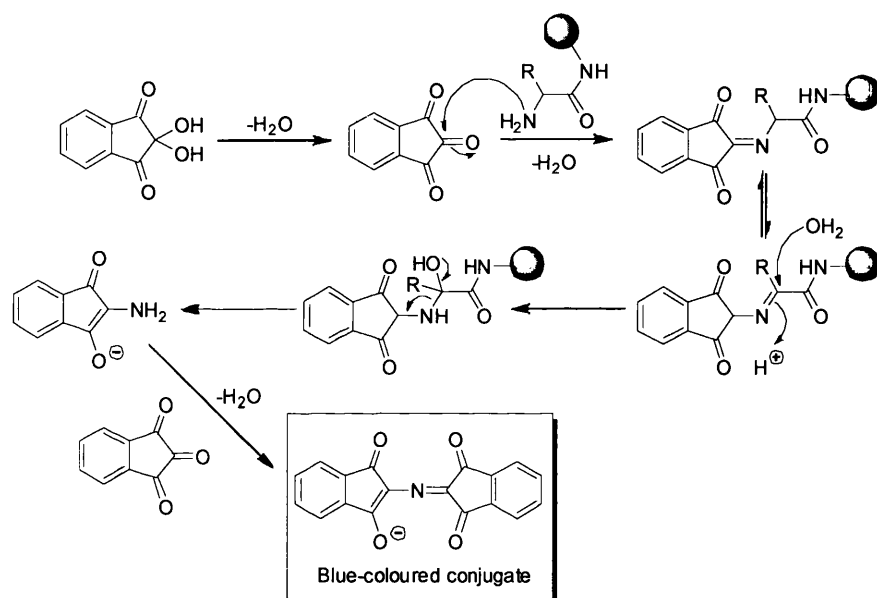


Figure 2.6: The reaction of ninhydrin with resin-bound primary amines

2.1.5 HPLC Peptide Purification and Analysis

Reverse-phase HPLC (RP-HPLC) is the standard tool for purification/separation and analysis of peptides and peptides mixtures. Using RP-HPLC, peptides are most often eluted and separated under gradient conditions. Acetonitrile is the organic modifier of choice and the mobile phase further contains tri-fluoroacetic acid (TFA), formic acid, etc. as ion-pair reagent (Sandra et al., 2008).

2.1.6 Mass Spectrometry

The absolute mass of a peptide can be precisely measured using different mass spectrometry techniques (Hoke et al., 2001). *Conditio sine qua non* for the structural analysis of a molecule via mass spectrometry is that the molecule is able to ionize. Ions are charged particles and they have to be in the gas phase before they can be separated using mass spectrometry. Separation occurs according to their mass-to-charge ratio (m/z), which is given by the mass of the ion on the atomic scale divided by the number of charges that the ion possesses (Hoke et al., 2001). The m/z number is dimensionless. To obtain a spectrum the mass spectrometer first must produce a collection of ions in the gas phase. These ions will be then separated according to their m/z values in vacuum. Different instruments have different apparatus for the generation of ions.

2.1.7 Electrospray Ionization/Mass Spectrometry (ESI/MS)

ESI is a means of producing ions from nonvolatile, thermally labile compounds (Lim and Elenotiba-Johnson, 2004). ESI is generally accomplished by forcing a solution of the analyte through a small capillary such that the fluid sprays into an electric field, thereby generating very fine droplets. Electrosprayed droplets will possess an excess of positive or negative charges depending on the capillary bias polarity, these droplets will diminish in size due to solvent evaporation either following the inflation of a drying gas at atmospheric pressure or in a heated chamber at reduced pressure. After size reduction the smaller droplets disintegrate to even smaller droplets due to coulombic repulsion of the charges in a process that will be repeating until the analyte molecule (M) is ejected into the gas phase along with some of the excess charges (Watson and Sparkman, 2007b). In most cases the charge is generated by protonation of basic sites or deprotonation of acidic sites (Figure 2.7).

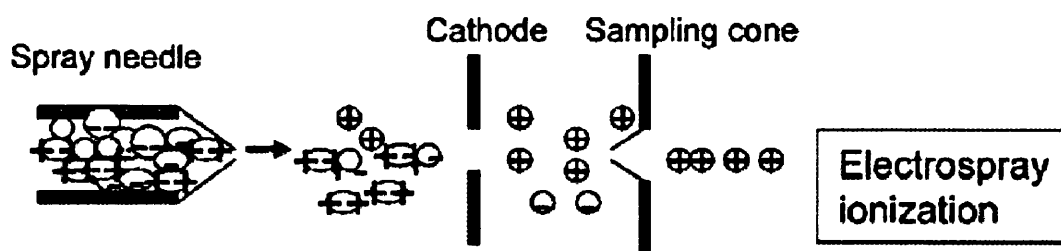


Figure 2.7: Schematic representation of ions production by Electrospray ionization (Lim and Elenotiba-Johnson, 2004).

2.1.8 Matrix Assisted Laser Desorption/Ionization – Time of Flight (MALDI-TOF)

MALDI has been used extensively in the structural characterization of proteins and peptides (Hoke et al., 2001). In MALDI, the sample is mixed with organic mixing compound, i.e. dihydroxibenzoic acid in a convenient solvent to achieve a molar ratio of analyte to matrix of approximately 1:5000, the matrix act to separate the analyte molecules (by dilution) to prevent analyte-analyte molecular (or ionic) interactions during the process.

The high energy density at the spot illuminated by the laser causes a phase transition from solid to gas (Figure 2.8). Desirable attributes of the matrix are high-absorptivity for the laser radiation and being able to form a fine crystalline solid during co-deposition with the analyte. Interestingly, very little increase in the internal energy of the analyte occurs as there is little or no fragmentation of the analyte, making MALDI one of the soft ionization techniques (Watson and Sparkman, 2007a).

Pulsed UV-laser energy is used to transfer matrix and analyte molecules from the solid phase support into the gaseous phase. In the transition from solid phase into the gas phase a charge transfer, usually a proton transfer, occurs between activated matrix and analyte molecules. The matrix can be a proton donor or acceptor, resulting in positively or negatively charged analyte molecules. The resulting charge state depends strongly on the nature of the analyte (Kafka et al., 2010).

For smaller molecules, such as peptides and small proteins, MALDI generates predominantly singly charged ions ($z = 1$), which minimizes spectral complexity and simplifies the interpretation of mass-to-charge values (El-Aneed et al., 2009)

In comparison to other ionization methods such as electron ionization, chemical ionization or fast atom bombardment, ESI and MALDI are mostly non-destructive to larger biomolecules, do not require chemical modifications and for most analyte molecules, result in high ionization efficiencies. Both ionization methods can be coupled interchangeably to various types of mass analyzers (Kafka et al., 2010).

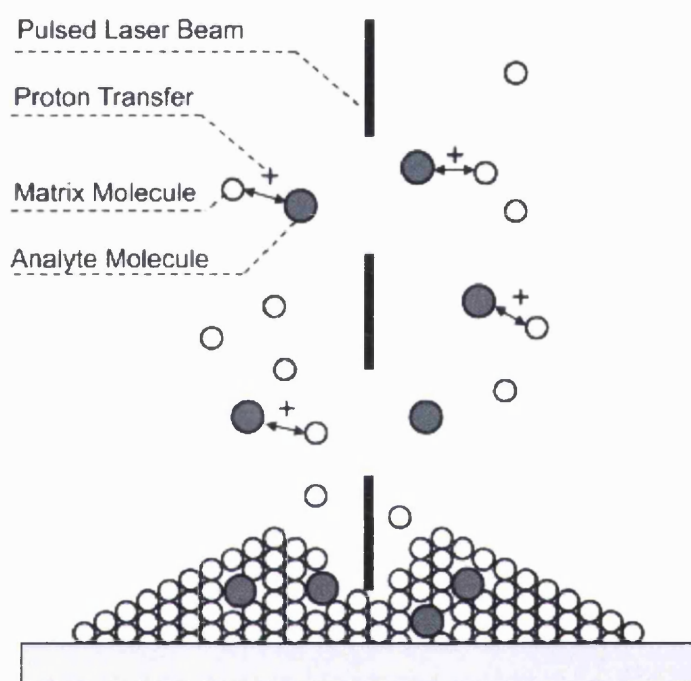


Figure 2.8: Schematic representation of the solid to gas transition in MALDI. Adapted from (Kafka et al., 2010)

2.1.9 Fragmentation in Sequencing of Peptides and Spectra Interpretation

The molecular mass of a peptide consists of the sum of the residue masses of all the amino acids in the peptide plus water (Hoke et al., 2001). Although many bonds in peptides could possibly undergo fragmentation, the most significant cleavages are along the peptide backbone. According to the Roepstorff Nomenclature for classifying N-terminal and C-terminal fragment ions of peptides, fragments retaining the positive charge on the C-terminal component of the peptide are represented by the

symbol X, Y, or Z, whereas fragments containing the positive charge on the N-terminal part of the original peptide are indicated with the letters A, B and C (Figure 2.9)

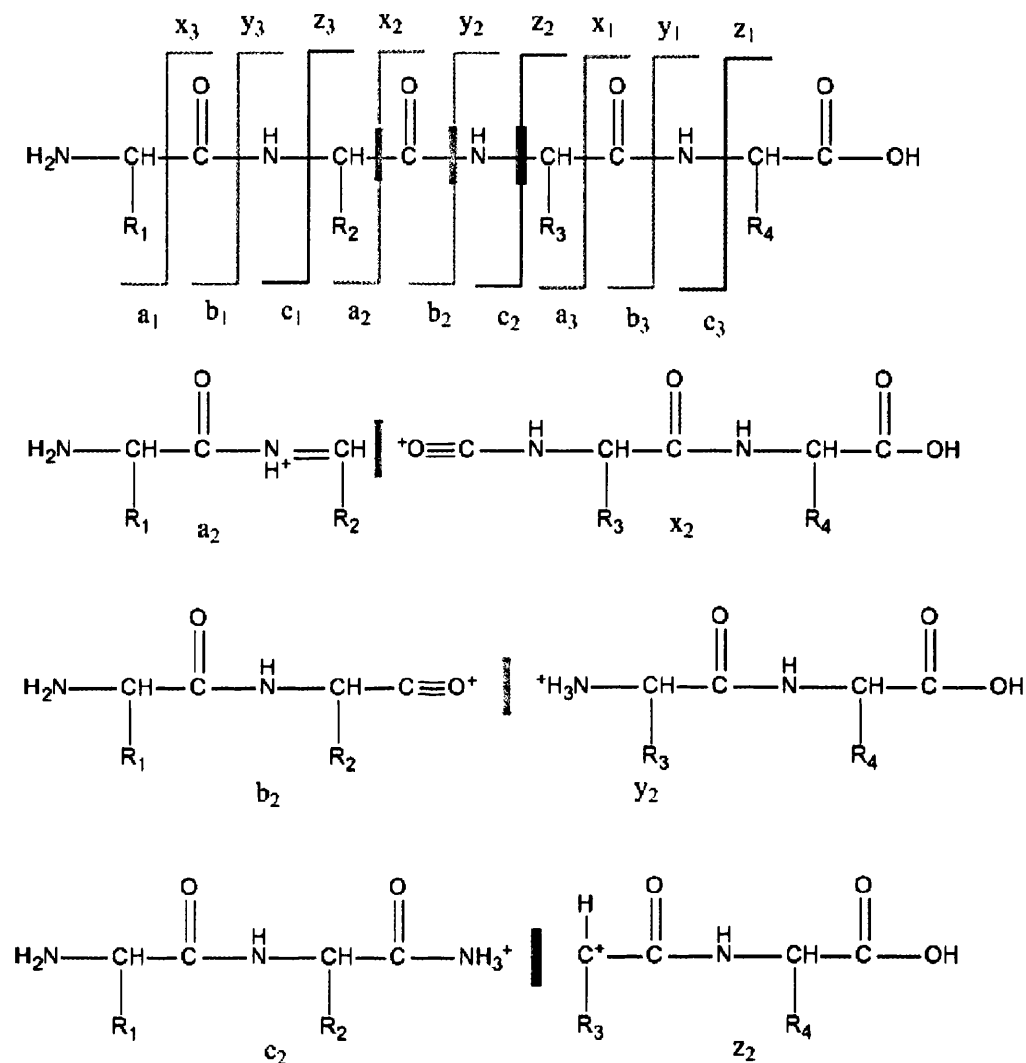


Figure 2.9: Fragmentation in sequencing of peptides. *Reproduction from* <http://employees.csbsju.edu/hjakubowski/classes/ch331/protstructure/olcompseqconfom.html>

During the fragmentation process, upon excitation by collisionally activated association (CAD), the ionizing proton (thought to be located initially at the most basic site within the peptide) becomes mobile and samples various amide oxygens and nitrogens as alternative protonation sites (Watson and Sparkman, 2007b). Thus for a CAD spectrum a Y ion is a fragment that is formed by cleavage at a peptide

bond with charge retention on the C terminal component of the original molecule. The Y ion will have a mass that consists of all the constituent amino acid residue masses, plus the mass of the carboxyl acid -OH group (at the C-terminus) and two hydrogens (one to complete the amino group at the N-terminus, the other in a form of proton to establish a charge). The formation of a Y ion results in the expulsion of an amino acid residue of the peptide (Watson and Sparkman, 2007b).

2.2 Materials

- GCPQA Synthesis

Glycol Chitosan	Sigma Aldrich, Poole, UK
Palmitic Acid N-hydroxysuccinimide ester	Sigma Aldrich, Poole, UK
Sodium Iodide	Sigma Aldrich, Poole, UK
Sodium Bicarbonate	Sigma Aldrich, Poole, UK
Cyanoborohydride	Sigma Aldrich, Poole, UK
Ethanol Laboratory Grade	Fisher Scientific, UK
Dyethyl Ether	Fisher Scientific, UK
Methanol HPLC Grade	Fisher Scientific, UK

- Peptide Synthesis

H-Arg(Pbf)-2(CI-Trt)-Resin (substitution 0.53 mmol/g)	Merck/Novabiochem, Darmstadt, Germany
Fmoc-Leu-OH	Merck/Novabiochem, Darmstadt, Germany
Fmoc-Phe-OH	Merck/Novabiochem, Darmstadt, Germany
Fmoc-Gly-OH	Merck/Novabiochem, Darmstadt, Germany
Fmoc-DAla-OH	Merck/Novabiochem, Darmstadt, Germany
Fmoc-Tyr-OH	Merck/Novabiochem, Darmstadt, Germany
HBTU	Merck/Novabiochem, Darmstadt, Germany
HOBt	Merck/Novabiochem, Darmstadt, Germany
Piperidine Biotech Grade 99%	Sigma Aldrich, UK
DMF (peptide synthesis grade)	Rathburn Chemicals
Trifluoroacetic Acid	Sigma Aldrich, UK

DIPEA	Sigma Aldrich, UK
DichloroMethane Rectapur	VWR, International, UK
Methanol Analytical Grade	Fisher Scientific, UK
Acetonitrile HPLC grade	Fisher Scientific, UK
Triethylamine	Sigma Aldrich, UK
Palmitic Acid N-hydroxysuccinimide ester	Sigma Aldrich, UK
Thioanisole	Sigma Aldrich, UK
Anisole	Sigma Aldrich, UK
Ethanedithiol	Sigma Aldrich, UK

2.3 Methods

2.3.1. Synthesis of GCPQA

The synthesis was carried out by modifying a previous protocol (Qu *et al.* 2006). Briefly, glycol chitosan (2 g, GC) was degraded in a solution of HCl (152 mL, 4 M) for 24 hours, dialysed against deionised water (5 L) in a dialysis bag (12-14 kDa molecular weight cut off (MWCO)) with 6 changes over 24h. After freeze-drying, Glycol chitosan (500 mg) and sodium bicarbonate (376 mg) were dissolved in a mixture of absolute ethanol (24 ml) and water (76 ml). A solution of palmitic acid N-hydroxysuccinimide (792 mg) dissolved in absolute ethanol (150 ml) was added drop wise to the glycol chitosan solution with continuous stirring over a period of 1 hour. The reaction solution was left to stir for 72 h and protected from light. Ethanol was evaporated on a rotavapor and the aqueous solution extracted with diethyl ether three times. The solution was then dialysed against deionised water (5L) in a dialysis bag (12-14 kDa MWCO) with 6 changes over 24 hours and lyophilized. The Palmitoyl glycol chitosan (150 mg) was dispersed in N-methyl Pyrrolidone (45 mL), an

ethanolic solution of Sodium Hydroxide (10 mg/mL) added, followed by Sodium Iodide (2 mg/mL) and Iodomethane (0.93 mL). The mixture was stirred under N₂ at 36°C for 4 hours, then the polymer precipitated with diethyl ether, redissolved in a minimal volume of water and dialysed against 0.1 M NaCl (5 L x3 changes) and deionised water (5 L x6 changes) before freeze-drying. The quaternary ammonium palmitoyl glycol chitosan (GCPQ) thus obtained (100 mg) was dissolved in a solution of Sodium Bicarbonate (0.08 M, 10 mL) and Methanol (20 mL). To this solution was added Methanol (5 mL) containing acetic anhydride (0.093 mL). After stirring for 24h, the reaction was stopped by adding NH₄OH. The solution dialyzed against deionised water (5 L) in a dialysis bag (12-14 kDa MWCO) with 6 changes over 24h and the dialysate lyophilized.

2.3.2 GCPQA NMR Analysis

¹H NMR and ¹H-¹H COSY (Bruker AMX 400MHz spectrometer, Bruker Instruments, U.K.) experiments were performed on all polymer solutions. Deuterium oxide and CD₃OD were used as solvents. The level of palmitoylation was calculated by comparing the ratio of palmitoyl methyl protons ($\delta = 0.89$ ppm) to sugar protons ($\delta = 3.5-4.5$ ppm), the level of quaternisation calculated by comparing the ratio of quaternary ammonium protons ($\delta = 3.45$ ppm), to sugar protons and the level of acetyl protons ($\delta = 2$ ppm) to sugar protons.

2.3.3 Gel Permeation Chromatography – Multi-Angle Laser Light Scattering (GPC- MALLS)

The molecular weight of degraded glycol chitosan and GCPQA was measured by GPC- MALLS equipped with DAWN® EOS MALLS ($\lambda = 690$ nm), Optilab DSP Interferometric Refractometer ($\lambda = 690$ nm) and QELS detectors (Wyatt Technology Corporation, USA). Fractionation was performed on a PolySep – GFC – P 4000 column (300 x 7.8 mm, Phenomenex, UK) and a guard column PolySep – GFC – P (35 x 7.8 mm, Phenomenex, UK), at a loading concentration of 5-10 mg/mL using a Waters 717 Plus autosampler. The mobile phase used were 1) acetate buffer (0.3M sodium acetate / 0.2 M acetic acid, pH 5.0) for degraded glycol chitosan and 2) a mixture of acetate buffer (0.3 M sodium acetate / 0.2 M acetic acid, pH 5) and methanol (35:65) in the case of GCPQA.

The mobile phase was pumped through the system using a Jasco PU-2080plus 7600 series pump connected to a Jones Chromatography system solvent degasser. Before injection the samples were filtered through a MILLEX GP syringe driver filter unit (PES 0.22 μm , sterile 33 mm). Data obtained were processed using ASTRA for Windows version 4.90.08 software. Toluene and BSA were used for DAWN[®] EOS MALLS calibration and normalisation.

The specific refractive index increment (dn/dc) of degraded glycol chitosan, and GCPQA was measured with an Optilab DSP Interferometric Refractometer ($\lambda = 690$ nm) at 40 °C. Filtered samples (0.2 μm filter) of five different concentrations ranging from 0.2 – 1 mg/mL were manually injected at a pump flow rate of 0.2-0.3 mL/min. The data were processed using Wyatt DNDC for Windows version 5.90.03 software.

2.3.4 Synthesis of dalargin

To the H-Arg-(Pbf)₂-Cl-Trt resin (0.943g, 0.53 mmol g⁻¹) was added dimethyl formamide (DMF, 4-8mL) and the resin left to swell for 1 hour. To the swollen resin was then added a solution of DMF containing the Fmoc amino acid (Fmoc-L-Leucine, 0.44 g, 1.25mmol), O-(1H-benzotriazole-1-yl)-N,N,N',N'-tetramethyluronium hexafluorophosphate (HBTU, 0.47 g, 2.5 mmol) and 1-Hydroxybenzotriazole (HOBt, 0.436 μL , 2.5 mmol). To the reaction was then added N,N-Diisopropylethylamine (DIEA, 191 mg, 2.5mmol) and the reaction allowed to proceed for 30 minutes. For each amino acid residue coupled, the above procedure was performed twice. After coupling each residue the Kaiser test was performed to ensure coupling was complete. Deprotection of the Fmoc moiety after washing the resin with DMF (150 mL) was achieved by adding piperidine (20% v/v in DMF, 10 mL) to the resin beads, which was then agitated for 10 minutes (performed twice). The process detailed above was repeated until synthesis of Fmoc-Tyr-D-Ala-Gly-Phe-Leu-Arg was complete. All peptide synthesis steps were performed at room temperature. Once peptide synthesis had been completed, the product bound to the resin was treated with the reagent R (trifluoroacetic acetic, ethanediol, thioanisole, anisole – 90:3:5:2, 1 mL for each 0.1 mg of the resin). The reaction mixture was evaporated under reduced pressure, the peptide precipitated with cold diethyl ether (4 °C, 4 mL) and the precipitate collected by centrifugation (2500rpm, 30minutes) in a Z323 Hermle centrifuge, (VWR, Poole, UK). The precipitated was again redissolved in water, and precipitation and

centrifugation repeated twice. The pellet was then redissolved in water and freeze-dried.

2.3.5 Synthesis of Palmitoyl Dalargin (pDal)

To the H-Arg(Pbf)-2-Cl-Trt resin (0.943g, 0.53 mmol g⁻¹) was added dimethyl formamide (DMF, 4-8 mL) and the resin left to swell for 1 hour. To the swollen resin was then added a solution of DMF containing the Fmoc amino acid (Fmoc-L-Leucine, 0.44 g, 1.25 mmol), O-(1H-benzotriazole-1-yl)-N,N,N',N'-tetramethyluronium hexafluorophosphate (HBTU, 0.47 g, 2.5 mmol) and 1-Hydroxybenzotriazole (HOBt, 0.436 μL, 2.5 mmol). To the reaction was then added N,N-Diisopropylethylamine (DIEA, 191 mg, 2.5 mmol) and the reaction allowed to proceed for 30 minutes. For each amino acid residue coupled, the above procedure was performed twice. After coupling each residue the Kaiser test was performed to ensure coupling was complete. Deprotection of the Fmoc moiety after washing the resin with DMF (150 mL) was achieved by adding piperidine (20% v/v in DMF, 10 mL) to the resin beads, which were then agitated for 10 minutes (performed twice). The process detailed above was repeated until synthesis of Fmoc-Tyr-D-Ala-Gly-Phe-Leu-Arg was complete. All peptide synthesis steps were performed at room temperature. Once peptide synthesis had been completed, the resin was washed with copious amount of DMF (250 mL), followed by copious amounts of dichloromethane (DCM, 100 mL) and then by a mixture of DCM, methanol (1:1, 200 mL). The peptide bound resin was dried under vacuum and then transferred to a glass container and left in a dessicator under vacuum for 24 hours.

Triethylamine (665 μL, 4.8 mmol) was added to a dispersion of the peptide bound to the resin (0.266 g, 0.1 mmol) pre-swollen in DMF (8 mL) and to the resultant suspension was added drop wise the N-hydroxysuccinimide ester of the palmitic acid (282 mg, 0.85 mmol) in DMF (8 mL). The reaction was left to react for 24 hours at 25 °C, during which time the suspension was agitated (120 rpm). The mixture was then concentrated under reduced pressure to remove volatile products and the residue dispersed in DMF (4mL). The DMF suspension was filtered and the residue washed with copious amount of DMF (100mL). The product bound to the resin was treated with the reagent R (trifluoroacetic acetic, ethanediol, thioanisole, anisole – 90:3:5:2,

1mL for each 0.1 mg of the resin). The reaction mixture was evaporated under vacuum conditions, the peptide precipitated with cold water (4°C, 4mL). Ethanol (20mL) was added to wash and redissolve the precipitate, and the solution incubated at 35°C for 45-60 minutes to allow re-precipitation. The precipitate was collected by centrifugation (2500 rpm, 30 minutes) in a Z323 Hermle centrifuge, (VWR, Poole, UK) and precipitation and centrifugation repeated twice. The pellet was then redissolved in acetonitrile and freeze-dried.

2.3.6 Peptide Purification.

Peptide purification was achieved using semi-preparative reverse phase HPLC (RP-HPLC) on a HPLC Agilent 1200 series (Agilent Technologies, Edimburgh, UK, Ltd). Crude peptide (6-8 mg ml⁻¹) dissolved in dimethylsulfoxide (DMSO) and chromatographed over a semi-preparative Waters Spherisor ODS₂ C18 column (10mm x 250 mm, pore size = 10 µm) using a 30 minute gradient from 5% aqueous (solvent A) to 100% organic (solvent B) and flow rate of 6 mL/min (solvent A = TFA 0.02% v/v; and solvent B = acetonitrile : water – 90:10, TFA 0.016%). Peptides were detected at 230nm using with a UV detector. Fractions having the same retention time were pulled together and freeze-dried.

2.3.7 Mass Spectrometry

For low resolution nominal mass, samples were prepared in acetonitrile/water (1:1) containing 0.1% v/v formic acid and measurements recorded on a ThermoQuest Navigator, operated under Electrospray ionization (ESI) and atmospheric pressure chemical ionization (APCI) interfaces for liquid sample introduction. All samples were analyzed using ESI. In *positive mode* samples were analyzed using acetonitrile/water (1:1) containing 0.1% v/v formic acid as solvent. In *negative mode* methanol was used.

Conditions were as follows: Cone voltage: 20-30 V, capillary voltage: 3.15 kV, source heater: 120 degrees Celsius, nebulizing gas (nitrogen) flow: 400 L/h.

High-resolution accurate mass measurements were achieved using either V mode or W mode positive or negative on a Micromass Q-TOF Ultima Global Tandem Mass Spectrometer. In positive mode samples were prepared in acetonitrile/water (1:1)

containing 0.1 % v/v formic acid for infusion (0.3 μ l/min) and in acetonitrile/water (1:1) for LC-MS using a Waters NanoEase 75 x 150 mm C18 3.5 μ m column. For the MALDI analysis the sample consisted of a 1:1 mix of peptide with α -cyano-4-hydroxycinnamic acid (10 mg/mL in acetonitrile/water (1:1) containing 0.1% v/v TFA). 1 μ L of mix was spotted onto a MALDI target plate and allowed to dry before analysis.

2.3.8 Nuclear Magnetic Resonance (NMR)

NMR characterization was carried out using a Bruker Avance 400MHz Spectrometer. Data were processed using Bruker NMR suite 3.5 in conjunction with Topspin 1.3 software. Chemical shifts are given in ppm and were calibrated to the residual proton peak of the deuterated solvent. Assignment of spectra was assisted using ^1H - ^1H COSY Correlation Spectroscopy.

2.3.9 Fourier Transformed Infrared Reflectance

The infrared absorption spectra for the peptides was recorded using a Perkin Elmer Spectrum 100 FTIR Spectrometer (Perkin Elmer, Cambridge, UK) equipped with a Universal Attenuated Total Reflectance accessory and a zinc selenide crystal (4000 – 650 cm^{-1}) and Spectrum FTIR software. A background spectrum was recorded on a clean zinc selenide window before a sample spectrum was recorded.

2.3.10 X-Ray Diffraction

Datasets were collected at room temperature on an Oxford Diffraction Xcalibur NovaT X-ray diffractometer (Agilent Technologies, UK, Ltd.). The sample for analysis was prepared by filling a capillary tube with the freeze-dried pDAL and sealing with wax the open side. The data were collected at 2θ range, processed and scaled using CrysAlis[™] (Oxford Diffraction).

2.3.11 Polarizing Microscopy Analysis

Freeze-dried pDal powder was deposited onto a glass cover slip and micrographs were recorded using a Nikon-Microphot-FXA light microscope using Nikon PlanAPO Chromatic lenses and a static and dioscopic crossed polarizing filters.

2.4 Results

2.4.1 GCPQA Synthesis

The synthesis of GCPQA was successfully achieved as confirmed by NMR and GPC-MALLS analyses.

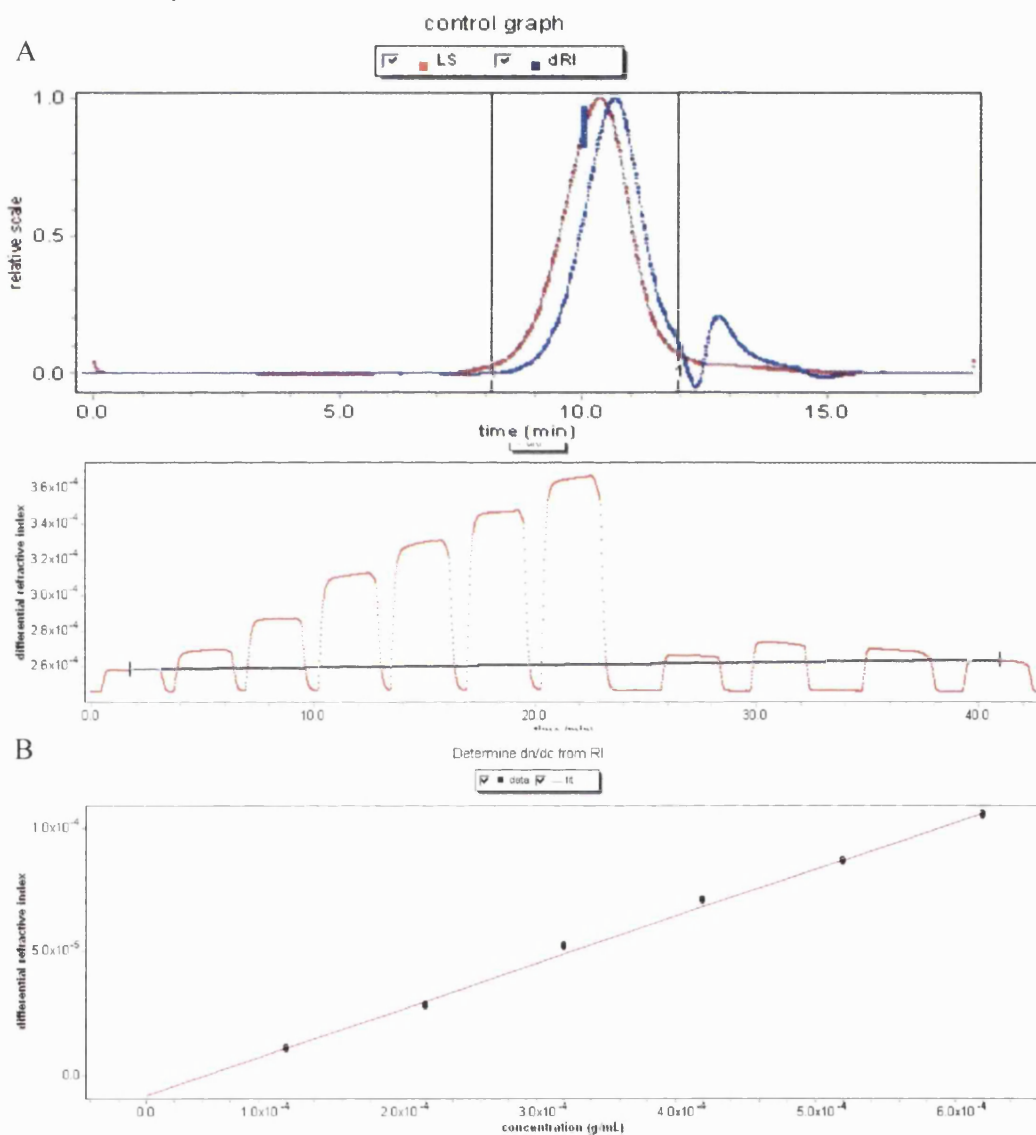


Figure 2.10: Examples of chromatogram of (A) degraded glycol chitosan obtained from GPC (sample concentration = 5mg mL^{-1}) and (B) measurement of dn/dc .

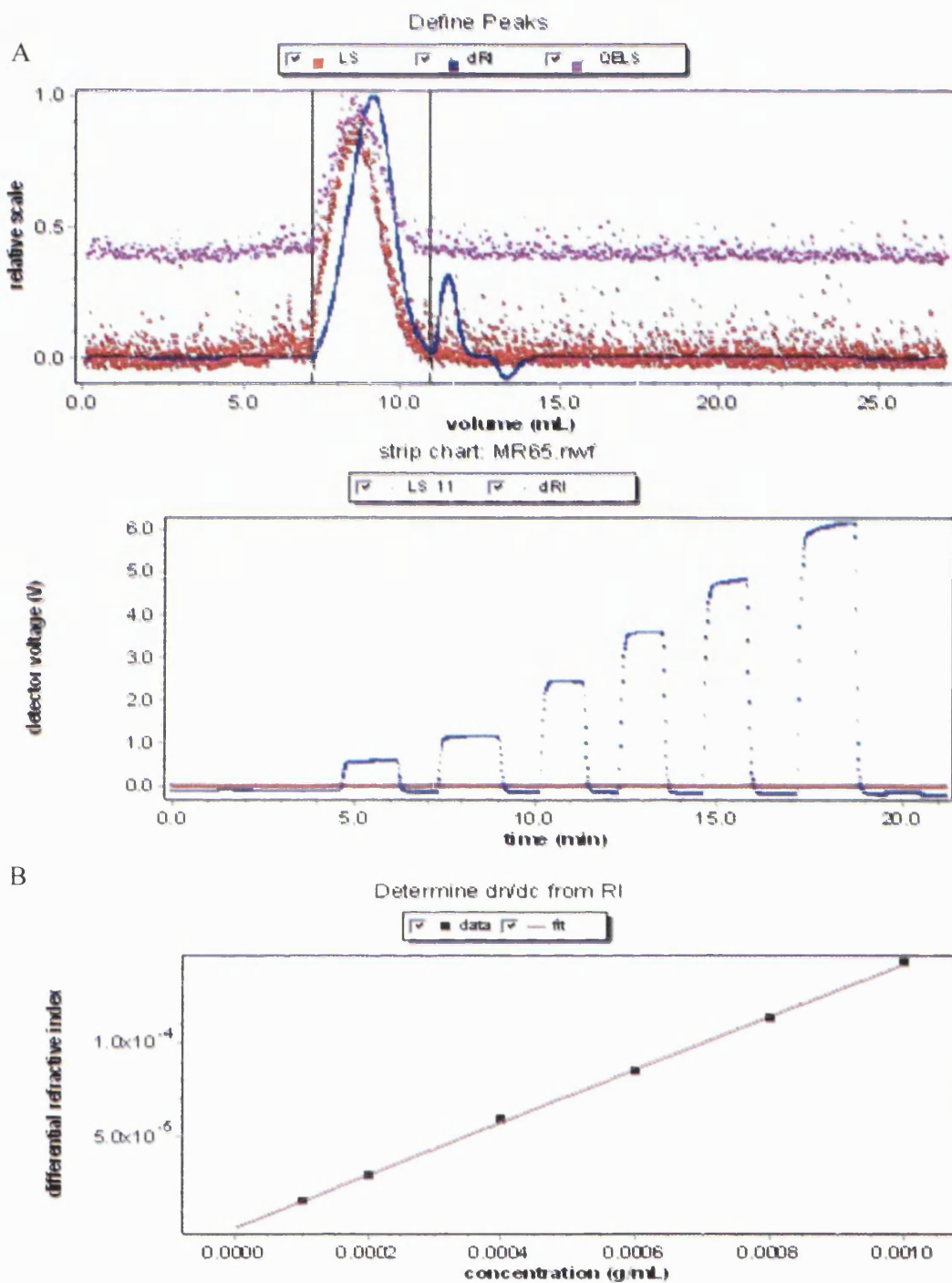


Figure 2.11: Examples of chromatogram of (A) GCPQA obtained from GPC and (B) measurement of dn/dc of GCPQA (batch MR67)

Glycol chitosan was subject to 24 hours acid hydrolysis. The polymer average molecular weights expressed in g/mol for degraded glycol chitosan ($n=3$) and GCPQA ($n=3$) were

Polymer	Mw	Mn	Mw/Mn	dn/dc
GC	$6.61 \cdot 10^3 \pm 0.57$	$7.843 \cdot 10^3 \pm 0.46$	1.198 ± 0.0896	0.13555 ± 0.00365
GCPQA	$2.521 \cdot 10^4 \pm 0.559$	$1.814 \cdot 10^4 \pm 0.130$	1.36 ± 0.198	0.16633 ± 0.013

Figure 2.10 and 2.11 are example chromatograms for degraded GC and GCPQA respectively and dn/dc curves obtained for the relative batches. The dn/dc of GC and GCPQA was calculated for each sample separately by injecting a number of concentrations varying from 0.1 to 0.8 mg mL⁻¹ diluted in mobile phase. The acylation resulting from the palmitoylation and acetylation, and the quarternarization are randomly distributed along the polymer, as previously reported by Wang (Wang et al., 2001).

The ¹H NMR spectra for GCPQ and GCPQA are shown in Figure 2.12 and 2.13 respectively. The proton chemical shifts are listed as previously reported by Uchegbu (Uchegbu et al., 2001): δ 0.89 (a, CH₃ palmitoyl), δ 1.30 (b, (CH₂)₁₂ palmitoyl), δ 1.65 (c, CH₂ palmitoyl), δ 2.05 (h, CH₃ acetyl), δ 2.2–2.3 (d, CH₂ palmitoyl), δ 2.7–3.2 (e, CH₃ dimethyl-amino-glycol chitosan), δ 3.45 (f, CH₃ dimethyl-amino-glycol chitosan), δ 3.5–4.5 (g, sugar protons).

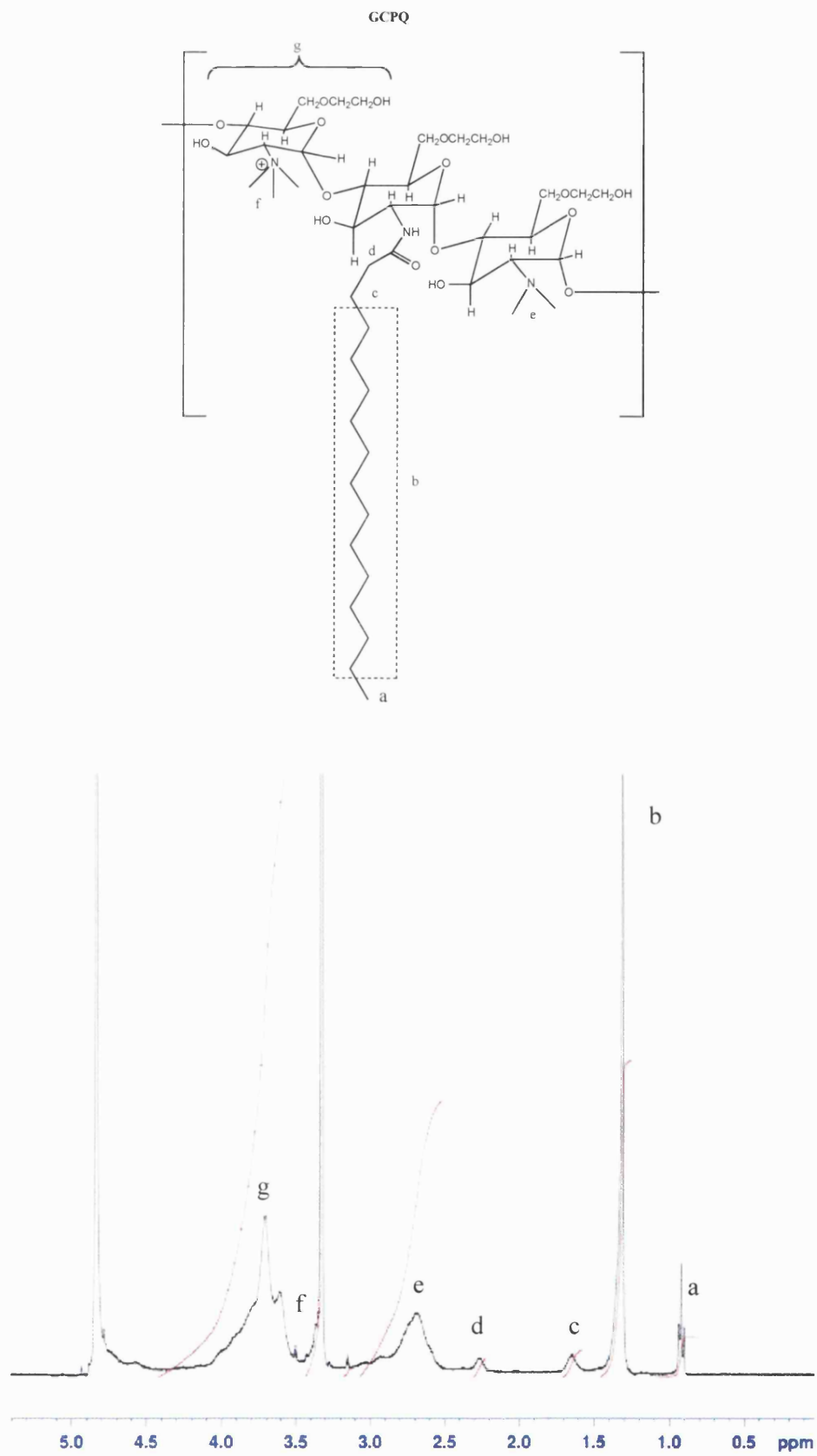


Figure 2.12: ¹H-NMR spectrum of GCPQ in CD₃OD

¹H NMR was used to estimate the levels of hydrophobic and hydrophilic modification of the polymers. The calculations were performed using the ratio of palmitoyl methyl protons (δ 0.89 ppm) to sugar protons (δ 3.5-4.5 ppm), the ratio of acetyl methyl protons (δ 2.05 ppm) and the quaternary ammonium (δ 3.45 ppm) to sugar protons. Using the spectrum of GCPQA in Figure 2.13 as an example the levels can be calculated as follows

$$\begin{aligned} \text{Palmitoylation} &= \frac{\delta \text{ chemical shift of palmitoyl methyl protons} / 3 \text{ protons}}{\delta \text{ chemical shift of sugar protons} / 9 \text{ protons}} \times 100 \\ (\text{mole } \%) & \\ &= \frac{3.32/3}{47.73 / 9} \times 100 = \sim 20.7 \% \end{aligned}$$

$$\begin{aligned} \text{Acetylation} &= \frac{\delta \text{ chemical shift of acetyl methyl protons} / 3 \text{ protons}}{\delta \text{ chemical shift of sugar protons} / 9 \text{ protons}} \times 100 \\ (\text{mole } \%) & \\ &= \frac{1.44/3}{47.73 / 9} \times 100 = \sim 9 \% \end{aligned}$$

$$\begin{aligned} \text{Quaternarization} &= \frac{\delta \text{ chemical shift of ammonium protons} / 9 \text{ protons}}{\delta \text{ chemical shift of sugar protons} / 9 \text{ protons}} \times 100 \\ (\text{mole } \%) & \\ &= \frac{1.35/9}{47.73 / 9} \times 100 = \sim 2.8 \% \end{aligned}$$

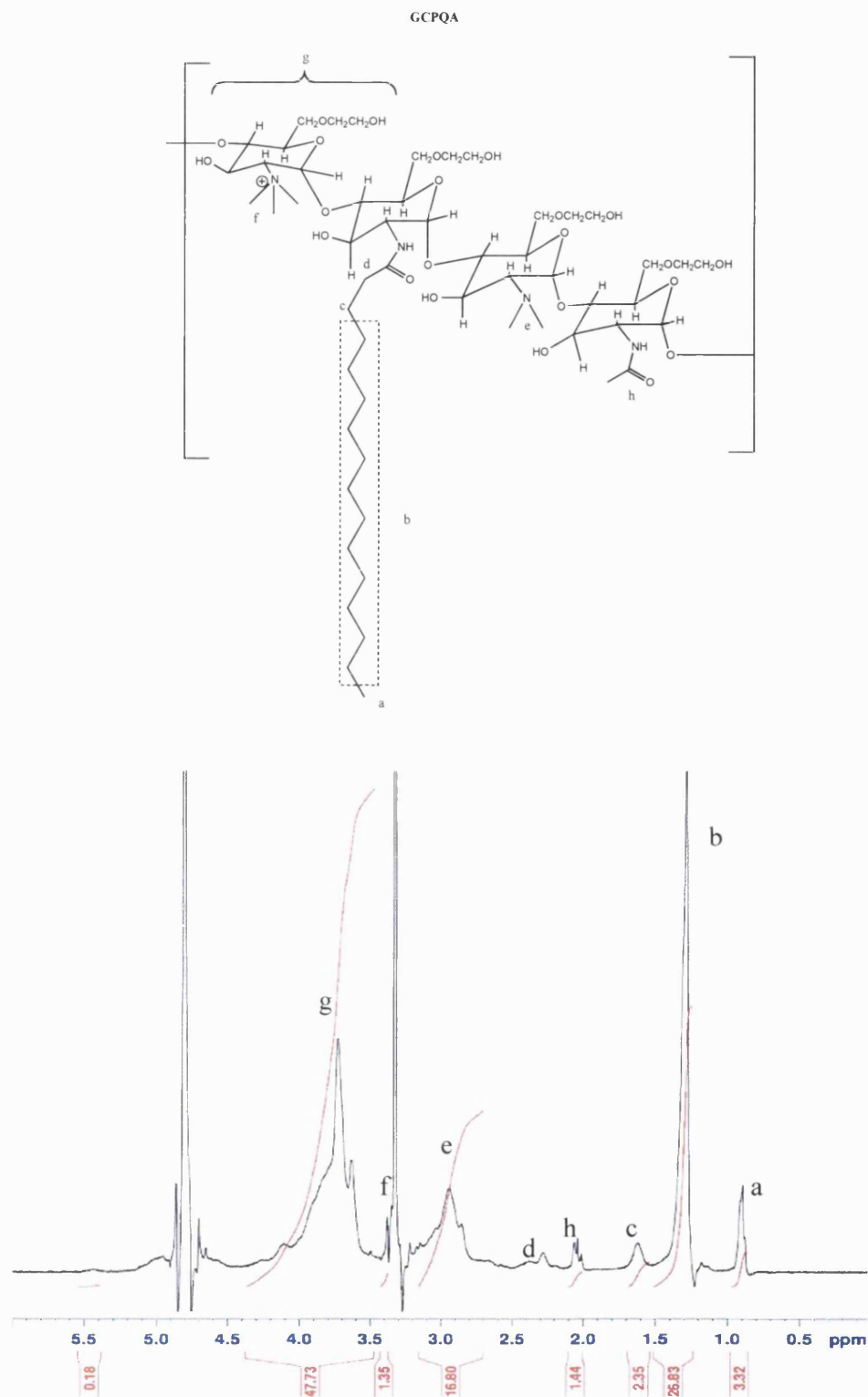


Figure 2.13: ^1H NMR spectrum of GCPQA in CD_3OD , upon reaction of GCPQ with acetic anhydride to form GCPQA

2.4.2 Peptide Synthesis

For peptide purification, the fractions were collected and analyzed via UV-absorbance after gradient elution (Figure 2.14); fractions showing the same retention time are pulled together and the solvent eliminated with freeze-drying.

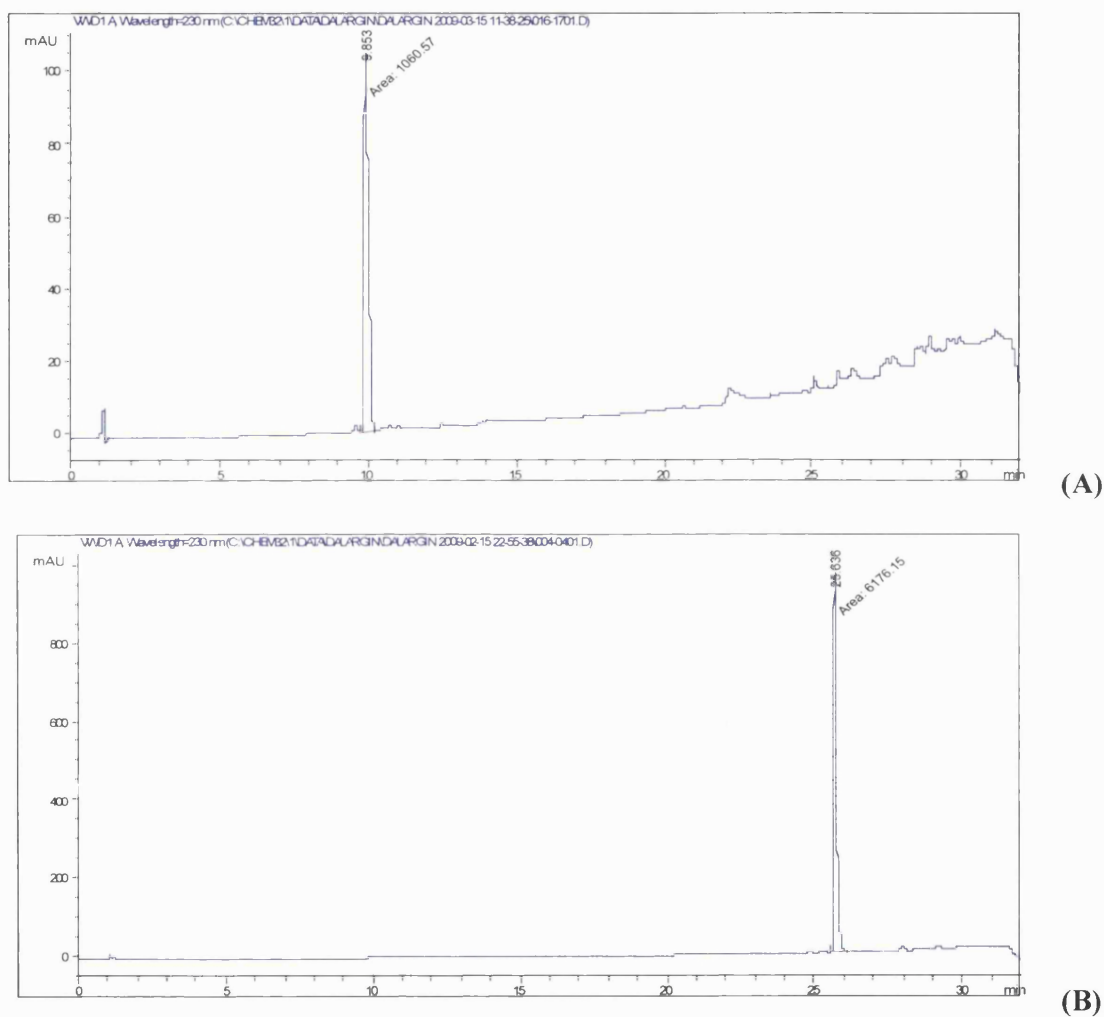


Figure 2.14: Dalargin (A) and pDal (B) purification via RP-HPLC via gradient elution.

The retention time of dalargin (9.8 min) is less than the retention time of pDal (25.6 min), as it would be expected considering the hydrophilic nature of dalargin versus the lipophilic nature of pDal.

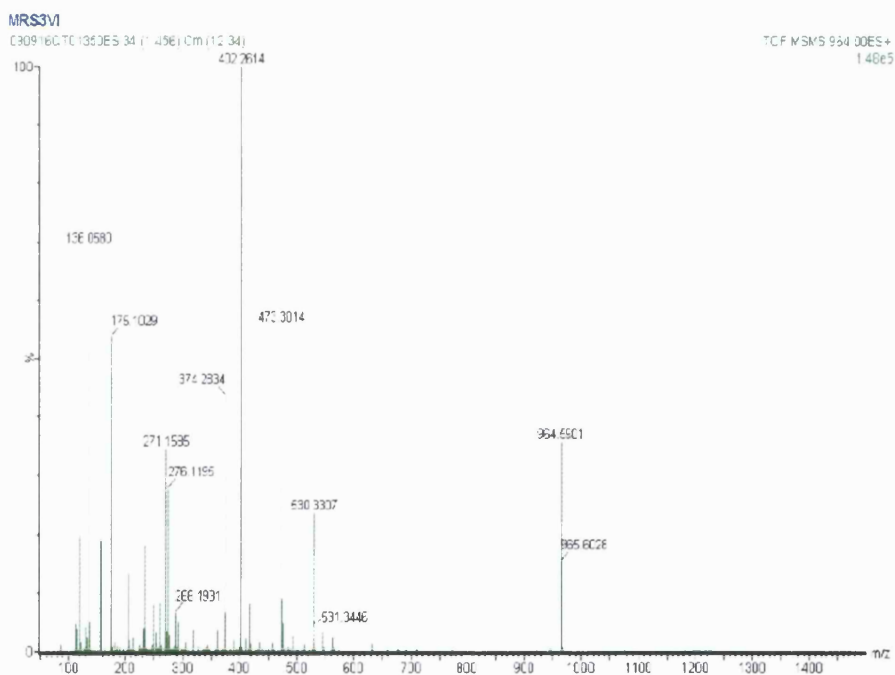
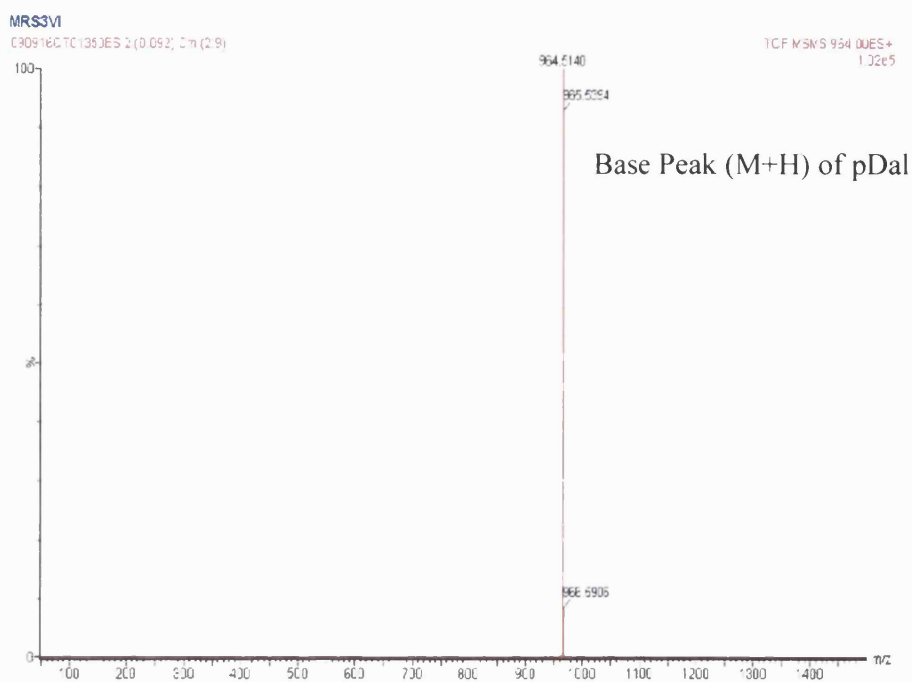


Figure 2.15: High Resolution MS spectra of pDal. m/z 964.5140 correlates with the expected $[M+H]$ mass for pDal.

Fragment ions can be assigned to the peptidic sequence as summarized in Table 2.2

Fragment Ion	m/z
pDal-H ₂ O	964.5
Palmitoyl-YAG	530.3
GFLR	473.3
Palmitoyl-Y	402.2
Palmitoyl-Y (immonium ion)	374.2
AGF	276.1
GF (G immonium)	176.1
Y (immonium ion)	136

Table 2.2 – Fragment ions assignment for pDal

The synthesis of dalargin and pDal was also confirmed by the MALDI-TOF spectra, as reported in Figure 2.16 and 2.17 respectively.

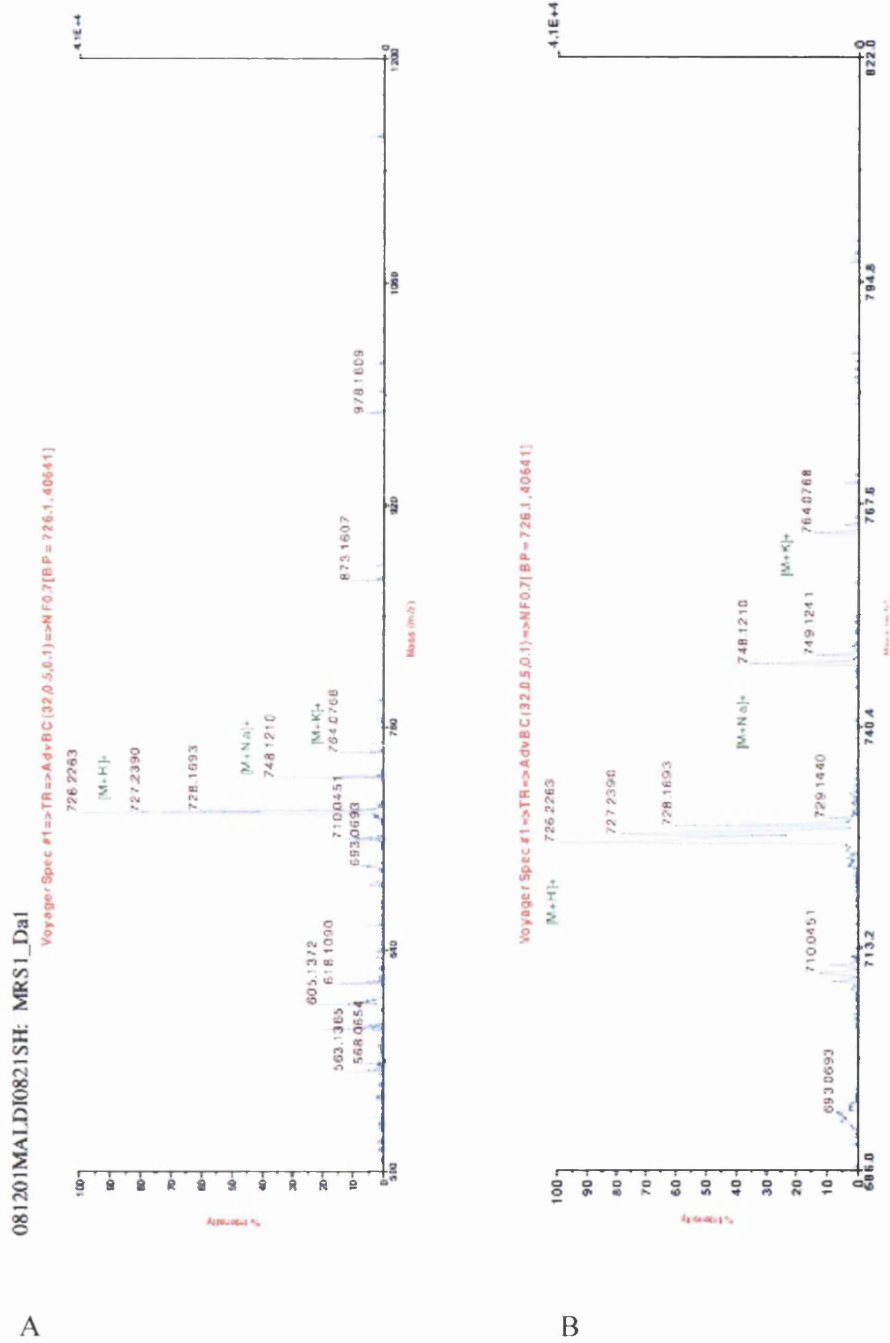


Figure 2.16: MALDI-TOF spectra of dalargin (A, B). No significant high molecular weight ions have been seen in the pDal spectrum. B

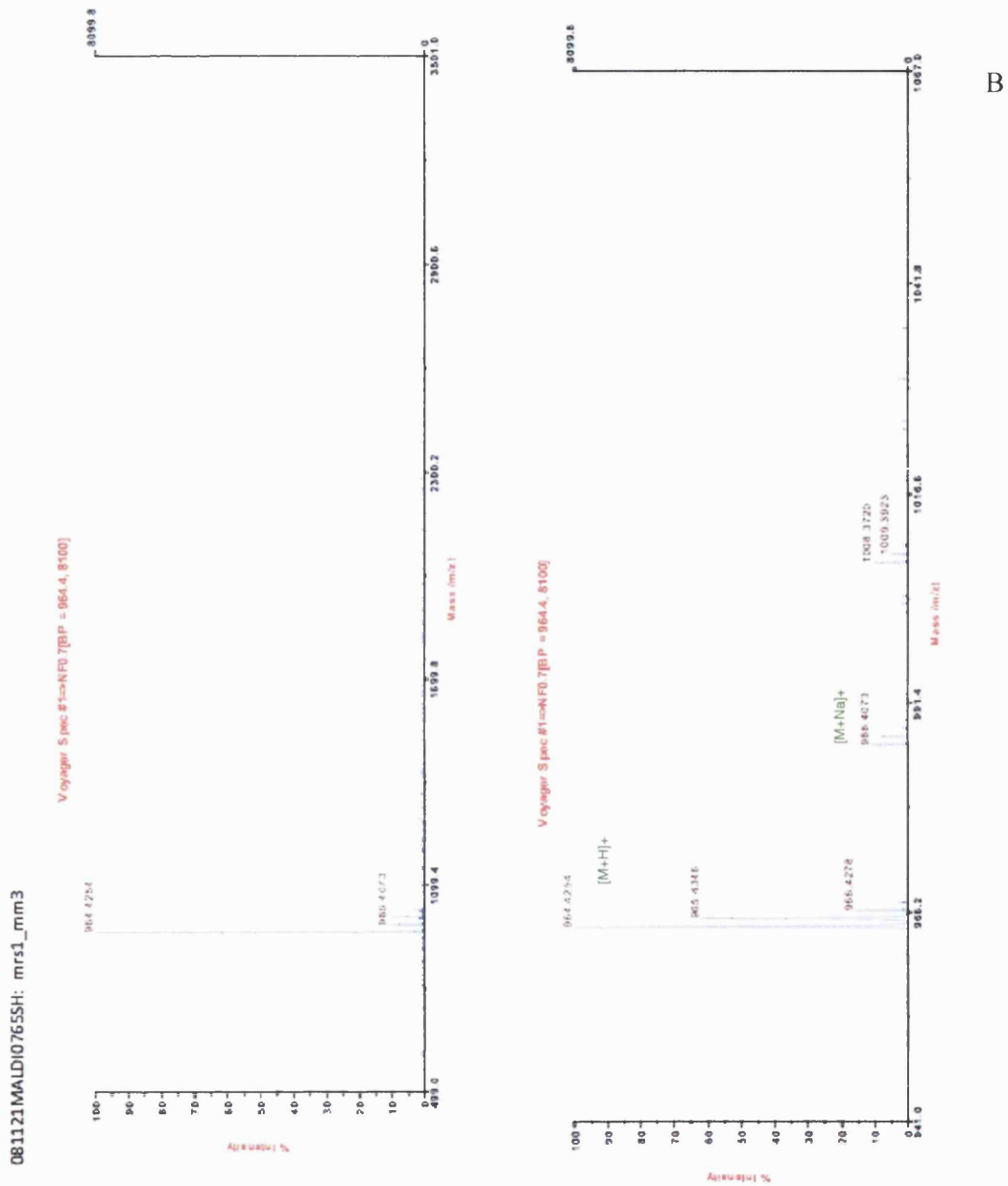


Figure 2.17: MALDI-TOF spectra of pDal (A, B).

The ^1H NMR spectrum for dalargin is shown in Figure 2.18. Chemical shift values in D_2O were found to be: δ 0.56 (d, $\text{H}_{\delta 2}$, Leu), δ 0.62 (d, $\text{H}_{\delta 1}$, Leu), δ 0.85 (m, H_{β} , Ala and H_{γ} , Leu), δ 0.9 (t, H_{γ} , Leu), δ 1.28 (m, H_{γ} , Arg), δ 1.47 (m, H_{β} , Leu), δ 1.61 (m, H_{β} , Arg), δ 2.8 (m, H_{α} , Phe), δ 2.90 (m, H_{α} , Leu), δ 3.42 (q, H_{α} , Ala), δ 3.55 (s, H_{α} , Gly), δ 3.86 (m, H_{δ} , Arg), δ 3.96 (m, H_{β} , Phe), δ 4.05 (m, H_{α} , Arg), δ 4.33 (m, H_{β} , Tyr), δ 6.60 (d, $\text{H}_{\epsilon 1\epsilon 2}$, Tyr), δ 6.86 (d, $\text{H}_{\delta 1\delta 2}$, Tyr), δ 6.95 (m, H_{ring} , Phe), δ 7.06 (d, $\text{H}_{\epsilon 1\epsilon 2}$, Arg). The ^1H NMR spectra for pDal is shown in Figure 2.18. Chemical shift values in $\text{DMSO-}d$ were found to be: δ 0.85 (m, $\text{H}_{\delta 2}$, Leu, CH_3 palmitoyl, $\text{H}_{\delta 1}$, Leu), δ 1.10 (d, H_{β} , Ala), δ 1.24 (m, H_{γ} , Leu and $(\text{CH}_2)_{12}$ palmitoyl), δ 1.37 (m, H_{β} palmitoyl), δ 1.49 (m, H_{γ} , Arg), δ 1.60 (m, H_{β} , Leu), δ 1.70 (m, H_{β} , Arg), δ 2.03 (t, H_{α} palmitoyl), δ 3.15 (m, H_{α} , Arg, H_{α} , Phe and H_{δ} Arg), δ 3.34 (s, H_{α} , Gly), δ 3.53 (m, $\text{H}_{\beta 2}$, Phe and $\text{H}_{\beta 2}$, Tyr), δ 3.53 (m, $\text{H}_{\beta 1}$, Phe and $\text{H}_{\beta 1}$, Tyr), δ 4.21 (q, H_{α} , Ala), δ 4.42 (m, H_{α} , Leu), δ 6.62 (d, $\text{H}_{\epsilon 1\epsilon 2}$, Tyr), δ 6.98 (d, $\text{H}_{\delta 1\delta 2}$, Tyr), δ 7.2 (m, H_{ring} , Phe), δ 8.2 (b, $\text{H}_{\epsilon 1\epsilon 2}$, Arg), δ 9.16 ($-\text{OH}$, Arg).

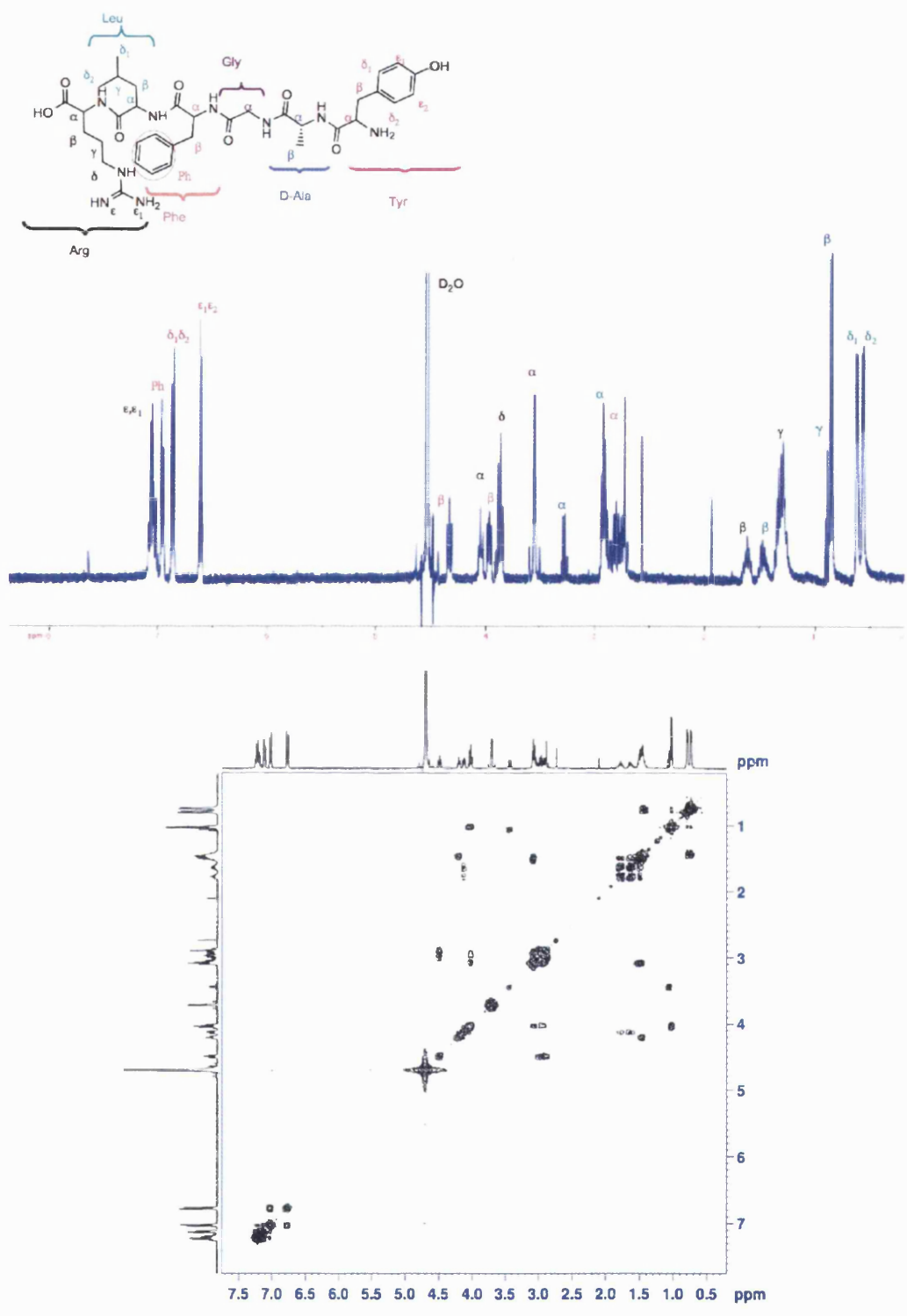


Figure 2.18: $^1\text{H-NMR}$ and $^1\text{H-}^1\text{H COSY}$ Dalargin in D_2O

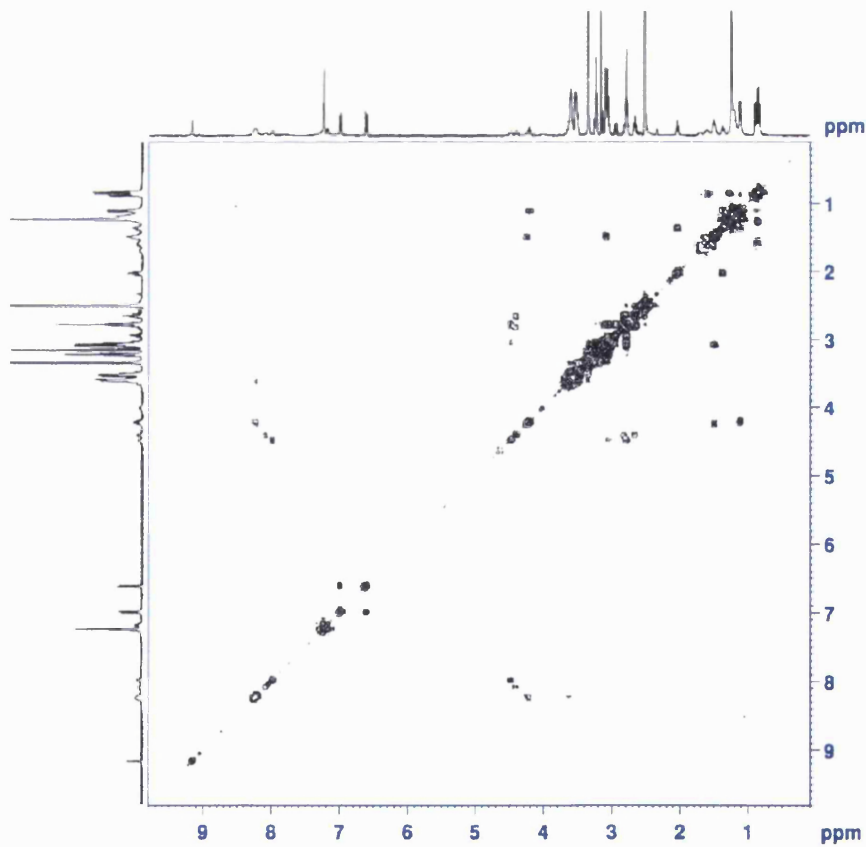
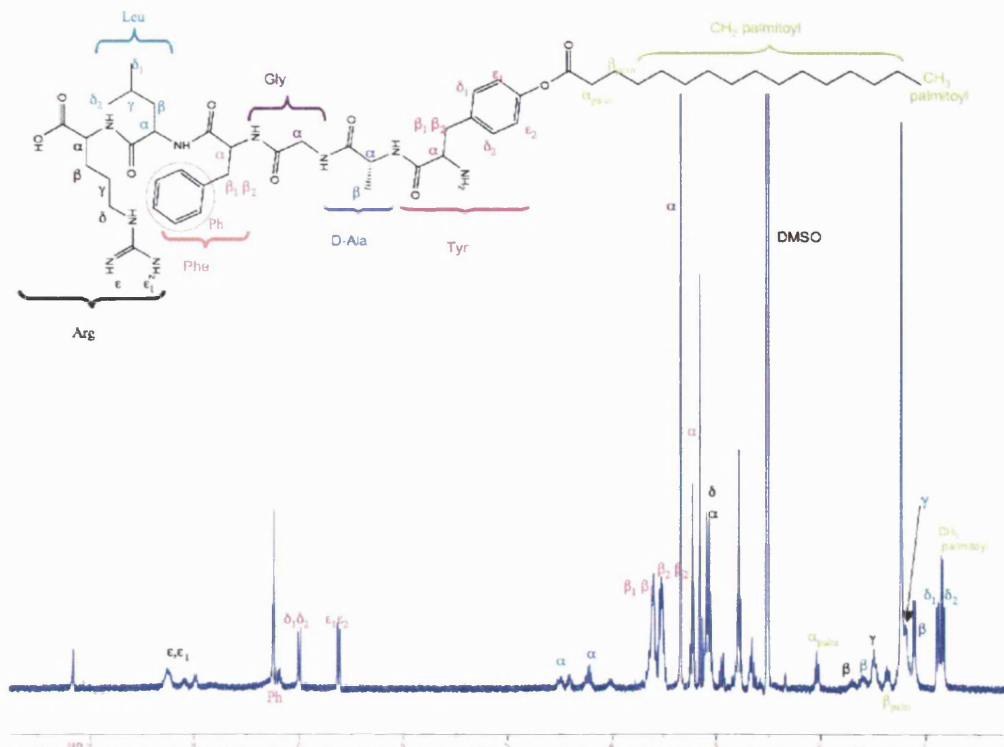


Figure 2.19: ^1H -NMR and ^1H - ^1H COSY of pDal in $\text{DMSO-}d_6$

Proton H-NMR and COSY confirm that the acylation reaction took place, giving rise to the formation of the amphiphilic derivative of Dalargin, palmytoil Dalargin. On the pDal spectrum (Figure 2.19) the presence of a triplet can be observed corresponding to the methyl group of the palmitic chain (multiplet $\delta = 0.85$ ppm), which overlaps with the doublet of doublets corresponding to the methyl groups of leucine.

In the spectrum of Dalargin (Figure 2.18) the triplet ($\delta = 0.9$ ppm, H_γ) of the methine of leucine is clearly visible, while the same signal on the pDal spectra is merged with the strong peak of the alkyl chain of the palmitic moiety $-(CH_2)_{12}-$.

The doublet corresponding to the methyl group on the alanine side chain (H_β) is clear both in the spectrum of Dalargin ($\delta = 0.85$ ppm) and pDal ($\delta = 1.10$ ppm).

Both signals of the protons attached in C_α and C_β of the palmitic chain are clearly visible on the pDal spectra (multiplet at 1.37 ppm = C_β), (multiplet at 2.03 ppm = C_α).

These signals are not present in the Dalargin spectra thus we can confirm that they belong to the palmitoyl chain.

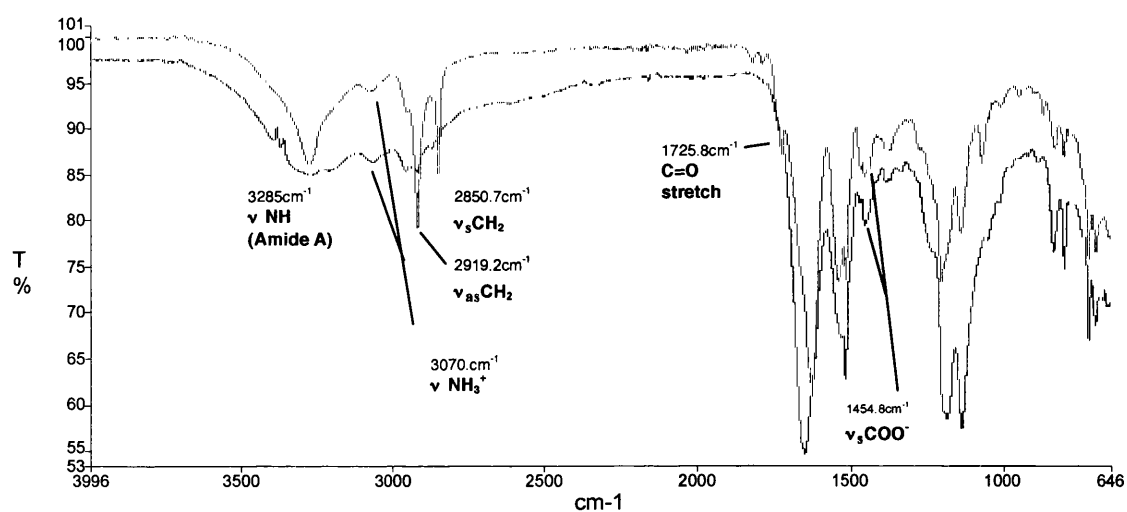


Figure 2.20: FTIR transmittance spectrum of freeze-dried pDal (red line) overlapped with the FTIR transmittance spectrum of dalargin (black line). Highlighted are some of the peaks relevant to the structure elucidation.

From the left to the right of the spectra in Figure 2.20, a pronounced Amide A band was observable for pDal but not for Dalargin. Both peptides are present in their

charged form as can be deduced by the presence of the ν NH_3^+ band around 3070 cm^{-1} and by the ν_s COO^- band around 1454.8 cm^{-1} .

In addition, the spectrum relative to pDal shows some important bands, absent in the spectrum of Dalargin, confirming the attachment of the palmitoyl moiety to the peptide: a band of stretching at 1725.8 cm^{-1} relating to the carbonyl ($-\text{C}=\text{O}$) of the ester linkage, a band at 2850.7 cm^{-1} relating to the $-\text{CH}_2$ symmetrical stretching and a band at 2919.2 cm^{-1} relating to the $-\text{CH}_2$ asymmetrical stretching of the palmitoyl chain.

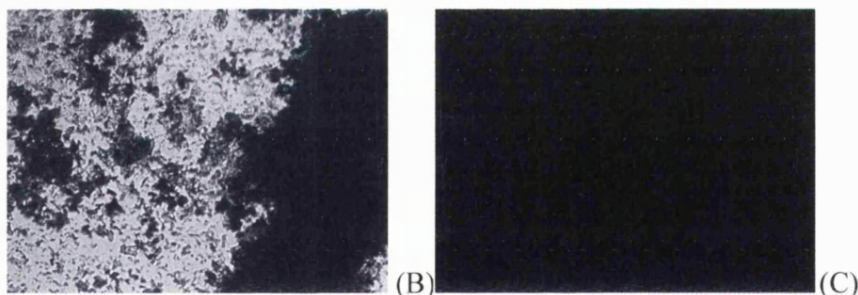
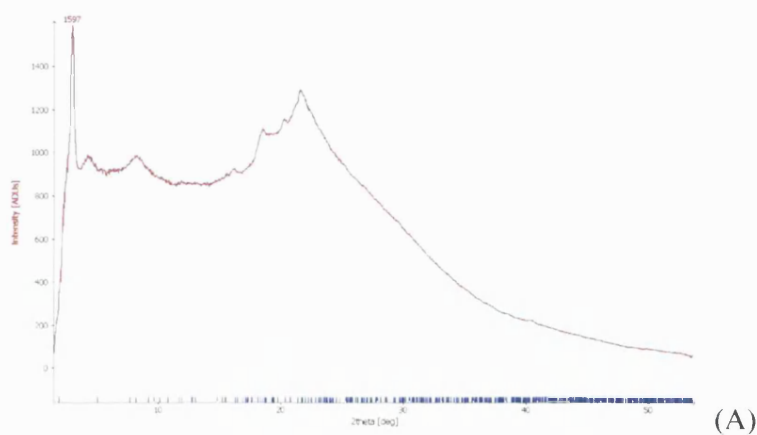


Figure 2.21: (A) XRD powder diffraction pattern of freeze-dried pDal; (B, C) micrographs of freeze-dried pDal viewed on an optical microscope without (B) and with (C) crossed polarized filters.

The freeze-dried product pDal showed small traces of ordered crystalline domains under crossed polarized filters (Figure 2.21 C), while the overall product was amorphous, indeed few little spots of light were visible when the filters were crossed

at 90°. This is confirmed as well by the X-ray diffraction pattern where no clear diffraction peaks were recorded (Figure 2.21 A).

2.5 Discussion

A series of polymeric and peptidic surfactant-like molecules were successfully synthesized and characterized. These amphiphiles will be investigated for the design of drug delivery system with different axial ratio, solubilizing agent for lipophilic molecules and carrier for the transport of drug molecules across biological barriers.

GCPQA is a chitosan-based polymer. Chitosan is a naturally occurring polymer which has been widely exploited for applications in the pharmaceutical field (Thanou et al., 2001a) (de la Fuente et al., 2010). Since chitosan is reported to have a great potential in the delivery of peptides via the oral route (Prego et al., 2005), this polymer was selected as candidate for the synthesis of an amphiphilic derivative such as GCPQA. However, to overcome the issue of the low solubility of chitosan, glycol chitosan was chosen as starting material and its molecular weight reduced upon acid hydrolysis to obtain a low molecular weight polymer. The free amine groups on the polymer backbone allow further modification while retaining its favorable biological interactions.

Derivatization of glycol chitosan resulted in an increase of molecular weight as measured with GPC-MALLS.

Grafting of the polymer with randomly distributed palmitoyl and acyl chain was confirmed by proton NMR.

The working hypothesis states that the grafting of the polymer should lead to the formation of small self-assembled micelles and the polymer will be investigated for its capability to act as a solubility enhancer and as peptide carrier to the brain, as previously reported in our group (Lalatsa, 2009, Uchehgbu IF, 2010). In addition to this, hydrophobically modified glycol chitosan has also been reported to encapsulate RGD, a small antiangiogenic peptide into nanoparticles (Kim et al., 2008). In vitro studies of this delivery system have shown that these nanoparticles were slowly releasing the peptide over one week time. When administered intratumorally in vivo,

the system showed a prolonged and sustained delivery of the RGD peptide compared to intravenous or intratumoral administration of RGD on its own (Kim et al., 2008).

Dalargin is a hexapeptide, synthetic analogue of Leu-enkephalin, having the structure Tyr-D-Ala-Gly-Phe-Leu-Arg (Figure 2.22), and has been used in USSR as remedy for peptic ulcers because of its gastric antisecretory and cytoprotective properties (Dajani et al., 1991). Dalargin acts also as an agonist on the opioid receptors, as the endogenous enkephalins and their synthetic analogues. Indeed, activation of the opioid receptors is involved in the induction of analgesia by all the endogenous opioid peptides, and their synthetic analogues (Davies, 2005).

The synthesis of both Dalargin and of its amphipathic derivative pDal (Figure 2.22 A and B) was achieved with a standard Fmoc-strategy.

The solid support chosen was a 2-chlorotrytil resin, with the first amino acid, arginine already loaded and protected on it. This is because loading of the first amino acid on to resins can be troublesome and decrease the final product yield if the loading is not optimal, especially in those cases where the amino acid carries bulky side-chain protective groups, as it was the case for the pentamethyldihydrobenzofurane-5-sulfonyl (Pbf) protecting group on the arginine side chain (Chan W.C, 2000).

A further advantage of this choice was that the cleavage conditions of peptides from the 2-chlorotrytil resins require mild acidic conditions, such as mixture of trifluoroacetic acid with phenol present as scavenger in ratio 95:5 (Barlos et al., 1991), and the protecting (Pbf) group is also more easily deblocked by TFA compared to other protective groups for the arginine side chain, such as 2,2,5,7,8-pentamethylchroman-6-sulfonyl (Pmc), thus allowing us to obtain in one single synthetic step removal of the side-chain protection and cleavage of the final product from the resin. The use of mild acidic cleavage makes the formation of possible side-products deriving from acidic degradation of the ester link between the palmitic chain and the tyrosine less likely to happen. The cleavage mixture used was then the reagent R, containing the scavengers anisole, thioanisole and ethandithiol for the deprotection of the (Pbf) group in less than 4 hours (Carpino L.A, 1993). Cleavage with reagent R was also preferred to the use of trifluoroacetic acid, H₂O, triisopropylsilane (95:2.5:2.5) because the latter was found to require much longer reaction times, in

acidic conditions and the final product would still contain arginine (Pbf) protected with the subsequent product containing significant quantities of a sequence with a Pbf protected arginine residue.

The attachment of the palmitoyl chain was achieved using a method previously reported for the esterification of the phenolic hydroxy moiety of Tyrosine (Uchegbu IF, 2010). An additional step was added, involving washing of the crude peptide with an organic solvent such as ethanol, that was optimal for removal of small impurities deriving from the use of the scavengers anisole, thioanisole and ethanedithiol.

Peptide and protein palmitoylation has been previously exploited to synthesize lipid derivatives (Foldvari et al., 1998) aiming to increase membrane permeation, because peptide and proteins are generally poorly transported across biological membranes. This is due to their hydrophilic nature, their high molecular weight and instability to enzymatic degradation. This modification thus increases the biological half-life of therapeutic peptidic molecules. For example reversible aqueous lipidization (REAL) conjugate fatty acids moieties via disulfide bonds that are then cleaved in vivo releasing the unmodified therapeutic peptide (Yuan et al., 2008, Yuan et al., 2005). Such modification enables a prolonged release of the peptide and it has been successfully applied for the lipidization of calcitonin (Wang et al., 2003), octeotride (Yuan et al., 2005), somatostatin analogues (Yuan et al., 2008), the Bowman-Birk protease inhibitor (Honeycutt et al., 1996) and desmopressin (Wang et al., 1999). For example lipidized calcitonine was found to have a plasma AUC four times higher than calcitonine after subcutaneous administration in mice (Wang et al., 2003). The oral administration in rats of the lipidized calcitonine showed 12 hours circulation, while calcitonine was undetectable in plasma after only 1 hour (Wang et al., 2003).

Dissolution of the peptide in the mobile phase was problematic, as the peptide was insoluble in the mobile phase only. Thus the peptide was first dissolved in DMSO and then purified running on a gradient elution. After RP-HPLC purification of the peptides the sequences were confirmed through spectroscopic mass analyses.

ESI-MS showed a fragmentation that matched the proposed structure for Dalargin and its amphipathic derivative pDal. Also peptide fingerprinting with MALDI-TOF confirmed the presence of the expected $[M+Na]^+$ and $[M+K]^+$ ions for each peptide.

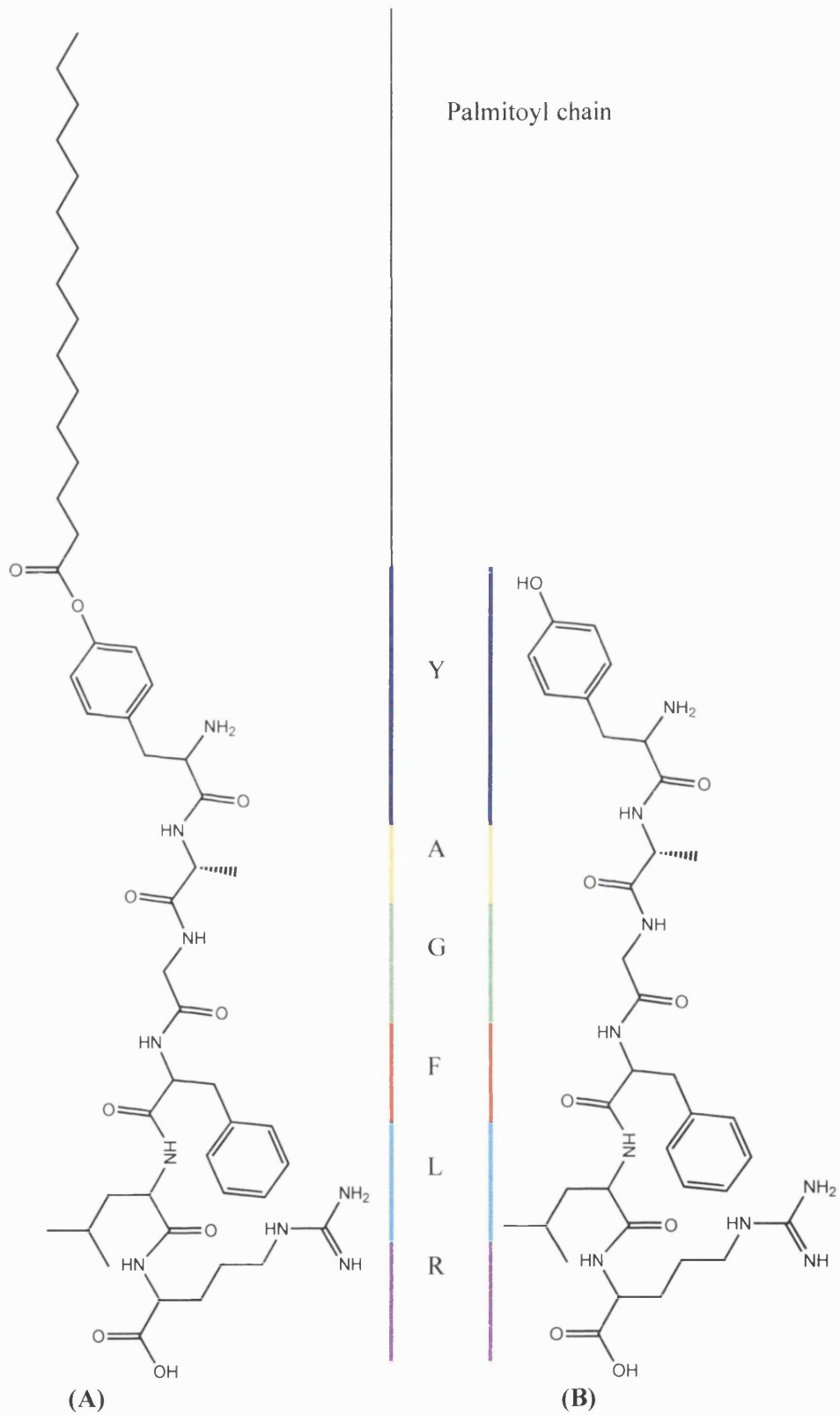


Figure 2.22: (A) chemical structure of palmitoyl Dalargin (pDal); (B) chemical structure of Dalargin.

The analysis of the NMR spectra provided further evidence that the correct sequence was achieved by the peptide synthesis. The structure assignment is based on the proton and COSY NMR spectra.

From the FTIR Absorbance spectra information regarding the peptide finger print region and the alkyl chain segment of the palmitic moiety were obtained to further support the data obtained from the mass spectrometry and NMR analyses.

The presence of the C=O stretching confirm the formation of the ester linkage between the phenol group of tyrosine and the carboxyl group of the C16 acyl chain.

The presence of the protonated amine at the N-terminus further confirms that no side products having the palmitic chain on the amino group of the Tyrosine are formed during the reaction.

In the last 5-6 years, there has been a dramatic rise in the interest in amphiphilic peptides due to the great potential that has been shown in the field of regenerative medicine and tissue engineering (Cui et al., 2010, Hamley, 2011). In Figure 2.23 are summarized several structures that have been explored by different groups.

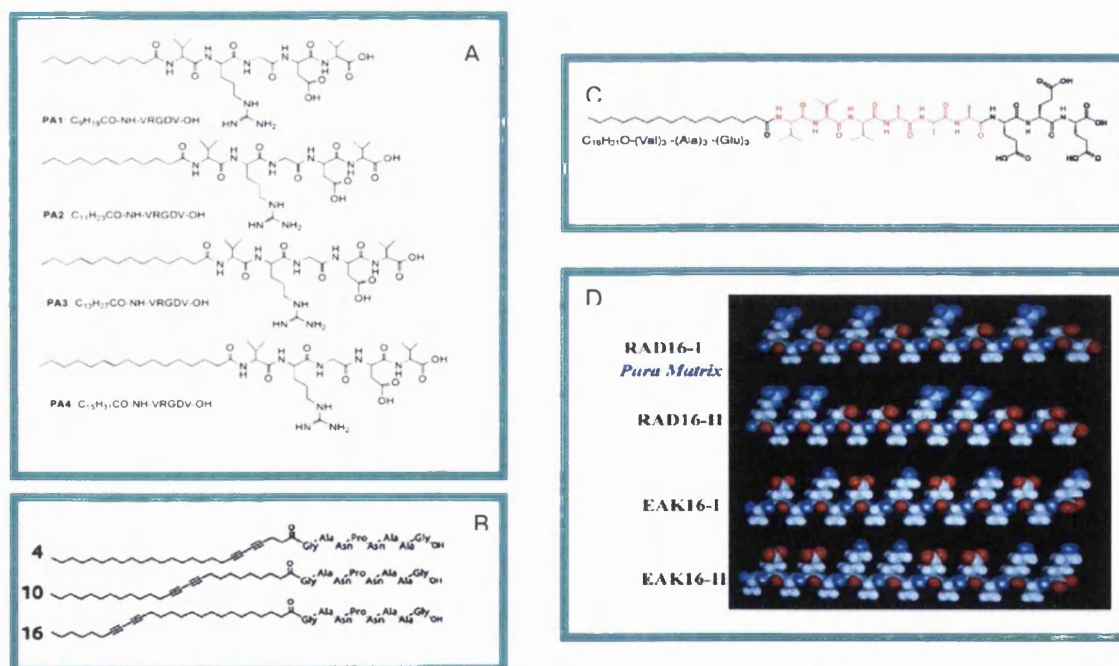


Figure 2.23: Chemical structures of peptide amphiphiles able to self assemble into high axial ratio micellar aggregates. Structures investigated by: A (Xu et al., 2010); B (van den Heuvel et al., 2010); C by Stop and co-workers (Pashuck and Stupp, 2010a, Hartgerink et al., 2001); D by Zhang and co-workers (Zhang et al., 2005).

Interestingly, a number of valuable papers have been published from different research groups around the globe, investigating the application of peptide amphiphiles of different nature as biomaterials for tissue engineering and 3D cell culturing.

Peptide amphiphiles have also found interesting non-biological applications such as template for metal nano-wires and nanoreactors (Ulijn and Smith, 2008).

Zhang and co-workers have developed peptide amphiphile that are made of amino acids only. The alternating alanine residues in the designer self-assembling peptides are similar to silk fibroin such that the alanines pack into inter-digital hydrophobic interactions (Zhang et al., 2005).

Stupp and co-workers have designed many peptide amphiphiles (PAs) similar to the one described in this work, having a palmitic moiety attached to the N-terminus of the peptidic sequence conferring a surfactant-like architecture to the molecules and enabling them to self assemble into nanofibres. Such nanofibres find a wide range of applications as biomaterials for tissue engineering (Webber et al., 2010a, Cui et al., 2010).

Other classes of peptide amphiphiles have been synthesized by varying the length of the alkyl chain (Yu and Tirrell, 2000, Forns et al., 2000, Xu et al., 2010) as summarized in Figure 2.22

Unlike the peptide amphiphiles mentioned above, to all these classes of PAs, pDal has a free N-terminus, to allow a free interaction of the pharmacophore with the opioid receptor. To explain the ligand-receptor interaction mechanism, opioid peptides are thought to interact with the opioid receptor via the tyrosine amino group, that is positively charged in physiological conditions, and the phenol, while the hydrophobic peptide region stabilizes the ligand at the level of the receptor site (Beck and Casey, 1954). The binding of the ligand to the receptor occurs via a salt bridge between the positively charged amino group on tyrosine and a negatively charged carboxylate group of an asparagine in the third loop of the receptor. There is also an H-bond formed between of the -OH- group on the tyrosine side chain and a histidine in the sixth loop (Kane et al., 2006). However, it has been shown that by changing the Tyrosine with a substituted phenylalanine, as in the case of 4- (carboxiamido)-phenylalanine substituted Leu-Enkephalin (Cpa-LE), the potency and selectivity towards δ -opioid receptors can be increased. This demonstrated that the assumption that a phenolic residue is required for high affinity binding of the ligand to the opioid

receptor can be challenged (Wang et al., 2007). Thus, palmitoyl Dalargin can be investigated for its activity on centrally-expressed opioid receptors.

In conclusion, two new classes of amphiphiles have been synthesized and characterized: a polymeric chitosan derivative, the amphiphile GCPQA, and a peptide amphiphiles, palmitoyl Dalargin (pDal).

Palmitoyl Dalargin is the first in class for a new nanotechnology platform for the delivery of peptides to the brain.

CHAPTER 3

pDal Nanofibres Preparation and Characterization

3.1 Introduction: Non-Spherical Shape Nanostructures.

Pharmaceutical research has always emphasized the importance of the carrier size for nanomedicine applications, but it has been only in the recent years that much attention has been focused on the importance of the shape for the pharmacological and biological function of drug delivery systems.

One of the characteristics that a good nanocarrier should aim to possess is long blood circulation (Nishiyama, 2007) and the shape of the carrier seems to play a key role in influencing this characteristic. For instance, block copolymers bearing a hydrophilic and hydrophobic segment can form different shapes and sizes and depending on rigidity, length and ratio of the polymer segments can self-assemble into structures of different shape and size (Figure3.1).

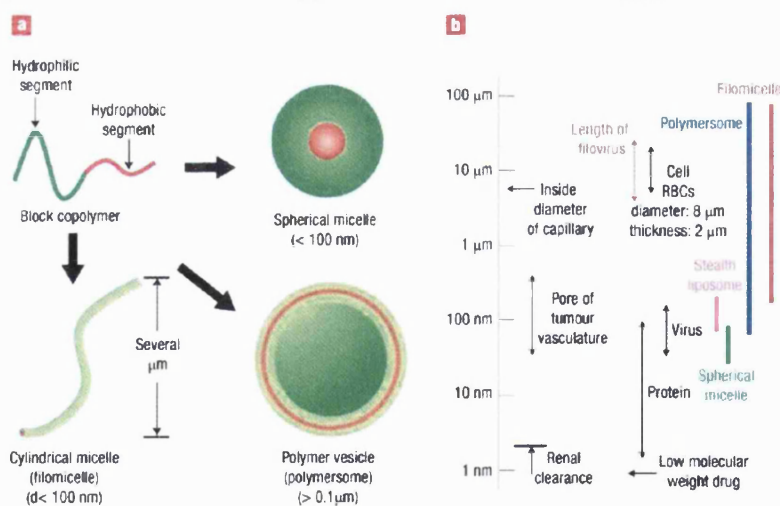


Figure 3.1: (a) self-assemble structures of different shape and size; (b) length scales showing how the various copolymer assemblies compare with structures in the body (Reproduction from Nishiyama 2007).

Nanoparticles, spherical and non-spherical, are cleared by the Reticuloendothelial System (RES) mainly through phagocytosis, while internalization of particles by all other cells takes place mainly by pinocytosis (Sahay et al., 2010). This latter can occur via a non-specific mechanism of adsorption, as discussed more in detail in the chapter 1 of the present thesis. Moreover, endocytosis can occur through at least 4 mechanisms: (i) clathrin-mediated endocytosis, (ii) caveolae mediated endocytosis, (iii) clathrin and caveolae independent endocytosis, (iv) macropinocytosis (Wang et al., 2011).

Although most current nanoparticle based drug delivery systems are spherical in shape, recent studies have shown that high axial ratio drug cargoes are capable of evading macrophage uptake and hence enjoy longer circulation times. An important report by Discher and co-workers (Geng et al., 2007) highlighted few years ago that circulating elongated vehicles were more persistent in the peripheral blood stream compared to their spherical counterparts (up to one week). Mitragotri and coworkers have shown that is the shape of the particles at the point where is in contact with macrophages, rather than the overall shape of the particles to influence internalization (Champion and Mitragotri, 2006), as the tangent angles of the particle surface at the point making the initial contact with macrophages has to be inferior to 45° to allow for particle internalization.

Theoretical studies by Decuzzi and Ferrari have shown that cylindrical particles laying parallel or orthogonally to the cell membrane can escape internalization while circular particles and quasi-spherical particles are wrapped by internalizing cells in the minimum time (Decuzzi and Ferrari, 2008). Also, several mathematical models have been proposed to describe the margination and adhesion of particles to the endothelial cell surface in circulation: Liu and co-workers have used numerical simulation to demonstrate that tumbling and “pin-over” effect of non-spherical particles could help adhesion under flow conditions. Thus rods and discs have higher adhesion probability over spheres because of tumbling and larger contact area (Figure 3.3). By simulating the blood flow conditions, the influence of nanoparticle shape, ligand, density and shear rate on adhesion probability where studied (Shah et al., 2011). Under the same conditions of shear flow, Brownian motion, volume of the particles, nanorods and the spherical nanoparticles presented different adhesion

probability: nanospheres could not get close enough to the wall surface and were washed away without touching the vessel surface, while nanorods could “tumble” and so deposit on the wall surface, as schematized in Figure 3.2.

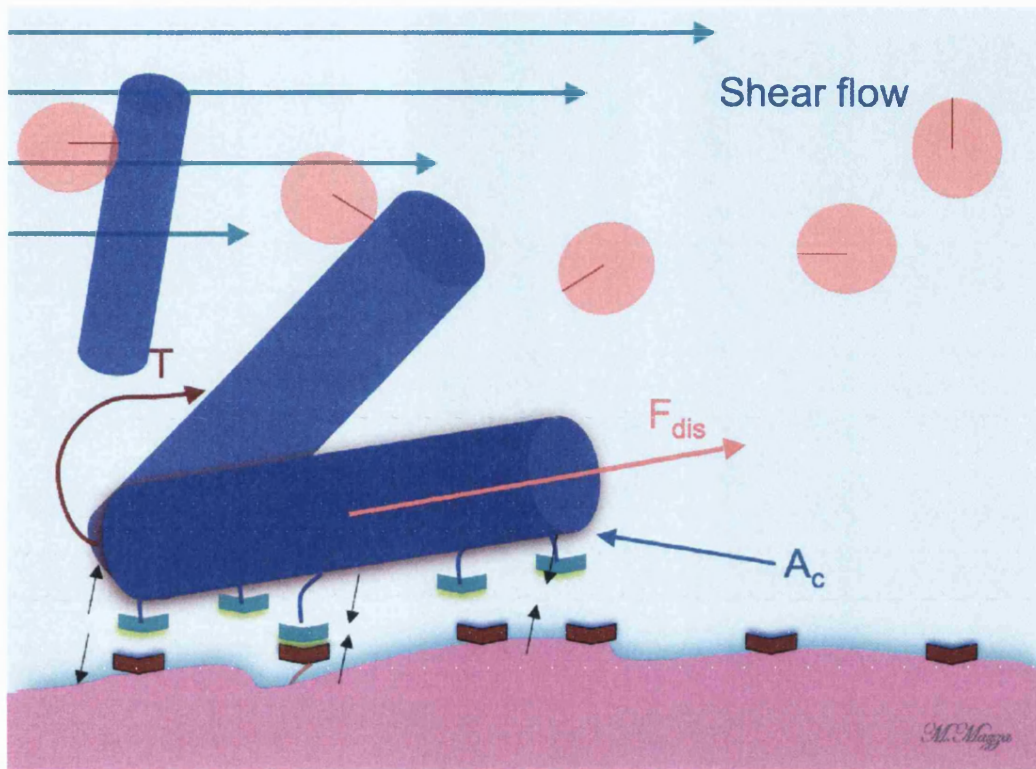


Figure 3.2: Shape dependent adhesion dynamics. The spherical particle is washed away. The rod nanoparticle in the blood circulation is subject to margination, tumbling, pin-over and adhesion. A_c is the contact area of particle to the cell surface, F_{dis} is the dislodging force comprised of two components, drag force along the flow direction and torque T due to tumbling (Shah et al., 2011, Tao et al., 2011).

The binding probability of a rod shaped nanoparticle was found three times higher than a spherical nanoparticle of the same volume and it was decreasing with increasing flow shear and channel height (Shah et al., 2011). Moreover, Decuzzi and Ferrari (Decuzzi and Ferrari, 2008) predict that the internalization of cylindrical particles depends on their aspect-ratio (γ) and volume. Particles with low γ are expected to be more easily internalized than particles with high γ . They observed that elongated particles in contact with their major axis (long dimension) parallel to the

interface are less prone to internalization than particles normal to the interface. The adhesion probability for nanoparticles of different shape is schematized in Figure 3.3.

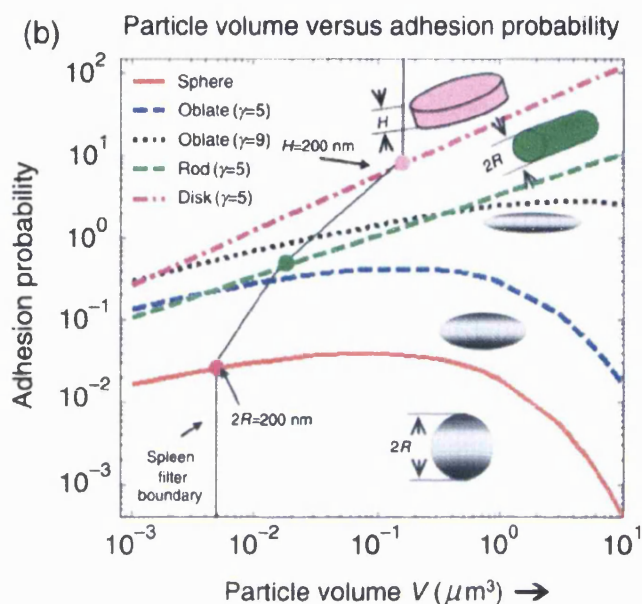


Figure 3.3: partial reproduction from Tao L. et al (Tao et al., 2011)

Most polymeric nanoparticles currently used for biomedical applications are fabricated using bottom-up chemistry methods and are spherical.

Bottom-up techniques can be employed also for the fabrication of worm-like micelles: for example, long worm-like micelles (22-60nm) have been prepared via self-assembly of PEG-polyethylene and PEG-poly(ϵ -caprolactone) incorporating paclitaxel (Geng et al., 2007). Self-assembly of Fe_2O_3 also resulted in the formation of worm micellar aggregates. Emulsification of poly(9,9-dioctylfluorene-cobenzothiadiazole) and poly(9,9-dioctylfluorene) formed nanoparticles of ellipsoid shape (Yang et al., 2005).

Some top-down approaches have also been applied to the preparation of nanoparticles of various shapes.

High-resolution soft lithography (PRINT[®]) has been extensively employed in the De Simone laboratory for the preparation of cubic, rod, conical and hex-nut nanoparticles (Petros and DeSimone, 2010). Nanoimprint lithography was also used for the preparation of nanoparticles incorporating Streptavidin-Cy5 fluorescent dye and

plasmid DNA (Glangchai et al., 2008).

Particles with determined size, shape and porous structure can be fabricated through a combination of photolithographic techniques and electrochemical etch. The resulting particle maintains a central nucleation site in the size and shape of the photolithographic pattern, surrounded by an external corona whose thickness is determined by the electrochemical etch. Ferrari and co-workers have fabricated particles with a circular nucleation site of size ranging from 400 nm to over 5 μm (Chiappini et al., 2010).

Studies of biodistribution on silica nanoparticles of different shape (spherical, discoidal, hemispherical, cylindrical) prepared using lithography in conjunction with etching techniques have shown that for the non-spherical particles, a larger accumulation of non spherical particles was observed in most of the organs (Decuzzi et al., 2010).

Filamentous nanomaterials are designed as transporters of therapeutic and/or diagnostic agents with desired control over their *in vivo* tissue navigation, cargo release and clearance profile (Kostarelos, 2010): e.g. carbon nanotubes have demonstrated considerably increased accumulation and retention in tumor tissues *in vivo* (Dai et al., 2007).

Our goal is to prepare drug carriers which will evade uptake by macrophage cells thus enjoying longer circulation times in the blood stream. We hypothesize that non spherical, high axial ratio self-assembling peptide nanoparticles may prove suitable in this regard.

3.1.2 Encapsulation of Pyrene within Self-Assembled pDal Amphiphile Nanofibers

There are five predominant vibronic bands in the fluorescence spectra of pyrene. The intensity of the first vibronic peak (I1) is significantly enhanced in polar solvent in contrast to the third vibronic peak (I3), which has minimal intensity variation with polarity. When pyrene encounters a non-polar environment such as the hydrophobic domain formed by polymer aggregates, there will be an increase in the intensity of I3 in relation to I1 hence causing an increase in the I3/I1 ratio. The intensities of the vibronic bands in pyrene monomer fluorescence are governed by the polarity of the

surrounding environment and these variations in the vibronic band intensity ratio ($I_{3/11}$) have been used to determine the Critical Aggregation Concentration (CAC) values of the amphiphilic peptide pDal. The $I_{3/11}$ ratio increases with increasing concentrations of pDal as the increase in the number of aggregates is directly proportional to the number of hydrophobic domains available for pyrene to partition into (Kalyanasundaram and Thomas, 1977).

3.1.3 Z-Potential

Particles suspended in an inert liquid can move by gravity and/or Brownian motion and their ionizable chemical groups on the surface form net charges (Particles CIC, 2008). The appearance of a net charge influences the distribution of surrounding ions and results in an increase in counterions (Figure 3.4). The region through which this influence extends is defined as the electrical double layer: one layer of ions strongly binds to the ionized charged groups at the particle surface, and it is also called Stern layer; one outer layer comprises loosely associated ions, and it is also known as diffuse layer (Sherman, 1970, Zetasizer Nano Series Technical Notes, 2010). Within the diffuse layer there is a notional boundary defined as “slipping plane” within which ions and particles form a single entity. Outside of this boundary ions stay free in the dispersant medium. The electric potential at the slipping plane is called Z-potential.

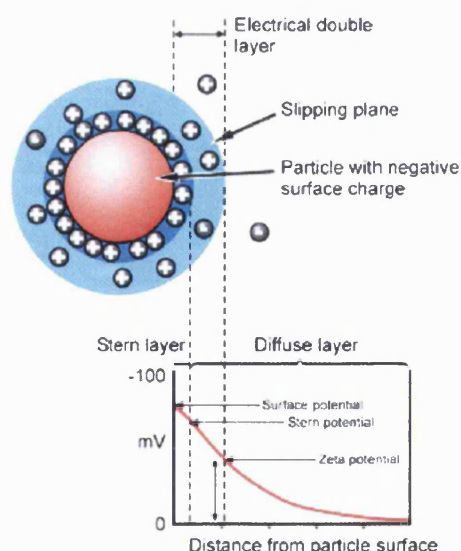


Figure 3.4: Schematic Representation of Z-potential. Reproduction from (Zetasizer Nano Series Technical Notes, 2010).

An importance consequence of the electrically charged particle is that they interact with an applied electric field and cause electrokinetic effects such as electrophoresis, electroosmosis, streaming potential and sedimentation potential. Charged particles within an electric field are attracted towards the electrode of the opposite charge with a constant velocity. The velocity of a particle in a unit electric field is defined as electrophoretic mobility. The zeta potential is related to the electrophoretic mobility by the Henry equation

$$U_E = \frac{2 \epsilon z f(\kappa a)}{3 \eta}$$

where U_E is the electrophoretic mobility, z the zeta potential, ϵ dielectric constant, η viscosity and $f(\kappa a)$ Henry's function. κa measures the ratio of the particle radius to electrical double layer thickness (Zetasizer Nano Series Technical Notes, 2010).

The magnitude of Z-potential gives an indication of the potential stability of a colloidal system. In general, when all the particles have a large positive or negative Z-potential they will repel each other and there is dispersion stability. On the other hand, when the particles have low Z-potential values there is no force to prevent the particles coming together. The dividing line between stable and unstable dispersions is generally taken at either +30 or -30mV, thus particles that are more positive or more negative than these values are normally considered stable (Sherman, 1970).

3.1.4 Fibre X-ray Diffraction

Fibre diffraction is a well established technique for the study of the core structure in amyloid fibrils and it is used to establish the position in space of the β -sheets with respect to the fibre long axis (Makin and Serpell, 2005b). It has also been used to determine the presence of β -sheet ordering in peptide amphiphile self-assembled nanofibres (Pashuck and Stupp, 2010a).

A diffraction pattern arises from the interaction of the X-ray with the electrons in the sample. The sample structure is three-dimensional as three-dimensional is its electron density. Therefore, what is seen on the X-ray detector plate is two-dimensional. The interaction between the X-ray and the sample electrons is also three-dimensional and it is related to the intensity of the Fourier Transform of the electron density. Visually

on the plate we see a projection of the two dimensional pattern. Diffraction from crystals results in a diffraction pattern comprising of sharp spots described by reciprocal lattice vectors a , b and c : all crystals with the same lattice will have a diffraction pattern with spots in identical places (Makin and Serpell, 2005b).

Self-assembled peptide nanofibres, like amyloid fibrils, consist of units that repeat along the fiber axis and because they are cylindrically symmetric the sharp spots are spread out into diffraction arcs and the appearance of the arcs depends on the *texture*, or crystallites within the material.

For data interpretation it is to be noted that the meridional direction of the fibre diffraction pattern contains the crystalline dimension data, whereas the equatorial direction combines the other two directions, thus spots in the meridional direction carry information about how the structure repeats in the direction of the fiber, as seen in figure 3.5 (Makin and Serpell, 2005b).

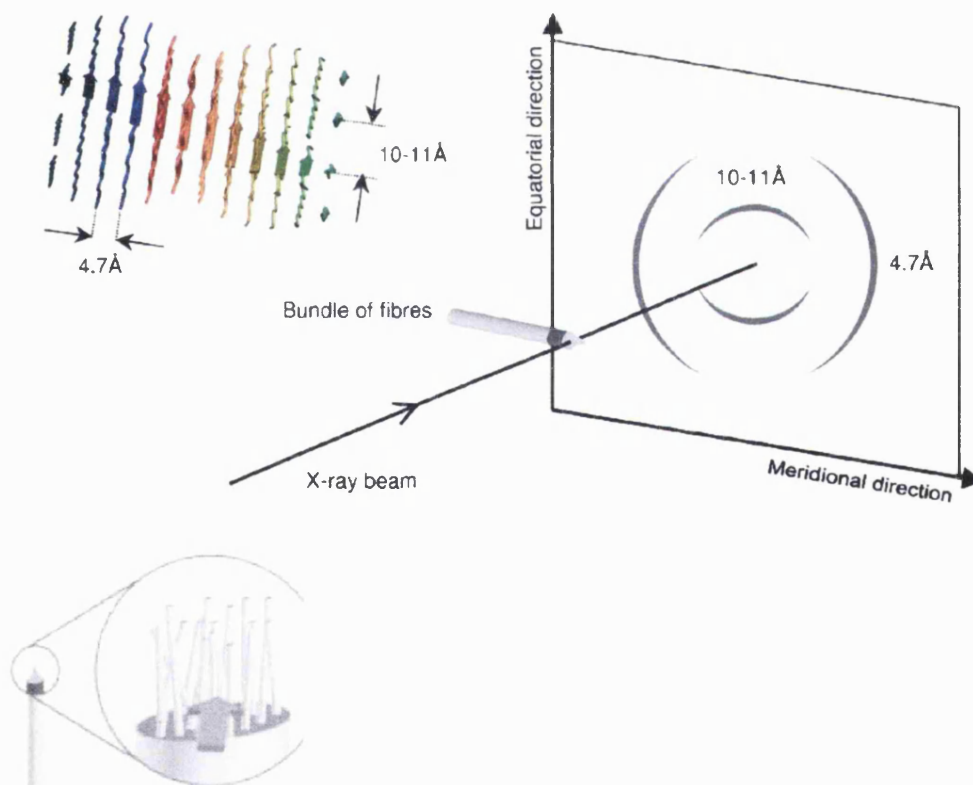


Figure 3.5: amyloid fiber diffraction showing the position and orientation of β -sheets and the resulting diffractogram. Adapted from Makin O.S. and Serpell L.C. (2004), *Fibre Diffraction Review 12*, 29-35.

3.1.5 Circular and Linear Dichroism Spectroscopy

Circular Dichroism (CD) is the difference in absorption of left and right circularly polarized light

$$CD = A_l - A_r$$

Because a chiral molecule has no reflection plane, any rearrangement of its electrons will miss reflection plane as well, thus electrons can be described as moving in helices; considering that in circularly polarized light the electric field vectors describe helices the interactions between circularly polarized light and a chiral molecule will be different: if the helix of electron motion is right-handed, then it is more easily induced by left circularly polarized light of appropriate frequency, than by right circularly polarized light, and a positive signal is observed (Nordén et al., 2010).

Linear Dichroism (LD) is defined as the difference in absorption, A , of light linearly polarized parallel and perpendicular to an orientation axis:

$$LD = A_{||} - A_{\perp}$$

LD requires the biological system under investigation to be intrinsically oriented or to be oriented during the experiment with respect to the incident light (Hicks et al., 2010).

In this chapter methods for the preparation of pDal nanofibres and their characterization will be discussed. The preferential formation of high axial ratio nanostructures has been investigated and the driving forces for the self-assembly of the nanofibres experimentally probed using different physicochemical approaches: X-ray diffraction and Dichroism Spectroscopy have been used for the analysis of the structural arrangement of the peptide backbones within the nanofibres. Fibre diffraction is used to study the mature nanofibre, Dichroism Spectroscopy provides insight into the organization of the secondary structure and the environment and

orientation of aromatic side chains which accompany self-assembly of the peptide nanofibres.

The interaction of the structure with other chemical entities has been used to probe the arrangement at a molecular level, both for the interaction between the peptide backbones and the interaction between the palmitoyl chains.

3.2 Methods

3.2.1 Preparation of Nanofibres

- **Probe Sonication**

Self-assembled pDal nanofibres were prepared by vortexing a suspension of pDal (1 mg mL⁻¹) in water, followed by probe sonication (MSE soniprep 150, MSE London, UK) with the instrument set at 50% of its maximum output for 5, 10 or 20 minutes on an ice bath. pDal nanofibres/ GCPQA were prepared by adding a freshly prepared solution of polymer in deionized water or buffer to the freeze-dried peptide using a ratio pDal: GCPQA = 1:1 w/w, followed by probe sonication (MSE soniprep 150, MSE London, UK) with the instrument set at 50% of its maximum output for 5, 10 or 20 minutes on an ice bath. Different buffers and surfactants were also tested as summarized in Table 3.1.

- **Microwave heating**

pDal nanofibres were prepared by applying a short microwave burst (Microwave Panasonic NN-3454 800W-D, Panasonic UK, Bracknell, Berks) for 10 seconds with the power level at Simmer (240W) and/or High (800W) to a suspension of pDal nanofibres (1 mg mL)

3.2.2 Pyrene

A dilute aqueous solution of pyrene (2 μM) was prepared by first dissolving pyrene in ethanol (0.4 mgml⁻¹). 100 μl of this solution was pipetted into a volumetric flask (100 ml) and the ethanol was evaporated off under a stream of nitrogen. The solution was then made up to 100 ml with distilled water. Using the aqueous pyrene solution

as the solvent, polymer solutions of various concentrations (1×10^{-4} mgml⁻¹ to 10 mgml⁻¹) were prepared by probe sonication as previously described. The fluorescence emission spectra of the pyrene polymer samples were recorded (340 – 600 nm) at an excitation wavelength of 335nm using the fluorescence spectrophotometer (Perkin Elmer LS50-B). The aqueous pyrene solution also served as a control. The I_3/I_1 ratio was calculated from the intensity of the third (383 nm) and first (375 nm) vibronic peaks in the pyrene emission spectra (Uchegbu et al., 2001, Yang et al., 2007). Measurements were performed in triplicates.

3.2.3 Z-Potential

The Z-potential was estimated on fresh nanofibres solutions using a NanoZS, Malvern Instruments Ltd., U.K, in clear disposable Zeta Cells (Malvern Instruments Ltd., U.K).

3.2.4 Electron Microscopy

The nanofibres were imaged using transmission electron microscopy (TEM). A drop of sample liquid was placed on Formvar[®]/Carbon Coated Grid (F196/100 3.05 mm, Mesh 300, Tab Labs Ltd, England). Excess sample was blotted off with No.1 Whatman Filter paper and negatively stained with uranyl acetate (1% w/v). Imaging was carried out using a Philips FEI CM120 BioTwin Transmission Electron Microscope operating at 120kV. Digital Images were captured using an AMT digital camera.

3.2.5 X-ray Diffraction (XRD)

Sample for XRD was prepared by modifying the stretch frame alignment method (Makin and Serpell, 2005a). A glass capillary holder was home-built at the Workshop of the Department of Pharmaceutics, The School of Pharmacy, University of London. The ends of two borosilicate glass capillaries were waxed and cut to a length of 2-3 cm. Two of these wax-plugged capillaries were placed about 0.5-1 mm apart (with the wax ends facing) and secured on the sample holder with some Plasticine. A droplet (10 μ L) of pDal nanofibres solution (10 mg/mL) was placed between the wax ends. The capillary holder was covered with its top to prevent dust contamination and the

sample left to dry at room temperature for several hours. Datasets were collected at room temperature on an Oxford Diffraction Xcalibur NovaT X-ray diffractometer (Oxford, UK).

3.2.6 Congo Red UV-Absorbance

A filtered solution of Congo Red (900 μ L, Sigma-Aldrich) in potassium phosphate buffer (5mM, pH 7.4, containing 150mM of NaCl) was added to a dispersion of 100 μ L of pDal nanofibres (1 mg mL⁻¹), such that the final concentration of pDal nanofibres was 100 mg mL⁻¹. The samples were incubated at room temperature (25°C) for 1 hour before the absorption was recorded using the UV-Vis UV-1650PC spectrophotometer (Shimadzu, U.K.) at a wavelength of 700-400 nm. The baseline was measured using the phosphate buffer (5mM) used to prepare the Congo Red stock solution.

3.2.7 Thioflavin-T Fluorescence

The sample was prepared by mixing Thioflavin-T (250 μ L, 22 μ M, Sigma-Aldrich), in EDTA buffer (10 mM Tris-HCl, 1 mM disodium EDTA, pH 8.0, Sigma-Aldrich) and a dispersion of pDal nanofibres (250 μ L, 1 mg mL⁻¹). The mixture was mixed and left to rest for at least 2 minutes before measurement were taken. Spectra were recorded on a Perkin Elmer LS Luminescence Spectrophotometer (Perkin Elmer, UK). Fluorescence was measured setting the excitation at 440 nm (5 nm slit width) and the emission between 460 and 700 nm (5 nm slit width).

3.2.8 Dichroism Spectroscopy

Circular (CD) and Linear (LD) dichroism experiments on pDal nanofibres (1 mg mL⁻¹, 0.2 mg mL⁻¹, 0.1 mg mL⁻¹) were performed on a Jasco J-815 CD at the Department of Chemistry, University of Warwick. Signal of CD, LD, and Absorbance were recorded scanning at a wavelength of 350-180 nm using a quartz cuvette with path 100 mm and 1cm. For flow LD experiments a Couette flow cell was used, so that the sample was endlessly flowed between a quartz capillary fitted and a quartz rod with a separated

quartz cylinder that create a pathlength of 0.5mm. The capillary was rotated so that a laminar flow was imposed on the sample, the molecules were subject to shear forces and the long axis of the fibres oriented along the flow direction.

For experiments with Congo Red and Thioflavin-T stained nanofibres the scan wavelength was 650-180 nm.

3. 3 Results

pDal nanofibres were quickly prepared by probe sonication when the peptide amphiphiles were suspended in deionized Millipore water (Figure 3.6). pDal nanofibres were also prepared by applying short burst of microwave heating. Under TEM the nanofibres prepared by microwave heating appear considerably longer than nanofibres prepared by probe sonication.

From TEM we observed a mixed population of twisted and straight nanofibres (Figure 3.6 B, C, D), and in some fresh samples we could also observe the presence of small spherical micelles, in accordance with some studies were mixed population of fibrillar aggregates were observed for amyloids deriving from human serum albumin (Krebs et al., 2004).

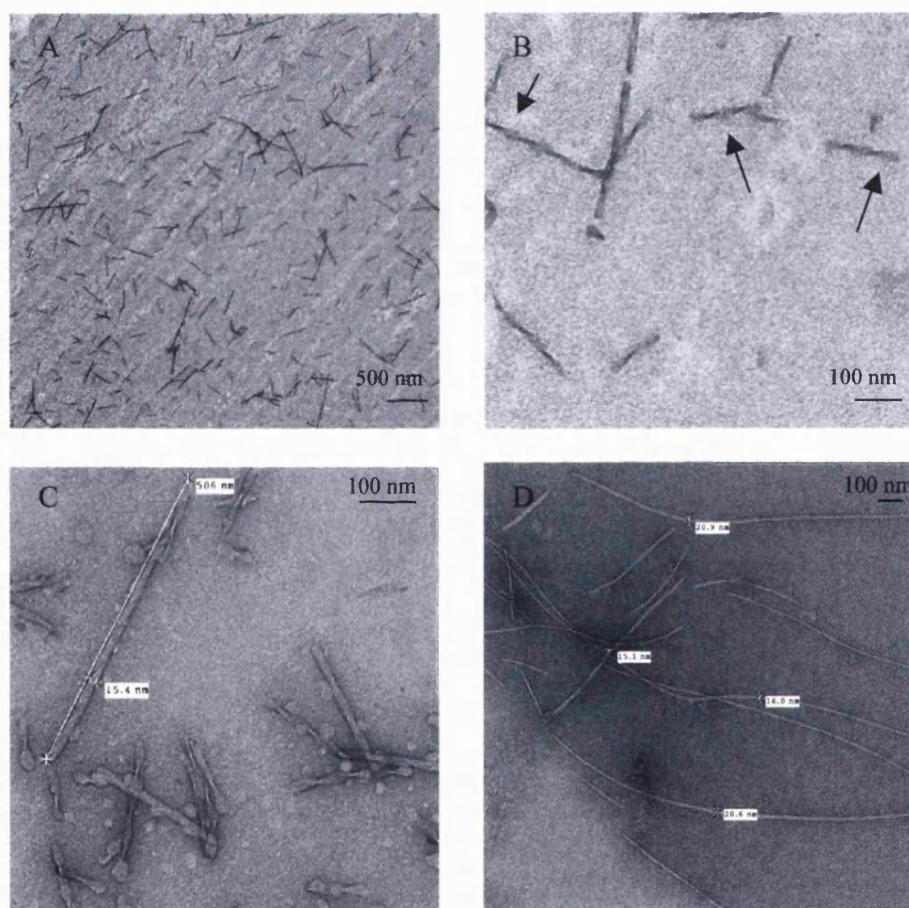


Figure 3.6: TEM Images of pDal nanofibres. (A, B, C) pDal 1mgmL^{-1} in Millipore water sonicated 5 minutes; (D) pDal 1mg/mL in Millipore water microwave heated for 10 seconds. Arrows in B highlight the twisted fibrillar conformation assumed by the nanofibres.

Moreover, spherical assembly of peptide amphiphile were observed on de novo designed peptide amphiphiles with repetitive glycines as hydrophobic portion (Santoso et al., 2002).

One possible explanation to this observation is that there is an evolution with time of the self-assembled nanostructures and the spherical micelles may be the short-lived species that tend to disappear.

The ability of pDal nanofibres to self-assemble into nanofibres was evaluated also in different media, with and without the presence of GCPQA or in presence of different surfactants at a fixed concentration of 1mg/mL, as summarized in TABLE 3.1.

Occasionally, at this concentration with both the techniques it was possible to observe visible aggregates in the solution forming after leaving the solution to stand for a couple of hours at room temperature. We propose that the aggregates can be removed by centrifugation (1000g for 1 minute).

TABLE 3.1 - pDal nanofibre formulations at 1mg/mL

Medium	pDal	pDal/GCPQA	shape
Water	1mg mL ⁻¹	1mg mL ⁻¹ , 1:1 w/w	nanofibre
NaCl 0.9%	1mg mL ⁻¹	1mg mL ⁻¹ , 1:1 w/w	nanofibre
10% EtOHv/v	1mg mL ⁻¹	1mg mL ⁻¹ , 1:1 w/w	nanofibre
PBS (0.01M phosphate buffer, 0.0027 M potassium chloride and 0.137 M sodium chloride, pH 7.4)	1mg mL ⁻¹	1mg mL ⁻¹ , 1:1 w/w	nanofibre
Acetate Buffer (0.3M sodium acetate / 0.2 M acetic acid, pH 5.0)	1mg mL ⁻¹	--	nanofibre
PF68 0.2% w/v	1mg mL ⁻¹	--	fibre/aggregates
PVP, 0.2% w/v	1mg mL ⁻¹	--	none
Polysorbate80 (Tween 80), 0.2%w/v	1mg mL ⁻¹	--	fibril mesh

The ability of pDal to form nanofibres in all the media, also in high concentration of surfactants, such as Polysorbate 80 (Figure 3.7 D) and pluronic PF68 (Figure 3.7 A, B) suggests that strong interaction between molecules drives the formation of the nanostructures, the presence of surfactants is not sufficient to solubilize the single pDal molecules suspended in water.

The use of a carbohydrate polymer (GCPQA) able to form micelles did not affect the formation of fibrils either. GCPQA is part of the family of carbohydrate polymers that can encapsulate lipophilic peptides such as Leu-Enkephalin and TPLENK, the

palmitoylated derivative of Leu-Enkephalin (Lalatsa, 2009). In this study we observed that while polymeric micelles were still forming, the amphiphilic nature of the pDal peptide was prevailing over its hydrophobicity, thus the peptide molecules were self-assembling in nanofibres, instead of being encapsulated in the hydrophobic pockets of the polymeric micelles.

Only the polyvinyl pyrrolidone was able to prevent the formation of fibrils. In these formulations was possible to observe a fine presence of micelles in the background and few big aggregates, while the appearance of the solution was clear to eye examination, that seemed suggesting complete solubilization.

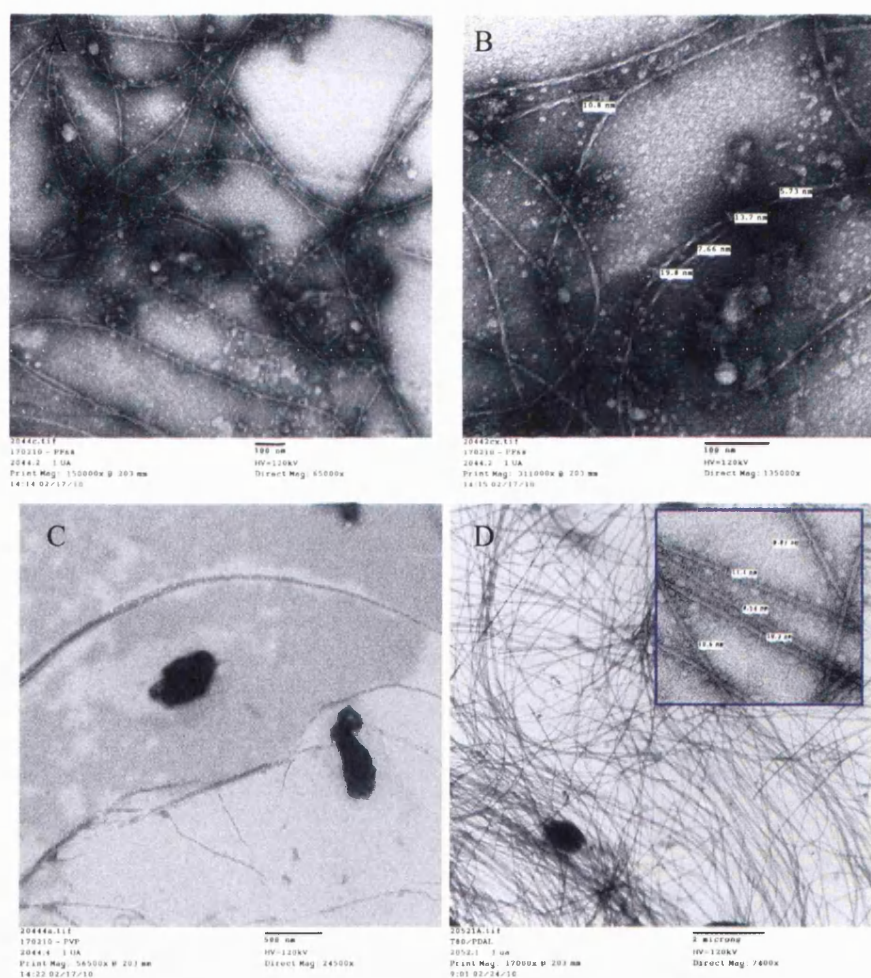


Figure 3.7: TEM images of pDal nanofibres. (A, B) pDal in water 1mg/mL in presence of PF68 (peptide: surfactant ratio= 1:2); (C) pDal in water 1mg/mL in presence of PVP (peptide: surfactant ratio= 1:2); (D) pDal in water 1mg/mL in presence of polysorbate (Tween 80) (peptide: surfactant ratio= 1:2). Sonication time 15 minutes.

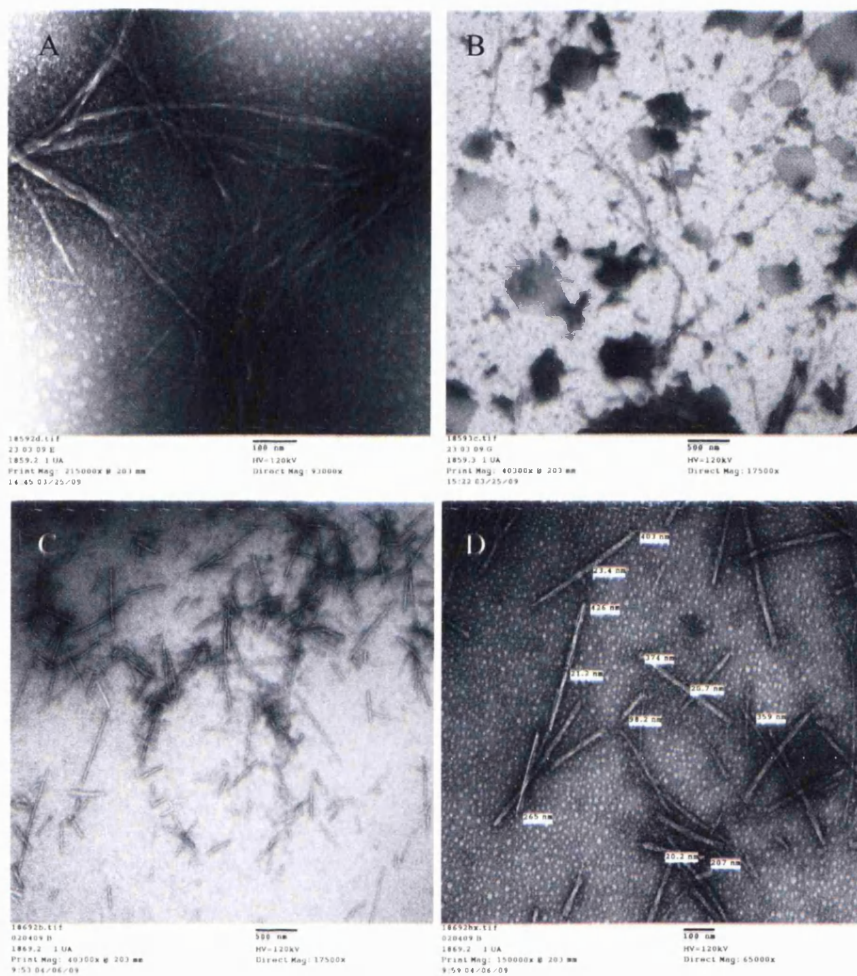


Figure 3.8: TEM images of pDal nanofibres. (A) pDal 1mgmL⁻¹ in PBS (B)pDal nanofibres in presence of the polymer GCPQA (ratio pDal:GCPQA = 1:1 w/w) in PBS sonication 15 minutes; (C, D) pDal nanofibres in presence of the polymer GCPQA (ratio pDal:GCPQA = 1:1 w/w) in water sonication 15 minutes.

The variations in suspending media, surfactant, method of preparation (sonication and microwave heating) and the use of polymer did not result in a complete control over the length or the shape of the nanofibres.

The critical aggregation concentration (CAC) was measured by vibronic band intensity variations in pyrene monomer fluorescence (Figure 3.9) and values fall in the range of 5×10^{-4} mgmL⁻¹.

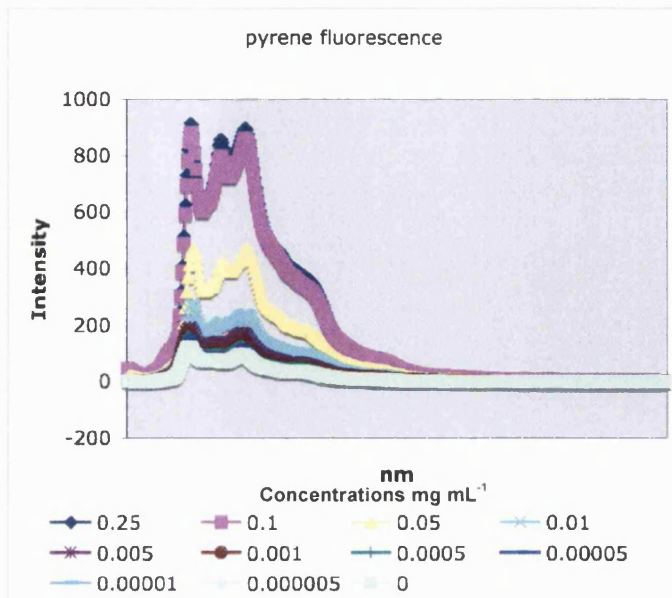


Figure 3.9: Critical Aggregation Concentration of pDal studied with the pyrene: vibronic band intensity variations in pyrene monomer fluorescence as function of the concentration (mg mL^{-1}).

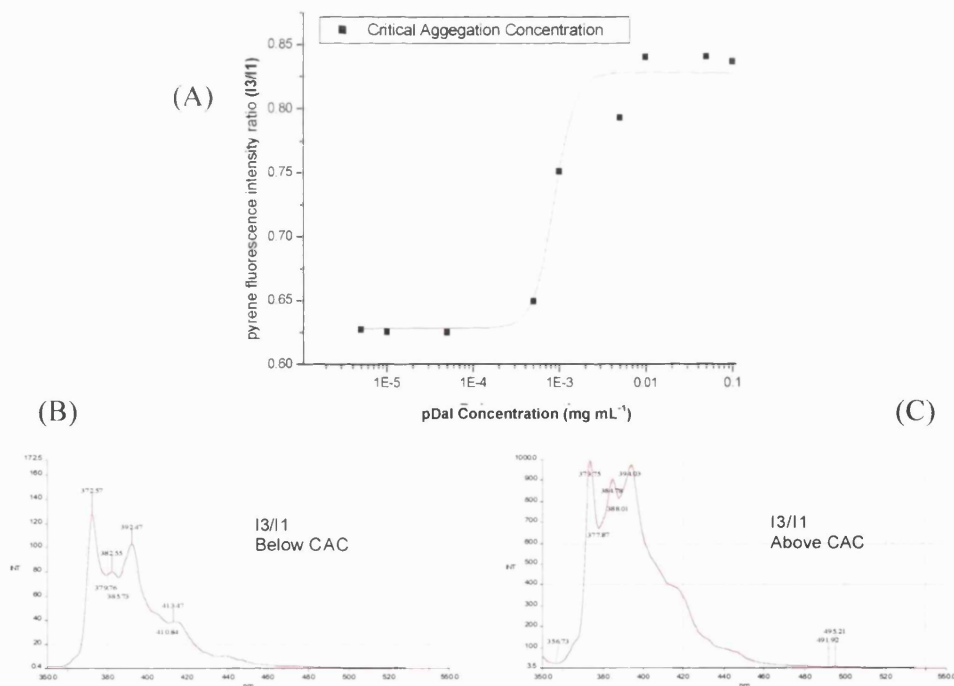


Figure 3.10: (A) plot of CAC of pDal concentration; I3/I1 ratio at concentration below (B) and above CAC (C).

The fluorescence emission of pyrene is highly sensitive to its local environment (Kalyanasundaram and Thomas, 1977). The I₃/I₁ ratio increase with increasing concentrations of pDal (Figure 3.10 A) because the number of hydrophobic domains where pyrene can partition is directly related to the increase of aggregates formed by pDal.

The pDal CAC concentration can be denoted from the plot of the CAC pDal expressed as fluorescence intensity versus the relative concentration (Figure 3.10 A).

The surface charge of the pDal nanonifibres was estimated by measuring the Z-potential.

Z-potential of pDal nanofibres dispersed in deionized water was found to be positive at 52.4 ± 4.93 mV.

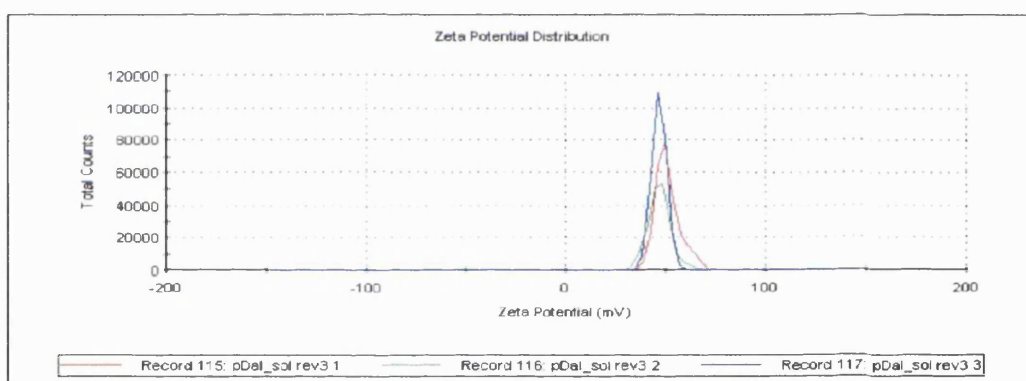


Figure 3.11: Z- potential plot of pDal nanofibres in deionized Millipore water measured with light scattering.

X-ray diffraction (XRD) data from aligned stalks has been used to extract orientational order parameters. Diffraction patterns were obtained for stalks prepared by drying filaments of the peptide along the waxed faces of two glass capillaries (Figure 3.12 A)

The specimen was partially aligned, but nonetheless the fibre diffraction arc was evident. The meridional diffraction arc at 4.8 \AA (Figure 3.12 B) is attributable to the

H-bonds distances in the β -sheets secondary structure that is formed between the amino acidic segments of the pDal molecule.

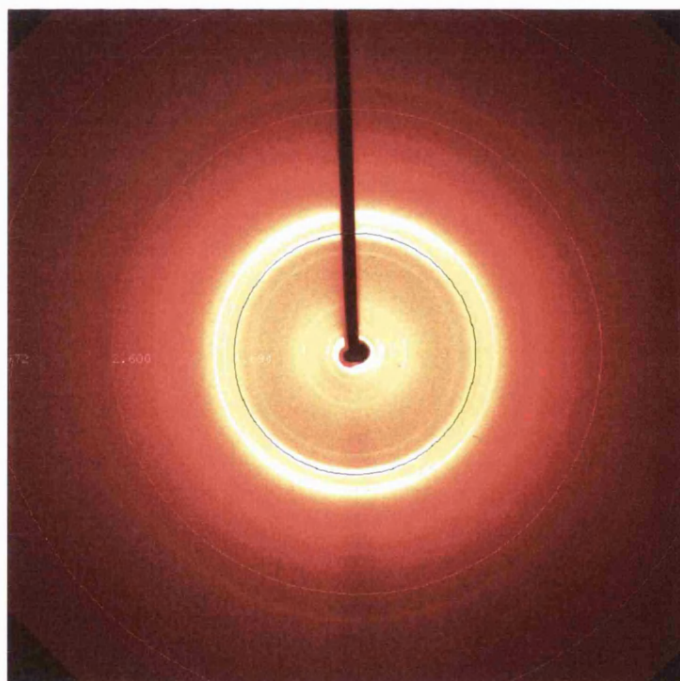
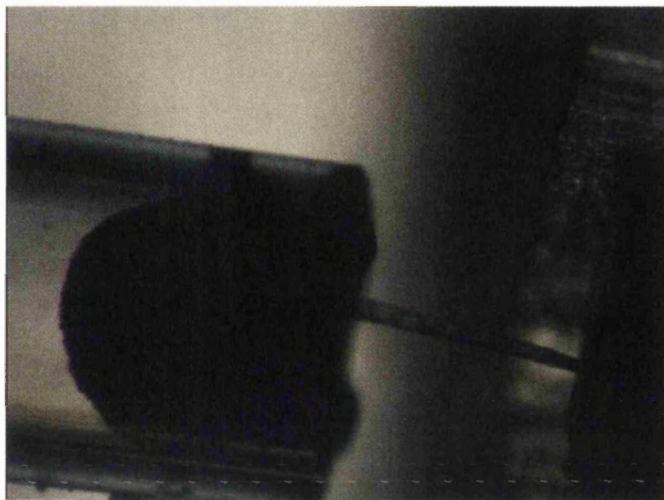


Figure 3.12: (A) drying stalk of pDal nanofibres 10mg/mL in water; (B) X-ray fibre diffraction pattern from a dried stalk of pDal nanofibres.

Circular and Linear Dichroism have been used for the investigation of the presence of β -sheet ordering in the pDal nanofibres.

CD spectra are not typical for β -sheet ordering, thus, in order to understand whether the CD signal was a true signal (not perturbed by the presence of LD artifacts) a series of static CD and LD experiments were performed, as summarized in Figure 3.13.

The LD signal is stronger than CD signal (Hicks et al., 2010) , however the CD signal arising with the cuvette oriented at 0deg is pretty much the same as the CD signal arising with the cuvette oriented at 90deg with respect to the light beam source, hence there shouldn't be an LD artifact contributing to the CD signal.

The LD signal arising with the cuvette oriented at 0deg is the almost mirror image of the LD signal arising with the cuvette oriented at 90deg with respect to the light beam source.

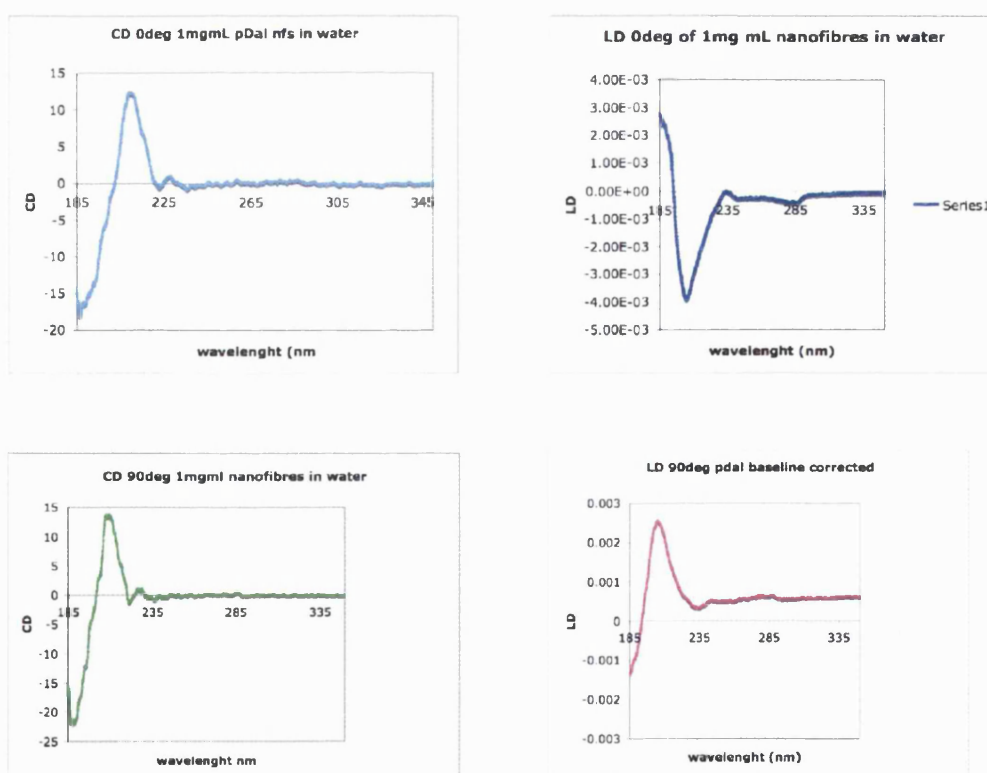


Figure 3.13: CD (left) and LD (right) spectra for pDal 1mg/mL in water

The LD signal is directly related to the orientation of the molecules, for this reason to confirm that the signal was not affected by the random distribution that nanofibres are free to acquire in water, these were oriented using a microvolume couette flow cell (Figure 3.14 A) built at the University of Warwick, where the experiments were performed under the supervision of Dr Matthew Hicks, in the Prof. Rodger's Lab.

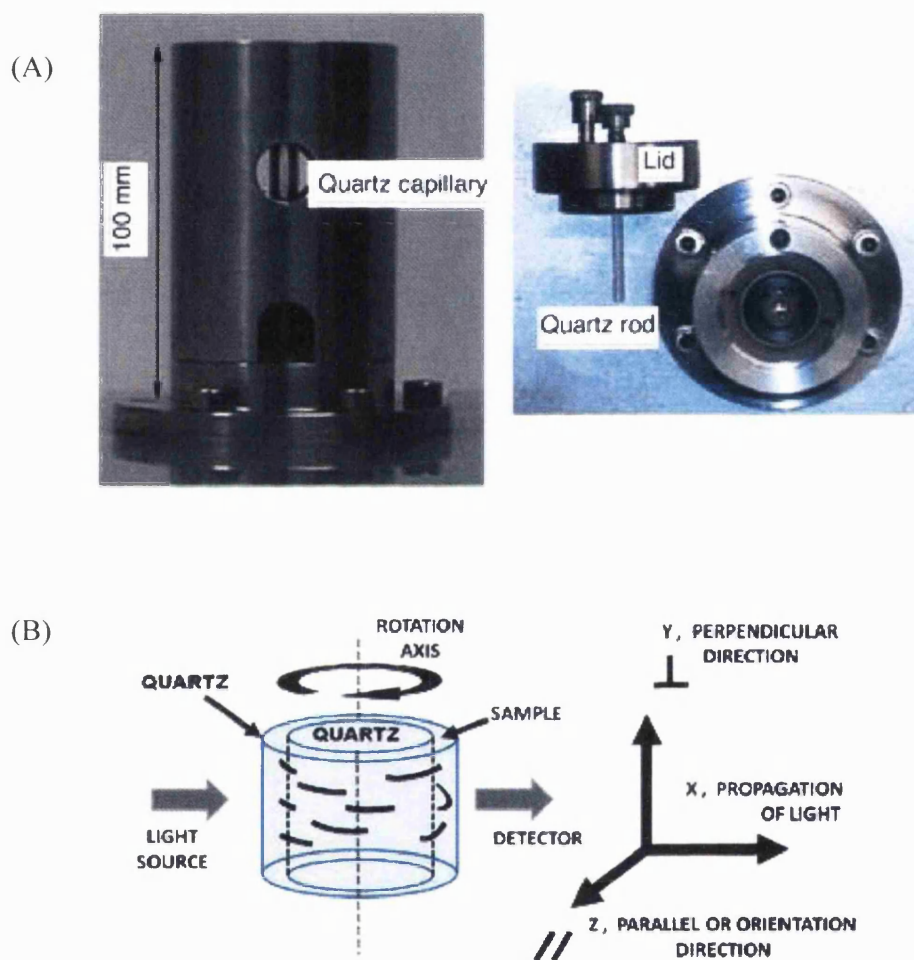


Figure 3.14: (A) Microvolume outer rotating Couette flow cell showing the outer quartz capillary (3 mm inner diameter) and inner quartz rod (2.5 mm outer diameter) making an annular gap of 250 μm ; (B) Schematic of a Couette flow cell showing flow orientation in a coaxial flow cell with radial incident light. {X, Y, Z} form a laboratory fixed axis system. Reproduction from (Hicks et al., 2010).

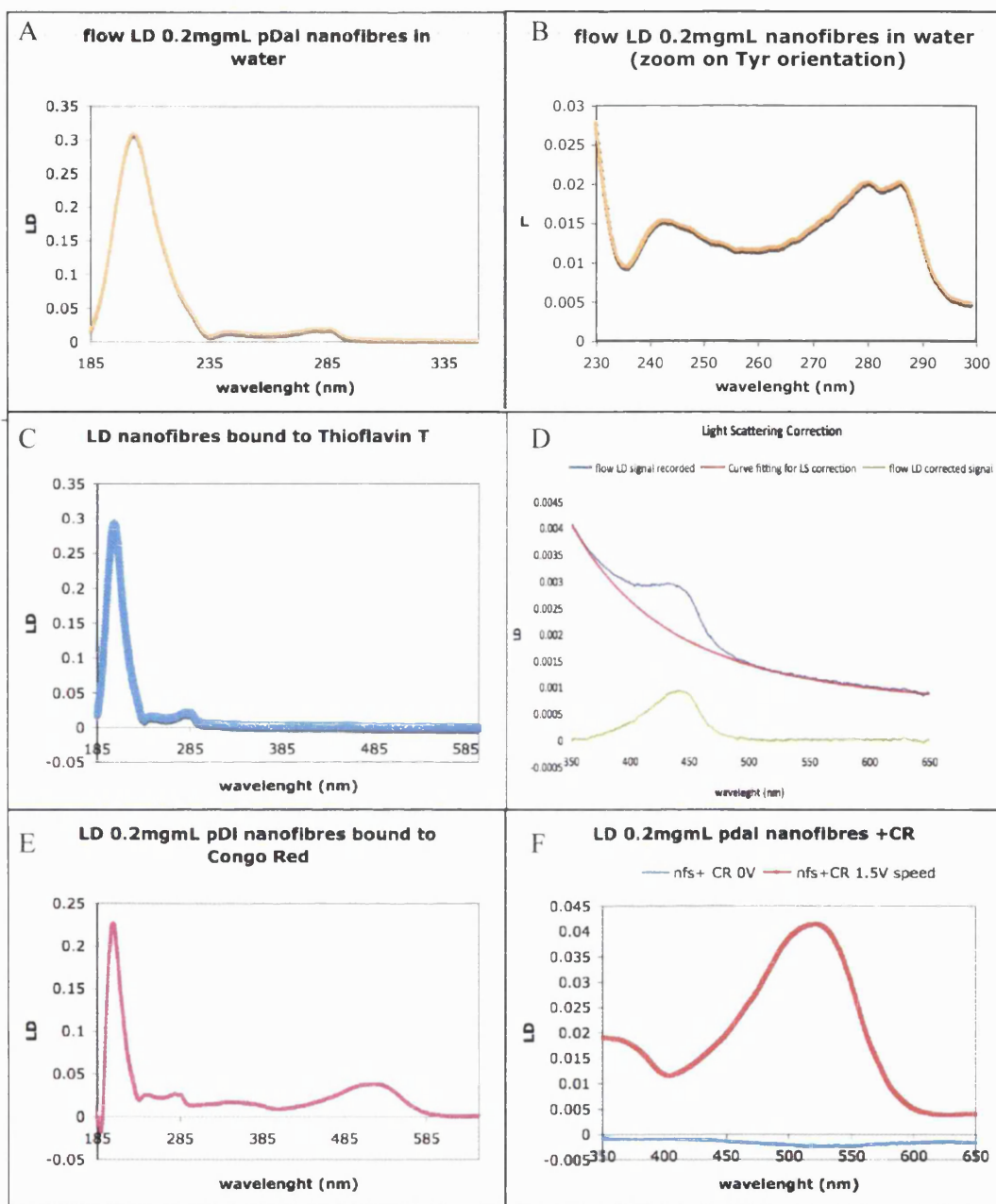


Figure 3.15: flow couette LD experiments. (A, B) LD spectrum of 0.2 mg/mL nanofibres, rotation speed 1.5V. (C, D) LD spectrum of 0.2mg/mL nanofibres in 22 μ m solution of Thioflavin T in EDTA buffer; rotation speed 1.5nm. (E, F) LD spectrum of 0.2mg/mL pDAl nanofibres in 10 μ M of Congo Red solution in 5mM PBS buffer and 150mM NaCl.

A solution 1mg/mL of pDal in water was diluted up to a concentration of 0.2mg/mL and LD spectra were recorded. The signal obtained from LD spectroscopy present a max $\sim 201\text{nm}$, that gives information with regard to the orientation of the $\pi \rightarrow \pi^*$ transitions in the peptide bond of β -sheets (Figure 3.15 A), the two tyrosine peaks at 279 and 286 are shifted higher in wavelength from the position that would be expected for aqueous media, this means that the Tyrosine residues are inside the fiber there is also a negative signal around 235nm, thus the transition moment along the O-alkyl group is pointing perpendicular to the fiber long axis (Figure 3.15 B) (Hamley et al., 2010). pDal nanofibres were also diluted up to 0.2mg/mL with a solution 22 μM of fluorescent Thioflavin T (Th-T) in EDTA buffer, as Th-T is a chemical probe used to reveal the presence of β -sheets in fibrillar amyloid structures, since it is known that Th-T is oriented parallel to the β -sheets (Krebs et al., 2005a) (Figure 3.15 C); scanning from 650-350nm at a long DIT we recorded a positive signal at 447nm,. The sample is affected by light scattering as can be deduced by the sloping baseline (Figure 3.15 D)

In our last LD experiment (Figure 3.15 E, F), pDal nanofibres were diluted to the same concentration with 10 μM Congo Red (CR) in PBS (5mM, 150mM of NaCL), as Congo Red is also a dyazo dye specific for β -sheets (Carnall et al., 2010), When nanofibres were stained with Congo Red a positive signal was recorded in the LD spectrum at 500nm under flow (1.5V), while the signal was absent when the flow was stopped (0V). Flow aligns the nanofibres orienting them with respect to the laser beam; orientation of the nanofibres is a prerequisite for LD analyses because LD is the difference in absorption of light linearly polarized parallel and perpendicular to an orientation axis.

Lastly, Congo Red and Thioflavin-T were used as molecular probes for the detection of β -strands secondary structure in pDal nanofibres (Figure 3.16 and 3.17).

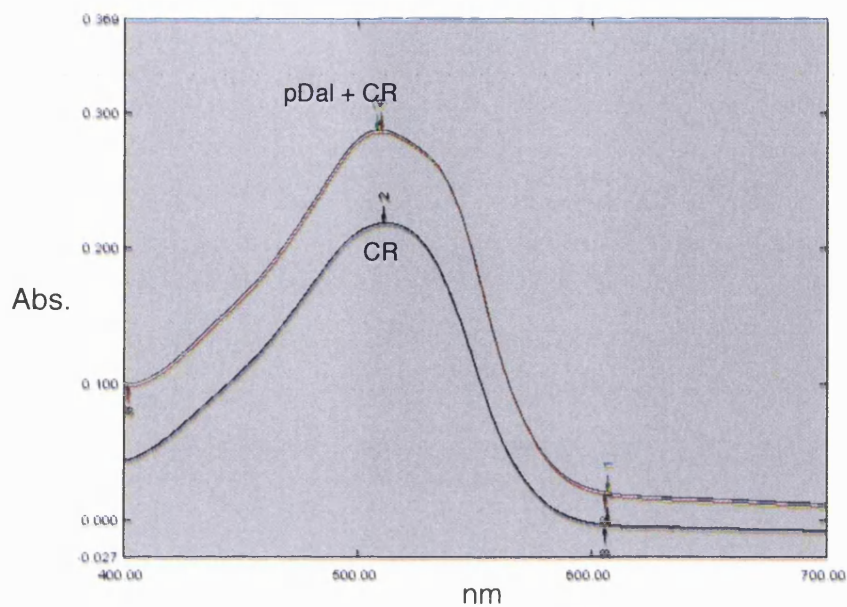


Figure 3.16: UV/Vis spectra of Congo Red (CR) alone (black line), and in the presence of pDal nanofibres

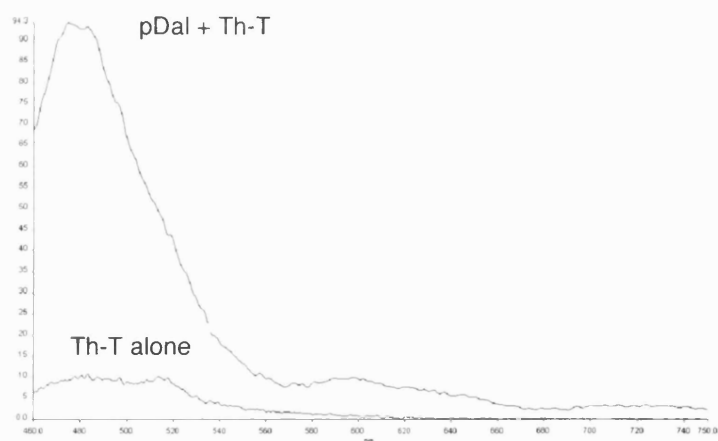


Figure 3.17: Fluorescence spectra of ThT, excited at 440nm, in the presence of pDal nanofibres.

The absorption spectrum of pDal nanofibres stained with Congo Red was recorded (Figure 3.16). The spectrum of Congo Red alone was compared to that of CR in the presence of fibers, and a red shift of the absorption band towards 540 nm and the increase in intensity were taken to indicate presence of β -sheets as it is normally seen for amyloid-like structures (Carnall et al., 2010).

Staining of the nanofibres with Thioflavin-T showed an enhanced emission at 490 nm (Figure 3.17) that indicates that pDal nanofibres bind also to Thioflavin-T, similarly to amyloid fibrils (Krebs et al., 2005b).

3.4 Discussion

The self-assembly of peptides and peptide amphiphiles can result into the formation of high axial ratio nanosized structures mimicking size and shape of various naturally occurring nanoparticulate objects (i.e. viral capsids, actin cytoskeleton, β -amyloid fibrils), as depicted in Figure 3.1.

The amphipathic derivative pDal of the hexapeptide dalargin is able to self-assemble into nanofibres.

Albeit self-assembling is a thermodynamically favorable event, the kinetic of the nanofibrils formation can take days or weeks to get to completion. It was recently reported that upon dissolution in ultrapure water of a hexapeptide amphiphile bearing aromatic side chain groups, short twisted bilayer ribbon segments were observed to be the dominant morphology after only thirty seconds, which then elongate in the time scale of minutes, and finally transform into helical ribbons over the course of weeks (Pashuck and Stupp, 2010b, Pashuck and Stupp, 2010a). Under the same condition a similar peptide lacking of the aromatic side chains was shown to form cylindrical nanoparticles and not undergoing any transition over a period of weeks (Pashuck and Stupp, 2010a). Thus, considering that the time for the self-assembly to occur may represent a *rate limiting step* for the preparation of nanofibres formulations, it has been considered to provide the necessary energy to the system using either sonication and/or electromagnetic radiation heating.

Sonication of proteins is known to cause formation of fibrillar aggregates (Stathopoulos et al., 2004). Probe sonication produces strong cavitation, a process generating growth, collapse and oscillation of gas bubbles into an otherwise inert liquid, creating high local temperatures, high sheer forces and free radicals from sonolysis of water (Brennan, 1995). Probe sonication of a solution of 1 mgmL⁻¹ of pDal in double deionized water resulted in the formation of elongated micellar aggregates of diameter of 8-20 nm and length varying from 100-1000 nm (Figure 3.6 A,B,C). Short microwave bursts induce the formation of longer fibrillar structures, with lengths of the order of microns, but again diameters ranging from 5-20nm (Figure 3.6 D).

High local temperature generated by sonication or by microwave burst contribute to the single peptide unfolding and enhance the aggregation of the single monomer units into nanofibres by promoting the hydrophobic interaction of the sixteen carbon chains and the formation of H-bonds in β -sheets structure among the peptide sequences, as it was observed for α -helical proteins such as BSA (bovine Serum Albumin) that undergo conversion to increased β -structure upon sonication (Stathopoulos et al., 2004). The presence of H-bonds and secondary β -sheet organization in the pDal nanofibres has been confirmed by the XRD, LD and dyeing experiments.

Single nanofibres form because of hydrophobic interactions of the alkyl chains as well as H-bonding formation among the amino acid sequences that give rise to the formation of β -sheet structures, as reported also by several authors (Velichko et al., 2008b, Guler et al., 2005, Hamley, 2011).

Several attempts to control the shape, diameter and length of the nanofibres were carried out using different types of surfactants. pDal nanofibres form in the presence of surfactants such as PF68 and Tween 80. The length of the nanofibres could not be controlled employing these surfactants, however qualitatively from the TEM it was possible to deduce that the nanofibres in the presence of these surfactants were generally in the range of microns rather than in the nanometer scale. Interestingly, it can be noted that the morphology differs considerably between the nanofibres in presence of PF68 and the nanofibres formed in the presence of Tween 80: while in the first case we can observe a regular twist on the length of the fibres (Figure 3.7 A,B), in the latter case the fibrils are of straight cylindrical shape (Figure 3.7 D). Only the presence of PVP was able to disrupt the formation and elongation of high-axial-ratio micellar aggregates (Figure 3.7 C). One possibility is that the interaction between PVP and pDal is stronger compared to PF68 and Tween 80 due the electrostatic interactions that can take place between the negatively charged oxygen on the PVP molecule and the positively charged Nitrogen on the pDal molecule on the basis of the resonance of the PVP molecule (Figure 3.18)

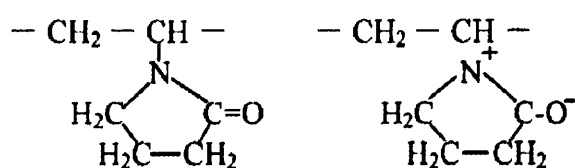


Figure 3.18 PVP molecule resonance.

The formation of nanofibres was also investigated in the presence of the polymer GCPQA, which was later chosen as the complement in the preparation of nanofibres formulations. The use of GCPQA allowed a control over the length of the nanofibres, which remain in a nanometers scale range conversely to the above-mentioned surfactants. It has to be pointed out as well that the length of nanofibres formed in the presence of GCPQA ranged from 100nm to 1000nm (Figure 3.8), as those prepared in absence of any additive (e.g. pDal in water alone, Figure 3.6).

The use of PBS instead of water mimicks the physiological conditions; also in this latter case pDal nanofibres were formed.

An important observation from these morphology determination studies has been that from the same monomeric unit (pDal) different nanofibre morphologies were formed, from twisted to cylindrical aggregates; although studies in literature have related that the different shape is due to changes in environmental conditions such as UV, pH variations (Palmer and Stupp, 2008). This structural polymorphism is known to exist already for amyloid like fibrils (Andersen et al., 2010). The mechanisms by which these early aggregates grow, and their structural relationship to mature amyloid fibrils, are issues under intense scrutiny. Amyloid fibrils formed from the same polypeptide can occur in a range of structurally different morphologies. The heterogeneity of amyloid fibrils reflects different types of polymorphism: (i) variations in the protofilament number, (ii) variations in the protofilament arrangement and (iii) different polypeptide conformations. This property differs significantly from native, monomeric protein folding reactions that produce, for one protein sequence, only one ordered conformation (Fandrich et al., 2009).

Insights on the Critical Aggregation Concentration (CAC) of the pDal molecules were obtained by studying with fluorescence spectrometry the ability of pDal nanofibres to encapsulate pyrene into their hydrophobic core (Figure 3.9 and 3.10).

Pyrene is a hydrophobic molecule, poorly soluble in water, that exhibits low fluorescence intensity due to self quenching (Kalyanasundaram and Thomas, 1977). When pyrene partitions into the interior non polar regions of amphiphilic aggregates, a change in the I₃/I₁ ratio of its emission spectra is observed as shown in Figure 3.10. Self-assembly of micellar aggregates is thermodynamically driven by entropy gain of freed water molecules in the system: the amphiphilic molecules shield their

hydrophobic groups from the aqueous environment. At low concentrations of amphiphiles molecules tends to accumulate at the surface of the aqueous system, increasing the concentration of amphiphiles determines an increase of the energy of the system and once the surface is saturated by amphiphiles molecules, these will start to aggregate in order to remove the alkylic moiety from the aqueous surrounding into an hydrophobic core (Florence and Attwood, 1998).

Pyrene excimer formation in these conditions can be monitored via fluorescence: as pDal molecules self-assemble into nanofibres, pyrene is encapsulated into their hydrophobic core.

This highlights also the importance of the hydrophobic interactions in the formation of these nanoparticulate systems. It is known, indeed, that even peptidic fragments that are normally not subject to fibrillation can self-assemble into nanofibres when chemically modified with the attachment of an alkyl chain (Deng et al., 2009a).

Furthrermore, these results will be at the core of further investigations as pyrene can be seen as a model hydrophobic drug that could be encapsulated into nanofibres and then these used as cargoes for insoluble molecules.

pDal nanofibres present a positive Z-potential distribution in aqueous environment (Figure 3.11), accordingly with what is theoretically expected: the only charged amino acid of the peptide sequence is the Arginine on the C-terminus, which will present a positive charge on the guanidinium group on the side chain at neutral, acidic and most basic conditions, considering that the pK_a is 12.48.

The Z-potential distribution is measured using the Henry function, which converts electrophoretic mobility to Z-potential, as mentioned in the Introduction to the present chapter. In the Henry function, $f(\kappa a)$, ' κ ' gives a measure of the "thickness" of the electrical double layer, and ' a ' refers to the radius of the particle double layer for a spherical particle. Electrophoretic mobility determinations of zeta potential were made in water. If getting a mobility reading for nanofibres is certainly possible using the Nanosizer (Dynamic Light Scattering), by assuming that the object is a sphere the Henry function inserts an error to the calculation. However, this error will be consistent for each measured sample, thus a trend estimation is still possible.

Z-potential values for pDal nanofibres are above +30mV, thus we can rule out that this delivery system is quite stable. Slight variations in these values are attributable to

the different length of the nanofibres in the system measured, as this will contribute to the values calculation by the Henry equation.

It was earlier pointed out that the self-assembly of peptide amphiphiles is driven by hydrophobic interactions of the alkyl chains as well as H-bonding among the amino acid sequences that give rise to the formation of β -sheet structures.

The elucidation of the core structure involved in the formation of nanofibres is essential to understand the mechanism of formation of these structures and also to speculate on their behaviour in biological systems.

X-ray diffractions was used to determine the presence of H-bonds and β -sheet ordering in the nanofibre. In order to determine the presence of β -sheets structures using XRD it is of primary importance to align the fibres in the samples. Little details on sample preparation were given on reports regarding peptide nanofibres used for scaffolding and tissue regeneration and yet again it was necessary to refer to protocols established for amyloids to obtain meaningful data.

For the XRD analysis of the pDal nanofibres a high concentration sample was used, to provide many nanofibres for the alignment procedure and to produce a large enough sample for diffraction. An indication of how well the sample is aligned can be obtained by examining it under cross-polarized light to test the presence of birefringence, which indicates that the fibres are aligned to some degree.

In pDal nanofibres the diffraction arc at a resolution of 4.8 \AA (Figure 3.12 B) corresponds to the spacing between the β -strands along the fiber axis, as it occurs in amyloid fibrils.

Further evidences for the β -strands arrangement of the peptide fragments in the nanofibres were acquired using two molecular probes that specifically binds to amyloid fibrils, Thioflavin-T (LeVine, 1993) and Congo Red (Divry and Florkin, 1927), as they interact with the β -sheets in the supramolecular organization.

Spectroscopic binding assay of nanofibres to the dyazo dye Congo Red (Figure 3.16) showed the typical increase in Absorbance intensity characteristic of interaction of the dye with the β -sheets structures (Carnall et al., 2010).

Congo Red intercalates in β -sheets as shown in figure 3.19

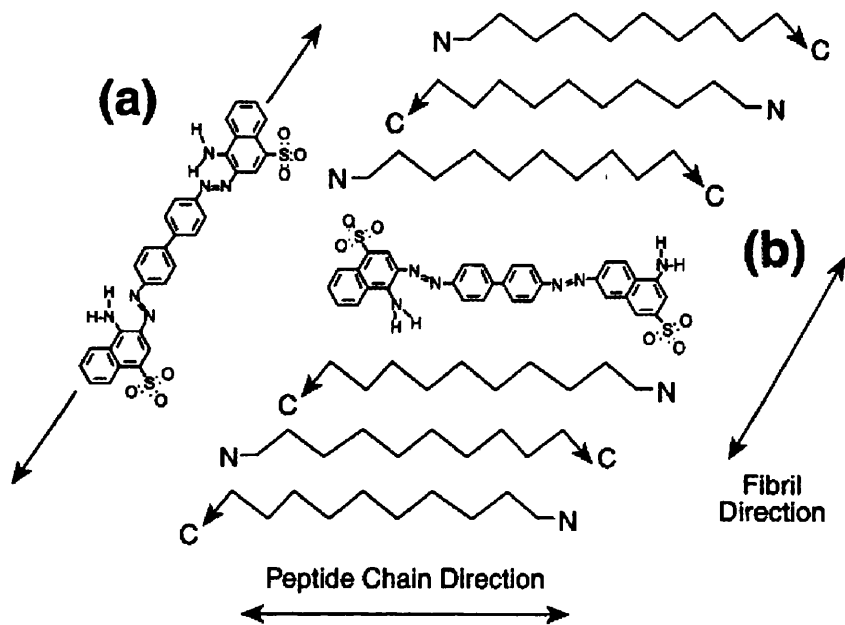


Figure 3.19: Model of alternative CR binding orientation. alignment of CR perpendicular (A) to the peptide chain direction. alignment of CR parallel to the peptide chains. Reproduction from (Carter and Chou, 1998)

The prevailing point of view is that unimolecular Congo red molecules are located parallel to the peptide chains (figure 3.19) (Carter and Chou, 1998).

The dye thioflavin-T is also used for the detection of amyloid fibrils. It is thought that thioflavin-T binds interleaves along the β -sheets as schematically depicted in Figure 3.20 B.

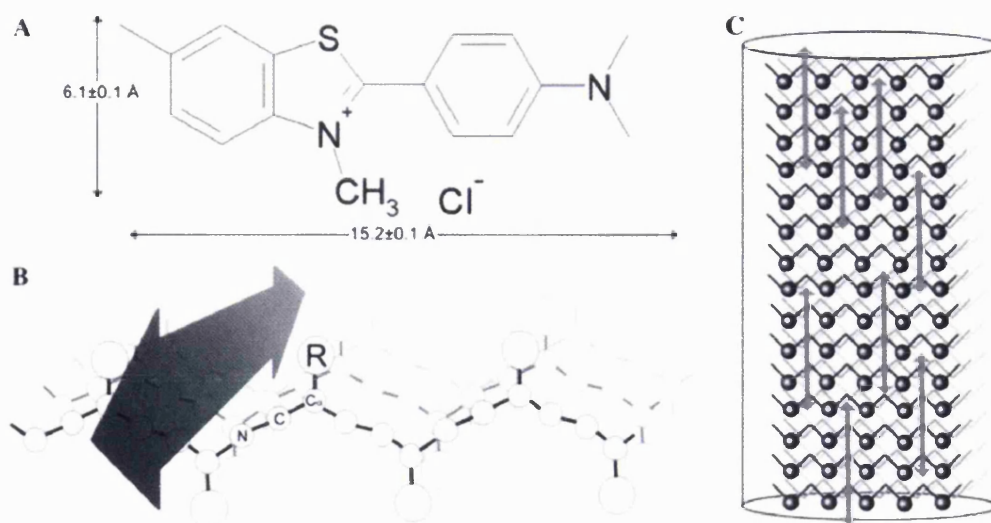


Figure 3.20: (A) thioflavin Structure; (B) binding site for Thioflavin-T along the β -sheets; (C) Individual β -strands are shown by zig-zag lines in black, dark and light grey. Dye molecules are represented by double headed arrows. Reproduction from (Krebs et al., 2005b)

The fluorescence spectra of pDal nanofibres stained with Thioflavin-T showed an enhanced emission compared to the solution containing the dye alone, indicating that the nanofibres strongly bind to the dye (Figure 3.17)

Secondary structure arrangement of the peptidic sequences was also investigated using Dichroism Spectroscopy.

Circular dichroism (CD) has been extensively used for the determination of β -sheets in peptide amphiphile assembled nanofibres as well as proteins. The signal obtained from the CD spectrum (figure 3.13) for pDal is not is not typical for β -sheet, it presents a positive maximum at ~ 210 nm, however CD signal for β -sheet is defined for proteins containing L amino acids, while in pDal, we have the presence of a D-Alanine, that can give rise to a different spectrum.

The CD signal for pDal is deviating from signal attributable to β -sheets, a possibility for this deviation can be the presence of the D-Alanine.

A similar CD signal as the one observed for pDal was observed in the study of nematic and columnar ordering of a PEG- peptide conjugate in aqueous solution

(Hamley et al., 2008). The PEG-peptide conjugate self-assembled into nanofibres and the CD signal arising from these nanofibres do not exhibit characteristics of typical secondary structures (α -helix, β -sheet or random coil); the effect is explained by the authors as the result of a significant contribution arising from phenylalanine chromophores in the peptide sequence, however the presence of fully formed β -sheets was clearly demonstrated with SAXS studies.

In the case of pDal, to resolve this dichotomy between XRD data and CD data, another polarized light spectroscopy technique was employed, Linear Dichroism (LD).

The LD for standard fibre geometry is defined by the equation

$$LD = A_{iso} \frac{3}{2} S (3\cos^2\alpha - 1)$$

Where

- A_{iso} defines the isotropic absorbance
- S defines the degree of orientation
- α defines the angle between the orientation axis and the transition moment

When $\alpha = 90\text{deg}$, $\cos^2\alpha = 0$, thus

$$LD = A_{iso} \frac{3}{2} S (0 - 1) = - \frac{3}{2} S A_{iso} \text{ (LD signal is negative)}$$

When $\alpha = 0\text{deg}$, $\cos^2\alpha = 1$, thus

$$LD = A_{iso} \frac{3}{2} S (3 - 1) = \frac{6}{2} S A_{iso} \text{ (LD signal is positive)}$$

The LD spectrum for pDal present a max $\sim 201\text{nm}$ (Figure 3.15 A), that gives information with regard to the orientation of the $\pi \rightarrow \pi^*$ transitions in the β -sheets; the two tyrosine peaks at 279 nm and 286 nm are shifted higher in wavelength from the position that would be expected for aqueous media (Figure 3.15 B), this means that the tyrosine residues are inside the fibre; there is also a negative signal around 235

nm, thus the tyrosine transition moment along the phenol –OH is pointing perpendicular to the fiber long axis (Hamley et al., 2010).

LD measurements have also been performed on stained fibres with Thioflavin-T and with Congo Red.

In the sample stained with Thioflavin-T a positive signal can be observed at 447 nm, a value that matches closely the fluorescence emission measured with spectrophotometry (figure 3.15 C, D and 3.17). The LD signal is affected by light scattering as can be deduced by the sloping baseline (figure 3.13 D) hence the effect of the light scattering can be corrected by applying the formula

$$LD_{Observed} = LD_{Abs} + LD_{Scattering}$$

Where

$$LD_{Scattering} = \alpha\lambda^{-k}$$

Where α and k are determined from the scattering profile outside the absorbance band and $k = 4$ for this data set.

In the last LD experiment pDal nanofibres were stained with Congo Red a positive signal was recorded in the LD spectrum at 500 nm, a value close to the measured Absorbance. Hence, the presence of β -sheets in the pDal nanofibres was definitively confirmed by the LD experiment set.

In conclusion, pDal peptide was proven to have an amphiphilic nature responsible for the supramolecular association of the single molecules into high axial ratio nanostructures. Contributions of hydrophobic interactions and H-bonding to the supramolecular assembly have been established. The affinity of the molecules is so high, that assembly is favoured even in the presence of surfactants and polymers (GCPQA) that normally encapsulate lipophilic molecules in their hydrophobic core.

CHAPTER 4

Coarse-grained Simulation Study of pDal Nanofibres Self-Assembly

4.1 Introduction

Biological cellular phenomena take place in a time frame that ranges from nanoseconds to seconds. Processes like self-assembly, vesicle fusion, protein folding and signal transduction occur on a time scale that is too long to be studied by atomistic simulations, but still, molecular simulations can provide an important tool in supporting experimental data that are difficult to probe experimentally (Ash et al., 2004). The dynamics of self-assembly of pDal into nanofibres have been studied applying a Coarse-grained (CG) simulation approach, as the all atomistic simulation approach would be too limited to study a system containing tens of thousands of atoms in a microsecond timescale.

4.1.1 Coarse-grained Molecular Modeling

Coarse-grained (CG) molecular modeling allows computer simulations to access longer time scales in comparison to atomistic simulations while still providing realistic structural details (Monticelli et al., 2008).

For instance, CG molecular dynamic simulations have been developed and successfully applied to the study of large scale protein motions in HIV-1 protease, elucidating the opening of the flaps in the mechanism of action of the protein as well as clarifying the presence of allosteric inhibition in specific regions of the molecule (Tozzini and McCammon, 2005). Later, many models for the study of the protein structure and internal dynamics have been developed allowing an understanding of the protein-lipid interactions, lipid mediated protein-protein interactions and peptide-membrane interactions (Shi et al., 2006, Muller et al., 2006).

The MARTINI force field was used in the present work to parameterize and carry out the molecular modeling simulations.

The MARTINI force field has been developed by Marrink and co-workers for the study of lipids and surfactants, giving good semiquantitative results for lipid simulations and it has been extended to protein modelling (Monticelli et al., 2008), as it is fast, easy to use and flexible enough to be applied to a large range of biomolecular systems. In the MARTINI model several atoms are grouped together in a virtual bead that interacts using a virtual potential. Clustering more atoms in a single unit decreases the degree of freedom, this, along with the use of shorter range potential functions determines a gain in simulation timescale of 2~3 order of magnitude with respect to the atomistic simulation models (Monticelli et al., 2008).

Clustering of atoms is defined as *mapping* and for the MARTINI model is based on a four-to-one mapping, as summarized in figure 4.1, with the exception of the molecules presenting ring structures on the side chain, where a higher resolution is applied (up to two-to-one). The choice of particle type for each amino acid is established on the basis of simulation results and the experimental results for the water/oil partitioning coefficients of the side chain of each amino acid.

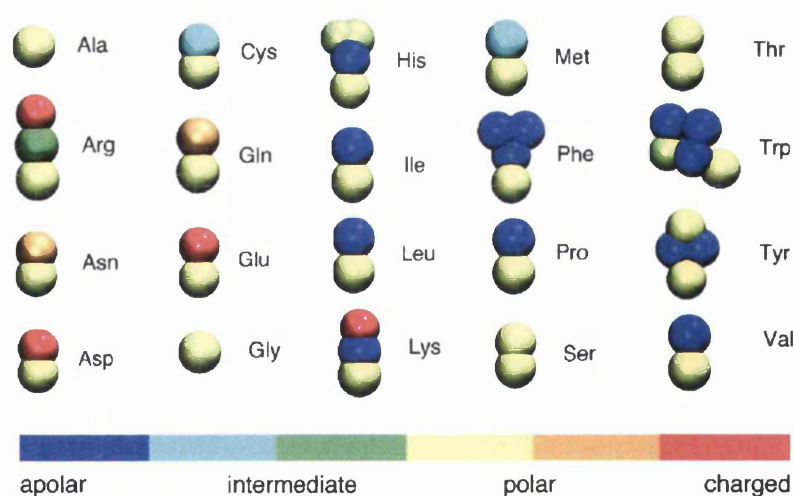


Figure 4.1: Coarse-grained representation of all amino-acids. Different colors indicating different particles type. Reproduction from Luca Monticelli et al. *J. Chem. Theory Comput.* **2008**, 4, 819-834

pDal is not a common amino acid sequence, as it contains the amino acid D-alanine stereoisomer and a palmitic chain attached to the -OH group on the Tyrosine side chain.

With the CG mapping it is easy to overcome the chirality issue posed by D-Ala, because the clustered bead will be always seen as a single one, whether its configuration is D or L, because this would not change its side chain water/oil partition coefficient.

The palmitoyl chain (representing 15 methylene groups) was modeled based on the CG model for hexadecane (Marrink et al., 2004), however the linker region between the peptide and the palmitoyl chain presents intermediate features between peptide and lipid not included in any model, thus it has been fully parameterized as explained in the methods section.

The main drawback of CG modelling is the reduction in accuracy compared to atomistic models due to all the inherent simplifications deriving from the *mapping*. Recently Marrink and co-workers have introduced an algorithm in the molecular dynamics program package GROMACS that allows one to re-introduce atomic details in a CG structure (Rzepiela et al., 2010). Using this algorithm a simulation annealing (SA) MD simulation, which is a simulation on a system first heated and then cooled, is carried out. This simulation is applied on an atomistic system that is coupled to its corresponding CG via restraints, during the SA simulation the system is allowed to cross the energy barriers and optimize under restraints. Finally, the coupling is gradually removed to ensure relaxation of the system (Schafer and Marrink, 2009).

In order to access the long time scales needed to observe the self-assembly of pDal into nanofibers it was necessary to model pDal using a coarse-grained (CG) forcefield. To optimize the CG forcefield atomistic molecular dynamics simulations were first carried out. A CG pDal model was built on the basis of the atomistic model by using GROMACS and applying the reconstruction algorithm developed by Marrink and co-workers.

4.2 Methods

4.2.1 Computational Details

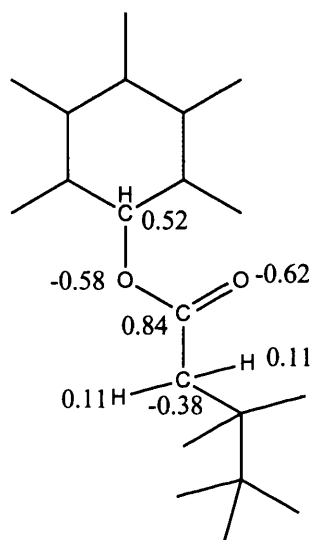
Molecular Dynamics simulations were carried out using the computing facilities at the University of Warwick Centre for Scientific Computing under the direct supervision of Dr. Rebecca Notman.

- **Atomistic simulations of pDal in water**

The pDal molecule was modeled using the CHARMM (Chemistry at HARvard Macromolecular Mechanics) all atom forcefield (Brooks et al., 1983, MacKerell et al., 1988). To define an initial molecular structure, a new amino acid residue (TYP), consisting of a palmitoyl tyrosine having the palmitic moiety attached to the phenoxy group was created.

The atomic partial charges for the region linking the tyrosine to the palmitic acid chain were derived from quantum mechanical calculations on the small molecule using Gaussian03 (Frisch, 2004) represented in the Scheme 1. Since partial charges on the rest of the palmitoyl chain are already included in the standard CHARMM force field. To achieve this model, geometry optimizations were performed first at the HF/STO-3G level and then at the HF/6-31G* level with the partial charges obtained by fitting the molecular electrostatic potential calculated from the HF/6-31G* charge distribution. HF/STO-3G refers to calculations based on the Hartree-Fock (HF) theory in combination with the Slater Type Orbitals (STOs), while HF/6-31G* refers to calculations based on the Hartree-Fock (HF) theory in combination with the basis functions used in molecular orbital calculations described through the acronym 6-31G. The final sets of partial charges are given in Scheme 1. All other atomic partial charges were taken from the standard CHARMM forcefield. We carried out a 40 ns simulation of a single pDal molecule in a cubic box of 11478 water molecules. The water molecule model used was TIP3P (Jorgensen et al., 1983). All bonds were constrained using the LINCS (Linear Constraint Solver) algorithm (Hess, 2008) and the time-step for integration was 2 fs. Full periodic boundary conditions were employed in all directions. The temperature of the system was maintained at 300K using the Nosé-Hoover thermostat, a deterministic method used in molecular

dynamics to keep the temperature around an average (Nose, 1984, Hoover, 1985) and the pressure was maintained at 1 bar using the Parrinello-Rahman scheme (Parrinello and Rahman, 1981, Nose and Klein, 1983). Long-range electrostatics were handled using the particle-mesh Ewald approach, that calculates direct-space interactions within a finite distance using a modification of Coulomb's Law, with a real-space cutoff of 1.0 nm. Lennard-Jones interactions were cutoff at 1.0 nm.



Scheme 1 – model building of pDal with highlighted the calculated partial charges

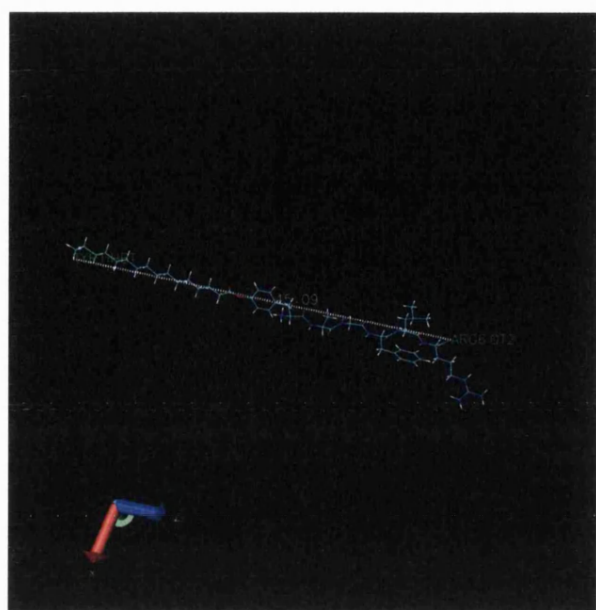
- **Development of a coarse-grained model of pDal.**

A modified version of the MARTINI (Marrink et al., 2007, Monticelli et al., 2008) forcefield was used to model pDal. The molecule was divided into 20 coarse-grained interaction sites as shown in Figure 4.2 B,C. We considered two different coarse-grained models, which differed in the region linking the peptide to the alkyl chain: (1) where the linker region was constituted by a bead containing only the carbonyl group and the parameters normally used for TYR were used for the modified residue, thus the Tyr will be formed of 2 apolar and 2 polar beads - Figure 4.2 B and (2) - where the bead included the ester oxygen -O-, and the carbonyl group, in this latter case the TYR will have four beads, of which 3 are apolar (as it normally applies to PHE), as shown in Figure 4.2 (C). As the MARTINI forcefield does not predict changes in secondary structure (this is an input parameter to the model), the peptide segment was

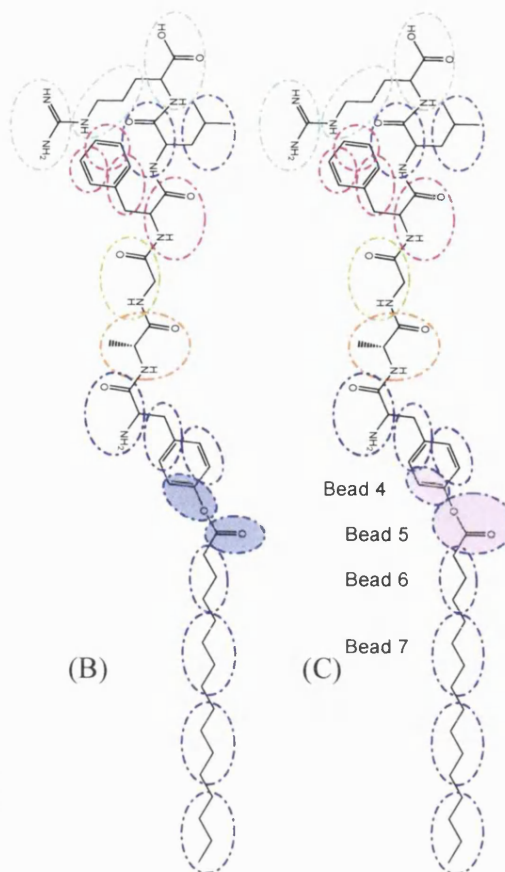
considered to adopt a β -sheet conformation. This is justified by the results from the LD and XRD reported in chapter 3 of this thesis, which provides strong evidence for a β -sheet arrangement of the peptide segments in the nanofibres. The CG model was optimized such that the dihedral and angle distributions within the molecule matched those from the atomistic simulation as close as possible. Thus, the trajectory obtained from the atomistic MD simulation was converted into its coarse-grained counterpart (fine-grained FG trajectory); bond angle and dihedral angle distributions for the FG and CG were calculated and compared. On the basis of the correlation between the FG and CG angle distributions, the second (Fig 4.2 C) of our two coarse-grained models performed best. We then refined the parameters to improve the match between the atomistic and coarse-grained models – specifically, we changed the equilibrium angle between beads A-B-C from 180 to 140 degrees. The angle and dihedral angle distributions obtained from the FG and CG simulations referring to the linker region of the palmitoyl tyrosine molecule in water are presented in Figure 4.2D and 4.2E. All other datasets are reported in Appendix.

- **Coarse-grained simulations of pDal**

Using the coarse-grained model of pDal we performed MD simulations of 512 pDal molecules in a range of different pDal:water ratios (1:10, 1:20, 1:25 and 1:50). A total of 512 chloride counterions were added to each system to neutralize the charge. Note that one CG water bead corresponds to 4 real water molecules and that the ratios given above refer to the number of CG water beads. In all cases the initial configuration of the system was generated by solvating a single CG pDal molecule and then replicating the solvated molecule eight times in each direction to generate a simulation cell containing 512 pDal molecules plus solvent. MD simulations were carried out for 500 ns - 1 μ s, using a time-step of 30 fs. The temperature of the system was maintained at 300K using the Nosé-Hoover thermostat and the pressure was maintained at 1 bar using the Parrinello-Rahman barostat with anisotropic pressure scaling (i.e. all three box dimensions were able to vary independently of each other). Electrostatic and Lennard-Jones interactions were shifted to zero between 0.9 and the cutoff distance 1.2 nm. Coordinates were saved every 5000 steps.

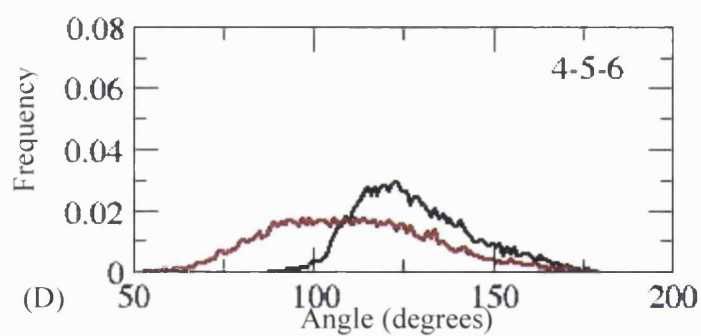


(A)

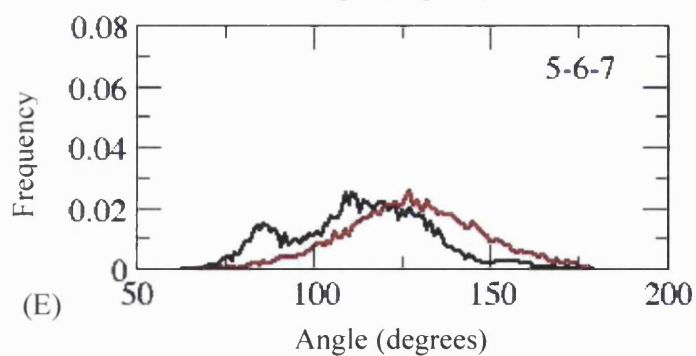


(B)

(C)



(D)



(E)

Figure 4.2: (A) starting structure of pDal in atomistic MD simulations; (B) configuration 1 in CG simulations; (C) configuration 2 in CG simulations; (D) angle distribution between beads 4, 5 and 6 and (E) angle distribution between beads 5, 6 and 7, for the second conformation of CG pDal (Figure C).

4.3 Results

The length of a single molecule of pDal is about 4.5 nm (Figure 4.2A) in its extended configuration and not considering any protrusion deriving from the Arginine side chain.

The atomistic simulation carried out on the single pDal molecule for 40 ns (Figure 4.3) shows that the molecule undergoes a continuous molecular rearrangement. This molecular mobility is clearly understandable if we consider the hydrophobicity of the palmitic chain that is unable to get shielded from the water molecules in any conformation assumed by the molecule. Molecular Dynamics simulations were performed in a solvated system with water molecules and adding ions Cl^- to obtain an electroneutral system.

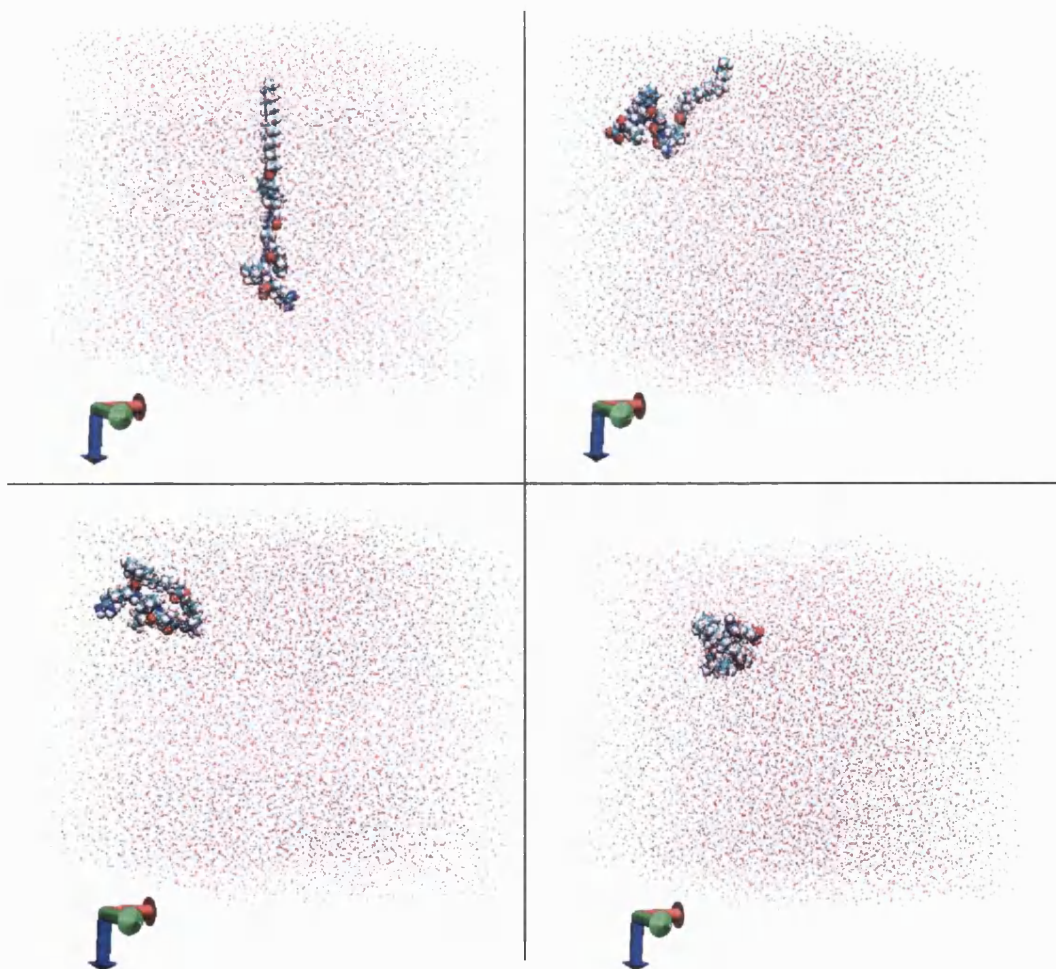


Figure 4.3: atomistic simulation of pDal over 40 ns. Red dots shows water molecule present in the simulation box.

Self Assembly of pDal molecules

Before starting the simulation an Energy Minimization Step has been performed on the system in order to avoid steric clashes and inappropriate geometry (Figure 4.4). Molecules in the simulation box tend to aggregate to minimize hydrophobic contact of the palmitoyl tails with the surrounding aqueous environment.

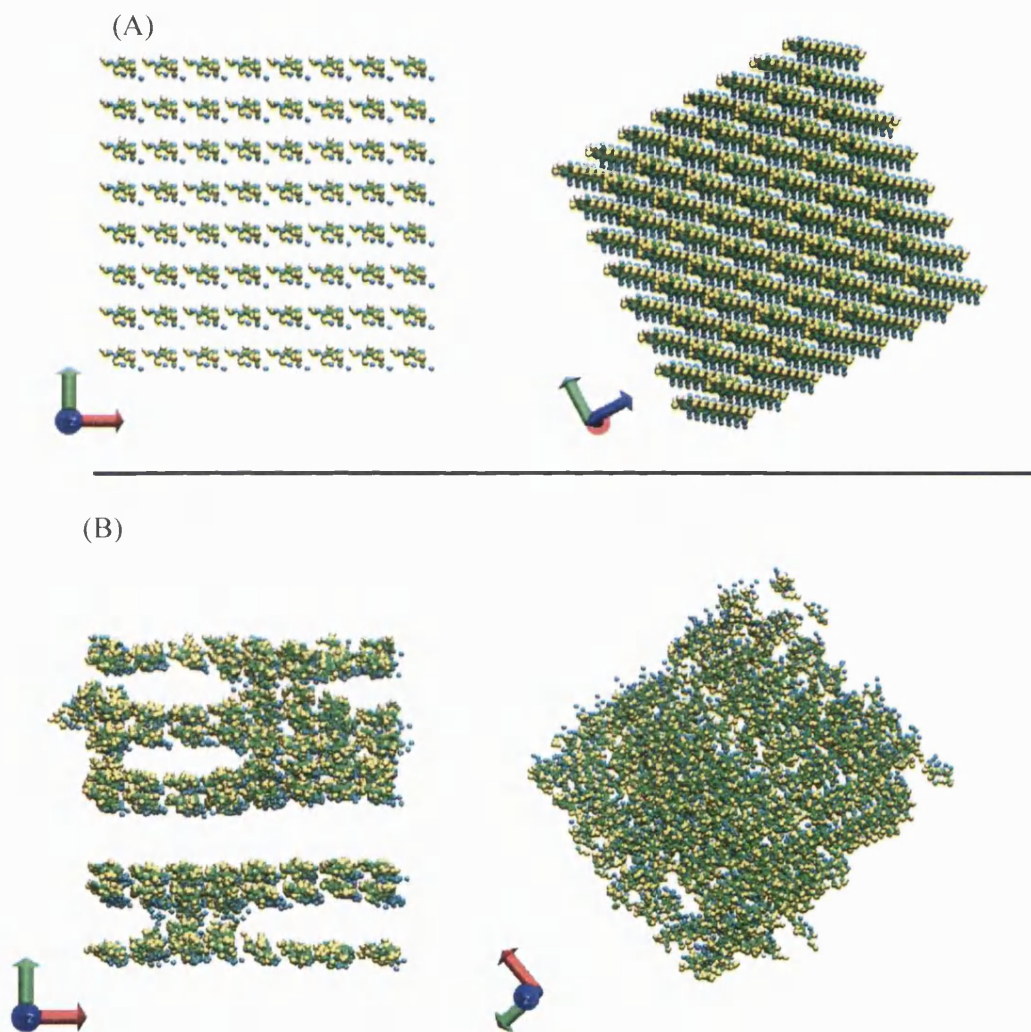
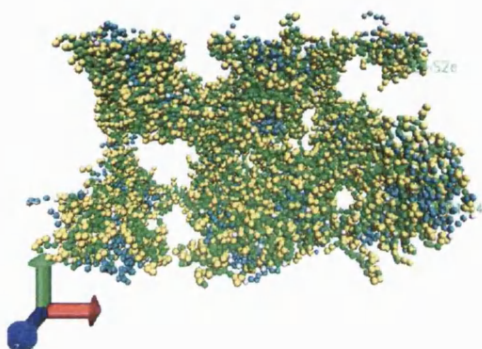


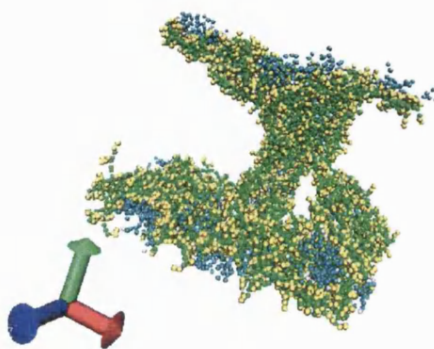
Figure 4.4: CG simulation of pDal self-assembly. (A) Starting Configuration 512 pDal molecules; pDal/ CG water ratio = 1: 25 before Energy Minimization Step. (B) Starting Configuration of the system after Energy Minimization Step (Time = 0 ns). Water and Ions are hidden in the graphical display.

Self-assembly progresses with the formation of clusters of molecules that tend to shield the hydrophobic tails from the surrounding water. After 21 ns a first micellar core forms and elongates over time acquiring the filamentous shape observed experimentally with Electron Microscopy (Figure 4.5).

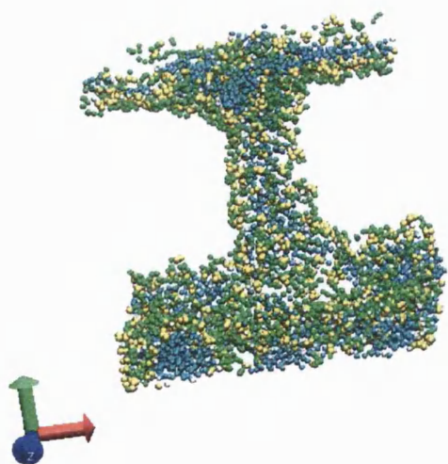
(A) Time = 7.860 ns



(B) Time = 21 ns



(C) Time = 60.3 ns



(D) Time = 924 ns

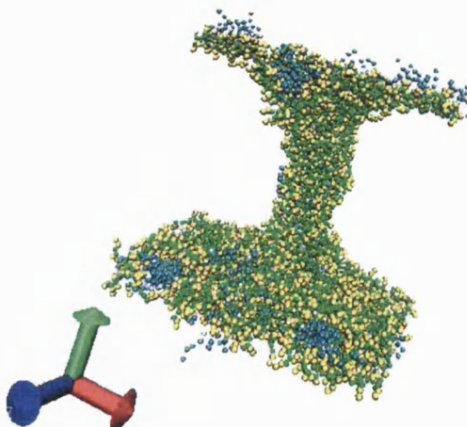


Figure 4.5: (A) pDal self-assembly CG simulation run for 1 μ s. Cyan beads = palmitoyl chain; green beads = peptide backbone; yellow beads = aromatic rings.

A well defined cylindrical nanostructure is observable in the centre of the simulation box containing a peptide to water ratio of 1:50 molecules, which corresponds to a real peptide to water ratio of 1:200 water molecules (Figure 4.6). Not all of the 512 molecules present in the simulation box will take part in the formation of the high axial ratio elongated structure .

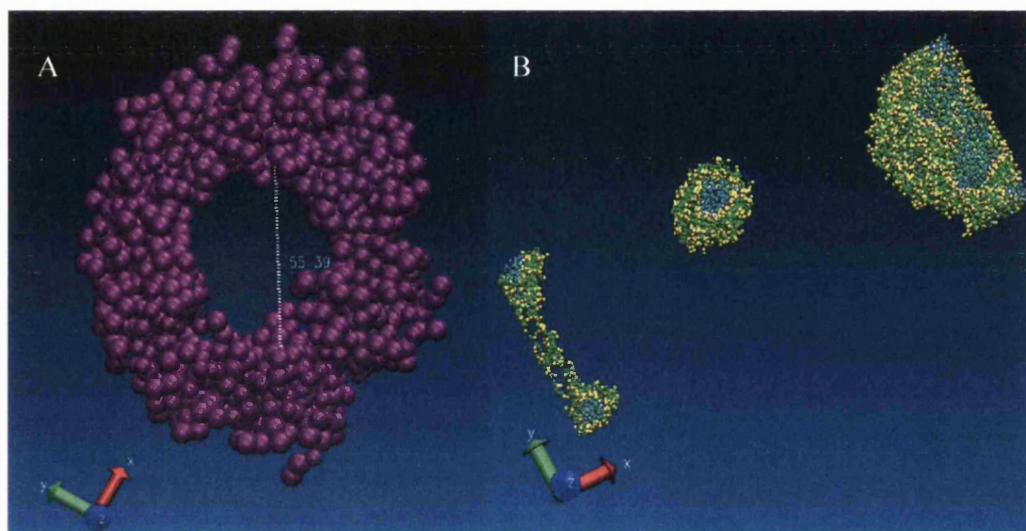


Figure 4.6: pDal nanofibre diameter (5.539 nm) measured on the assembled structure from the simulation peptide:water 1:50 ratio. (A) Palmitic tails are hidden on the graphical rendering, peptide backbone is rendered with magenta beads. (B) simulation containing pDal nanofibre formed in the middle after $1\mu\text{s}$

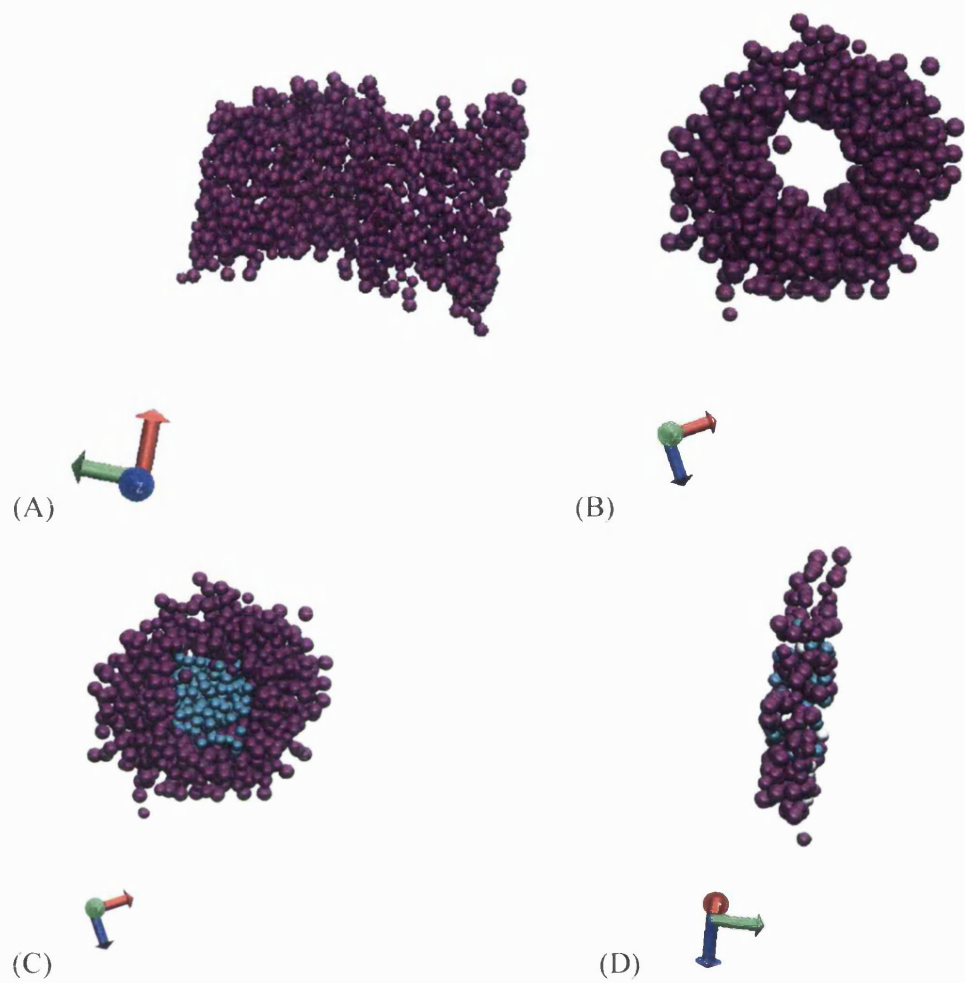


Figure 4.7: width of nanofibre after 1 μs of time. Hollow (A,B) and full (C,D) sections. (A) x,y plan; (B, C) z, x plan; (D) thin filled section cut on the z,y plan. Magenta beads = peptide back bone; cyan beads = palmitoyl chain.

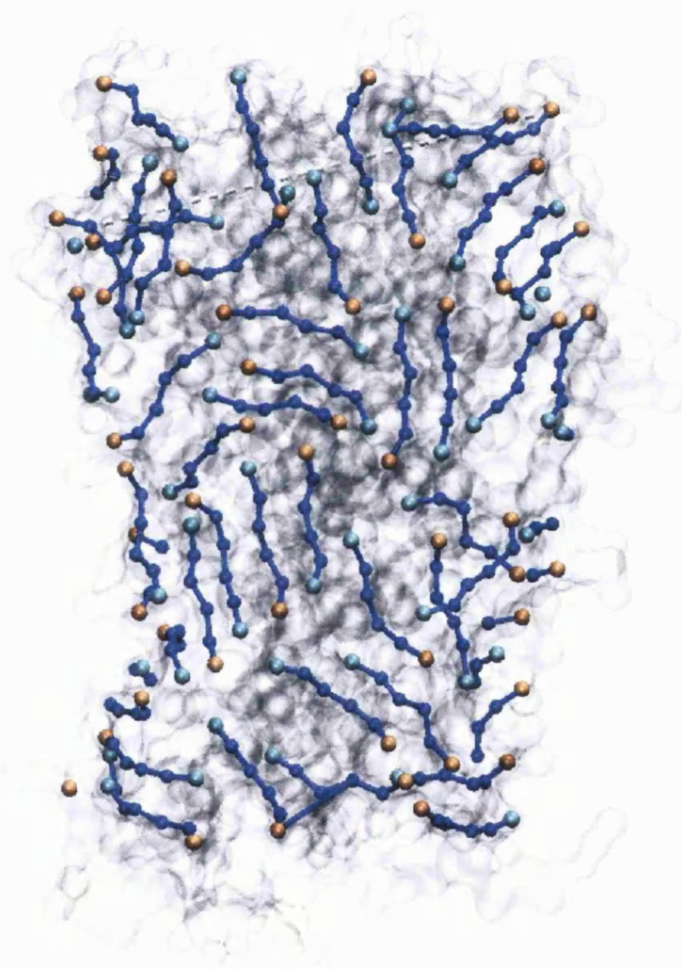


Figure 4.8: peptide-peptide packing. peptide - peptide alignment along the nanofibre surface (highlighted peptide backbone); peptide - peptide order along the alignment (cyan residue = palmitoyl Tyrosine; orange = Arginine). The snapshot seems to

suggest a preferential antiparallel alignment of pDal molecules on the surface, as peptides are aligned mostly with opposite sequence. Peptide: CG water 1:50.

A 90-degree angle is formed between the peptide backbone and the palmitoyl chain. The vector from bead 4 to bead 9 was calculated and then the angle that this vector made with the nanofibre axis was also calculated over the course of the simulation. This calculation was used to construct a histogram (Figure 4.9). It is possible to observe a clear peak at $\sim 90^\circ$ degrees, showing that the plane of the alkyl chain is perpendicular to the long axis of the fibre. This is supported by the experimental results observed with Linear Dichroism Spectroscopy, that confirms that the vector along the $-O-$ group of the aromatic ring in the palmitoyl tyrosine is pointing perpendicular to the long axis of the fibre.

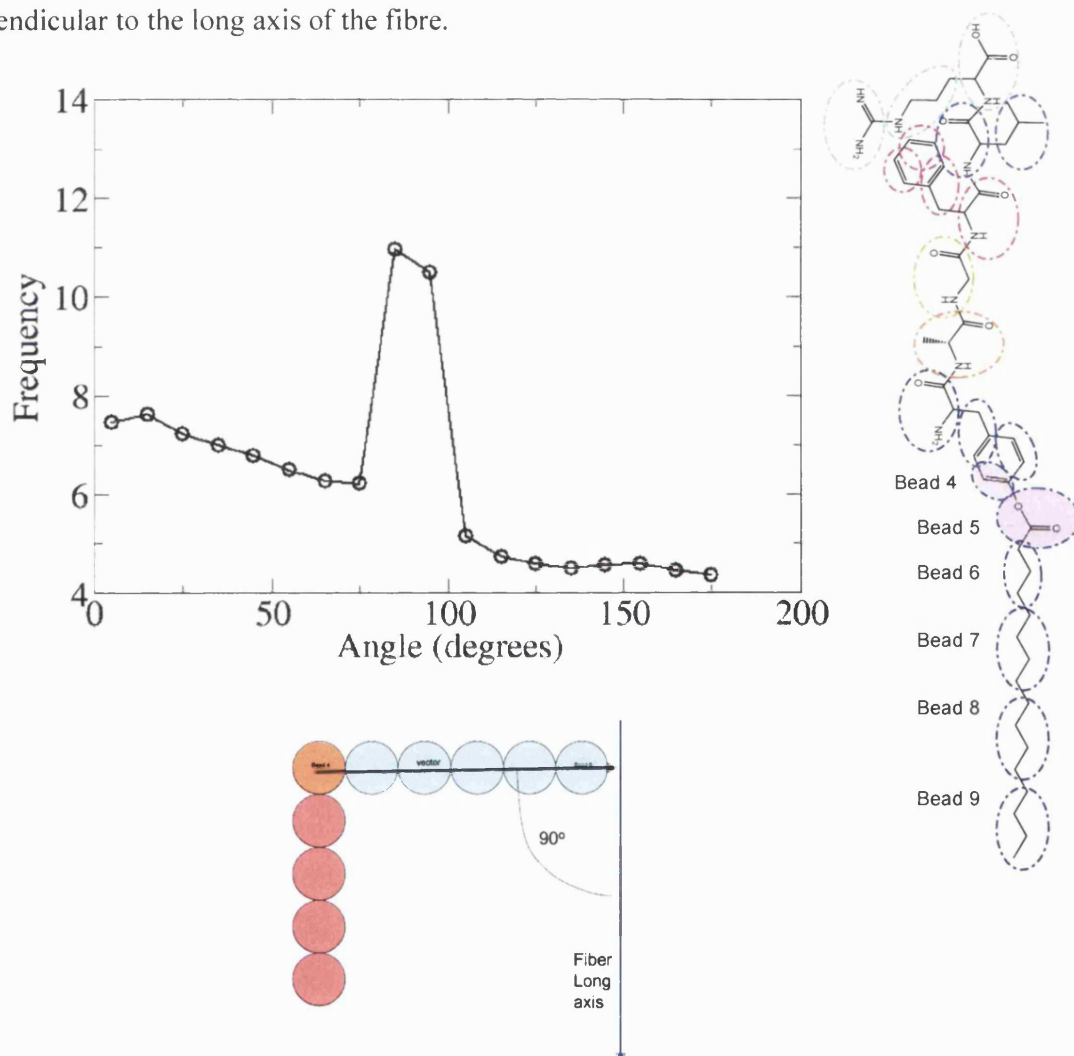


Figure 4.9: histogram plot of the angle formed between bead 4 and bead 9 of the palmitoyl tyrosine.

The Radial Distribution Functions (RDFs), (g) , have been calculated for each of the six amino acid residues in pDal sequence (Figures 4.10-4.15) to estimate the distances between the amino acids.

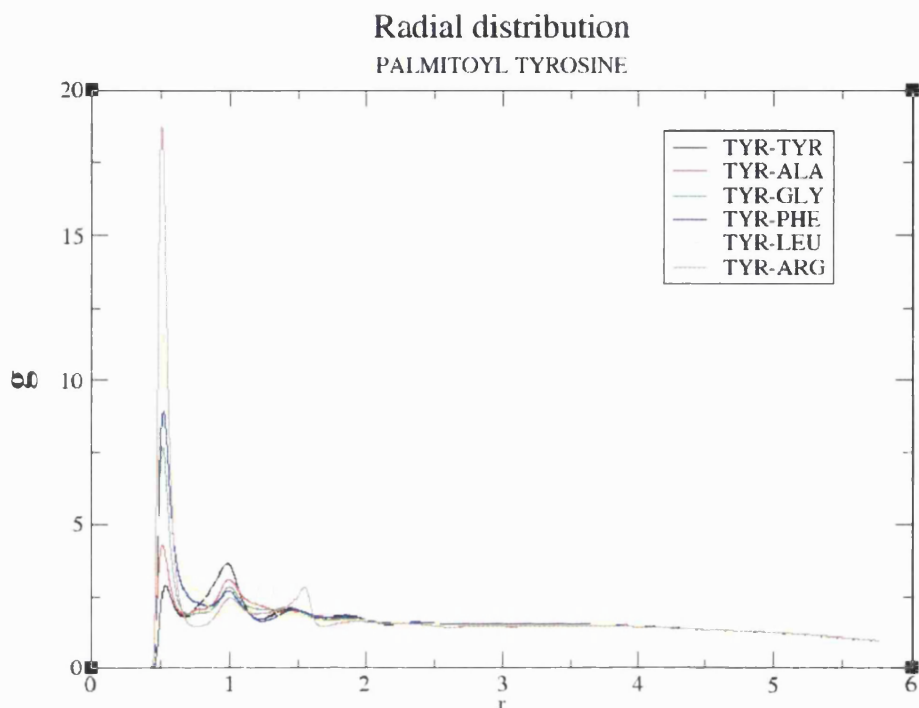


Figure 4.10: (A) Radial Distribution Function of palmtoyl Tyrosine ($r = \text{\AA}$).

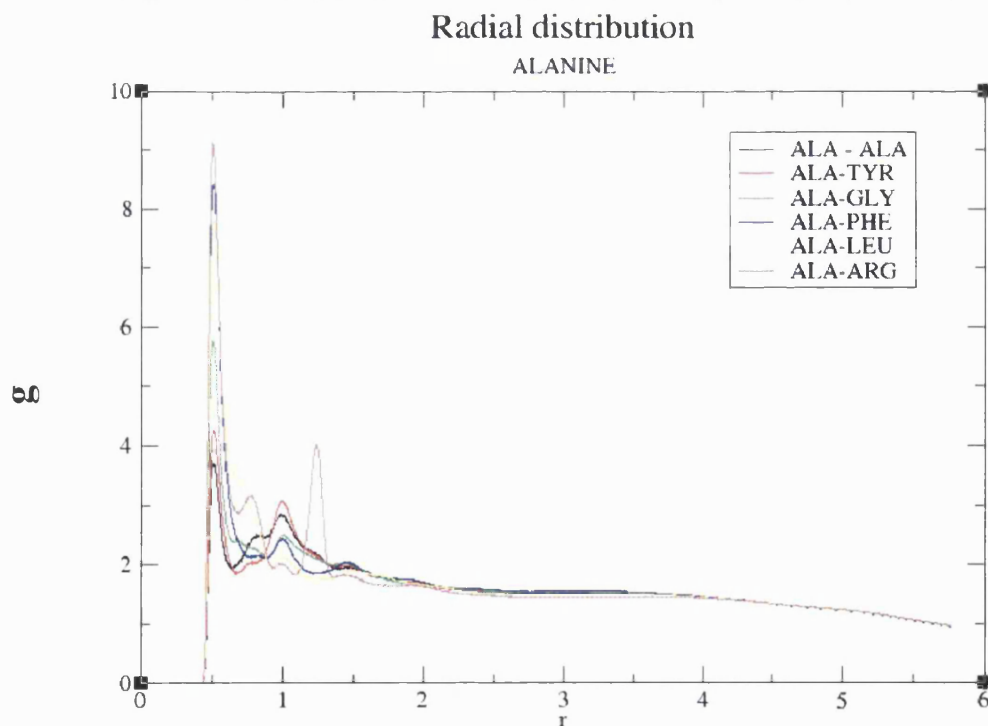


Figure 4.11: Radial Distribution Function of Alanine ($r = \text{\AA}$).

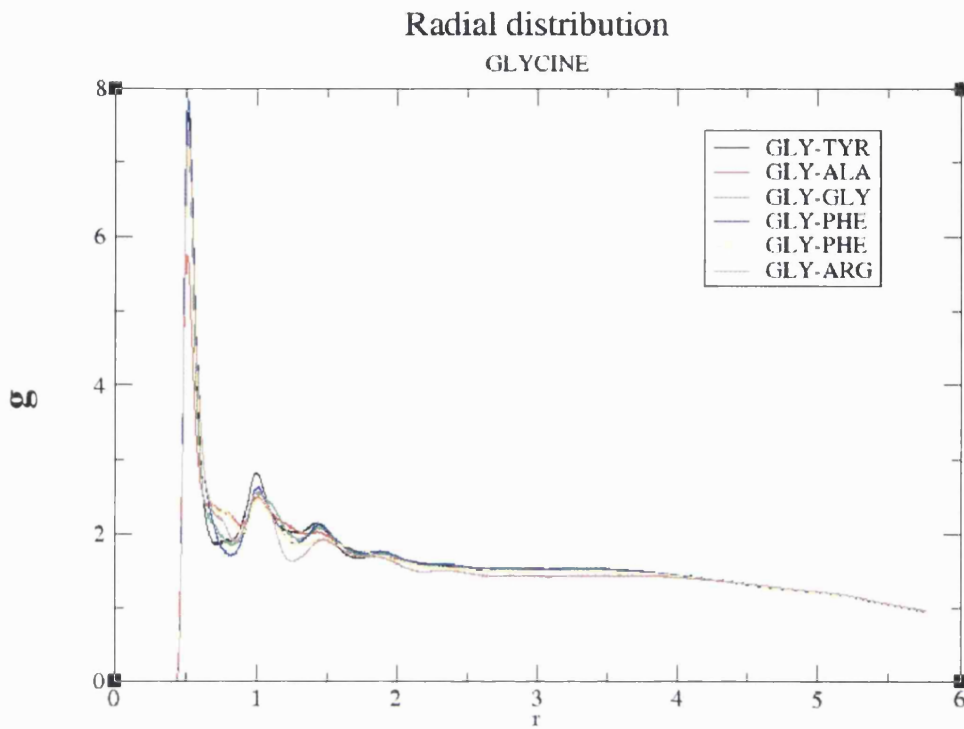


Figure 4.12: Radial Distribution Function of Glycine ($r = \text{\AA}$).

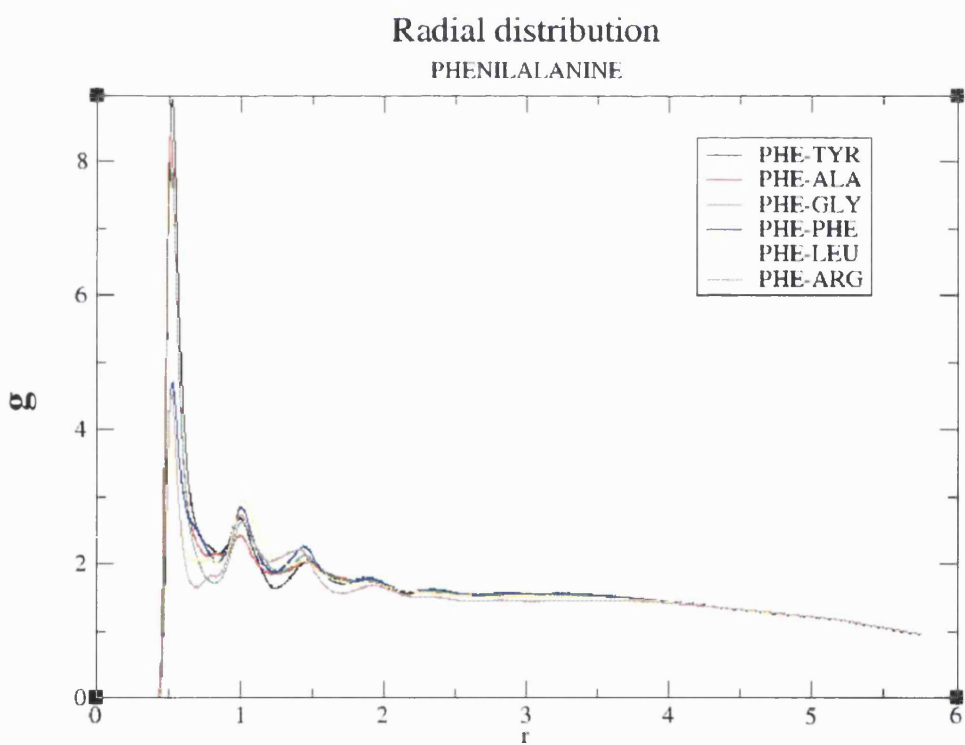


Figure 4.13: Radial Distribution Function of Phenilalanine ($r = \text{\AA}$).

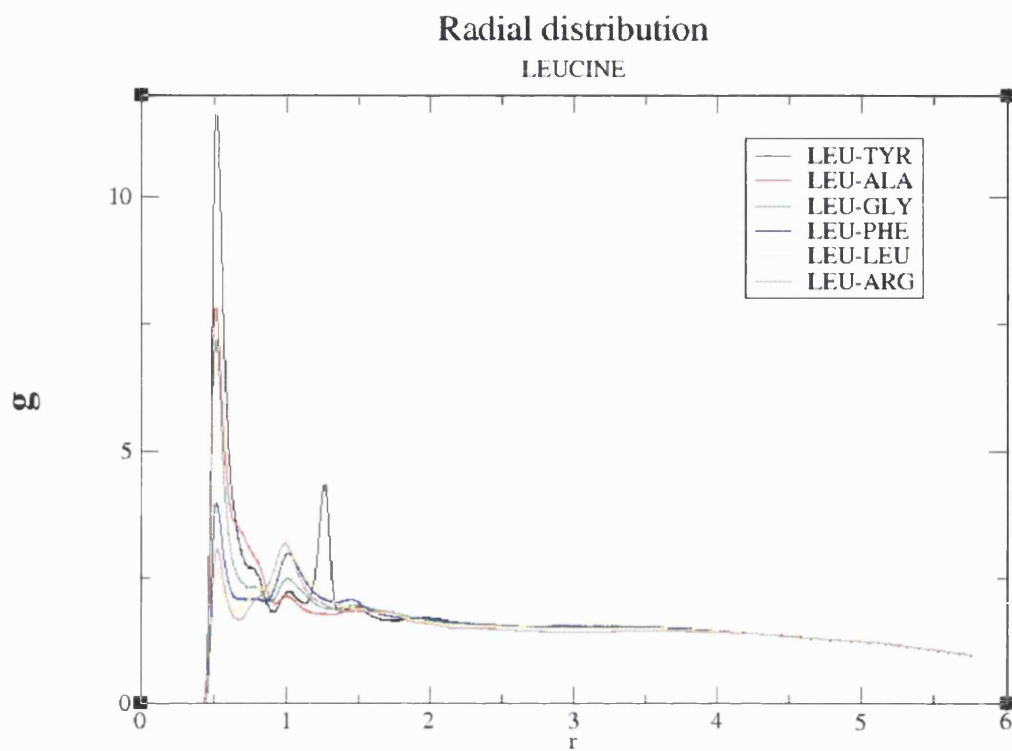


Figure 4.14: Radial Distribution Function of Leucine ($r = \text{Å}$).

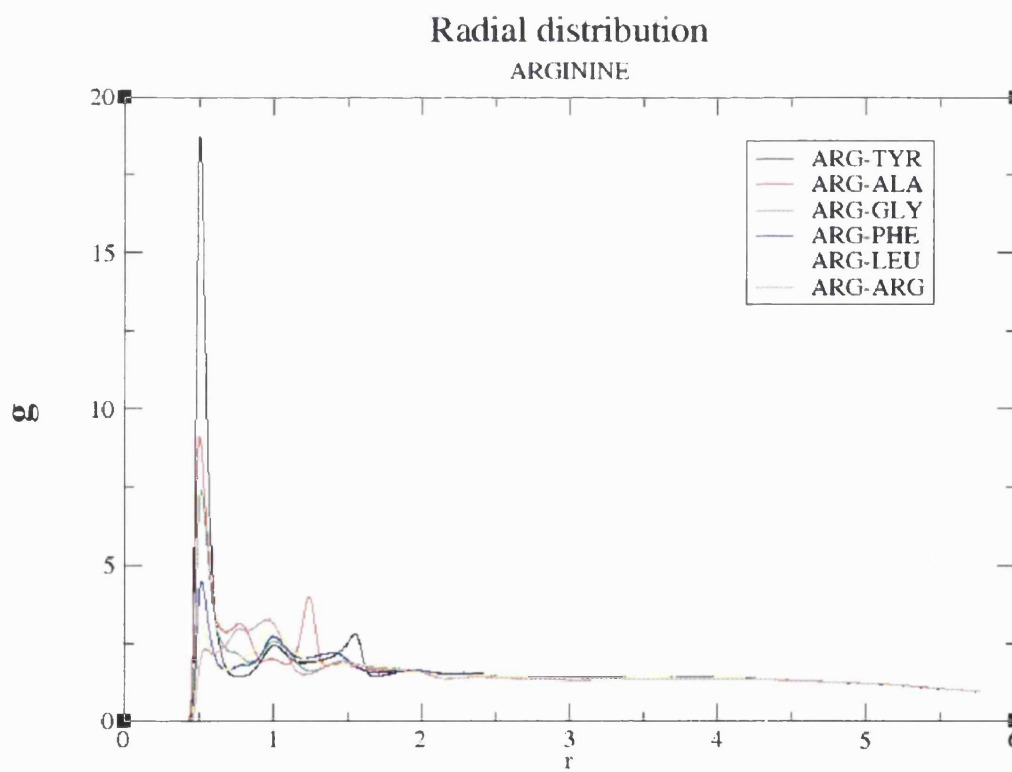


Figure 4.15: Radial Distribution Function of Arginine ($r = \text{Å}$).

4.4 Discussion

We performed MD simulations of pDal using the CHARMM force field with the starting structure of the backbone of each molecule is assumed to be with an extended conformation (Figure 4.2A). The single molecule of pDal does not have a final stable conformation as the entropy of the system is too high for the molecule which has a strong lipophilic nature due to the chemical derivatization obtained by attachment of the palmitic chain.

With particular reference to the pDal system an all-atomistic MD simulation approach was not suitable to get insights on the self-assembly process and nanofibres formation experimentally observed with the peptide amphiphile. This unapplicability is probably attributable to computer hardware and algorithms limitations that prevent from accessing longer simulation time scales. During this study some all-atomistic simulation were attempted for the evaluation of the self-assembly process. A series of simulations, each one containing 10 pDal molecules were performed with a different initial configuration (Figure 4.16). However results obtained were not sufficient to obtain information on the formation of high axial ratio nanostructures (which were not observed). Furthermore no insights on the peptide-peptide interaction, or on the hydrophobic palmitoyl chains interactions could be extrapolated. After 10ns of simulations pDal molecules were still randomly rearranging within the simulation box.

Self-assembly of peptide amphiphiles molecules is governed by hydrophobic interactions between alkyl tails and a network of hydrogen bonds between peptide blocks. Velicko *et al.* suggest that the formation of nanofibres of peptide amphiphiles obeys an open association model, which resembles living polymerization (Velichko *et al.*, 2008b).

Recently an all atomistic simulation relative to peptide nanofibres has been published (Lee *et al.*, 2011). In this report the initial structure of assembled nanofibre is constructed *a priori* (Figure 4.17) and arranged in a cylindrical nanofibre and then the relaxation of the assembled nanostructure is observed over a time of a 40 ns MD simulation.

The initial model present by Stupp and co-workers (Figure 4.17 A and B) seems to be far from reality and in contradiction with their own results (Pashuck and Stupp, 2010a), because if the packing of the molecules is radial from the fibre long axis the H-bond distance would not be 4.6-4.8 angstroms at all points, which is the distance in for H-bonds in β -sheets.

β -sheet alignment of the peptide sequences of pDal is strongly suggested also from the experiment results already discussed in chapter 3 (congo red absorbance and thioflavin-T fluorescence, XRD and LD experiments).

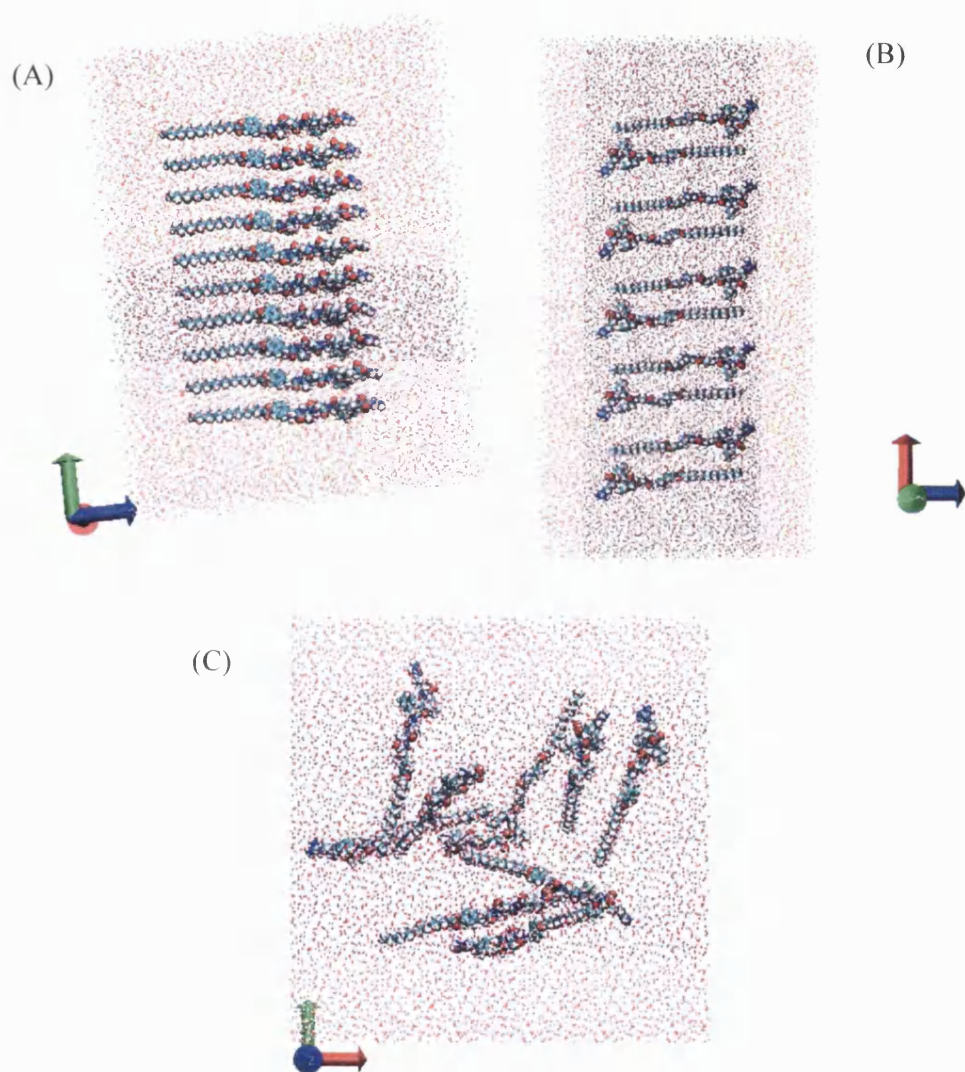


Figure 4.16: Starting configurations of all-atomistic pDal self-assembly MD simulation (A) stacked configuration; (B) rotated configuration; (C) random configuration. Red dots represent water molecules in the simulation box

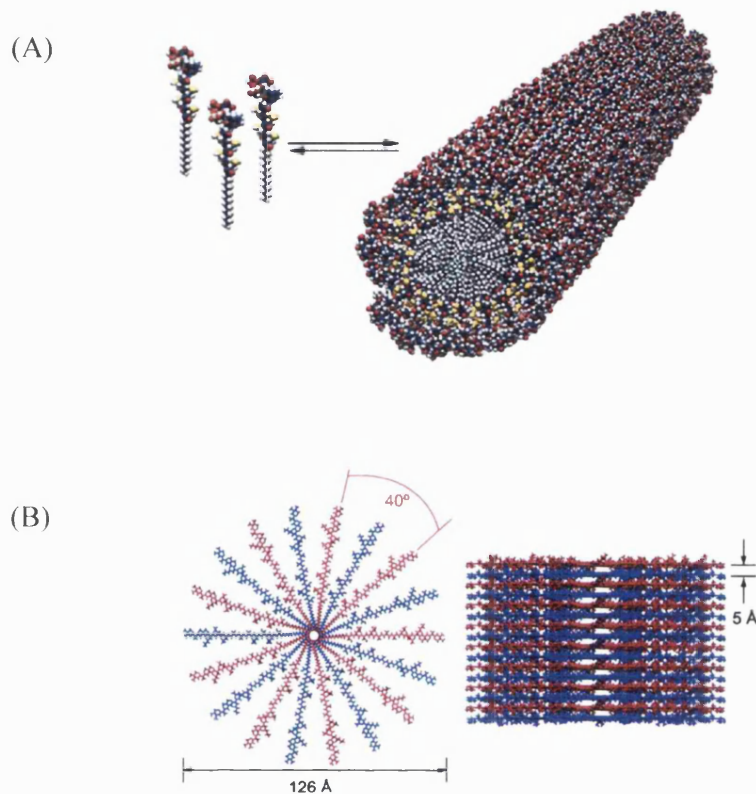


Figure 4.17: Proposed model of self-assembly of peptide amphiphiles into cylindrical nanofibres. (A) radial distribution model for peptide amphiphiles molecules; reproduction from (Hartgerink JD et al., 2003); (B) The starting structure of the PAs for MD simulations. Nine PAs are placed radially in the first layer (red) where their tails are pointing inward. The second layer also has 9 PAs (blue) and is rotated by 20° relative to the first layer. The angle between neighboring PAs is 40°, and the distance between layers is 5 Å. Reproduction from (Lee et al., 2011).

As discussed in the introductory section, to map an atomistic model onto a coarse-grained (CG) model, several atoms are grouped together into a relatively simple representation of them, the CG bead. The interaction energies between respective CG beads have to be obtained by the application of an optimization procedure that reproduces the structural distributions obtained from atomistic simulations.

On the basis of the quantum mechanical calculations pDal was parameterized for the CG simulation using the MARTINI forcefield. To establish the centers of mass with better correlation with the atomistic simulated molecule, we have studied two different configurations: i) one (Figure 4.2B) in which the linker region was constituted by a bead containing only the carbonyl group, in this case the same parameters normally used for TYR apply for TYP, thus the Tyrosine will be formed of 2 apolar and 2 polar beads ; ii) one (Figure 4.2C) in which the bead was including the ester oxygen -O-, and the carbonyl group, in this latter case the TYR will have four beads, of which 3 are apolar (as it normally applies to PHE).

The MARTINI parameters were optimized such that the angle distributions obtained from the linker-region within the coarse grained model matched those from all-atom simulations as closely as possible. Thus, the trajectory obtained from the MD simulation was converted into its coarse grained counterpart (fine-grained FG); angle distributions for the CG and FG system were calculated and compared such that the CG parameters were revised to match the FG parameters as close as possible.

On the basis of the correlation between the angles we have decided to choose the second configuration (Figure 4.2C) as the starting structure, furthermore we have changed one of the angle in the linker region from 180 to 140, because by changing this angle the matching between the CG and the FG was improved.

An initial configuration of 512 pDal was used to set up the CG simulations on the self-assembly of the nanofibres (Figure 4.4).

Anisotropic pressure coupling was preferred to isotropic pressure, so that each box vector, along the x, y and z axis, changes independently from each other allowing the self-assembled structure to elongate.

An initial Energy Minimization Step was carried out to allow relaxation of the system (Figure 4.4) and it was noticeable that once the simulation started the molecules tended to collapse all together to eliminate the voids between them.

At the earlier stages of the simulation it is possible to see a mass of molecules packing together that will tend to shield the hydrophobic tails from the aqueous environment. After 60 ns of simulation (Figure 4.5 C), we can see that the shapeless mass starts to organize in such a way that the majority of the molecule will be along the z and y planes at the periphery of the simulation box and a continuous structure starts to grow to connect them. Overtime, because of the anisotropic pressure scaling, the box increases in length, because all three box dimensions, x, y and z, are able to vary independently from each other, allowing the elongation of the pDal self-assembled structure for a total time of 1 μ s of simulation.

Taking a section of the *growing nanofibre* (Figure 3.7A) along the y and x plane we can observe that the palmitic tails are hidden in the core of structure (cyan beads in Figure 4.7C). We used VMD software to hide all the beads belonging to the palmitic chain and we can see that the elongating fibre is left with a hollow core that runs through the length of the fibre (Figure 4.7B). The diameter of the self-assembled structure along the fibrillar section is about 5.5 nm (Figure 4.6A).

The radial distribution function (RDF) applied represents the probability to find an amino acid in a shell dr at the distance r of another amino acid chosen as reference point. Because the structure under investigation is a coarse grained model, we have been considering only the beads on the backbone (BB_e) of the molecule.

Figure 4.10 shows the probability to find the palmitoyl Tyrosine in the vicinity of the others amino acids. From the plot we can see that the probability of finding a tyrosine in the proximity of another tyrosine is very low, while there is a higher probability of finding a Tyrosine in proximity of an Arginine. Also the probability of finding a Tyrosine in the vicinity of a Leucine is higher compared to the probability of finding a Tyrosine in the vicinity of an Alanine. This trend can be explained if we consider that the peptide – peptide interaction in the nanofibre structure is more likely to be antiparallel rather than parallel, as represented in the Figure 4.18. However, for clarity it has to be reported that this can be deduced from the Radial Distribution Function Analyses but is less evident looking at the snapshot of the whole nanofibre.

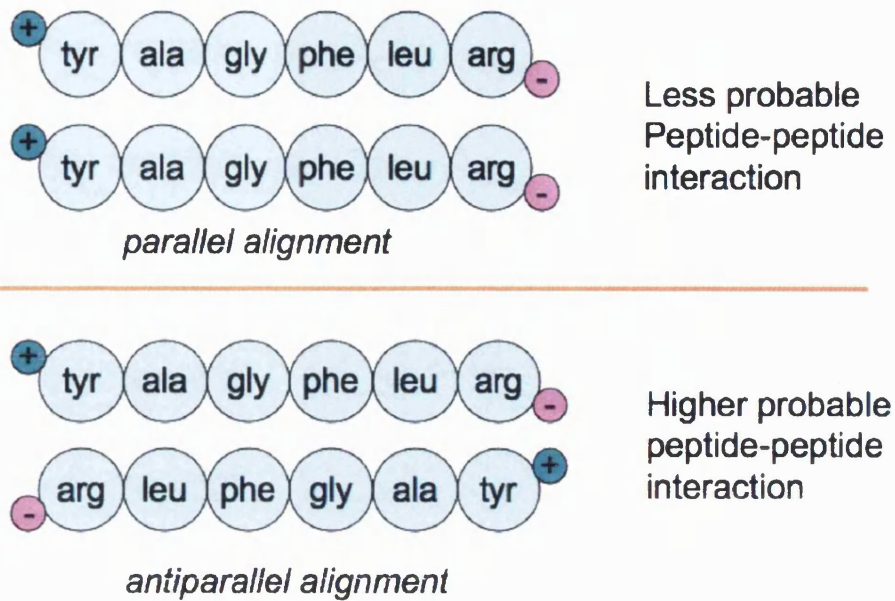


Figure 4.18: Backbone beads possible interactions

Furthermore, we can also suggest that the antiparallel alignment could be slightly shifted, as depicted in the Figure 4.19, because the probability of finding the alanine close to the phenylalanine is higher compared to the probability of finding the alanine close to the leucine.

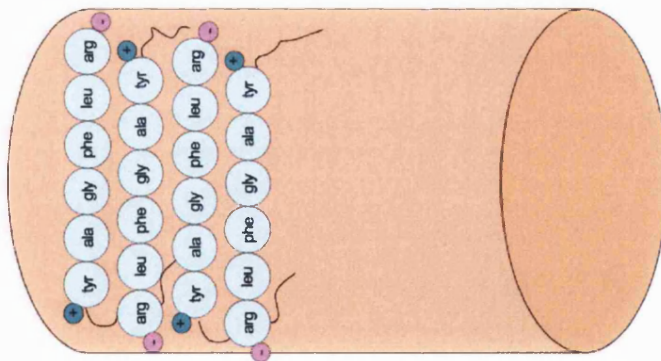


Figure 4.19: peptide-peptide interaction: shifted antiparallel alignment hypothesis

It has been experimentally probed for amyloid fibrils of A β (11-25) that the molecule was able to form slightly different packing arrangements where the molecules are able to slide across from one another (Petkova et al., 2004, Castelletto et al., 2010b) and it has been shown that a sliding arrangement is possible for single wall peptide

nanotubes of the backbones in the high axial ratio structure (Figure 3.20), hence it is reasonable to think that this can occur also for peptide nanofibres.

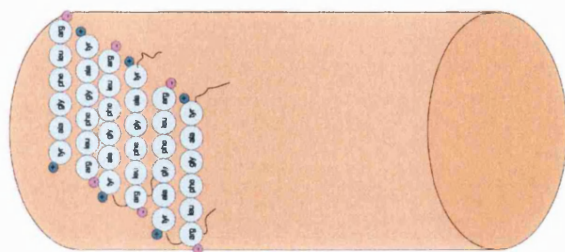


Figure 4.20: sliding arrangement of peptide sequences

The RDF plots for glycine (Figure 4.12) and phenylalanine (Figure 4.13) are very similar, confirming that in both case scenarios, parallel or antiparallel peptide interaction, these two amino acids maintain the same distances from the other amino acids, and this is also reasonable if it is considered that they are in the middle of the amino acidic sequence of pDal.

Interestingly, the RDF plots for Leucine and Arginine support the idea of shifted antiparallel configuration: the probability of finding a Leucine close to a Tyrosine is higher compared to the probability to find a Leucine close to an Arginine (Figure 4.14), as well as the probability to find an Arginine in the vicinity of a Tyrosine is higher than the probability to find an Arginine close to another Arginine (Figure 4.15)

In the simulation presented in this thesis molecules are allowed to follow the natural trend for the self-assembly. Our results seem to suggest that the packing of the peptide molecules in the self assembled structure is not radial from the fibre long axis, but the peptide backbones lay parallel to the long axis of the fibre on the surface of the structure (Figure 4.8). Furthermore from the visual representation in Figure 4.8 we could see that in many cases the backbones tend to assume an antiparallel β -sheet alignment.

In conclusion, this study shows that the amphiphilic pDal tends to self-assemble into nanofibres in an aqueous environment, that the palmitic chains form the hydrophobic core of the fibre and that the peptide sequences align themselves parallel to the long fibre axis rather than radially, as it has been reported into literature up to this date

(Hartgerink JD et al., 2003, Lee et al., 2011). It can also be hypothesised that the alignment of each peptide sequence is more likely to be antiparallel than parallel, and that the antiparallel strands are shifted along them.

From the results it is difficult to conclude whether it is the hydrophobic interaction that is the driving force to start the self-assembly process rather than the peptide – peptide interaction (eg. β -sheets), but interestingly this results shine a new light on the supramolecular organization of the molecules in the self-assembled structure compared to the theories that have been reported in literature so far.

CHAPTER 5

pDal Nanofibre Gels

5.1 Introduction

Peptide nanofibrous systems mimic the architecture of naturally occurring cellular structures (i.e tethers, extracellular matrix components), present a high surface to volume ratio, and are constituted of biocompatible materials. For these reasons they represent a good candidate for applications in the field of regenerative medicine and drug delivery systems.

Naturally occurring and synthetic peptide amphiphiles self-assemble into high axial ratio fibrillar nanostructures that are able to form gels (Zhang et al., 2010b, Aulisa et al., 2009a, Lee et al., 2009).

Gelation of peptide nanofibres can occur in response to pH, ionic strength (Niece et al., 2008, Anderson et al., 2009), or thermal stimuli (Ryu and Park, 2009, Zhang et al., 2010a), for example on prolonged exposure to high temperature, these nanofibre dispersions further self assemble into bundles and plaques on cooling (Zhang et al., 2010a).

The advantages of peptide nanofibres gels for biological applications are that they pose a minimal risk of carrying biological contaminants (as it is in the case of collagen derived materials), elicit no immune response and show excellent physiological compatibility and low cytotoxic response (Ellis-Behnke and Schneider, 2011), such that they have been also employed to fabricate cell culture scaffolds commercialized first as Puramatrix by 3DM, Inc. (Cambridge, MA, USA), and more recently by Sigma-Aldrich as HydraMatrix™ in the form of 12, 24 and 96 well plates.

Self assembling peptide nanofibres gels containing osteopromotive domains with high affinity for the Bone Morphogenic Protein (BMP) receptor were able to

promote osteoblastic differentiation of human bone marrow stromal cells (Lee et al., 2009).

Self-assembling peptide nanofibres gels have also been prepared using the RGDS cell adhesion epitope to exploit the control of cell adhesion, proliferation, differentiation, and organization (Guler et al., 2006). Bone marrow stem cells have been encapsulated in RGDS nanofibre gel and have been found to be proliferative, viable and able to divide. When tested *in vivo* by subcutaneous injection in mice, luciferase-expressing cells encapsulated in the RGDS nanofibre gel determined a 3.2 fold increase in bioluminescent signal measured by an imaging system able to detect the photon transmission signal emitted from the intracellular luciferase, suggesting proliferation of the transplanted cells (Webber et al., 2010c).

The studies on bone marrow stromal cells by Lee and Webber highlight how versatile and highly specific nanofibre peptide gels can be, as the amino acid epitope of interest can be varied depending on the specific needs of the therapeutic goal. In these two different studies the same goal, bone marrow regeneration, was achieved using strategies having as an objective two different cellular targets.

Peptide nanofibres gels have been shown to have good biocompatibility in the Central Nervous System when stereotactically injected in mice (Yang et al., 2009), showing good potential for applications as CNS depots.

Peptide nanofibre gels are also studied for brain repair and axon regeneration. Using the mammalian visual system as a model, a gel made of peptide amphiphile (RADA16-I) containing arginine, alanine, aspartate and alanine repeated sequences was implanted in the CNS site of injury where it was able to promote axon regeneration, promoting functional return of vision (Ellis-Behnke et al., 2006b). RADA16-I nanofibre gel has been shown to promote complete hemostasis immediately when applied directly to a wound in the brain, spinal cord, femoral artery, liver, or skin of mammals in less than 15 seconds (Ellis-Behnke et al., 2006a). Developing a hemostasis system based on these findings can be of great importance in the prevention of blood loss during surgical procedures, thus promoting a decrease in the amount of transfusion blood necessary during surgery.

Peptide nanofibres gels may also be used as angiogenesis-promoting materials. Gels presenting the Heparin-Binding peptide epitope have promoted formation of *de novo* vascularized connective tissue both in static histological assessment and in a dorsal skinfold model (Ghanaati et al., 2009).

Peptide nanofibre gels may also be exploited as drug delivery system. Peptide delivery is definitively a hot topic in pharmaceuticals, as many peptides have potential therapeutic use. However, most peptides are not only unable to cross biological barriers, but degrading enzymes in biological fluids, such as plasma or gastrointestinal fluids, easily metabolize them (van der Walle CF and O, 2011).

The work presented here originated from the idea to use self-assembling peptide nanofibres gels for oral administration of peptides, as the lipophilicity of pDal should facilitate cellular membrane crossing at the intestinal level.

In this chapter we report a fast and facile method for the preparation of gels based on peptide self-assembling nanofibres. These gels are prepared by a rapid microwave heating and cooling cycles. These materials can provide new transporting biocompatible materials that form an efficient network of nanochannels with potential application, for instance, as a depot system for sustained release of pharmaceuticals.

5.1.1 Thermal Analysis by Differential Scanning Calorimetry

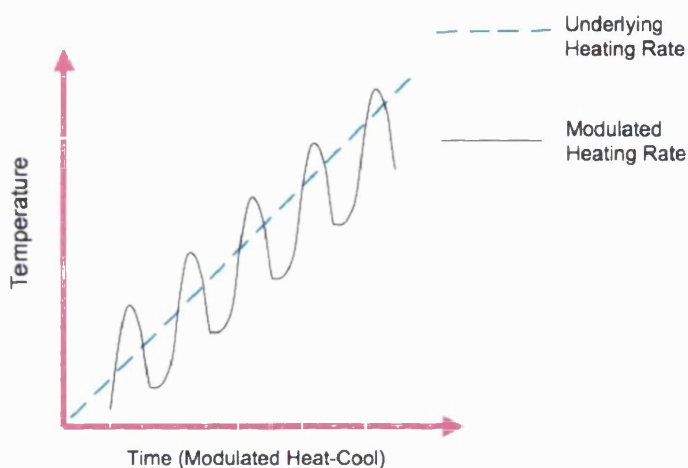
Calorimetry is one of the most widespread techniques used to characterize a variety of physicochemical parameters of high importance in the preformulation stage of any pharmaceutical product (Rabel et al., 1999, Gill et al., 2010). Differential Scanning Calorimetry (DSC) is a technique able to study thermally induced transitions and particularly, the conformational transitions of biological molecules (Bruylants et al., 2005) and common parameters such as melting point, glass transitions and crystallization of solid forms of pharmaceuticals (Gaisford, 2007).

Several methodologies based on the calorimeter type (conventional DSC or MTDSC), measured parameters and experimental conditions are used for monitoring the behavior of pharmaceuticals, biopharmaceuticals and new nanoscale pharmaceutical formulations (Gill et al., 2010).

One of the goals of this work was to develop a new stable nanosized drug delivery system, therefore it was essential to understand the bulk properties of the peptide amphiphile pDal molecules, of which the system was made of, and link these properties to the final physical form of the pDal molecules supramolecular assembly. Conventional DSC measures how physical properties of a sample change by determining the temperature and heat flow associated with the transitions in the

material as a function of time and temperature (Haynie, 2008). During a change in temperature, DSC measures a heat quantity, which is radiated or absorbed excessively by the sample on the basis of a temperature difference between the sample and the reference material (Haines, 2002).

Modulated DSC (MTDSC) provides some advantages over conventional DSC, such as the separation of complex transitions into its components, increased resolution without loss of sensitivity, measurement of heat flow and heat capacity in a single experiment by superimposing a modulated heating rate on the top of a linear heating rate, as schematically shown in Scheme 5.1, so that the linear change allows the measurement of heat flow, while the modulated change permits the calculation of the heat capacity (Simon, 2001).



Scheme 5.1: Modulated Temperature profile versus time

Rapid-Heat DSC (RH-DSC) offers heating rates up to 2000 °C/min, has a much higher sensitivity, as the same name suggest, but lower resolution than conventional DSC. Faster heating rates increase the sensitivity and productivity, but do so at the expense of temperature resolution and accuracy, thus, one challenge with the use of high heating rates is that while the furnace may achieve a rapid rate, there is a finite time delay before the sample achieves the same rate (Bruce Cassel, 2008).

Thermal analysis by DSC on the pDal bulk will enable insights into the bulk properties of the peptide amphiphile.

5.1.2 Thermal Microscopy and Polarized Light Microscopy

The optical microscope is used extensively in pharmaceutical development with the primary application being solid-state analysis.

Thermal microscopy simply requires the addition of a heating and/or cooling stage to an optical microscope and it is a useful mean to obtain information on the melting point, indeed, it enables a visual observation of the melting point, solid-solid transformations, such as the transition between crystal polymorphs, and solid-liquid-solid transitions, such as transformation from one crystal form to another one (Carlton, 2011b). There are three important melting temperatures that can be observed in a melting experiment on the thermal microscope: onset melting temperature, final melting temperature, and equilibrium melting temperature (Carlton, 2011b). The last one is of particular interest in phase transitions processes. The use of polarizing filters in an optical light microscope provides the opportunity to study unique features of the material under characterization. Light passing through a polarizing filter will become oriented relative to that filter, so that when a second polarizer is positioned above the sample and perpendicular to the first filter, cross polarization is achieved (Vitez and Newman, 2007), as schematized in Figure 5.1.

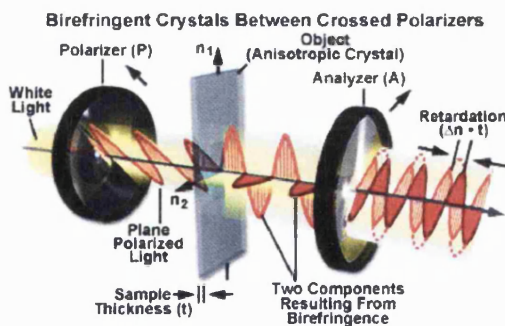


Figure 5.1: Birefringence of an anisotropic crystal under crossed polarizers.

When a crystalline material is placed under cross-polarized light, some particles will not be visible and are characterized as isotropic, whereas crystals that appear to be white or colored are termed anisotropic (Vitez and Newman, 2007). An anisotropic crystal is characterized as birefringent because the two components of polarized light being transmitted through the particle recombine in a fashion such that one

component emerges slightly ahead relative to the other component (Vitez and Newman, 2007).

The use of polarized light on the optical microscope allows us to determine the optical crystallographic properties of a material. When visible light irradiates an object, the light can be reflected, transmitted, or both. Reflection and transmission can occur such that the light retains all of its energy or some energy can be absorbed in the process. Birefringence is observed for those materials of crystalline nature and interference (anomalous) colours are also observed for organic fibres and liquid crystals (Carlton, 2011a).

5.1.3 Fourier Transform-Infra Red Attenuated Total Reflectance Spectroscopy (FTIR-ATR)

IR spectroscopy is an absorbance vibrational spectroscopy technique. The radiation of interest is comprised between 400-4000 cm^{-1} . For a molecule, in order to absorb IR radiation, it is necessary that the energy of the radiation is equal to the difference in energy between two vibrational states of the molecule (Rees, 2010). Actually, each functional group in a molecule can have different vibrational states, such stretching and bending, as shown schematically in Figure 5.2 A, giving rise to specific bands of IR absorbance minimally influenced by the complexity of the molecule (Figure 5.2 B), and that can for this reason be used to study chemical structure, orientation and secondary or tertiary structures in peptides and proteins (Vigano et al., 2000).

In attenuated total reflectance mode the sample is placed directly in contact with an optically dense crystal having a high refractive index (such as ZnSe, Germanium or Diamond), when the infrared beam comes in contact with the sample the system measures the changes that occur in a totally internally reflected infrared beam. Basically, the infrared beam is reflected and amplified by the crystal (Figure 5.3) and each time redirected onto the sample, thus creating an evanescent wave protruding only a few microns beyond the crystal surface and into the sample, held tightly in contact. In regions of the infrared spectrum where the sample absorbs energy, the evanescent wave will be attenuated or altered. The attenuated energy from each evanescent wave is passed back to the IR beam, which then exits the opposite end of the crystal and is passed to the detector in the IR spectrometer.

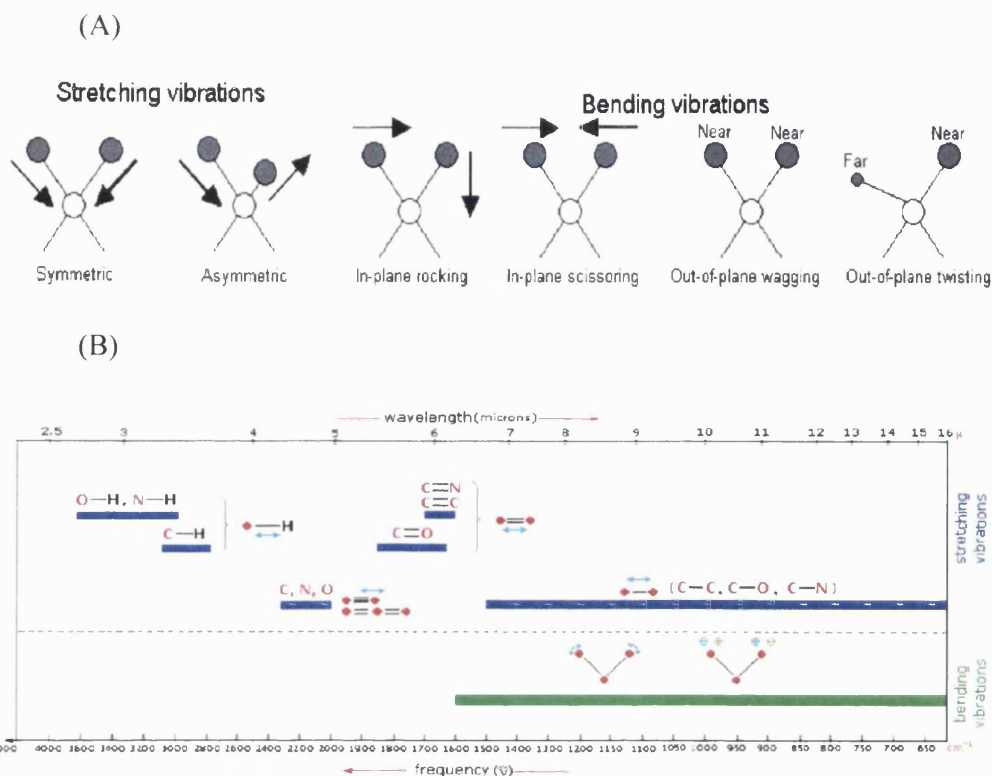


Figure 5.2: (A) vibrational states; (B) functional groups frequencies in IR spectroscopy.

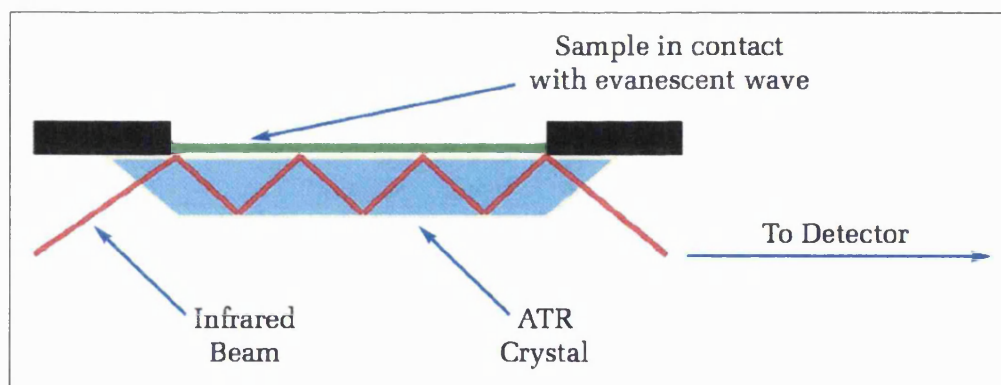


Figure 5.3: a multiple reflection ATR system (from www.perkinelmer.com/CMSResources/Images)

Here we report a method for the preparation of peptide nanofibre gels using a rapid heating/cooling cycle employing electromagnetic radiation heating. The thermal history of the peptide amphiphile pDal was determined using differential scanning

calorimetry and Hot Stage Microscopy and the properties of the gel forming peptide which influence their self-assembly into gels also characterized. Short microwave bursts applied to a dispersion of peptide amphiphiles in water results in the formation of a gel made of branched peptide nanofibres, as the ultrastructure analysis performed by transmission electron microscopy and scanning electron microscopy as shown.

5.2 Methods

5.2.1 Differential Scanning Calorimetry

DSC and MDSC were performed on a Q2000 DSC (TA Instruments). The DSC analysis was carried out by equilibrating the system first at -10°C , followed by an isothermal step for 5 minutes and finally a heating rate of $10^{\circ}\text{C}/\text{min}$ was applied. For the modulated temperature analysis two independent experiments were performed: in the first experiment the pDal in its solid freeze-dried form was subject to a Heat/Cool cycle at $4^{\circ}\text{C}/\text{min}$ heating rate, modulated with a ± 0.639 amplitude every 60 seconds; in the second experiment, the sample was subject to a Heat only cycle at the same conditions as for the first experiment. pDal samples were annealed by storing the pans containing the glassy sample in a temperature controlled Plus II Incubator (Gallenkamp) at 40°C . A third experiment was carried out on a Rapid Heating DSC (RH-DSC) at a heating rate of $100^{\circ}\text{C}/\text{min}$.

5.2.2 X-ray Diffraction

The aged glass resulting from the annealing of the pans in a Plus II Incubator (Gallenkamp) at 40°C . were glued on the top of a cryo-loop holder. Datasets were collected at room temperature on an Xcalibur NovaT X-ray diffractometer (Oxford Diffraction, Oxford, UK).

5.2.3 Microwave Sample Preparation

pDal $3\text{mg}/\text{mL}$ and $10\text{mg}/\text{mL}$ solutions in deionized water were prepared in an Emrys vial, sealed with a reseal septum. The solution was rapidly heated with a short

microwave burst (10 seconds) first at 60°C, subsequently at 88°C in an Emris Optimizer Microwave Station (Personal Chemistry, Cambridge, UK). Alternatively, a short microwave burst was applied using a Microwave Panasonic NN-3454 800W-D (Panasonic UK, Bracknell, Berks) to solution prepared in unsealed glass vials for 10 seconds with the power level at Simmer (240 W) and/or High (800 W). Samples were left to cool at room temperature for 30minutes or in the fridge (4°C) for ten minutes.

5.2.4 FTIR –ATR

The FTIR experiment was performed using a Perkin Elmer Precisely, Spectrum 100, FT-IR Spectrometer (Perkin Elmer, Cambridge, UK); samples were measured using attenuated total reflection (ATR) on a single bounce diamond/ZnSe ATR crystal. All samples were measured between a frequency range of 4000 to 650 cm^{-1} resolution with a Strong Beer-Norton apodization. A total of 16 background and sample scans were measured for each sample. Data were collected with a temperature-stabilized deuterated triglycine sulfate detector (DTGS). The samples were measured separately by placing each in contact with the ATR crystal and applying force from the pressure applicator supplied with the ATR accessory. The application of pressure enabled the sample to be in intimate contact with the ATR crystal, ensuring a high-quality spectrum was achieved.

5.2.5 Optical Microscopy Analyses

The freeze-dried pDal or a chip of the aged glass was deposited on a glass microscopy cover slip 1mm thick in submicrogram quantities with a brush. The cover slip was then mounted on the hot stage accessory (Linkam TC93) and analyzed using a Nikon-Microphot-FXA microscope equipped with Nikon PlanAPO Chromatic lenses, and a static and dioscopic crossed polarizing filters.

The nanofibre gel was analyzed under a polarizing microscope (Stemi SV6, Zeiss) and pictures recorded with a Sony Carl Zeiss Acc Thermal MPEG MOVIE EX Digital Still Camera (DSC-S75).

5.2.6 Congo Red Staining

Congo Red (100 μ L) in potassium phosphate buffer (5mM, pH 7.4, containing 150mM of NaCl) was added to the gel (10 μ L) deposited onto a microscope slide. After 10 minutes excess buffer is removed with filter paper.

5.2.7 Electron Microscopy

SEM images were acquired with an EI Quanta 200 FEG Scanning Electron Microscope (Philips Electron Optics, Eindhoven, The Netherlands). The gel was immersed in liquid Nitrogen and immediately freeze-dried and images acquired on uncoated samples in backscattered electron mode and on coated samples with a 3-5 nm gold patina. Coating was achieved with a sputter coater prior to imaging. TEM images were captured using an energy filtering electron microscope (FEI CM120 Bio Twin, Eindhoven, The Netherlands) operating at 120kV.

5.2.8 Pilot Study: Peptide Release in Simulated Gastric (SGF) and Intestinal Fluids (SIF).

The simulated gastric fluid (SGF) and intestinal fluid (SIF) were prepared according to the U.S. Pharmacopeia (USP-NF, 1995). The SGF was prepared by dissolving 2.0 g of sodium chloride and 3.2 g of purified pepsin (Sigma Aldrich) that is derived from porcine stomach mucosa, with an activity of 800 to 2500 units per mg of protein, in 7.0 mL of hydrochloric acid and sufficient water to make 1000 mL.

The SIF was prepared by dissolving 6.8 g of monobasic potassium phosphate in 250 mL of water, then mixed. To the mixture was added 77 mL of 0.2 N sodium hydroxide and 500 mL of water. To this, 10.0 g of pancreatin (Sigma Aldrich) were added, the mixture stirred and the resulting solution was adjusted with either 0.2 N sodium hydroxide or 0.2 N hydrochloric acid to a pH of 6.8 ± 0.1 . The resulting solution was diluted with water to 1000 mL.

pDal gel (0.25 mL, 10mg/mL) was prepared by adding a solution of GCPQA in deionized water (10mg/mL and 20mg/mL) to the freeze dried peptide in order to obtain two gels with a different peptide to polymer ratio, respectively of 1:1 and 1:2.

The gels were prepared according to microwave sample preparation described in the section 5.2.3 of this thesis at a temperature of 88°C for 10 seconds.

The resulting gels were placed in dialysis cassettes (Slide-A-Lyzer G2 Dialysis Cassettes, 0.25 mL, Thermo Fisher Scientific,) and separately dialyzed against SGF (50 mL) for 120 minutes. A 0.5 mL aliquot of the SGF was taken at different time points (0, 15, 30, 45, 60, 90, 120 minutes) and replaced with 0.5 mL of fresh SGF each time. The dialysis was maintained at $37 \pm 0.1^\circ\text{C}$ and agitated at 130 cycles per minute (Grant OLS 200 water shaking bath, Cambridge Ltd, Herts, UK). Subsequently the gels were transferred in SIF (50mL) and dialyzed for 360 minutes. A 0.5 mL aliquot of the SIF was taken at different time points (0, 15, 30, 45, 60, 90, 120, 150, 180, 240, 270, 300, 360 minutes) and replaced with 0.5 mL of fresh SIF each time. The dialysis was maintained at $37 \pm 0.1^\circ\text{C}$ and agitated at 130 cycles per minute (Grant OLS 200 water shaking bath, Cambridge Ltd, Herts, UK).

Aliquotes were analysed by HPLC using a Onyx Monolithic C18 column (100 x 4.6 mm) attached to a guard cartridge on a Agilent Technologies 1200 Series HPLC system using a mobile phase of acetonitrile: water – 80:20, TFA 0,01% v/v at a wavelength of 230 nm and flow rate of 1mL min^{-1} .

5.2.9 Pilot Study: Pharmacokinetics of pDal Gels Following Oral Administration

CD-1 male out bred mice (18-24g, 4 weeks old, Harlan, Oxon, UK) were used to measure blood, plasma and liver concentrations of Dalargin control and pDal gels after oral administration. The animals were housed in groups of 5 in plastic cages in controlled laboratory conditions with ambient temperature and humidity maintained at $\sim 22^\circ\text{C}$ and 60% respectively with a 12-hour light and dark cycle (lights on at 7:00 and off at 19:00). Food and water were available *ad libitum* and the animals acclimatised for 5-7 days prior to any experiments in the Animal House, School of Pharmacy, University of London (London, UK). Animals were only used once and were acclimatised in the testing environment for at least 1 hour prior to testing. All experiments were performed in accordance with the recommendations and policies of the Home Office (Animals Scientific Procedures Act 1986, UK) and the Ethics Committee of the School of Pharmacy, University of London guidelines for the care and use of laboratory animals.

Groups (n = 5) of animals were administered either: Dalargin, pDal nanofibres gel, Dalargin/GCPQ, and pDal nanofibres/GCPQ gel, the polymer/peptide ratio was 1:1.

a 0.2 μm Millex filter, as the disperse phase.

The Dalargin control solution was prepared at a concentration of 5.83 mg mL^{-1} and the Dalargin/GCPQ control solution was prepared at a concentration of 5.83 mg mL^{-1} with a peptide/polymer ratio of 1:1. The mixture was vortexed, then sonicated for 10 minutes in an ice bath at 50% of the maximum output of the instrument. The pDal nanofibres gel was prepared by applying a 10 seconds microwave burst to a suspension of 7.75 mg mL^{-1} according to the preparation method described in the section 5.2.3. The hot solution was transferred into syringes and left to cool down to reach gelation in the fridge (8°C) for 10 minutes without perturbation. The pDal/GCPQ nanofibres gel was prepared by adding a freshly prepared solution of GCPQ in water (7.75 mg mL^{-1}) to the freeze dried pDal to obtain a final peptide/polymer ratio of 1:1. The mixture was vortexed, then sonicated for 10 minutes in an ice bath at 50% of the maximum output of the instrument.

At various time points (30 min, 1 hour, 2 hours, 4 hours and 6 hours) after administration, animals were killed and their brain, liver and plasma taken for analysis.

PK analyses were performed using LC-MS as described in detail in the sections 6.2.3 (Sample Handling), 6.2.4 and 6.2.5 of the Chapter 6 of this thesis.

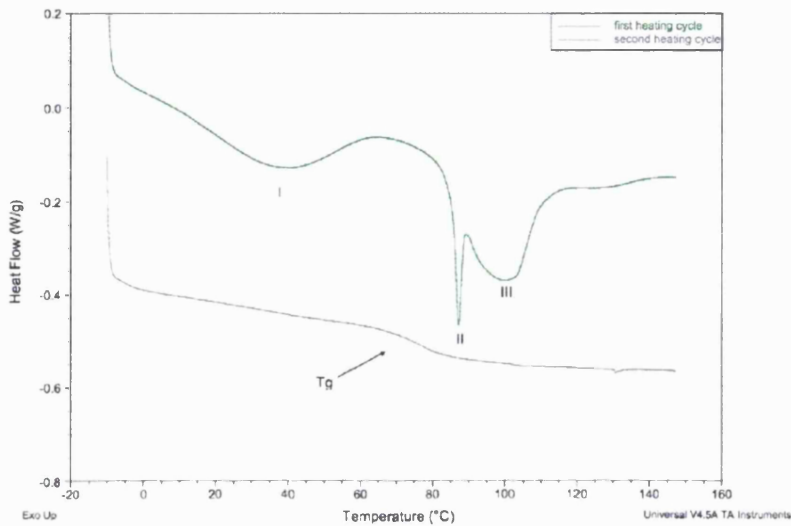
5.3 Results

Thermal analysis of pDal helps to clarify the thermal properties of the monomer starting material and the influence of these properties on the molecular self-assembly. The DSC analyses of pDal freeze-dried powder shows three endothermic events (Figure 5.4A), at low temperature a broad peak (peak I) of solvent loss, as well as two high temperature endothermic transitions: one sharp peak with onset at 85°C (peak II) of hydrocarbon chain melting, which merges with a broader endothermic peak (peak III).

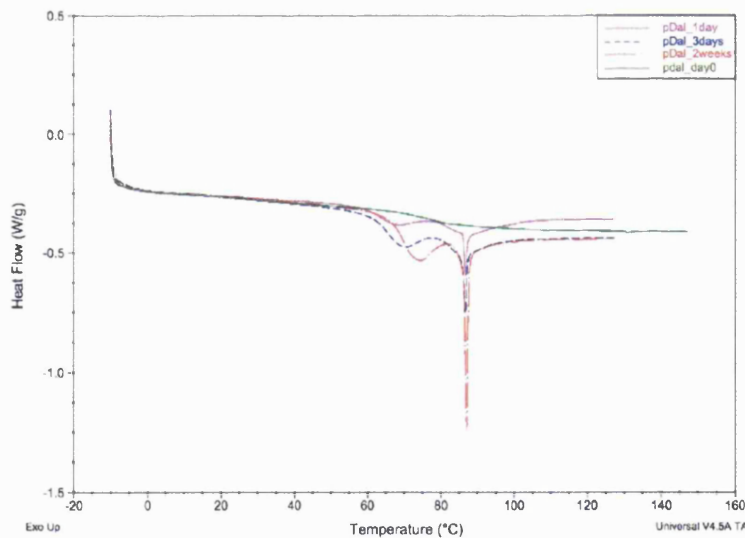
Upon cooling at room temperature, the samples coming out from the DSC were aged below their glass transition temperature in order to perform an annealing experiment. Amorphous glassy materials are thermodynamically non-equilibrium systems, which tend to reach equilibrium state over extended periods of time when aged below their glass transition temperatures (Wunghanagorna and Schmidt, 2001). The aged glass

has a lower molecular mobility (corresponding to an increased molecular density), thus during heating an enthalpy relaxation occurs.

Annealing the glass formed after the first DSC cycle at a temperature below the T_g for up to 2 weeks showed recovery of the endothermic peak of the alkyl chain melting as well as enthalpy relaxation at the T_g , as shown in Figure 5.4 B. The enthalpy relaxation increases with increasing ageing time.



(A)



(B)

Figure 5.4: (A) DSC scans of pDal freeze-dried; (B) DSC scans of aged glassy solid. Heating rate 10°C/minute.

The MDSC analysis (Figure 5.5) helps to discern the reversible events from the non-reversible events: the broad low temperature endothermic peak (peak I) as well as the

broad high temperature peak (peak III) are both non-reversible events, as they both fall in the non-reversible heat flow signal (brown line in the graphs of Figure 5.5). Peak II (blue line in the graphs of Figure 5.5), corresponding to the melting of the palmitoyl chain, is a reversible event, as it would be expected considering that by aging the sample we could observe annealing.

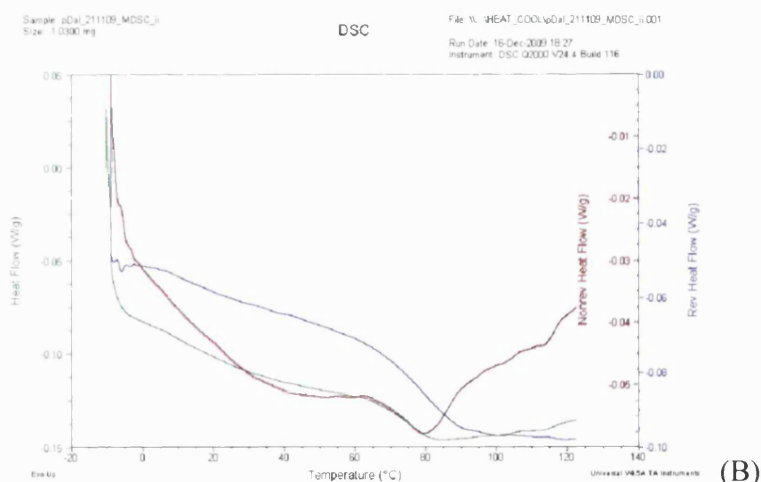
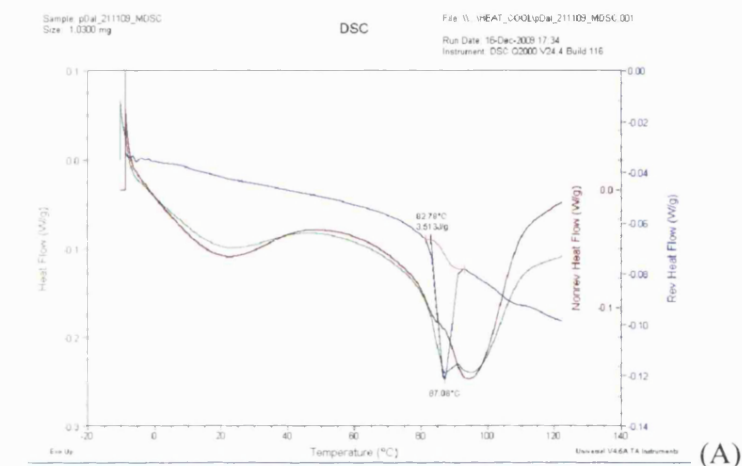


Figure 5.5: (A) MDSC Heat/Cool first cycle; (B) MDSC Heat/Cool second cycle. Heating rate 4°C/minute \pm 0.639 amplitude every 60 seconds.

A fast scan with RH-DSC (Figure 5.6) is performed on the pDal freeze-dried sample using a heating rate (100°C/min) ten times higher than the heating rate used on the normal DSC (10°C/min), thus definitively proving that the peak around 87°C is true melting, indeed although there is a loss in resolution the peak is not moving from the temperature range measured by conventional DSC.

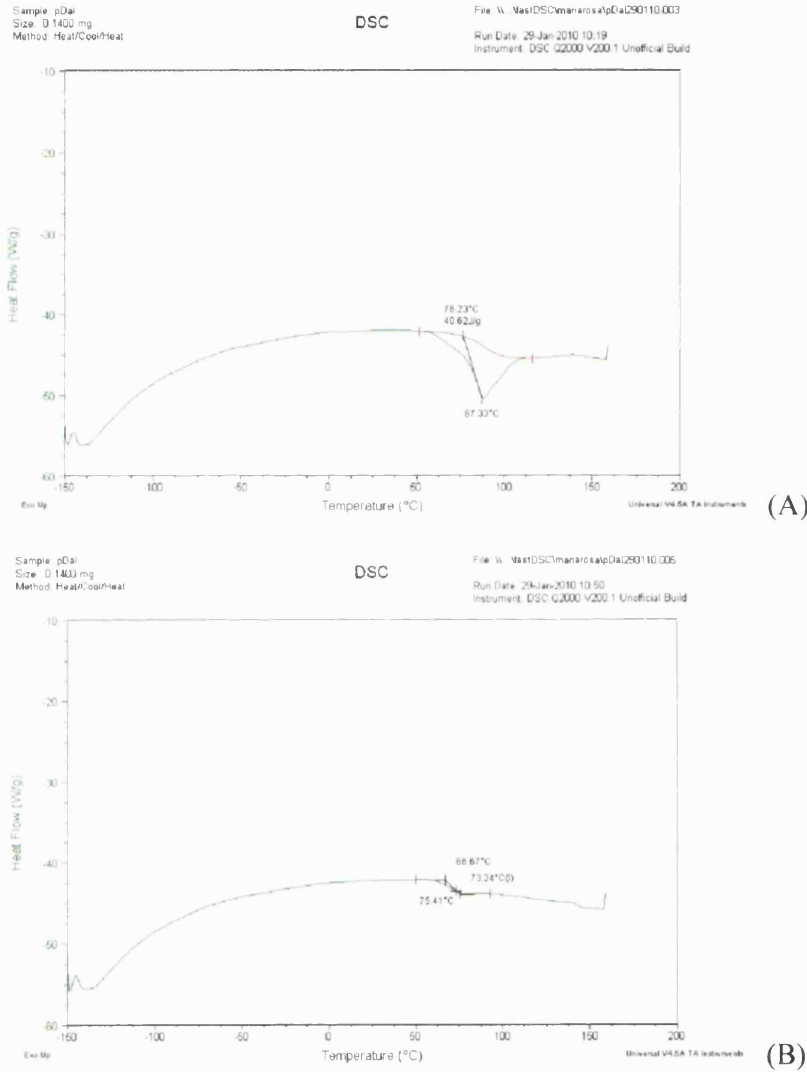


Figure 5.6: (A) RH-DSC first cycle; (B) RH-DSC second cycle showing the glass transition ($T_g = 66.67^\circ\text{C}$). Heating rate 100°C/min.

The optical micrographs (Figure 5.7 E-F) of the aged glass show a clear birefringence attributable to the areas crystalline ordering within the glassy solid. Indeed, by XRD analysis of the aged glass (Figure 5.8) it can be seen that the solid is mainly amorphous, although a little intensity can be spotted.

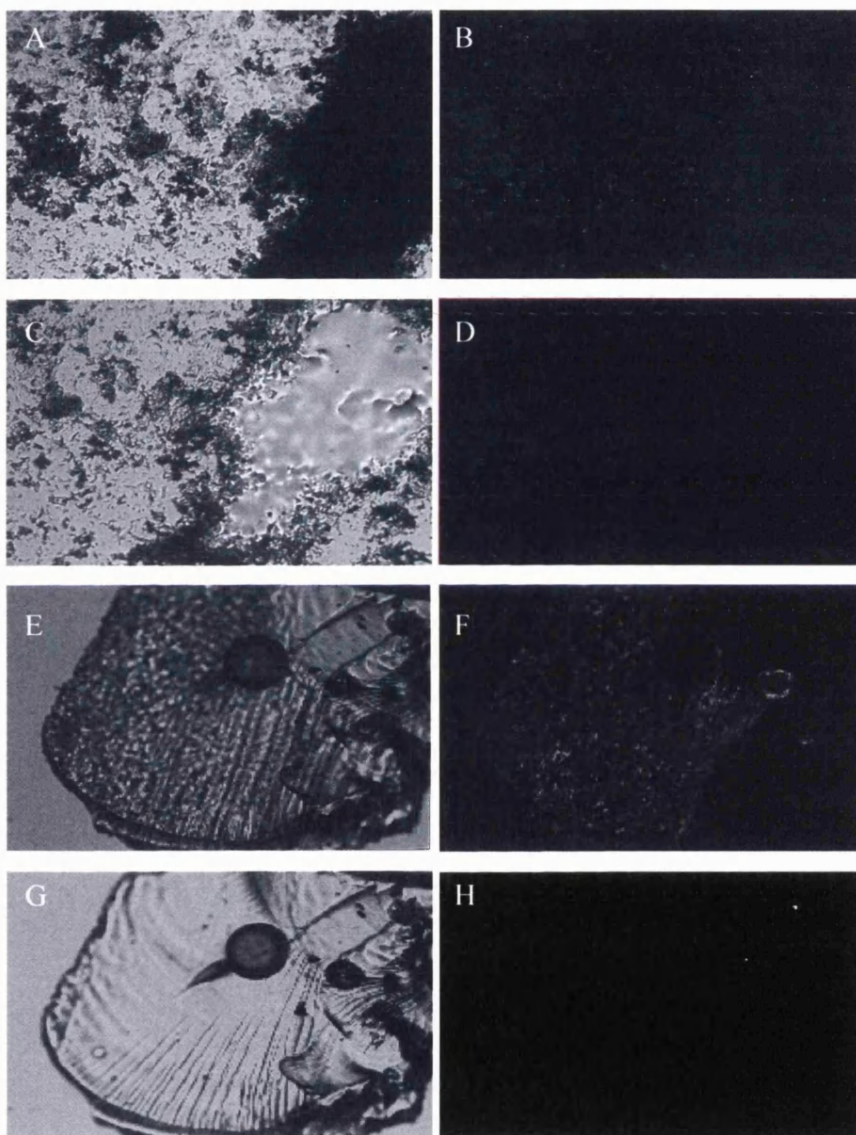


Figure 5.7: Optical micrograph of pDal:(A) powder at 25 °C;(B) under cross-polarized filters;(C) powder at 93°C(D) under cross-polarized filters;(E) aged glass at 25 °C,(F) under cross-polarized filters; (G) aged glass at 93°C, (H)under cross-polarized filters. Birefringence is attributable to c16 crystalline ordering.

The XRD of the aged glass shown in Figure 5.8 shows a mainly amorphous profile, however small peaks can be seen (arrows 1, 2 and 3).

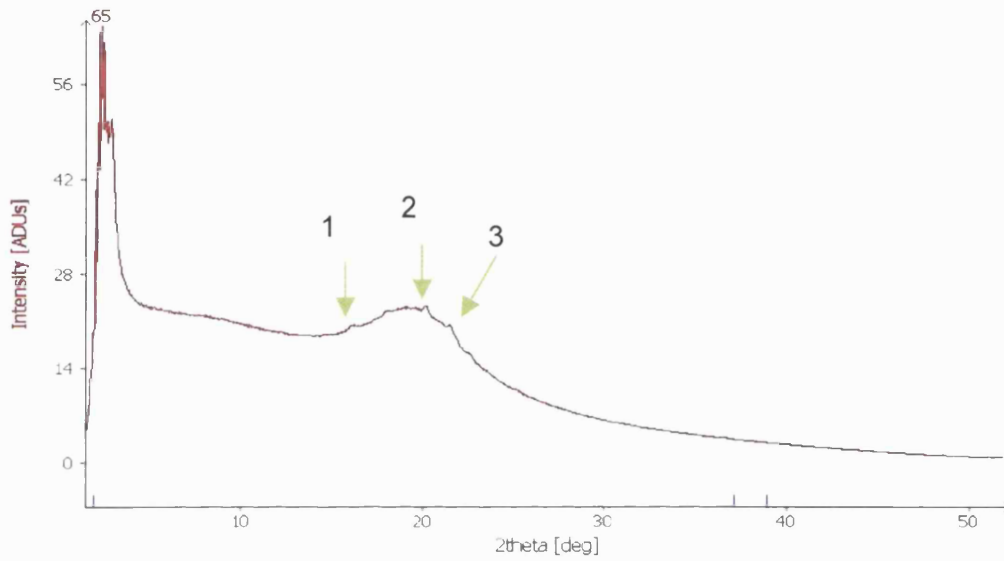
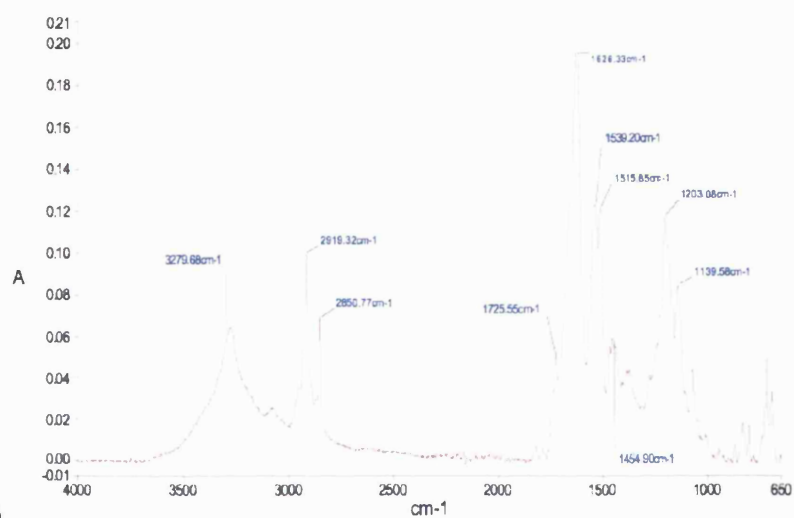
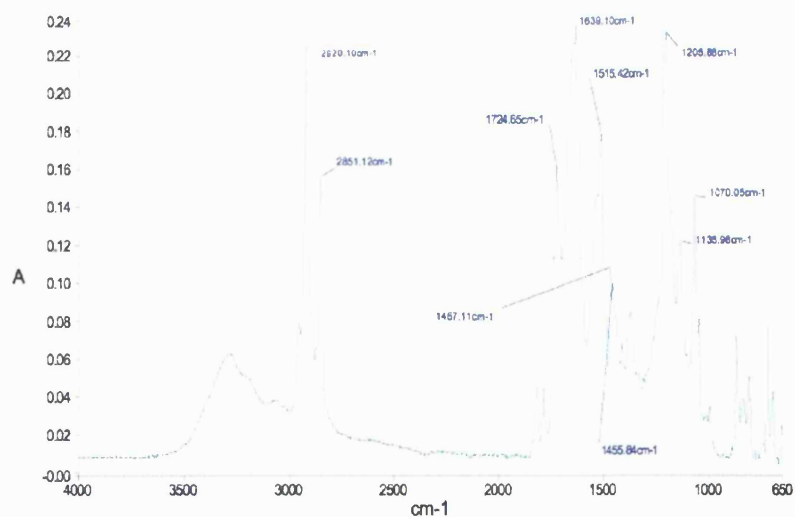


Figure 5.8: XRD of pDal aged glass

FTIR analyses of the glassy solid (Figure 5.9 B) show an increase in the Absorbance intensity of the palmitic chain compared to the pDal freeze dried powder (Figure 5.9 A), which present mainly amorphous features as discussed in the Chapter 1 of this thesis.



(A)



(B)

Figure 5.9: FTIR Absorbance bands of pDal freeze dried powder (A) and pDal aged glass (B).

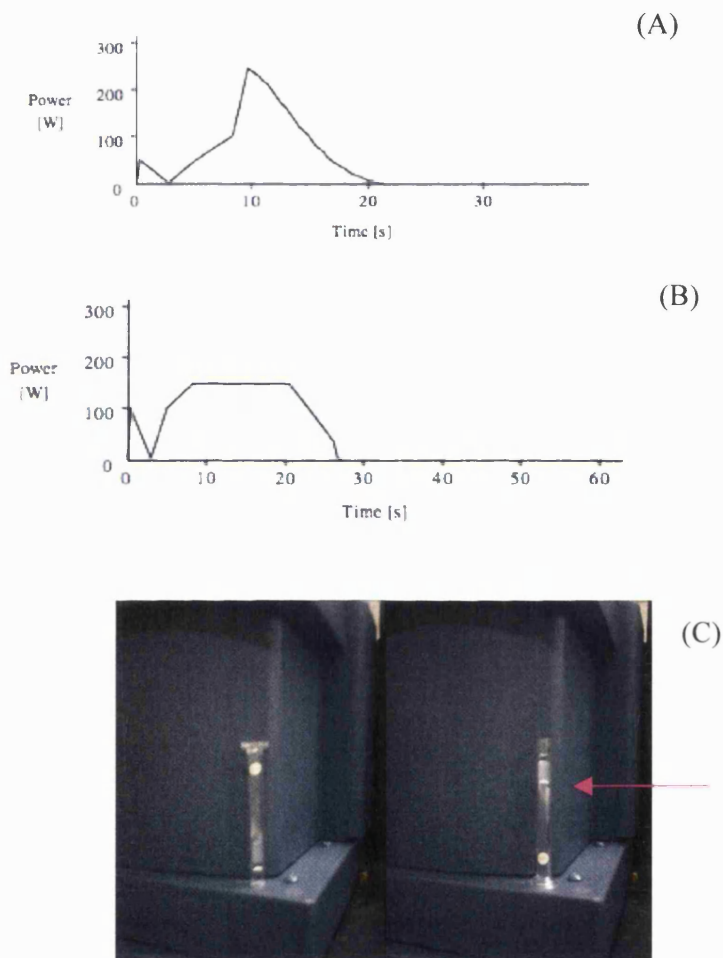


Figure 5.10: Power profiles for the microwave experiments, (A) when the experimental temperature = T_g ; (B) when the experimental temperature = melting temperature; (C) inverting the sample vial upon cooling shows that the gel (arrowed) does not flow.

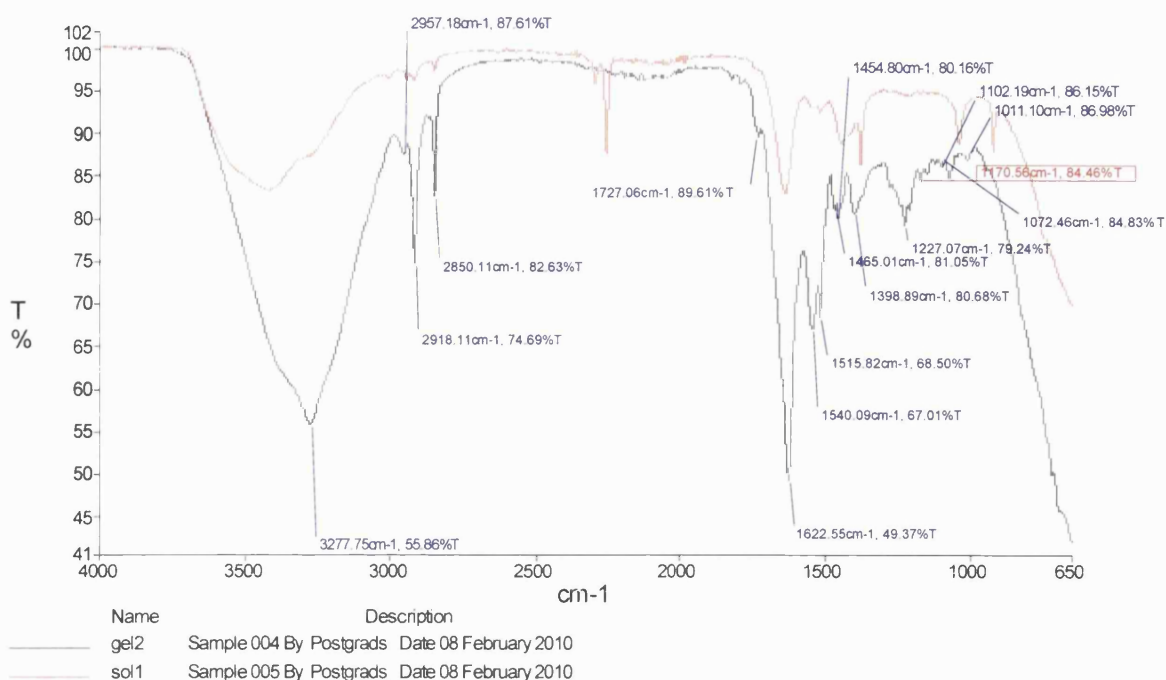


Figure 5.11: FTIR transmittance spectrum of pDal gel (black) overlapped to the FTIR transmittance spectrum of pDal suspension (red) in deionized water.

In the FTIR spectra (Figure 5.11) a strong Amide I band is exhibited around 1622 cm^{-1} indicating that the peptide segments in the nanofibres network adopt mainly a β -sheet conformation as it has been confirmed by staining the gel with the Congo Red dye and observing the stained gel under crossed polarizing filters (Figure 5.12 C).

pDal nanofibre gel showed a pronounced pattern of interference colours, predominantly red and green, when the gel was observed under polarizing light, as seen in Figure 5.12 A and B.

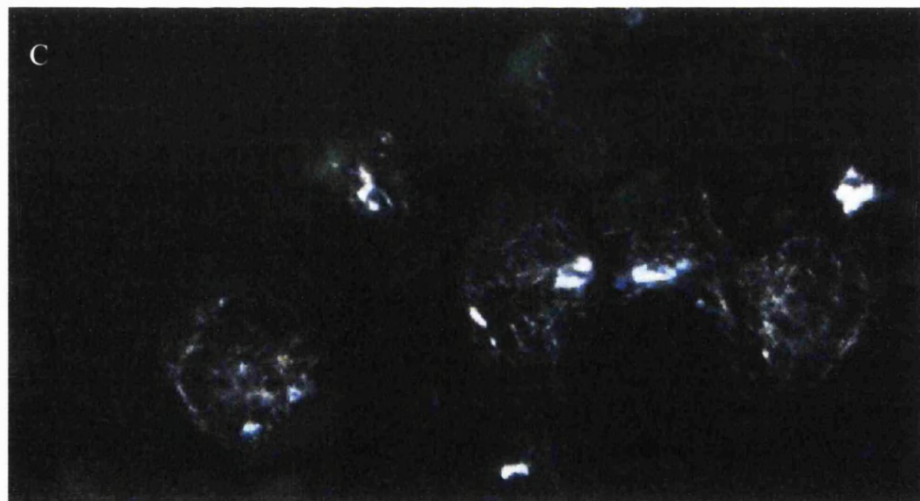
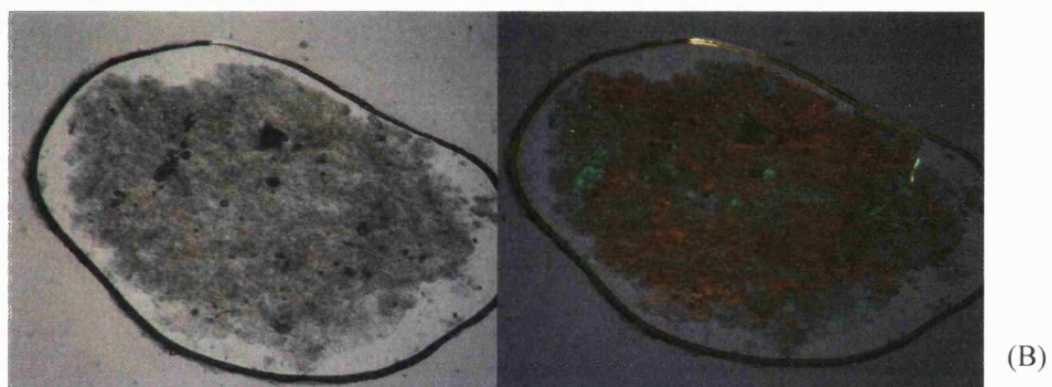
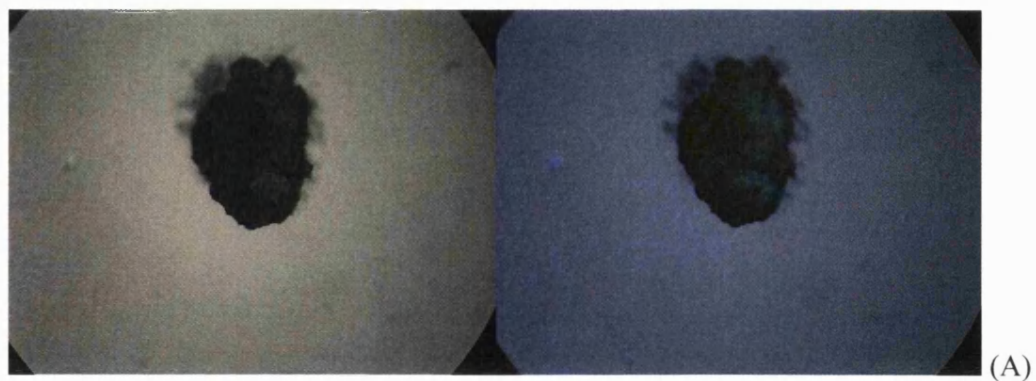


Figure 5.12: (A) pDal gel and sheared gel (B) under polarizing light microscope; (C) pDal gel stained with Congo Red.

The ultrastructure of the pDal gels observed by electron microscopy shows a dense nanofibre network with nanosize pores.

For imaging under the scanning electron microscope the xerogels were prepared by freeze-drying of the freshly made gels to remove the water from the system. Imaging of the uncoated sample was insufficient to resolve the ultrastructure of the fibre network at the nanometer range (Figure 5.13 A). Thus a 3-5 nm gold coating was applied (Figure 5.13 B): a dense network of entangled and branched nanofibres forms the pDal gel.

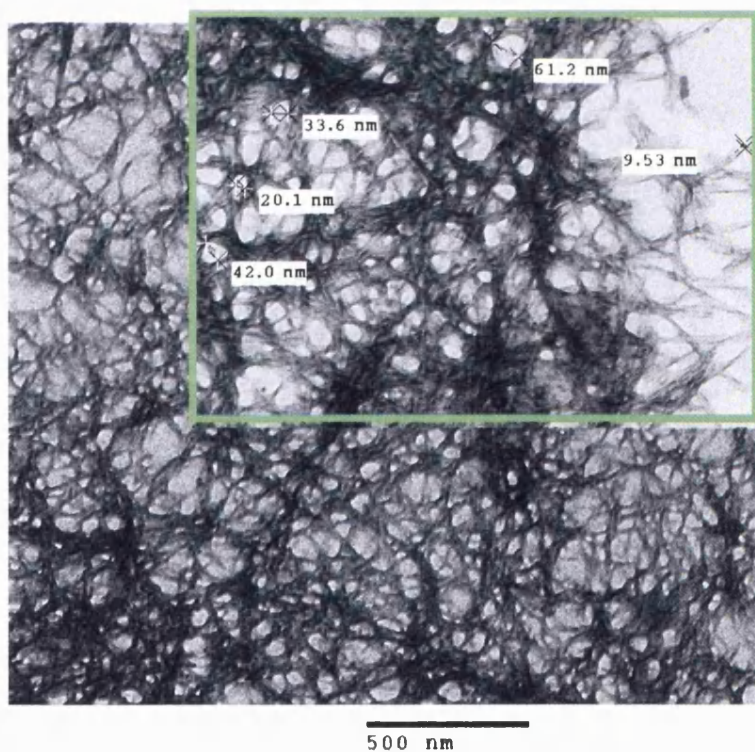
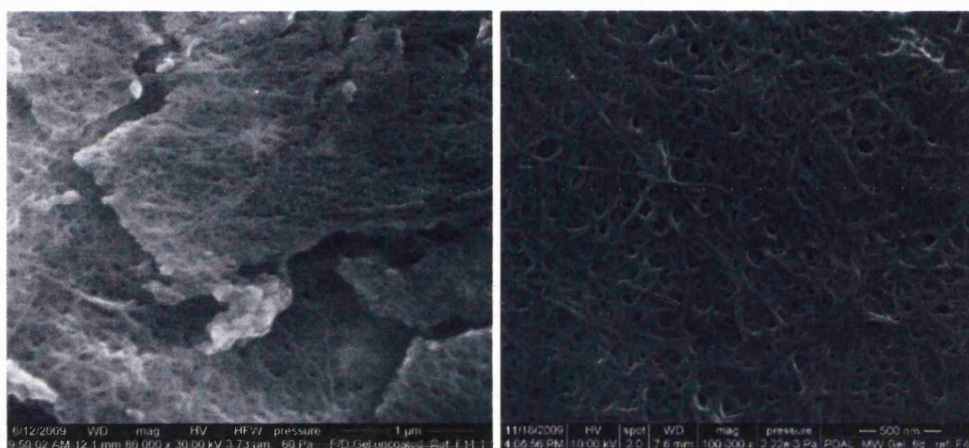


Figure 5.13: SEM pictures of pDal xerogel (upper photos); TEM picture of pDal gel.

Under TEM the gel was confirmed to be formed by a tightly three-dimensional matrix of branched nanofibres able to retain water in the formed nanosized channels.

To investigate the feasibility of the oral application, a pilot experiment was performed to study the ability of the gel to release the peptide in simulated gastric (SGF) and intestinal fluids (SIF), (Figure 5.14).

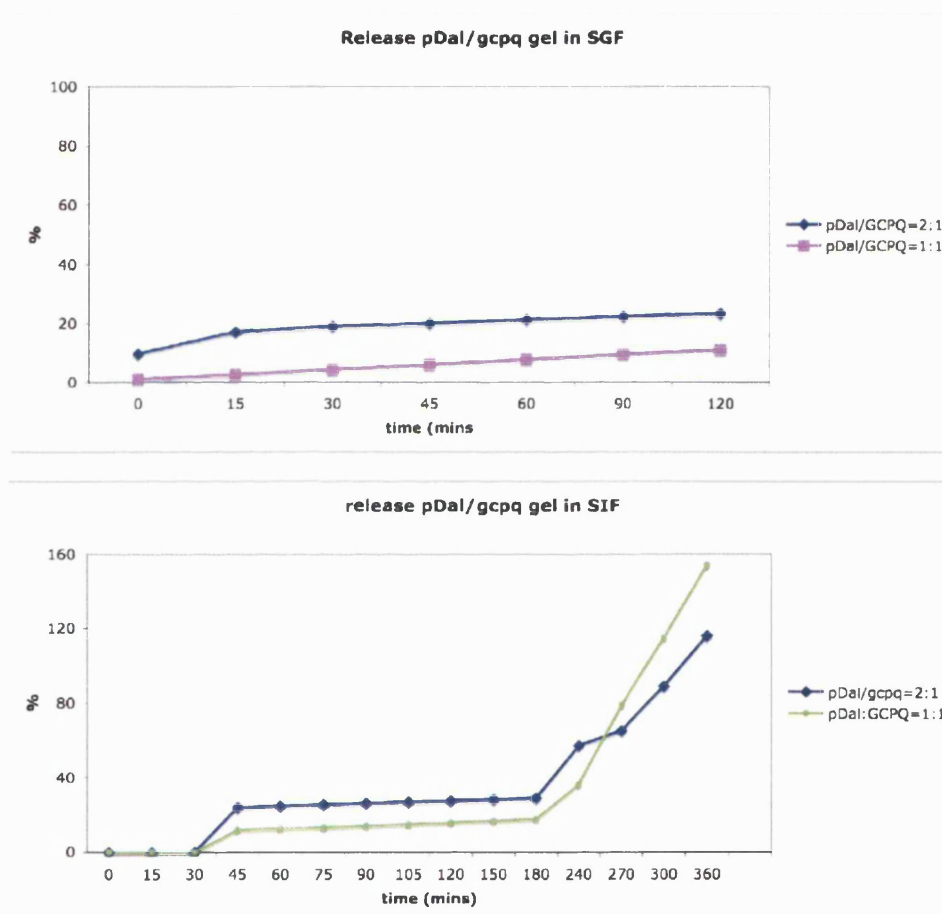


Figure 5.14: Pilot study – release testing of pDal gels in (A) simulated gastrointestinal fluid (SGF) and (B) simulated intestinal fluid (SIF).

A pilot *in vivo* experiment was conducted to evaluate the pharmacokinetics of the nanofibre gel formulations. CD-1 albino mice were divided in four groups and received a dose of 70 mg Kg^{-1} of peptide. Each group was administered respectively

a control of dalargin solution in deionized water, pDal nanofibres gel in deionized water, a control of dalargin/GCPQ solution, and pDal/GCPQ gel having a peptide/polymer ratio of 1:1. Five time points (30 min, 1 hour, 2 hours, 4 hours and 6 hours) were considered and 5 animals per time point were included.

However, when orally administered to CD-1 mice we found absence of pDal levels in plasma, liver and brain samples analyzed with LC-MS. The formulation containing pDal nanofibres alone did not give rise to any level (ng/mL) of pDal in the biological matrices and surprisingly the same result was obtained with the formulation of pDal/GCPQ gel, with a peptide/polymer ratio of 1:1.

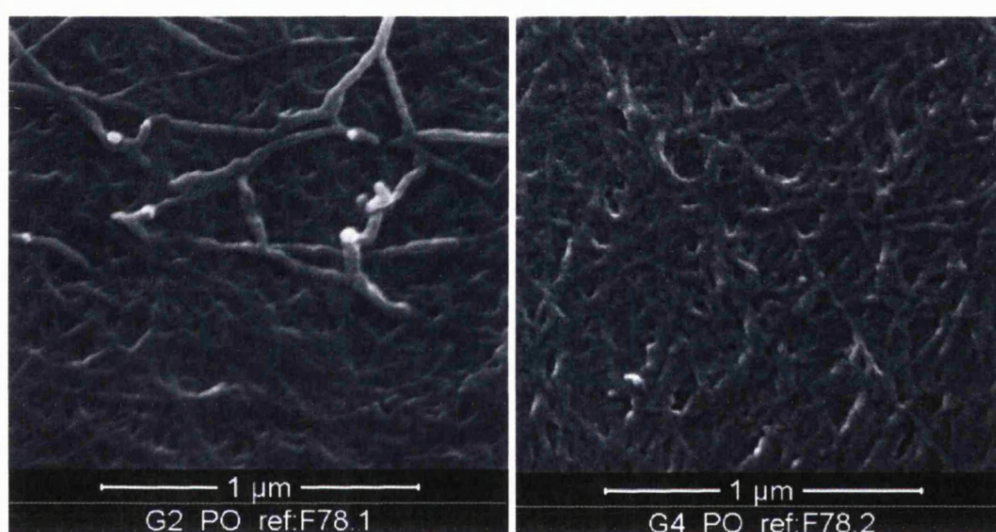


Figure 5.15: SEM images of pDal gel (G2_PO) and pDal/GCPQ gel orally administered to mice to evaluate the oral delivery of peptide.

5.4 Discussion

Self-assembly is a naturally occurring event, however the kinetics of the nanofibril formation mean that self-assembly of peptide amphiphiles into nanofibres it can take days to get to completion (Pashuck and Stupp, 2010b). Nanofibres made of surfactant-like peptides have been prepared with probe sonication and microwave heating, as described in detail in the Chapter 3 of this thesis. While the probe sonication of proteins is already known to cause the formation of fibrillar aggregates (Stathopoulos et al., 2004), to the best of our knowledge this is the first time that nanofibres have been formed using electromagnetic radiation heating.

The high local temperature generated by sonication or by microwave bursts contributes to the single peptide unfolding and enhances the aggregation of the single monomer units into nanofibres by promoting the hydrophobic interaction of the sixteen carbon chains and the formation of H-bonds in the peptide β -sheets structure. It has been observed for α -helical proteins such as BSA (Bovine Serum Albumin) that they undergo conversion to increased β -structure upon sonication (Stathopoulos et al., 2004). We have prepared a self-assembling peptide nanofibre gel applying a rapid microwave heating and cooling cycle to a concentrated dispersion of pDal (Figure 5.13). This nanofibre gel has potential applications as a biomaterial for various applications, e.g. as a drug delivery system.

Thermal analysis of pDal helps to clarify the thermal properties of the monomeric starting material and the influence of these properties on the molecular self-assembly. Thermal analysis also clarifies the range of temperatures to be used for the preparation of these gels that have potential applications as drug delivery systems.

Thermal stability of the collagen like structure of peptide amphiphiles was found to increase as the monoalkyl tail chain length is increased over a range of C₆ to C₁₆ in studies with circular dichroism (Yu et al., 1998).

The freeze dried pDal is a solid phase with the characteristics of an amorphous material, such as the lack of three-dimensional order characterized by the absence of sharp peaks in powder XRD (Chapter 2, Figure 2.21 A), a glass transition and the formation of a glassy solid material upon heating.

DSC analyses (Figure 5.4 A) of the freeze-dried peptide showed three endothermic events, at low temperature a broad peak (peak I), as well as two high temperature endothermic transitions, one sharp peak with onset at 85°C (peak II) which merges with a broader endothermic peak (peak III). Peak I is due to solvent loss, probably entrapped during the freeze-drying process (indeed cooling down the system and heating up again shows that the event is not recoverable-data not shown). Peak (II), with an onset of 85°C (typical of palmitoyl chain melting (Saxena et al., 1999)), is followed by a broad endotherm. Although not conclusively proven, peak III could be a liquid crystal transition (Lechuga-Ballesteros et al., 2003), which is in conflict with the definition of the sample being amorphous. We will return to this apparent dichotomy in the discussion. Upon heating in the DSC, the sample melts and becomes a glassy solid upon cooling to room temperature. The glassy solid, when subjected to

a second DSC heating cycle at the same conditions, showed a step in the baseline typical of glass transition (T_g), confirming the material formed was a glass.

Peak I is a non-thermoreversible process as upon cooling of the sample the transition was not recovered and this was also confirmed by performing an MTDSC scan on the sample (Figure 5.5) where it is observable that the Peak I ends up on the non reversible signal. Annealing the glass formed after the first DSC cycle at a temperature below the T_{ag} for up to 2 weeks showed recovery of the endothermic peak of the alkyl chain melting as well as enthalpy relaxation at the T_g (Figure 5.4 B).

Enthalpy relaxation is a consequence of the amorphous material progressively approaching its equilibrium structure during storage below T_g (Henkel et al., 2007). Molecules in an amorphous system are considered “kinetically trapped”, since the time-scale of the long range molecular interaction is smaller than the experiment scale (thus long term interaction are not recorded in the DSC signal during the experiment). Consequently, the glassy solid system formed during cooling has an excess of enthalpy that is lost during ageing, as the molecules move towards a more stable conformation. The amount of enthalpy lost during ageing is recovered by the sample during the second cycle heating run (Figure 5.4 B) and is a reflection of the molecular mobility in the glassy state. Glasses that have undergone enthalpy relaxation will exhibit enthalpy recovery during heating, which is manifested as an overshoot in the heat capacity near T_g .

Peak II is a true melting event as confirmed by HS-DSC, indeed there is no shift in the range of temperature observed for the event in HS-DSC and in conventional DSC.

Microscopic examination of the freeze-dried powder under cross-polarized filters showed some birefringence, which would not have been expected if the material was a true amorphous glass (Figure 5.7 A, B). A phase transition was observed when the material reached 93°C whereupon birefringence was lost (Figure 5.7 C, D).

A similar observation was noted when the aged glass was studied under the microscope (Figure 5.7E-H). Analyses of the aged glass by XRD showed that the glassy solid is mainly amorphous, as it should be expected, however peaks of weak intensity can be spotted, that might be resolved by employing more powerful techniques, such as SAXS or SANS.

Microwave experiments have highlighted that heating the solution up to the T_g temperature did not result in formation of gels, increasing the heat generated from the electromagnetic radiation was necessary to obtain a gel upon cooling of the solution. The heated solution was left to cool unperturbed at room temperature for at least 30 minutes; alternatively the solution was directly placed in the fridge (5°C) for 10 minutes to produce the gel (Figure 5.10).

Microwave radiation causes the surfactant-like molecules to melt, creating two partially miscible fluids (as the peptidic portion of the molecule is water soluble). However the conformational disorder of the lipid chain due to the water-palmitic tail moiety contact is very high and so the system needs to escape it. We can thus hypothesize that the system rearranges in a three-dimensional ordered array with a bicontinuous micellar cubic phase. For example, lamellar phases formed by biological amphiphiles (e.g. membrane bilayers, one of the ubiquitous lyotropic liquid crystal forms), can escape curvature frustration arising from an increase of temperature by becoming an inverse hexagonal phase formed of inverted cylindrical micelles packed into an hexagonal lattice (Seddon et al., 2006). However, because of the presence of voids in the packing that are available to solvating molecules, a “packing frustration” still exist due to these hydrophobic volume areas that the system cannot tolerate and some chains must deviate from their preferred conformational state in order to eliminate the hydrophobic voids (Seddon et al., 2006). Thus, as for lyotropic liquid crystals, the palmitic chains may rearrange in a 3D ordered array of lamellar bicontinuous micellar cubic phase such that the water-chain contact is minimized determining the formation of a nanofibre gel with nanoporous size as depicted in Figure 5. 16. Macroporus bijels, a bicontinuous cubic phase, have also recently been reported to be formed by electromagnetic radiation heating (Lee and Mohraz, 2010).

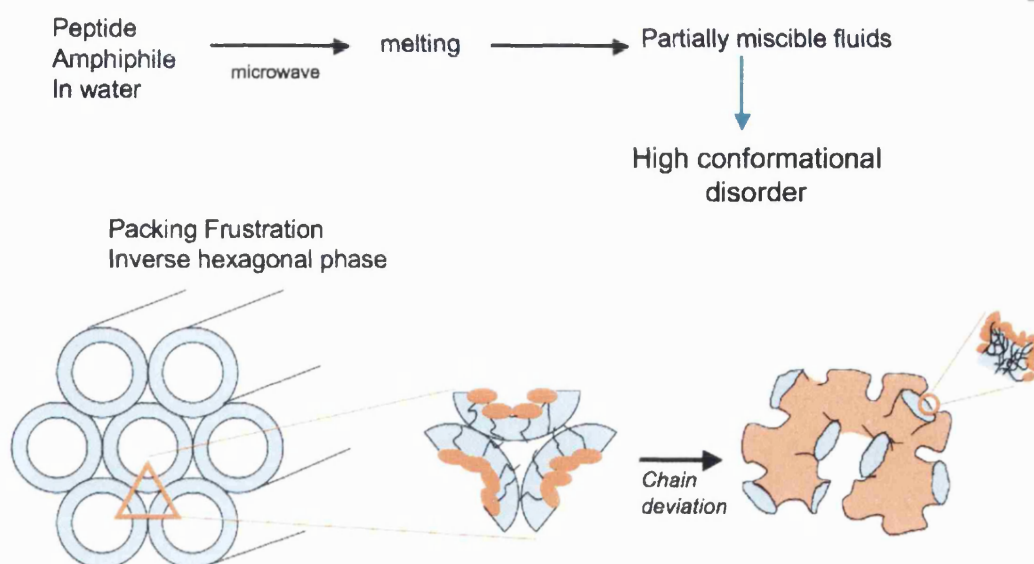


Figure 5. 16: Schematic depiction of the reorganization of peptide amphiphiles in response to the microwave thermal stimulus

When the sample is heated above its T_g or melting temperature there is a concomitant increase in the power supplied by the microwave in order to attain the programmed heating rate (Figure 5.10 B). This is a reflection of the increased molecular mobility (effectively heat capacity) in the sample and is the same phenomenon that underpins analysis by DSC.

In order to investigate whether the peptide structure undergoes chemical degradation under heat treatment, the FTIR was recorded (Figure 5.11) and it is possible to see from the results that there is not chemical denaturation after heating, furthermore the presence of the Amide I band further support the hypothesis of β -sheets between the peptide sequences of the peptide amphiphiles, as already discussed in the Chapters 3 and 4.

The pDal gel sheared between a microscope slide and a cover slide displayed a color pattern when seen under polarized light, however XRD of the gel showed no sharp diffraction peaks (data in Appendix). In order to elucidate the nature of the interactions between the molecules in the tight entangled gel-like network the gel was stained with Congo Red.

Congo Red it has largely been used as diagnostic tool for the detection of amyloid deposits and in general for the detection of the presence of β -sheets (Divry and

Florkin, 1927, Hamley et al., 2010) as it has been shown to interleave between two strands of β -sheets in amyloid fibrils (Jin et al., 2003). The stained sample, under cross-polarized filters, shows the apple-green color associated with the interleaving of the Congo Red into the β -sheets as well as birefringence. Thus the peptide chain contributes to the self-assembling process by forming β -sheets.

Returning to the apparent dichotomy noted earlier, the DSC and XRD data suggest that the glass is amorphous while the microscopy and Congo Red dyeing data suggest the presence of ordered (liquid crystal and β -sheet) regions. Such a dichotomy has been noted in an earlier study of cyclosporine, the first naturally occurring peptide that exists as a thermotropic liquid crystal (Lechuga-Ballesteros et al., 2003). One explanation is that both DSC and XRD measure bulk properties (i.e. they have the resolution only to measure change on a relatively macroscopic scale) and hence neither is sensitive to order on a molecular scale. The microscopic and Congo Red analyses, conversely, are sensitive to molecular structure and hence show evidence of the ordered phases. It is likely, therefore, that the glass formed in the DSC post melting is not truly amorphous but has liquid crystal and β -sheet regions.

The gel form of pDal nanofibres is of high interest as it could be used for the oral or subcutaneous administration of the peptide. However with the formulations of pDal gels investigated in the present work were unable to give measurable concentrations of peptide in blood when orally administered to mice.

In conclusion, this work shows that electromagnetic radiation heating of peptide amphiphiles bearing acyl chains is a fast method of producing peptide nanofibres gels. Molecules with similar amphiphile architecture to pDal could be used to prepare supramolecular assemblies and could offer a simple and cost-effective way to generate viscoelastic materials. An accurate rheological investigation could help to define the exact parameters (i.e. hydrodynamic correlation length, entanglement length, contour length and relaxation time) that the system should aim to possess in order to be exploited for drug delivery applications.

CHAPTER 6

Biological Evaluation of Peptide Nanofibres as Carrier for Brain Delivery

6.1 Introduction

Peptide and proteins are important targets for the drug design of many Central Nervous System (CNS) pathologies; it has been shown that they play a key role in the pathogenesis, the regulation and the symptomatology of a wide number of neurodegenerative diseases (Brasnjevic et al., 2009, Carter et al., 2010a). Many CNS disorders could be treated with peptide-based drugs, these would include Alzheimer disease, stroke/neuroprotection, brain and spinal cord injury, brain cancer, HIV infection of the brain, various ataxia-producing disorders, amyotrophic lateral sclerosis (ALS), Huntington disease, Parkinson disease (PD) and multiple sclerosis (MS)(Pardridge, 2003).

Because neurodegenerative diseases strike primarily in mid- to late-life, as human longevity increases the incidence is expected to soar and it is estimated that people with neurodegenerative disorders will raise up to 100 millions by 2040 {Farooqui, 2010 #76}. It follows that the neuropharmaceutical sector represents an enormously under penetrated market share. Many small biotechnology companies focusing on the development of novel therapeutic peptides have attracted the attention of the big-pharma industries. Only last year (August 2010), Roche signed a drug-development deal worth up to \$1.1 billion with the biopharmaceutical company Aileron Therapeutics (Cambridge, MA) to discover, develop, and commercialize “stapled peptides,” or drug candidates that use peptide-stabilization technology to enhance potency and cell permeability.

The BBB protects the brain from exposure to many substrates, both endogenous and exogenous.

As discussed in Chapter 1, in contrast to the periphery, brain endothelial cells (Figure 6.1) have continuous tight junctions, no fenestrations and very low pinocytic activity, furthermore are surrounded by a basal membrane and extracellular matrix, as well as pericytes and astrocytes foot processes which further form the BBB and mediate its permeability (J F Deeken, 2007). Peptide and proteins have a highly restricted access to the brain because of the presence of the blood brain barrier (BBB).

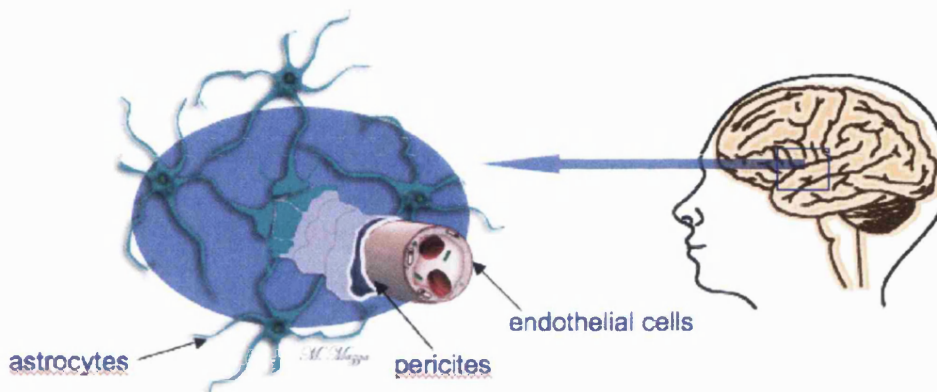


Figure 6.1: Schematic depiction of the BBB and its accessories components.

Different strategies to overcome the BBB have been implemented, each having its advantages and drawbacks, but in most cases at the present time in clinics it is still necessary to administer the drug into the brain by means of invasive techniques such as intracerebral, intracerebrovascular or intratechal administration (Wang et al., 2002b, Rainov et al., 2008), convection enhanced drug delivery (Rainov et al., 2008) or transient blood-brain barrier disruption (Madsen and Hirschberg, 2010).

Using convection-enhanced delivery the drug is infused directly into the brain tumor through strategically placed catheters; this technique has progressed from animals to clinical trials in the past 12 years (Ferguson et al., 2007, Debinski and Tatter, 2010). Polymer-based local drug delivery has been approved by the FDA since 1996 when the carmustine wafers were introduced into the clinics for the treatment of recurrent glioblastoma multiforme, but it still requires surgical *in situ* implantation (Wang et al., 2002a).

Drugs can also be delivered to the brain by intraventricular infusion using an Ommaya reservoir, a plastic reservoir implanted subcutaneously in the scalp and connected to the ventricles within the brain via an outlet catheter that pumps the drug by manual compression of the reservoir through the scalp (Misra et al., 2003, Reeve and Todd, 1990)

The difficulty in delivering therapeutics drugs to the CNS, the paucity of therapies available for most neurological disorders, and the difficulties related to the invasive methodologies employed in the clinic open the way for translational research to address the problem of brain delivery and should lead to research in advanced strategies for brain delivery.

A non-invasive, chemically-based strategy employed in the past decades for brain delivery is the prodrug formulation, where a hydrophobic moiety is chemically linked to a molecule in order to increase its lipophilicity and give rise to a compound able to cross the BBB via passive diffusion. However, this approach results in the formation of a derivative with increased molecular weight, which is unlikely to get across the brain endothelial cell membranes because the permeation of drugs through a biological membrane decreases exponentially as the molecular size of the drug increases (Fischer et al., 1998), thus the molecular weight of most CNS acting molecules, which become clinical compounds show a molecular weight threshold of 400-500Da (Lipinski, 2000).

With the advent of the bionanotechnologies much research has been carried out to template carriers able to reach the brain parenchyma through alternative routes to passive diffusion. Nanocarriers injected by the systemic route and used for drug delivery have to possess some essential characteristics. A general overview of the nanotechnologies exploited for delivery of therapeutics across the blood-brain barrier (BBB) has been discussed in Chapter 1 of this thesis.

The efficacy of nanocarrier systems to deliver across the BBB has been often assessed using dalargin as model drug (Schroeder et al., 1998, Ramge et al., 1999, Kreuter et al., 2003, Das and Lin, 2005, Rousselle et al., 2003). Dalargin is an opioid receptor agonist that does not cross the blood brain barrier, because it is a hydrophilic hexapeptide (Kalenikova EI, 1988). Thus, when enabled by nanotechnology engineering to reach its targets into the brain parenchyma it exerts its pharmacological

antinociceptive effect. Data concerning the selectivity of this enkephalin analogue for the μ , δ and κ opioid receptors are rather contradictory, Korobov *et al.* reported a mixed μ/δ activity, while Pencheva and collaborators showed a high selectivity and high potency of dalargin for μ -opioid receptors (Pencheva et al., 1999). The agonist response of dalargin on the opioid receptors determines an antinociceptive effect in pain relief tests conducted on animal models. Dalargin is a Leu-enkephalin analog comprising a D-alanine in second position in order to prevent enzymatic degradation and an arginine at the C-terminus. First synthesized as an anti-ulcer compound and employed in the USSR as alternative to misoprostol (Dajani et al., 1991), it is often employed as a model compound to study the efficacy of nanocarriers in delivering drugs across the BBB.

Here we report on the investigation of nanofibres made of the self assembling peptide amphiphile pDal, a lipophylic derivative of dalargin, as an approach to brain delivery. This approach has never been attempted before. The toxicity and the cell uptake of the peptide nanofibre delivery system have been evaluated *in vitro* and the ability to deliver the peptide to the brain established *in vivo* via pharmacokinetics, pharmacodynamics and *ex-vivo* imaging studies.

6.1.1 Cell Viability Assay

The cell viability after exposure to pDal nanofibres formulations was determined by MTT (3-(4,5-dimethylthiazol-2-yl)-2,5-diphenyltetrazolium bromide salt) assay, which is the most commonly employed procedure for detection of cell proliferation and cytotoxicity (Mosmann, 1983).

MTT is a water-soluble substance that is converted to the insoluble formazan crystals by mitochondrial enzymes in living cells. The reduction of MTT is an index of the redox status of the cell: the amount of formazan produced indicates the reductive potential of the cytoplasm and the cell viability (Wilson, 2000). Yellow water soluble MTT is taken up by endocytosis by the living cells, reduced by mitochondrial dehydrogenase in the endosomal/lysosomal compartment, and then transported to the extracellular space through exocytosis in the form of needle-like purple water insoluble formazan. A solubilizing solution (i.e. DMSO) is added to dissolve the insoluble formazan into a colored solution, its absorbance can then be quantified

using UV spectrophotometry (Wilson, 2000).

The concentration of formazan crystals is directly proportional to the number of living (viable) cells, as the reduction takes place only when mitochondrial reductase enzymes are active (Mosmann, 1983) (Figure 6.2).

Conditions and parameters of the MTT assay vary widely. The amount of formazan produced depends upon a number of parameters including the initial concentration of MTT used, incubation time, method of extraction and other physiological attributes of the cell line. For example, increased mitochondrial enzyme activity on drug-treated cells can influence formazan production (Mosmann, 1983).

It is good practice, to do a preliminary screening to check that long incubation time will not determine formation of big crystal of insoluble formazan, because these will be more difficult to redissolve. Formazan crystals produced by treated cells can be visually checked under an optical microscope, this will help to establish the incubation time to be used for the experiment.

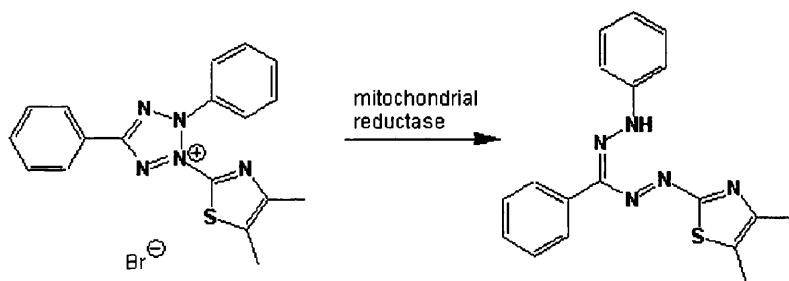


Figure 6.2: Enzymatic conversion of MTT into formazan by mitochondrial reductase in living (viable) cells

The main advantages of the colorimetric assay are its rapidity and precision, (Mosmann, 1983).

6.1.2 Cell Uptake of pDAl Nanofibres Studied by Electron Microscopy

Transmission Electron Microscopy (TEM) provides the necessary characterization method that enables accurate structural and functional analysis of the interactions

occurring during the subcellular events that take place at the interface among nanosized carriers and cell membrane surfaces in studies of endocytosis (Zensi et al., 2010).

An *in vitro* cell culture model was chosen for endocytosis studies, consisting of bEND5 monolayers cells, to evaluate the ability of peptide nanofibres to act as brain drug delivery systems. The bEND5 cell model has been established by immortalization of primary cells of Balb/c mice. The bEnd5 cells have endothelial-like morphology, in fact they are positive for endothelial specific proteins (PECAM-1, Endoglin, MECA-32, Flk-1). Endothelial cell line bEnd5 expresses important tight junctional proteins, ZO-1, occludin and claudin-1, as well as the transporters P-glycoproteins (P-gp), NaK₂Cl Cotrasporters, GLUT1, and most Protein Kinase C isoforms and form a tight barrier that compares to well-established *in vitro* BBB models, such as the bovine brain endothelial cell model BBMEC (Yang T, 2007).

6.1.3 Measuring Compound Permeation into the Brain

Several assays are used to quantify the uptake of drugs into the CNS, i. e. microdialysis, jugular bulb blood sampling, imaging (Upton, 2007). Most of them measure the unidirectional uptake of the molecules, giving no information about the fate of the therapeutics after its penetration in the brain tissue (van Rooy et al., 2011a, Upton, 2007).

Molecules could be in fact subject to cellular binding, degradation and/or efflux. The intravenous injection is one of the most employed techniques for brain uptake studies because it involves fully physiological conditions (Bickel, 2005).

Information on the extent of penetration into whole brain can be obtained by determining the brain/plasma ratio, however this does not provide information about the rate of brain penetration (Reichel, 2009a). For this calculation the total brain concentration is measured using brain homogenates, the presence of drug remaining in the brain vasculature is not taken into account, and since homogenization destroys all tissue compartments, this method cannot provide information on compound levels in any specific effect compartment (Reichel, 2009a).

One way to remove the intravascular content of drug is to flush the brain with heparinized buffer before the brain is taken out and homogenized. Alternatively, a correction of the intravascular content can be applied. Several studies with vascular

markers (i.e. radiolabelled sucrose or inulin) have established that the brain vascular volume for mice and rats is usually about 12 $\mu\text{L}/\text{gram}$ of brain (Murakami et al., 2000, van Rooy et al., 2011a). This value can be then used as an estimate to subtract from the total brain quantity of the compound of interest detected by means of an analytical technique (i.e. LC-MS). The quantity of a compound penetrating into the brain parenchyma can thus be calculated using the following equations (van Rooy et al., 2011a)

$$Q_{\text{corr}} = Q_{\text{tot}} - V_v C_{p(T)}$$

Where

Q_{tot} is the total quantity of compound detected in brain, including the vascular content (mass/g brain)

V_v is the brain vascular volume (mL/g)

$C_{p(T)}$ is the concentration of compound in the blood at the time point T (mass/mL).

6.1.4 Liquid Chromatography-Mass Spectrometry (LC-MS) in Pharmacokinetics Studies

The LC-MS apparatus used in the pharmaceutical industry as “gold standard” for distribution studies of drugs is API LC-MS; API (atmospheric pressure ionization) mass spectrometry produces analyte ions at atmospheric pressure (Brewer and Henion, 1998).

There are two common alternatives for producing ions at atmospheric pressure for LC/MS applications. They include atmospheric pressure chemical ionization (APCI) and electrospray. As these ions are guided inside the mass spectrometer vacuum system, the bulk of the HPLC effluent is excluded from this region.

The electrospray LC/MS interface produces gas-phase employing a coaxial nebulizing gas of nitrogen or air to facilitate the use of aqueous eluents and higher HPLC flow rates. This pneumatically assisted electrospray LC/MS interface (Figure 6.3) readily accommodates the total HPLC effluent of typically 0.05-0.40 mL/min, which is passed through a capillary housed inside an external tube through which a high linear velocity of nebulizing gas is coaxially directed. An applied high voltage on the inner

capillary coupled with the coaxial nebulization gas produces gas-phase ions from very polar compounds by an ion evaporation process. These ions are produced very close to a small orifice housed in the front of an API mass spectrometer, where the ions are sampled and mass- analyzed (Brewer and Henion, 1998).



Figure 6.3: Pneumatically assisted electrospray ionization. Adapted from (Brewer and Henion, 1998)

Low-energy analyte ions are produced at atmospheric pressure which are representative of the relative molecular mass (molecular weight) of the compound under investigation. To obtain the desired fragmentation for added structural information and qualitative identification of drugs, their active product intermediates and metabolites or the very high selectivity required for rapid bioanalytical assays of complex samples, tandem mass spectrometry can also be used.

For quantitative analyses, another very common use of LC-MS experiments is called selected reaction monitoring (SRM), as represented in Figure 6.4. In these experiments one monitors only a “selected” MS/MS or CID (collision-induced dissociation) transition(s) rather than a full-scan acquisition of all product ions produced from the precursor ion.

SRM LC/MS was used for the pharmacokinetic studies of Dalargin and pDal nanofibres formulations discussed here.

As the components in the HPLC effluent elute to the API tandem mass spectrometer, the first quadrupole is set to continuously monitor the precursor ion of the selected target analyte(s). These are typically the parent drug and its metabolite(s). In fact, several different precursor ions may be monitored in rapid succession. As each selected precursor ion is focused into the collision cell (Figure 6.4 A) fragmentation occurs, the third quadrupole is set to monitor only one characteristic product ion from

each compound under study. The relationship between m/z of the parent compound and the m/z of the product ion is called a precursor-product ion transition and represents a molecular characteristic that is unique to the specific molecule under the set experimental conditions.

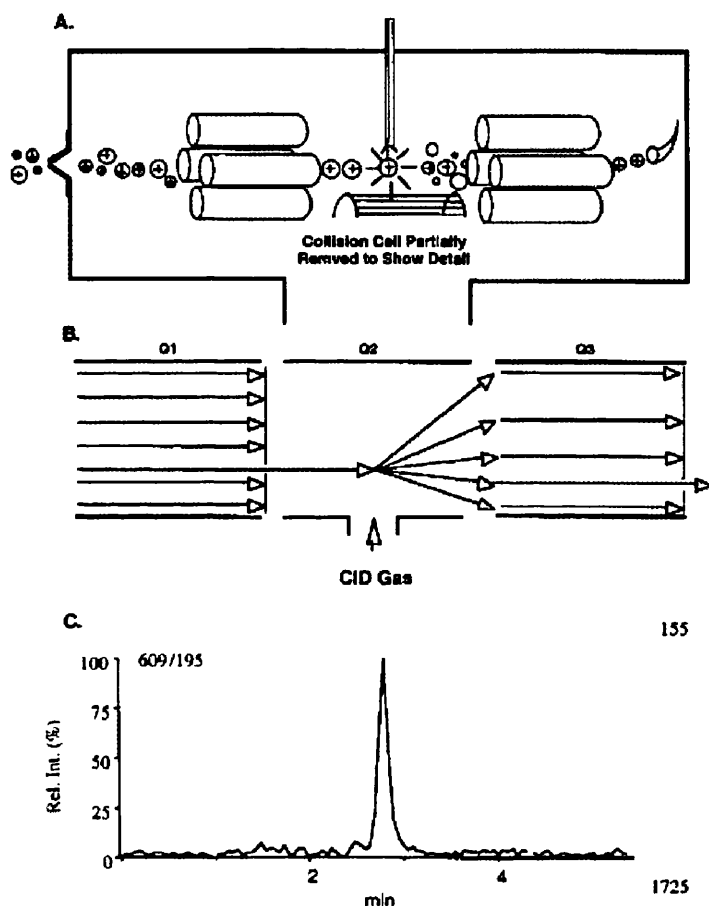


Figure 6.4: Schematic representation of an SRM LC/MS experiment. (A) Atmospheric triple quadrupole mass spectrometer. (B) Example of SRM precursor-product experiment. (C) Example of chromatogram for SRM LC/MS experiment. Adapted from (Brewer and Henion, 1998).

The combination of this transition with the HPLC retention time of the molecule followed during the analysis determines high selectivity for the compound. When this kind of experiment is carried out on an analyte in the presence of high levels of biological matrix components, a very high gain in signal-to-noise ratio is obtained, due to the ability of the first quadrupole to “select” the parent m/z ion from all other ions present. This is depicted in Figure 6.4B, where one mass-to-charge ratio ion denoted by the longer arrow in Q1 is shown to be “selected” from all the other

components. Following the fragmentation of this selected ion in Q2 only one product ion is selected to be monitored by Q3 although additional product ions that may be present could also be monitored in rapid succession. This capability of SRM LC-MS provides a significant reduction in chemical noise and thus an improvement in the overall signal-to-noise ratio. The combination of the precursor-product ion transition and the HPLC retention time (Figure 6.4 C) are highly selective for the analyte that has to be detected.

There are several benefits afforded by the API SRM LC-MS process described above. Because the SRM LC-MS technique has the ability to select ions characteristic of the target analyte(s) from the matrix components, less sample preparation and method development may be needed. For the same reasons, much shorter HPLC run times may be used. Thus, instead of 15-30 min HPLC/UV runs, one often employs 2-5 min run times for API SRM LC/MS applications. With the advent of UPLC systems, LC-MS apparatus have been able to reach analysis times of less than 2 minutes (Brewer and Henion, 1998).

6.1.5 Coherent Raman Scattering (CRS) Imaging: Label Free Detection Imaging

CRS imaging offers a label free microscopy method of detection. CRS refers to both Coherent anti-Stokes Raman Scattering (CARS) (Zumbusch and Muller, 2007) and Stimulated Raman Spectroscopy (SRS) (Freudiger CW, 2008).

In CRS laser beams at two frequencies, defined as the pump, ω_p , and the Stokes, ω_s , are used to visualize the sample. When the difference frequency between the two laser beams is tuned to match an intrinsic molecular vibrational frequency in the sample ω_{vib} , several non linear interactions occur: new light is generated at the anti-Stokes frequency, $\omega_{as} = 2\omega_p - \omega_s$, by the CARS process, and some intensity is transferred from the pump to the Stokes beam by the SRS process (Saar et al., 2011). Both processes offer chemical selectivity and high spatial resolution, but SRS offers more desirable contrast and is free from image artifacts that plague CARS imaging (Saar et al., 2011).

SRS allows three-dimensional sectioning of samples and monitoring of label-free

molecules in *ex vivo* tissue samples (Freudiger CW, 2008) and more recently also *in vivo* (Saar BG, 2010).

The working principles of SRS are summarized in Fig 6.5. The signal is generated by focusing two synchronized ultra-fast pulse trains (Figure 6.5 C), the Stokes beam and the Pump beam, into a sample with a difference in frequency matched to a Raman active mode of a molecular species of interest. SRS leads to an intensity increase in the Stokes beam (SRG) and an intensity decrease in the pump beam (SRL), as represented in Figure 6.5 B. The Stokes beam is modulated at high frequency (MHz), at which the resulting amplitude modulation of the pump beam due to SRL can be detected. The transmitted or reflected pump beam is filtered and detected by a large-area photodiode (PD), as schematized in Figure 6.5 D. The SRL is measured by a lock-in amplifier to provide a pixel of the image. Three-dimensional images are obtained by raster-scanning the laser focus across the sample, and microspectroscopy can be performed by automated tuning of the pump wavelength.

A considerable gain in peak resolution is achieved using the more complex set up of Stimulated Raman Spectroscopy compared to the more classic Coherent Anti-Stokes Spectroscopy (CARS) Imaging, in fact the CARS spectrum can present peak shift, dispersive shape and nonresonant background from the original Raman signal, as explained by Freudiger and co-workers (Freudiger CW, 2008) and summarized in Figure 6.5 F,G.

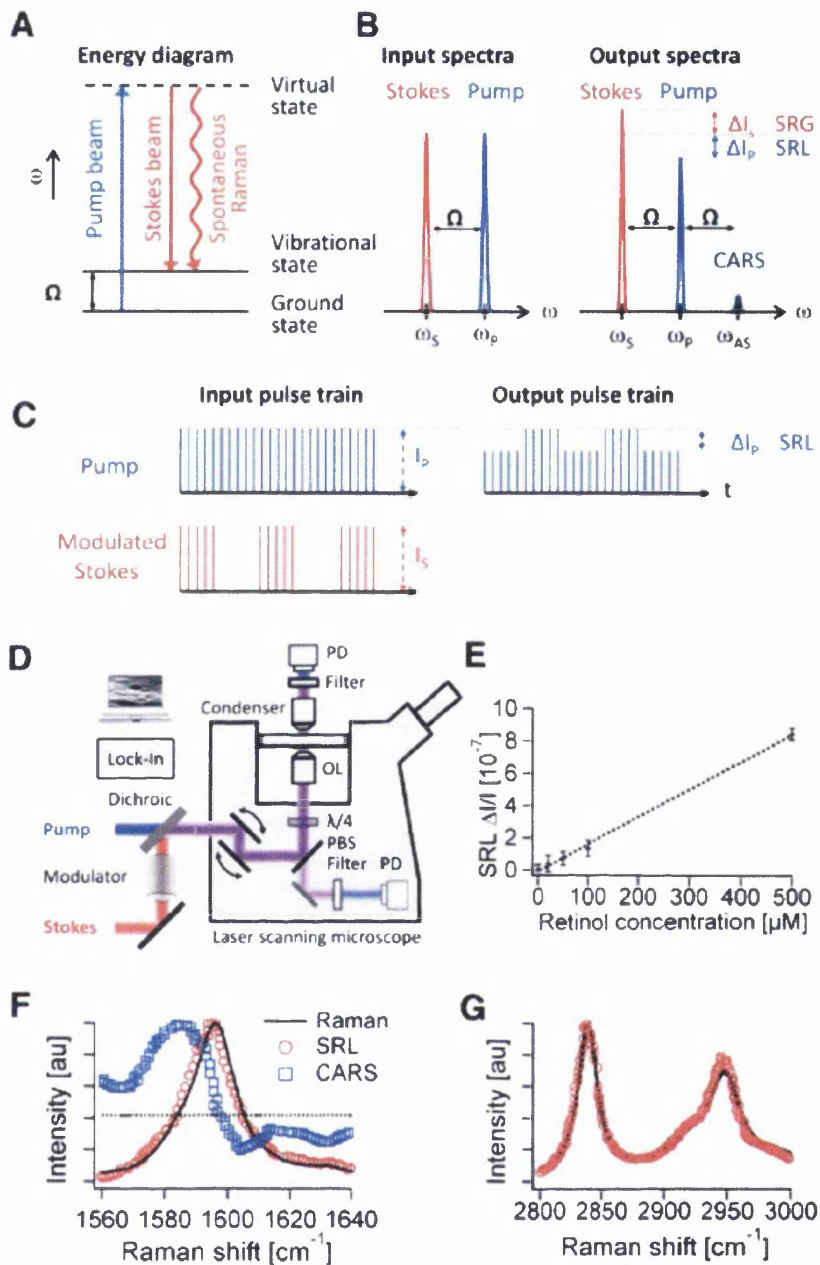


Figure 6.5: Working Principle of SRS microscopy: (A) Energy diagram for SRS. (B) Input and output spectra of SRS. (C) SRL detection scheme.. (D) SRL microscope with both forward and epi detection. (E) Linear dependence of SRL on concentrations of retinol in ethanol at 1595 cm^{-1} . (F) Agreement of SRL spectrum (red circles) with the spontaneous Raman spectrum (black line) of the Raman peak (1595 cm^{-1}) of 10 mM retinol in ethanol. The distorted CARS spectrum (blue squares) exhibits a typical peak shift, dispersive shape and nonresonant background. (G) Agreement of the more complex SRL spectrum of methanol (red circles) with the spontaneous Raman spectrum (black line). Reproduction from (Freudiger CW, 2008).

6.1.6 Pharmacodynamics: Pain Relief Studies in Animal Models

Drugs that normally cannot cross the blood-brain barrier could potentially be encapsulated and delivered to the brain by means of different nanotechnology platforms. The effect of the drug in the brain can be monitored through behavioral tests thus assessing the brain delivery of the carrier system. One way to assess brain delivery via nanoparticles is by employing nociceptives tests.

The assessment of nociception in animals can be obtained only by indirect methods, as obviously animals are unable to communicate. For testing the potency of analgesic drugs, several nociceptive tests have been developed for animals. The International Association for the Study of Pain (IASP) established that pain is defined as “an unpleasant sensory and emotional experience associated with actual or potential tissue damage or described in terms of such damage” (Le Bars et al., 2001).

Different nociceptive tests depend on the choice of the pain stimulus source, which can be of a different nature, thermal, electrical, mechanical or chemical (Figure 6.6), but all are based on the determination of a negative sensorial experience related to tissue damage that generates an avoidance behaviour response to the original stimulus.

	Thermal	Mechanical	Chemical	Electrical	
				Long Trains	Single Shocks or Short Trains
Phasic pain models	Tail-flick test Paw withdrawal test Hot-plate test	Randall and Selitto	Mechanical stimulation following chemical sensitization (carrageenin, capsaicin, etc.)	Tail Flinch-jump test	Tail Dental pulp Limbs
Tonic pain models		Distension of hollow organs	Intradermal injections (formalin test) Intraperitoneal injections (writhing test)		

Figure 6.6: Summary of principal animal models of acute pain (Le Bars et al., 2001)

In the present work a thermal stimulus deriving from a hot water bath was used as method to test analgesia. Thermal stimuli applied to the animal tail in the case of rodents causes stimulation of the tail skin but not of muscular or visceral tissues. Thermal stimuli are reported to be more selective for cutaneous receptors, because they determine the direct excitation of thermosensitive and nociceptive peripheral axons (Le Bars et al., 2001), furthermore the immersing the tail in hot, soaking water results in an almost immediate increase in tail skin temperature by comparison to

other heat sources as summarized in Figure 6.7 C.

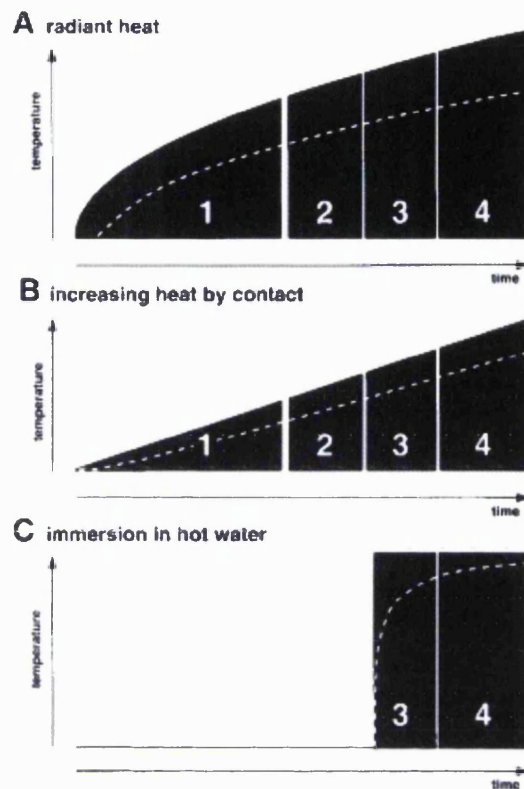


Figure 6.7: (A) The temperature of the skin surface increases in proportion to the square root of time, when subject to a constant-power heat source. (B) increase in temperature can be proportional to time when contact thermodes are used. (C) when part of the body is immersed in a hot water, the temperature of the skin almost immediately achieves the temperature of the bath. In this case the increase in temperature within the skin (broken white line) will be smoother and more gradual in comparison to the previous two heating sources. Adapted from (Le Bars et al., 2001).

6.2 Methods

6.2.1 MTT assay

Cell viability was evaluated by using a [3-(4,5-dimethylthiazol-2-yl)-2,5-diphenyltetrazolium bromide] (MTT) assay. The experiments were carried out in triplicate. Brain human glioma cells U87GM were cultured in 75 cm² flasks (TPP, Switzerland) with Dulbecco Modified Eagle Medium (DMEM) supplemented with 10% Fetal Bovine Serum, L-glutamine (1% w/v) and sodium pyruvate (1mM). Briefly, cells were seeded at an initial density of 5x10³ cells/mL in 96-well plates (NUNC, Roskilde, Denmark) and incubated at 37°C, with 5% CO₂ for 24 hours. The cells were then treated with nanofibre formulation (3 mgmL⁻¹), GCPQA micelles (5 mgmL⁻¹) and pDal nanofibres/GCPQA formulation (2.5:7.5 mgmL⁻¹).

For pDal nanofibre formulation freeze-dried pDal (12mg) was suspended in deionized water (1mL), the suspension was probe sonicated (50% output of the sonicator) for 15minutes to form nanofibres using a probe sonicator (MSE Soniprep 150). From the stock solution an aliquote (0.25 mL) was diluted to 1mL with supplemented DMEM. All the other concentrations were prepared by dilution. For GCPQA micelles the polymer (20 mg) was dissolved in 1mL of deionized water, the solution was subsequently probe sonicated (50% output of the sonicator) for 15minutes to form micelles. From the stock solution an aliquote (0.25 mL) was diluted to 1mL with supplemented DMEM. For pDal nanofirbes/GCPQA formulation 5mg of freeze dried pDal were suspended in 0.5mL solution of GCPQA (30 mgmL⁻¹) in Millipore water, the suspension probe sonicated (50% output of the sonicator) for 15 minutes to form the final formlation containing nanofibres. . From the stock solution an aliquote (0.25 mL) was taken and diluted to 1mL with supplemented DMEM. All the other concentrations were prepared by dilution.

For each formulation tested three 96-well plates were seeded. Cells (5*10³ per well) were incubated after each treatment for 24 hours. After treatment, MTT was added to each well at a final concentration of 500 µgmL⁻¹, and the cells were incubated for 1.5 h at 37 °C. The cells in the first column were lysated with 1% Triton. The medium was then removed, and the formazan crystal dissolved with dimethylsulfoxide (DMSO). The formazan reaction product was quantified spectrophotometrically at

570 nm using a ELX-808 absorbance microplate reader (Bio Tek Instruments, Inc, USA). The results are expressed as percentage cell viability (%) calculated as

$$\text{Cell viability \%} = \frac{\text{Well absorbance} - \text{Mean absorbance of the Triton treated wells}}{\text{Mean absorbance of the untreated cells}} \times 100$$

6.2.2 TEM Studies of Nanofibres Endocytosis

Cells Culture

To simulate the blood brain barrier in vitro, mouse brain endothelial cells bEnd5 were used. The bEnd5 cell line is a BBB in vitro model which has been established from brain endothelial cells of BALB/c mice. Immortalization has been carried out by infection of primary cells with retrovirus coding for the Polyoma virus middle T-antigen.

The cells used for this study were purchased from the Health Protection Agency (cat no: 96091930) and were at passage 19 for experiments.

The bEnd5 cells were grown at a density of 4×10^4 cells/cm² on 4 well plates without any specific coating. Once the cells had reached confluence were incubated with a suspension of pDal nanofibres (0.5 mg mL^{-1}) for 90 and 120 minutes long at 37°C and 200 rpm. After the specified time of incubation the cells were washed with cell culture medium to remove all residual nanoparticles remaining in at the cell surface.

Electron Microscopy (EM) sample fixation

EM was used to visualise the pDal nanofibres in the stock solution and also to investigate the uptake of the pDal nanofibres by the bEnd5 cells. Imaging was performed at Imaging Facility at the Guy's Campus, King's College, London, in collaboration with Dr Larisa Mihoreanu.

Cell monolayers were fixed with a fixative solution containing glutaraldehyde (2.5% w/v) in sodium cacodylate buffer (0.1 M) for 2 h at room temperature. Subsequently, cells were and washed in cacodylate buffer to remove the fixative. Postfixation was performed with osmium tetroxide (1% w/v) in cacodylate buffer (0.1 M) for 2 h to stabilise the lipids and membranes of the cells. Samples were embedded in TAAB

Embedding Resin (TAAB Laboratories Equipment Ltd, Berks, UK) and sections of 75 nm up to 110 nm were cut and double stained in uranyl acetate 50% ethanol saturated solution. Images were viewed with a Hitachi H7600 TEM microscope at 75 kV accelerating voltage.

6.2.3 Pharmacokinetics Study

In vivo experimental setup

ICR (CD-1) male out bred mice (18-24g, 4 weeks old, Harlan, Oxon, UK) were used for the pharmacokinetics evaluations. The animals were housed in groups of 5 in plastic cages in controlled laboratory conditions with ambient temperature and humidity maintained at ~22°C and 60% respectively with a 12-hour light and dark cycle (lights on at 7:00 and off at 19:00). Food and water were available *ad libitum* and the animals acclimatised for 5-7 days prior to any experiments in the Animal House, School of Pharmacy, University of London (London, UK). Animals were only used once and were acclimatised in the testing environment for at least 1 hour prior to testing. All experiments were performed in accordance with the recommendations and policies of the Home Office (Animals Scientific Procedures Act 1986, UK) and the Ethics Committee of the School of Pharmacy, University of London guidelines for the care and use of laboratory animals.

Groups (n = 5) of animals were administered either: NaCl (0.9% w/v), Dalargin, pDal nanofibres, Dalargin/GCPQA, and pDal nanofibres/GCPQA. In the last two groups the ratio peptide to polymer was 1:1.5. Animals received a dalargin dose of 30mgKg⁻¹ and sodium chloride (0.9% w/v) was used as the disperse phase. All formulations were prepared by vortexing (WhirliMixer, Fisherbrand) and then by probe sonication (MSE Soniprep 150) with the instrument set at 50% of its maximum output for 20 minutes. The volume of injection was 0.2 mL per 25 g of mouse weight. At various time points (3, 10, 30, 60, 90, 120 and 240 minutes) after administration, animals were killed and their brain, liver and plasma taken for analysis.

Samples Handling

Brain and Livers were immediately frozen in liquid N₂ then stored at -80 °C until the day of analysis. Plasma was obtained by cardiac puncture following euthanasia. Blood samples (0.4 - 0.8mls per mouse) were collected and transferred into a sterile tube

spray coated with tripotassium ethylenediamin tetraacetic acid (K3, 3.6mg) medical grade (3 x 75mm K3E Vacutainer ©, PET tubes, BD Biosciences, Oxford, UK) and maintained on ice (4°C) till centrifugation. Plasma was obtained as the supernatant after centrifugation of blood samples (1, 600 g for 15 minutes at 4°C) in a Hermle Z323 centrifuge (Hermle Laborteschink GmbH, Germany), and was pipetted into 1.5 mL Eppendorf tubes and stored at -80°C until the day of analysis.

6.2.4 Extraction and Sample Preparation for LC-MS Analysis

On the day of analysis all plasma, brain and, liver samples were removed from the freezer and thawed. The brain and liver weights were determined and 2mL water per g of tissue was added to each sample (equivalent to 2 g of solvent to 1g of tissue). All brain and liver samples were homogenised using the Tomtec Autogeizer (cutter). Aliquotes of plasma samples (50 µL), once thawed, were placed into 1.5mL Matrix tubes. Aliquotes of brain and liver samples (100 µL), once homogenised, were sub-aliquoted (100 µL) into 1.5mL Matrix tubes. The extraction volume was 250 µL, the internal standard concentration (Aricept, GSK) was 10 ng/mL. Ethanol (50 µL) was added to all samples. Appropriate extraction volume (250 µL) of working "IS" solution added to all standards and samples. Samples were shaken for 20mins on a vortex mixer then centrifuged for 15 minutes at 2,465 g and the supernatant reserved for LC-MS analysis.

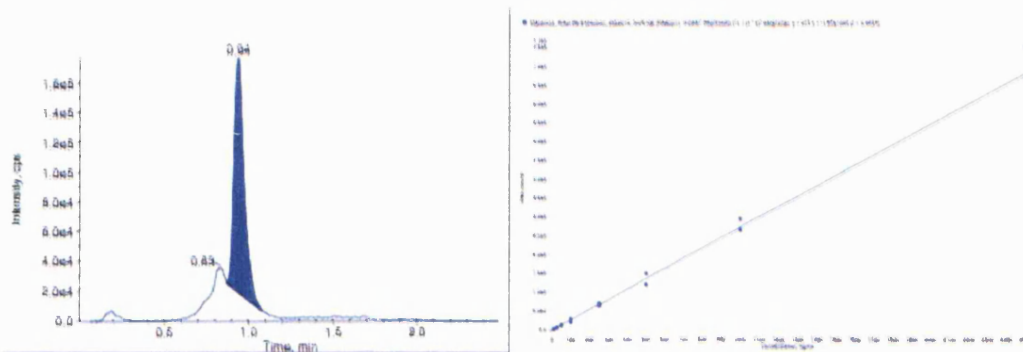
6.2.5 LC-MS Analysis

Analyses were carried out at the Neurosciences Centre of Excellence for Drug Discovery, GSK, Harlow, UK. Analyses were carried out on a Mass Spec Instrument (Applied Biosystems API4000, Mode of operation: Positive-ion / Turbo Ion spray, Source Temperature: 625°C, Software version: Analyst 1.4.2, Multiple Reaction Monitoring Transitions for Dalargin: 726.6 -> 136.2, Palmitoyl Dalargin 964.8 -> 136.2, [D-Ala2]-Leucine 570.4 -> 136.1, Pump Instrument Type: JASCO XLC, HPLC Column (type/size): Thermo Gold (Aqua) 30 X 3mm, pore size = 3µ, Column temp (°C) = 50°C, Flow rate = 1.0 mL min⁻¹, Volume split from LC into source: No split, Run time = 2.5 min; Injection volume = 20 µL, Solvent A: 10mM Ammonium

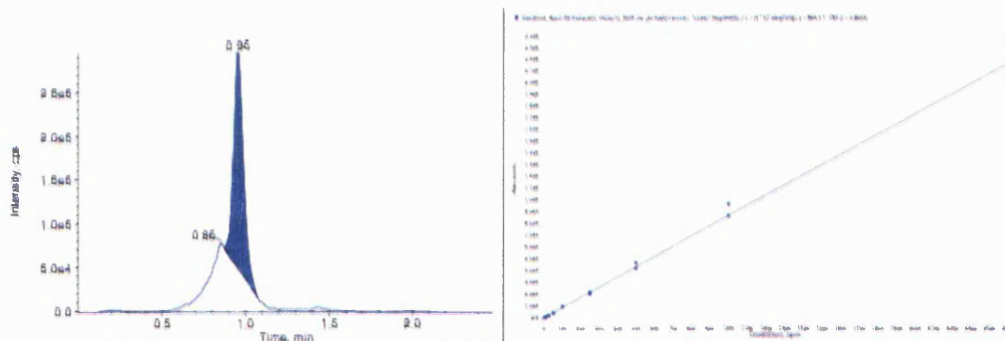
acetate , Solvent B: Methanol, Autosampler Instrument Type: Presearch PAL CTC Autosampler.

Gradient elution:

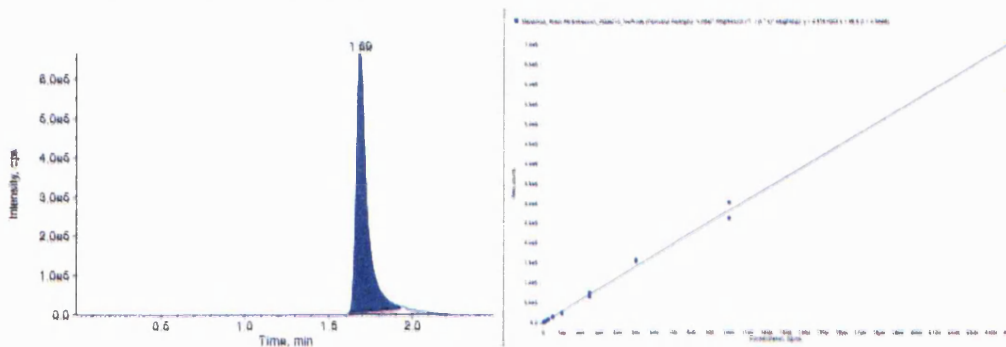
Time (min)	Solvent B (%)	Flow Rate (mL/min)
0	20	1.0
0.8	90	1.0
1.8	90	1.0
1.81	20	1.0



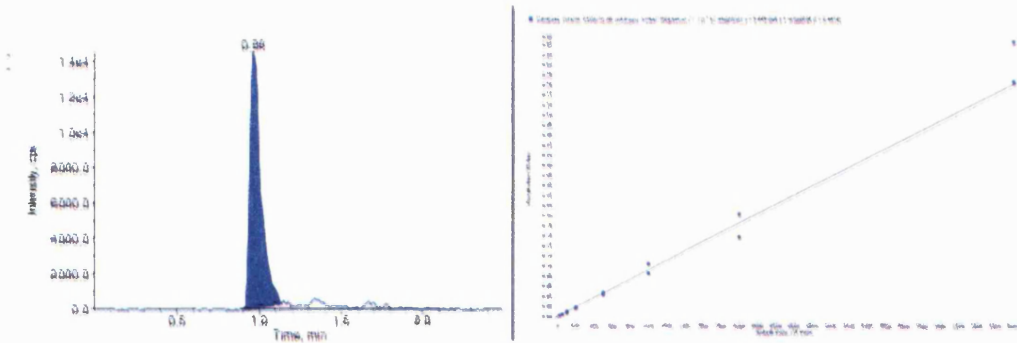
Dalargin peak (726.6/136.2 amu) extraction from brain



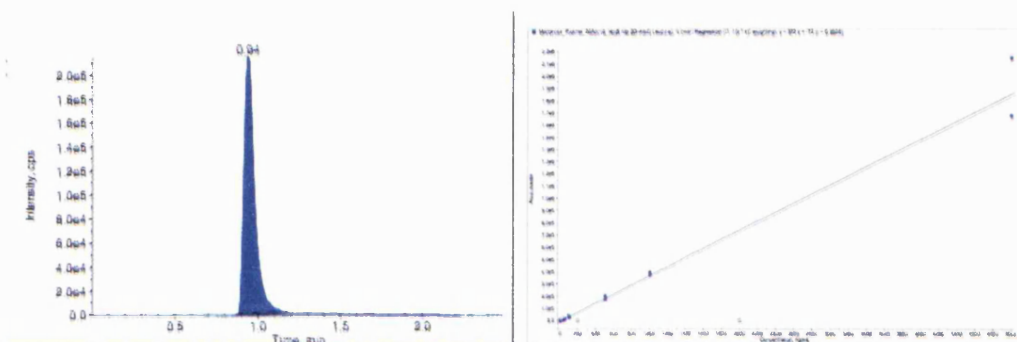
D-Ala-Leu Enkephalin peak (570.4/136.1 amu) extraction from brain



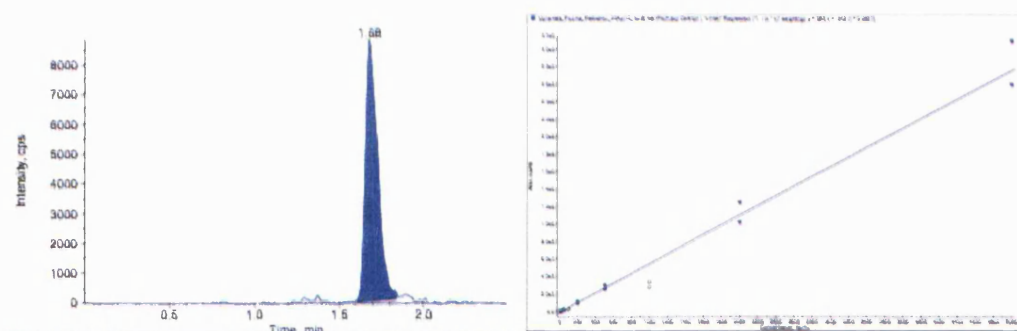
pDal peak (964.8/136.2 amu) extraction from brain



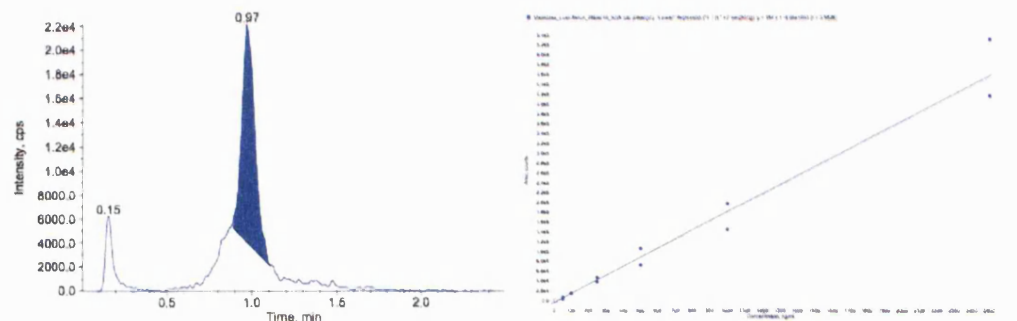
Dalargin peak (726.6/136.2 amu) extraction from plasma



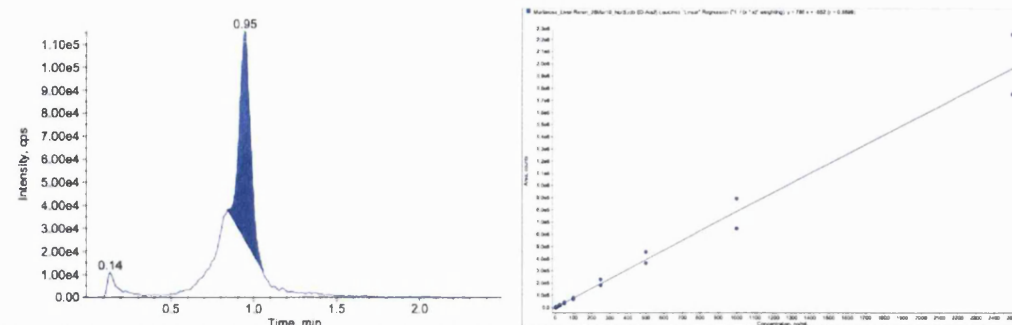
D-Ala-Leu Enkephalin peak (570.4/136.1 amu) extraction from plasma



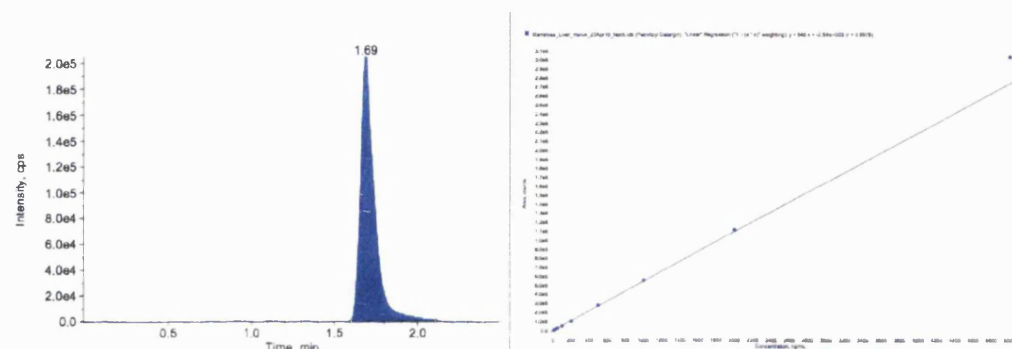
pDal peak (964.8/136.2 amu) extraction from plasma



Dalargin peak (726.6/136.2 amu) extraction from liver



D-Ala-Leu Enkephalin peak (570.4/136.1 amu) extraction from liver



pDal peak (964.8/136.2 amu) extraction from liver

6.2.6 Spontaneous Raman Spectroscopy Imaging

Spontaneous Raman Scattering

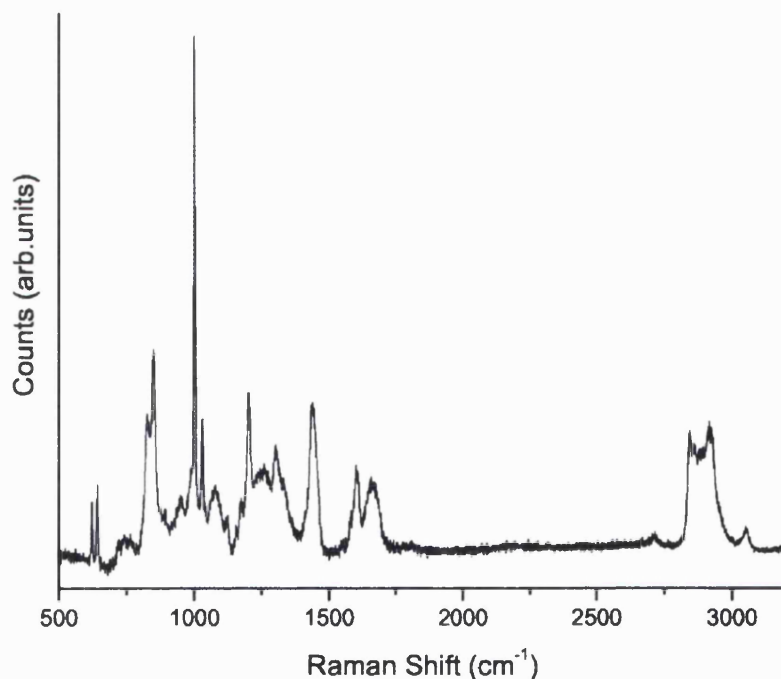
Spontaneous Raman spectra of the pDal formulation were acquired using a commercial Raman microspectrometer (Renishaw RM1000, Wootton Under Edge), using a 785 nm laser with 30 mW power at the sample and a 50X0.75 numerical aperture objective (Lieca). Spectra were acquired using a 20 s integration time and 5 averages to obtain good signal-to-noise ratio. A 1200 lines mm^{-1} grating was used.

Coherent Raman Scattering (CRS) Microscopy Instrument Set up

Coherent anti-Stokes Raman scattering (CARS) and stimulated Raman scattering (SRS) microscopy were performed simultaneously using a ps laser system and a custom modified commercial inverted laser scanning microscope (FV300/IX71, Olympus UK Ltd, UK). Coherent Raman scattering (CRS) microscopy was performed using a custom-built system at the Biophysical Department of the University of Exeter, in collaboration with Dr Julian Moger and Dr Natalie Garrett,

that provided two complimentary coherent Raman scattering contrast mechanisms simultaneously. (1) Coherent anti-Stokes Raman scattering (CARS) to detect the pDal nanofibres, and (2) stimulated Raman scattering (SRS) to delineate the brain vasculature and surrounding cellular structures.

CARS is a four-wave mixing process in which two laser beams, a pump and a Stokes beam, at frequencies ω_s and ω_p respectively, are focused into a sample. Matching the difference in frequency ($\omega_p - \omega_s$) to that of a Raman active molecular vibration of the chemical species of interest resonantly leads to the generation of a strong anti-Stokes signal at frequency ($\omega_{as} = 2\omega_p - \omega_s$) when the chemical species of interest is present in the sample volume. Since the CARS signal scales quadratically with the number of vibrational modes within the sample volume, it is particularly powerful for detecting polymeric particles due to the high bond repetition. In the case of the pDal nanofibres strong contrast could be achieved by tuning ($\omega_p - \omega_s$) to 2855cm^{-1} , the CH_2 vibrational mode that is abundant in the palmitoyl group – see Raman spectrum of pDal below.



SRS was performed using the same pump and Stokes beams (ω_p and ω_s) to excite chemical bonds of interest, however, in SRS amplification of the Raman signal is achieved by virtue of stimulated excitation. The intensity of the Stokes beam, I_s , experiences a gain, ΔI_s (stimulated Raman gain, SRG), and the intensity of the pump beam, I_p , experiences a loss, ΔI_p (stimulated Raman loss, SRL). Imaging is achieved

by recording the SRL signal ΔI_p , which scales linearly with the concentration of a vibrational mode. For the purpose of locating the BBB we make use of an artifact in the SRS images that is not derived from a Raman active mode, non-linear photothermal lensing (NL-PTL). Due to the strong optical absorption band of hemoglobin red blood cells exhibit strong NL-PTL. CARS and SRS/NL-PTL images were acquired simultaneously by recording the anti-Stokes signal (at $\omega_{as} = 2\omega_p - \omega_s$) in the epi direction and ΔI_p in the forwards direction. The NL-PTL contrast from the RBCs was distinguished from the SRS by their distinctive bi-concave shape. The origin of the NL-PTL was confirmed by investigating the phase of the RBC signal with respect to the phase of the SRS signal from myelin in the surrounding nerve fibres.

Images of 512×512 pixels were acquired with a pixel dwell time of 200 μ s, resulting in a total of 53 s per frame. All images were acquired using Olympus FV5 software. All processing was performed using ImageJ.

Tissue Preparation for CRS Microscopy

The brains were fixed in a neutral buffered formalin solution containing 4% formaldehyde w/v (Sigma Aldrich) and were stored at 4 – 6 °C prior to experimentation. Coronal sections were cut using a mouse brain slicer matrix with 0.5 mm slice spacing intervals (Zivic Instruments, Pittsburgh, US). The brain slices were briefly immersed in phosphate buffered saline (Invitrogen) prior to plating onto cleaned glass coverslips (Menzel-Gläser). Each section of brain was surrounded by strips of Parafilm (Pechiney Plastic Packaging Company) 2 layers thick, which acted as spacers before the sample was covered with a second glass coverslip. Using a point heat source applied to the top coverslip, the Parafilm spacers were heated to their melting temperature of 60 °C to form a water-tight seal around the brain slice, at a distance sufficiently far from the sample to prevent damage.

6.2.7 Warm Water Bioassay

Groups ($n = 6$) of animals were administered either: NaCl (0.9% w/v), Dalargin, Dalargin -GCPQA, pDal and pDal - GCPQA. Animals received a dalargin dose of 15mg kg^{-1} and sodium chloride (0.9% w/v) was used as the disperse phase. The volume of injection was 8mL Kg^{-1} of mouse weight. Antinociception was assessed in

mice using the tail flick warm water bioassay (Le Bars et al., 2001). The protruding distal half of the tail (4 - 5cm) of mice held in a tube restrainer was immersed in circulating warm water maintained at $55^{\circ}\text{C} \pm 0.1^{\circ}\text{C}$ (19, 20) by a thermostatically controlled water bath (W14, Grant Instruments, Cambridge Ltd, Herts, UK). The temperature was also checked using a thermometer (Gallenkamp, Griffin, THL-333-020L, 76 mm x 1mm, UK) before the start of the experiment. The response latency times, recorded for each mouse to withdraw its tail by a “sharp flick” were recorded using a digital stopwatch capable of measuring 1/100th of a second. The first sign of a rapid tail flick was taken as the behavioural endpoint. Mice not responding within 5 sec were excluded from further testing (Baseline cut-off = 5 seconds) and the baseline latency was measured for all mice prior to dosing. The maximum possible cut-off was set to 10 seconds to avoid unnecessary damage to the epidermal tail tissue, A maximum score was assigned (100%) to animals not responding within 10 seconds to the thermal stimuli. The response times were then converted to the percentage of maximum possible effect (% MPE) by a method reported previously (Kreuter et al., 2002) according to the equation

$$\% \text{ MPE} = \frac{\text{post drug latency} - \text{pre drug latency}}{\text{cut off time} - \text{pre drug latency}} \times 100$$

Data are presented as the mean \pm SEM for groups of 6 mice per group.

6.2.8 Statistical Analysis

Statistical significance ($p < 0.05$) was tested with one-way analysis of variance ANOVA using SPSS, IBM (2011) statistical software.

6.3 Results

6.3.1 MTT assay

As summarized in the graph in Figure 6.8 treatment of the polymer GCPQA did not show signs of cell toxicity under the experimental conditions in all the concentration intervals tested. Interestingly, pDal nanofibres without GCPQA polymer started to show signs of toxicity at concentration above 1mg/mL, in fact cell viability of the U87MG cells decreased around 30%. The addition of GCPQA to the formulation of pDal nanofibres caused an overall decrease of the citotoxicity. IC50 values for the different formulation were

FORMULATION	IC50
GCPQA micelles	$>5\text{mgmL}^{-1}$
pDal nanofibres	1.26 mgmL^{-1}
pDal nanofibres/GCPQA	$>2.39\text{ mgmL}^{-1}$

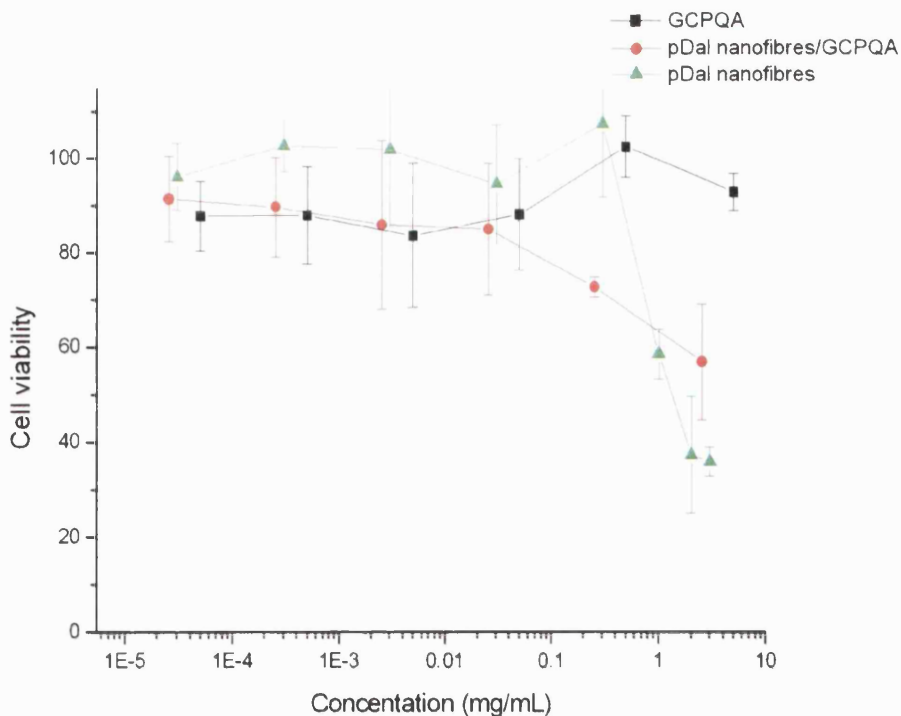


Figure 6.8: Cell viability of U87MG cells exposed to pDal nanofibres formulations for 24h assessed by the MTT assay.

6.3.2 Transmission Electron Microscopy Cell Uptake Studies

Results of the cell uptake experiment performed using TEM are shown in Figure 6.9 and 6.10. Peptide pDal nanofibres were easily detectable in the TEM images on the luminal side of the bEnd5 cells monolayer. No migration of nanofibres through tight junctions, or a close association was observed. It is possible to observe interaction between the nanofibres and the cell surface: nanofibres approach the cell surface at both a parallel and perpendicular orientation. Endocytotic vesicles have been observed in close proximity of the nanofibres, and nanostructures resembling the pDal nanofibres have been detected inside the endocytotic vesicle.

After treatment with pDal nanofibres the tight junctions and the cells retained their normal morphology indicating that the BBB integrity is not disrupted by the nanofibres. The nuclei appear normal, while mitochondria and smooth and rough endoplasmic reticulum are abundant in the cells, implying high levels of metabolism and protein synthesis.

Peptide nanofibres are reported to penetrate cells by endocytosis, thus 3D networks of peptide nanofibres gels are studied as suitable matrices for tissue engineering (Beniash et al., 2005, Cui et al., 2010). Also, prodrug approaches generating hydrophobic peptide derivatives have shown that these are able to be endocytosed, nevertheless, these hydrophobic peptide derivatives can be subject to the effect of the efflux pump transporters (Ouyang et al., 2009).

Dense black boundaries are observable on the cell surface on the right bottom picture in Figure 6.9. These densities are reported in the literature (Herve et al., 2008) as the glycocalyx structures involved in the mechanism of adsorptive mediated endocytosis, that was thoroughly discussed in Chapter 1 of this thesis.

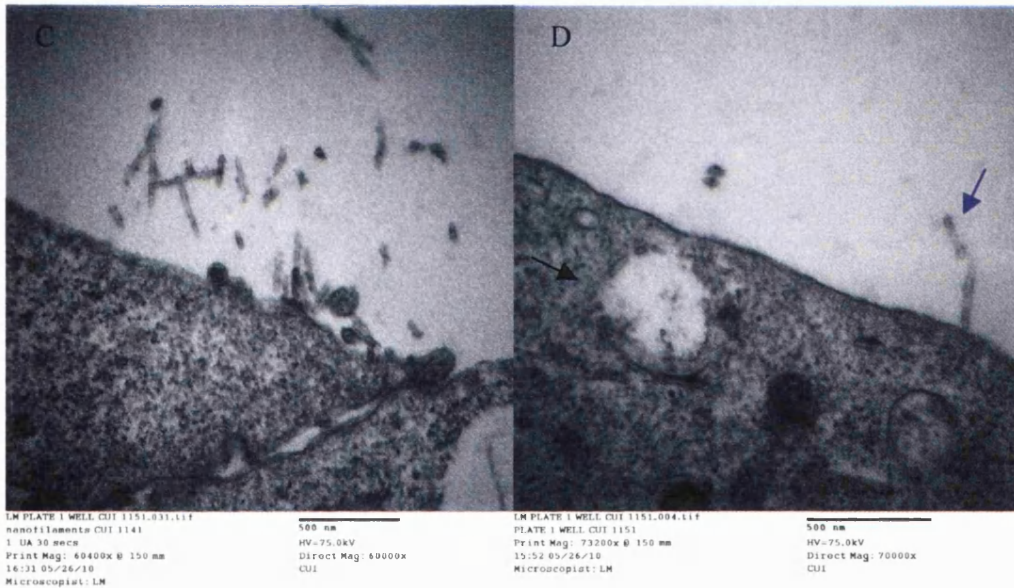
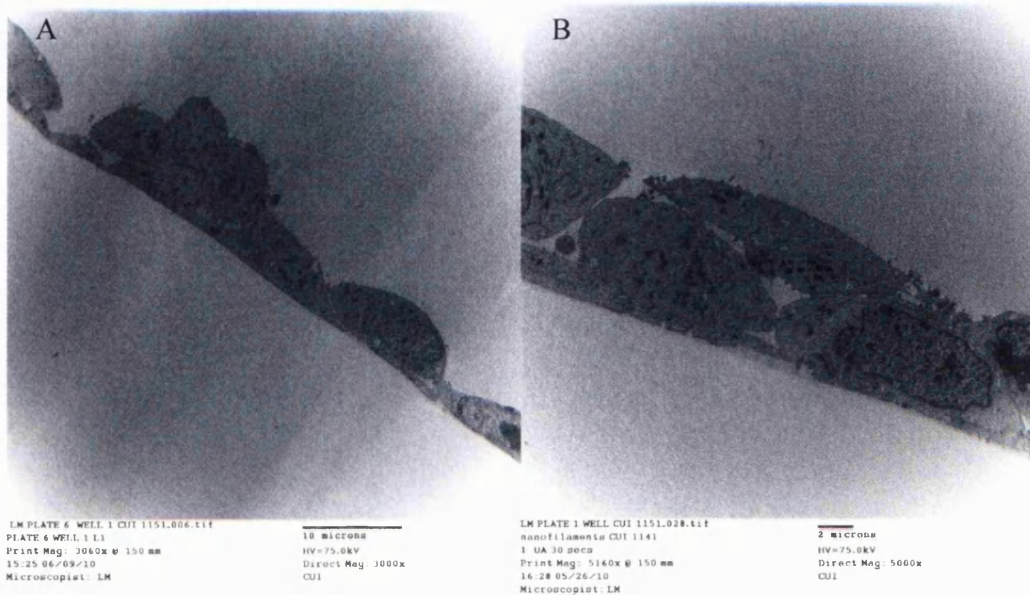


Figure 6.9: Sections of bEND5 cells monolayers embedded in resin after exposure to pDal nanofibres (0.5 mgmL^{-1}). The black arrow highlights the endocytic vesicle in proximity of the cell surface on the luminal side. The blue arrow points at nanofibres approaching the cell surface with a perpendicular orientation. Tight junction present as sealing points between adjacent cells (Figure C). Absence of nanofibres transit is observed between the tight junctions (Figure C).

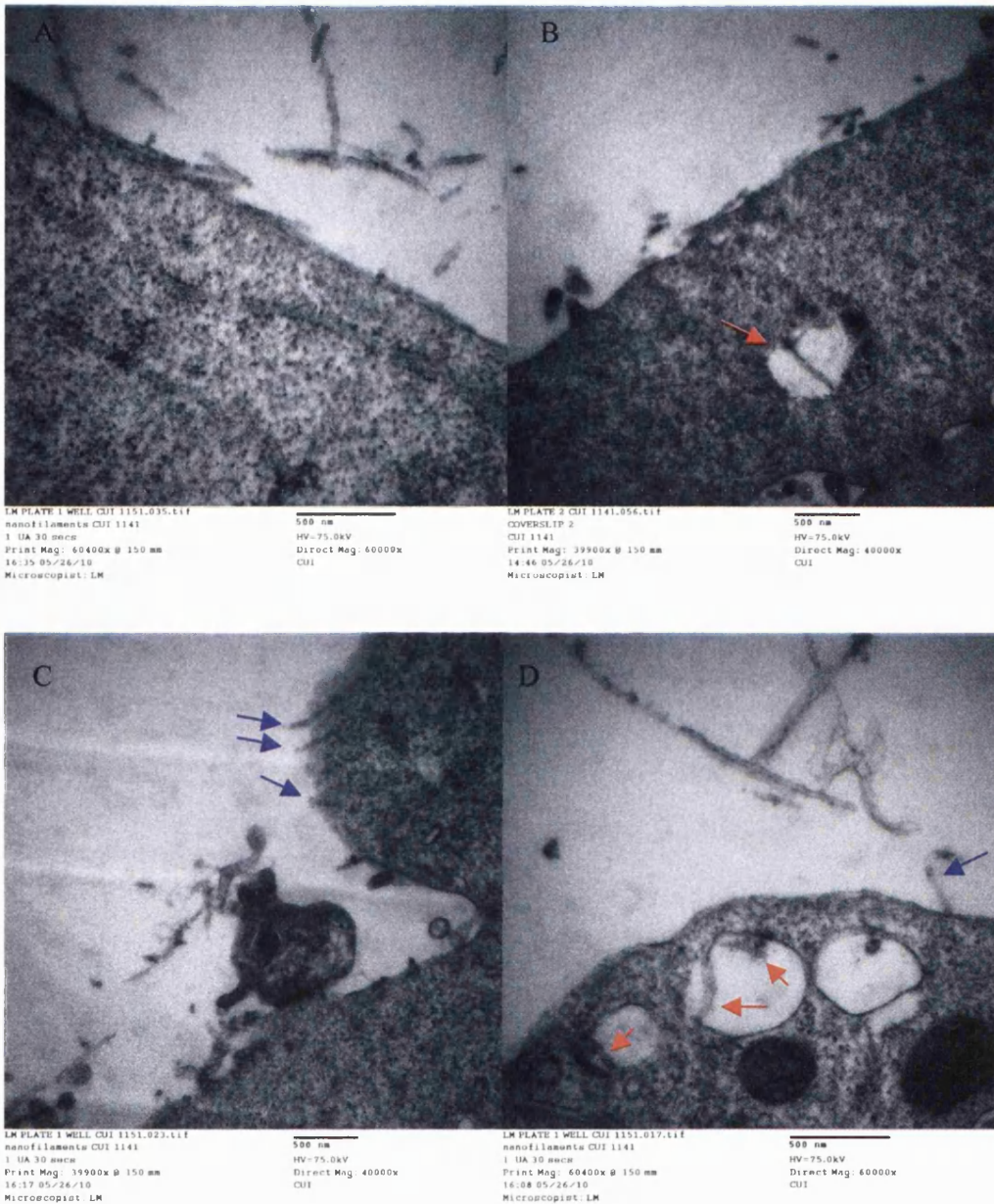


Figure 6.10: Sections of bEND5 cells monolayers embedded in resin after exposure to pDal nanofibres (5 mgmL⁻¹). The Blue arrows point at nanofibres perpendicularly interacting with the cell membrane. Red arrows point at nanosized structures within endocytotic vesicles.

Many pDal nanofibres sticking parallel to the cell surface are observable in Figure 6.10 A and B. Also, pDal nanofibres are seen to perpendicularly approach the cell surface at the luminal side (Figure 6.9 D and Figure 6.10 C and D).

6.3.3 Pharmacokinetics Studies: LC-MS Analyses

pDal, Dalargin and its metabolite D-Ala-Leu-Enkephalin were identified in plasma, brain and liver after organic sample extraction by monitoring the precursor product ion transitions, 964.8/136.2 amu, 726.6/136.2 amu, 570.4/136.1 amu respectively. The relative peptide quantities detected are reported in Table 6.1.

After a dose of 30mg/kg of mouse weight it is possible to see that in the control groups of Dalargin and GCPQA/Dalargin, Dalargin was not detected in the brain, but was degrading in the plasma into its metabolite D-Ala-Leu-Enkephalin within 3 minutes after the intravenous injection administration (Figure 6.10 A). Indeed, in the first case the D-Ala-Leu-Enkephalin was detected only up to 30 minutes after injection, while in the latter it was possible to detect it up to 90 minutes after injection (Table 6.1 and Figure 6.10A). It is possible that a fraction of Dalargin adsorbes onto the surface of the GCPQA micelles, and hence is more resistant to degradation.

pDal was identified and quantified in all the biological matrices analyzed, up to 4 hours after intravenous administration of the pDal nanofibre formulations. Both pDal nanofibres and pDal nanofibres/GCPQA resulted in pDal delivery to the brain (Figure 6.11 A). The amounts of pDal detected for both groups were comparable as there was no statistically significant difference between the pDal brain levels when pDal was administered either alone or formulated with GCPQA.

D-Ala-Leu-Enkephalin was also detected in plasma, but not in brain and liver, in animals dosed with pDal nanofibres and pDal nanofibres/GCPQA at the earliest time points, as shown in the Table 6.1.

The plasma levels obtained with both the nanofibre formulations are quite remarkable if we consider that the half life of most peptides is of few minutes, e. g. Dalargin was not detected in plasma after only three minutes. In the case of the formulation of pDal nanofibres the %ID/mL remaining in plasma was 10.39 ± 2.71 , while for the pDal nanofibres in formulation with GCPQA the %ID/mL was 18.84 ± 2.14 . After four hours since the intravenous administration a residual 0.02 ± 0.005 ID/g 0.08 ± 0.053 %ID/mL of pDal could still be detected respectively for pDal nanofibres alone and for the pDal nanofibres in formulation with GCPQA.

Table 6.1: Formulation pharmacokinetics – peptides detection by LC/MS in biological matrices (std = standard deviation). Averaged values (n=5) for each time point. In brackets it is specified the peptide detected.

pDal nfs (pDal)								
time (min)	Plasma (ng/mL)	std	Brain (ng/mL)	Std	brain corrected	Std	Liver (ng/mL)	std
3	61467.26	35985.58604	3071.34	1908.137618	2746.181478	1763.612655	81686.04	57493.55081
10	4888.24	3293.985161	581.28	344.7695491	555.0566621	327.3332528	63641.88	45150.0328
30	1010.9	669.4120405	566.925	105.4067479	448.0695012	266.1093475	73829.7	41573.96304
60	374.8	260.1815424	260.55	145.8657259	206.397263	170.363236	47805.78	40655.30611
90	167.88	96.31984219	227.22	118.5452572	226.3091542	115.0322774	23322.96	17703.86794
120	108.52	71.92549617	57.225	23.31185321	45.23421024	32.14917959	2705.325	1563.711995
240	117.24	67.78114044	57.3	33.37828636	56.67581568	33.25242352	2062.68	1173.556682

pDal/GCPQA (pDal)								
time (min)	Plasma (ng/mL)	Std	Brain (ng/mL)	std	brain corrected	Std	Liver (ng/mL)	std
3	90971.14	18158.28552	2650.68	1244.608268	2190.415458	1164.893308	105857.04	45959.98738
10	28540.12	10640.57781	668.1	192.7519261	515.7641875	160.6972861	120436.74	22266.16428
30	34107.48	56597.97179	588.45	165.1169585	288.4345186	415.2267616	85399.98	48134.25567
60	589.46	420.5065731	56.625	15.74047331	42.38807256	26.84198663	63759.48	43260.63422
90	416.92	120.446183	445.8	332.887098	355.2755076	349.827931	10795.02	7940.309428
20	365.14	75.12258648	25.26	11.30765228	23.6322672	11.07282713	12459.18	9615.543176
40	97.64	93.85271973	7.44	16.63634575	7.19213568	16.08210428	1749.6	901.1228496

dalargin (d-ala-leu-enkephalin)								
time (min)	Plasma (ng/mL)	std	Brain (ng/g)	Std	Liver (ng/g)	std		
3	1845	1629.596679		0	0	0	0	0
10	71.7	46.17396453		0	0	0	0	0
30	3.716666667	0		0	0	0	0	0
60	0	0		0	0	0	0	0
90	0	0		0	0	0	0	0
120	0	0		0	0	0	0	0
240	0	0		0	0	0	0	0

dalargin/GCPQA (d-ala-leu-enkephalin)								
time (min)	Plasma (ng/mL)	std	Brain (ng/g)	Std	Liver (ng/g)	std		
3	2448.2	449.9780757		0	0	29.55		2.74
10	134.5	11.63053739		0	0	0		0
30	37.6	7.981415914		0	0	0		0
60	11.7	0.894762538		0	0	0		0
90	3.2	0.314006369		0	0	0		0
120	2.8	0.3		0	0	0		0
240	0	0		0	0	0		0

Table 6.1 - Continued

pDal /GCPQA (d-ala-leu-enkephalin)							
time (min)	Plasma (ng/mL)	std	Brain (ng/g)	Std	Liver (ng/g)	std	
3	112.8	35.8107805		0	0	0	0
10	15.1	5.205477884		0	0	0	0
30	8.0	4.005829086		0	0	0	0
60	0.0	0		0	0	0	0
90	1.8	0		0	0	0	0
120	0.0	0		0	0	0	0
240	0.0	0		0	0	0	0

pDal nanofibres (d-ala-leu-enkephalin)							
time (min)	Plasma (ng/mL)	std	Brain (ng/g)	Std	Liver (ng/g)	std	
3	128.3	48.22415543		0	0	0	0
10	0.0	0		0	0	0	0
30	9.4	0		0	0	0	0
60	4.2	0		0	0	0	0
90	0.0	0		0	0	0	0
120	0.0	0		0	0	0	0
240	0.0	0		0	0	0	0

One of the metabolites of pDal was expected to be dalargin, as a result of the enzymatic cleavage operated by esterases in blood and brain. However dalargin is never detected in any of the biological matrices of the animal dosed with the pDal nanofibre formulations. This phenomenon suggests two possible scenarios: 1) the presence of the palmitoyl chain creates steric interference for the action of the esterases enzyme; 2) the pDal molecules circulate and partition into the organs in their nanofibrous form, thus the linker region is less available to be accessed by the enzyme, because it is hidden inside the fibre.

However, a small fraction of pDal is converted into D-Ala-Leu-Enkephalin (Table 6.1) in plasma suggesting that the esterases can cleave the palmitoyl group attached on the tyrosine side chain, although the kinetics of the process must be very slow. The slow kinetics of degradation may be dependent on the presence of the D-alanine, a not natural amino acid. In fact, the presence of D-alanine may determine a conformation that confers more resistance, but does not completely blocks the hydrolysis of the palmitic chain.

The metabolism of the peptide is more likely to happen by action of the carboxypeptidase that breaks down the peptide into its amino acid units starting from the C-terminus. The fact that D-Ala-Leu-Enkephalin is detected, suggests that by the

time that the aminopeptidase can cleave the tyrosine the carboxypeptidase as already removed the arginine, thus dalargin is not detected.

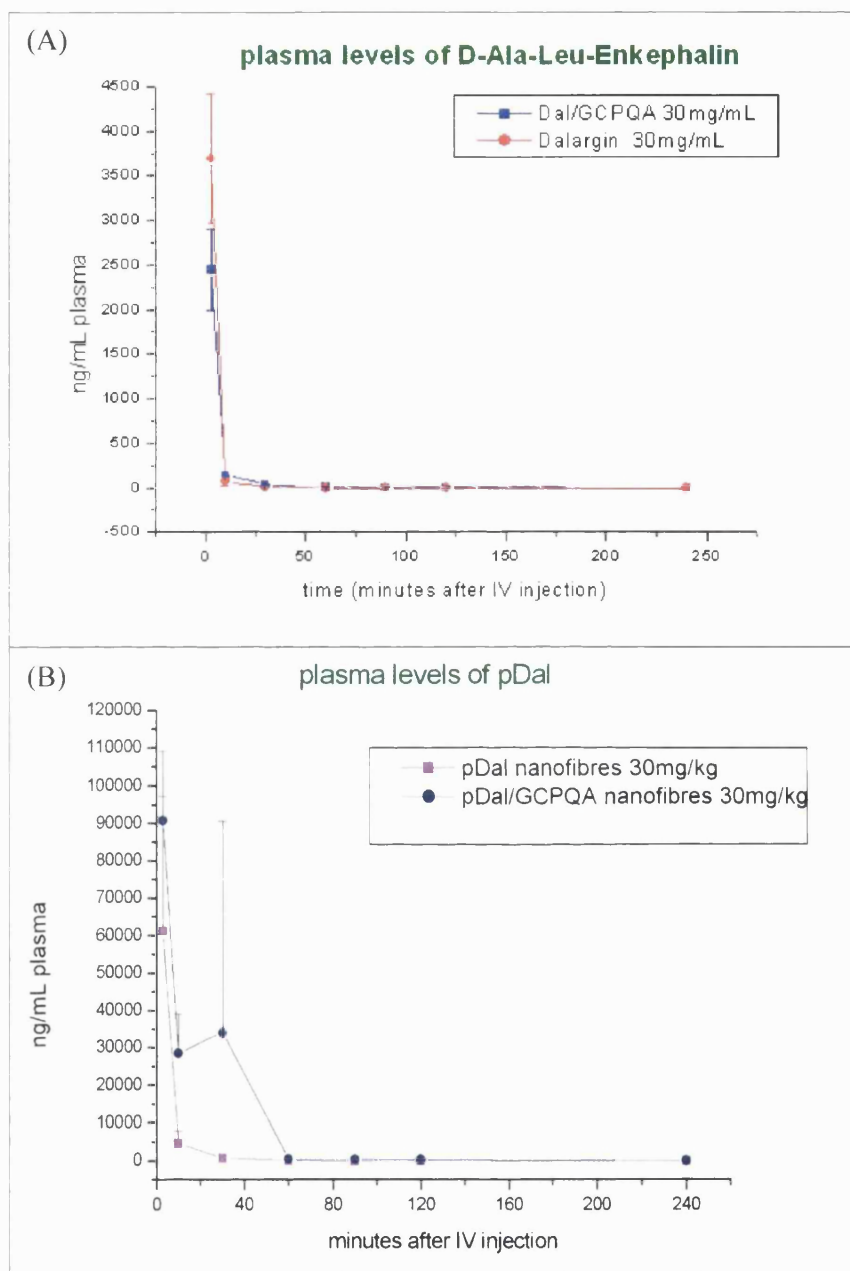


Figure 6.11: (A) plasma levels of D-ala-Leu enkephalin measured in plasma, in control groups dosed with Dalargin and Dalargin/GCPQA; (B) plasma levels of pDal in plasma (bottom) in groups dosed with nanofibre formulations. One-way ANOVA ($p < 0.05$) shows no statistically significant difference.

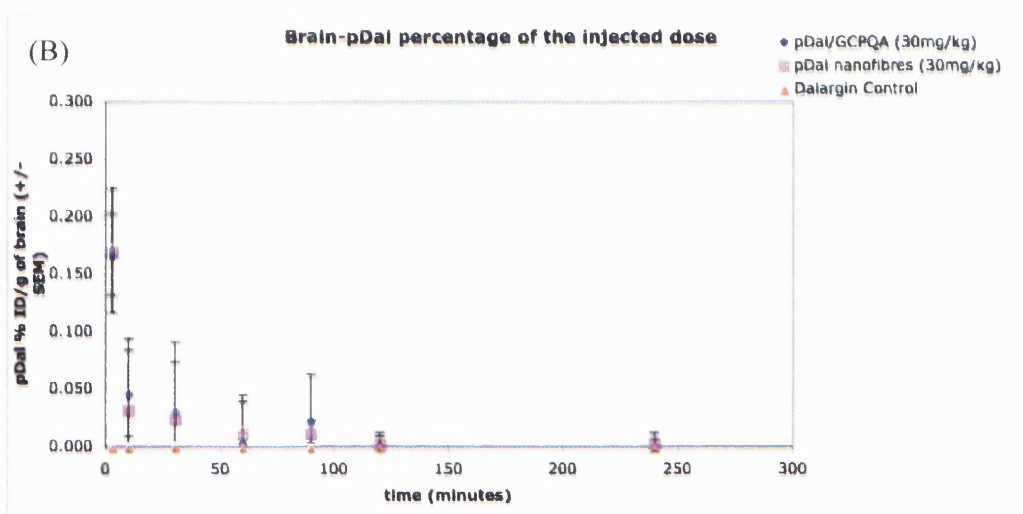
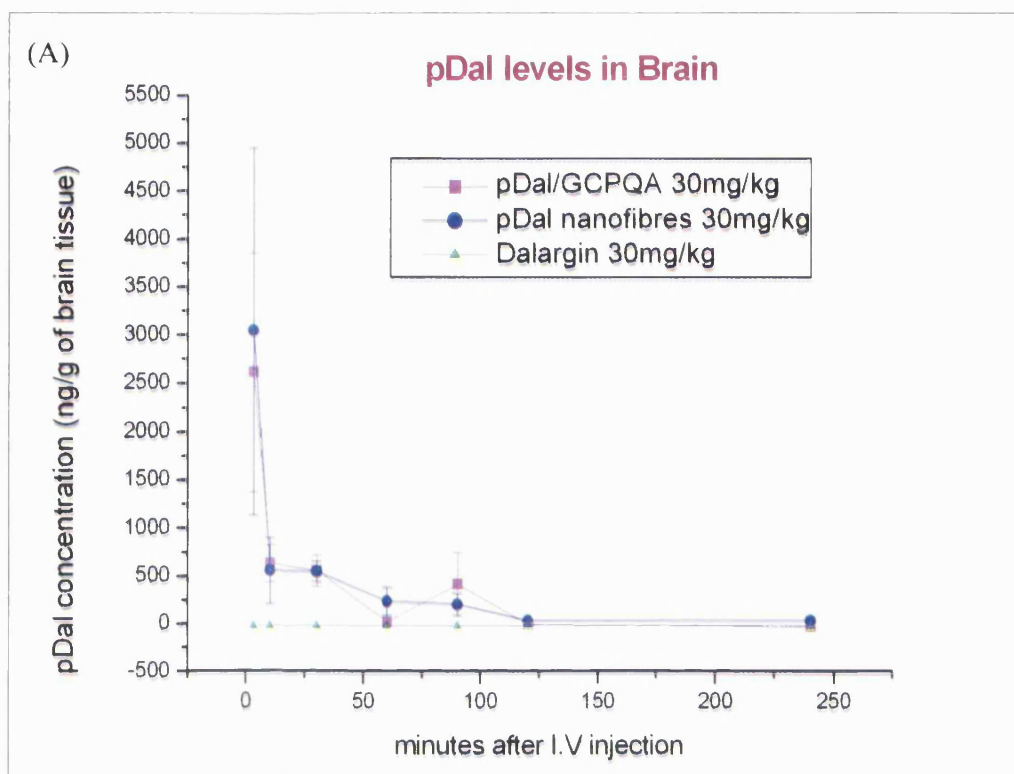


Figure 6.12: (A) pDal levels detected by LC-MS in brain homogenate of animals dosed with pDal nanofibres formulation. Error bars indicate standard deviation; (B) percentage of the injected dose / gram of brain recovered in the tissue. Error bars indicate the standard error median. One-way ANOVA ($p < 0.05$) shows no statistically significant difference between the two nanofibres formulation.

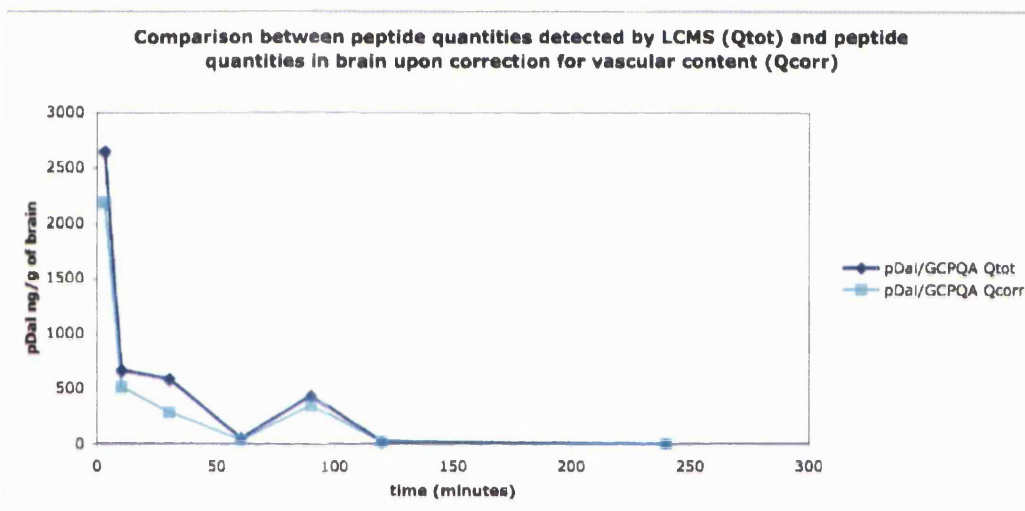
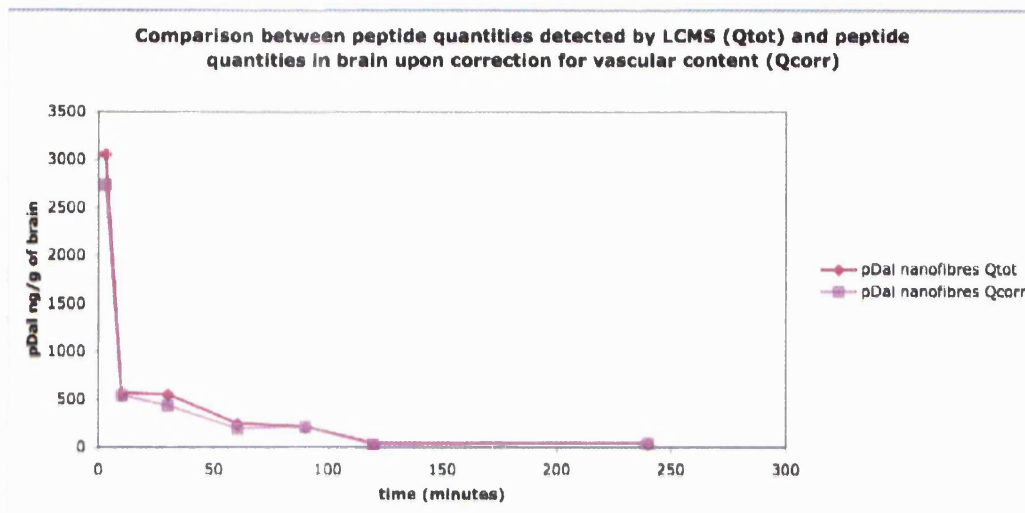


Figure 6.13: quantities of pDal in brain tissue obtained after intravascular content correction. One-way ANOVA ($p < 0.05$) shows no statistically significant difference.

There is no statistically significance difference between the two nanofibres formulations for brain quantities of pDal (Figure 6.12 A).

Since the brain vascular volume is $12 \mu\text{l}/\text{gram}$ of brain, the peptide levels by LC-MS were reprocessed using this value to correct for intravascular content of peptide. Also when the intravascular content correction is applied (Figure 6.13) there is no statistically significance difference between the two nanofibres formulations.

The pDal that reaches the brain parenchyma after 3 minutes following I.V. injection, expressed as percentage of the injected dose per gram of tissue (%ID/g), it is $0.166 \pm 0.035\%$ ID/g for pDal nanofibres formulated with GCPQA and $0.170 \pm 0.054\%$ ID/g for pDal nanofibres alone. In this latter case there is a residual $0.003 \pm 0.008\%$ of the inject dose still present after 4 hours (or 240 minutes) from the intravenous administration. Data are reported in Figure 6.13 B and Table 6.2.

These results are remarkable if one considers that

- 1) controls of dalargin and dalargin/GCPQA did not give rise to any detectable concentration in the brain parenchyma;
- 2) these %ID/g values are achieved without employing a specific targeting strategy to overcome the BBB;
- 3) nanoparticles strategies for the delivery of drugs to the brain result often in values below 0.5% and can be as low as 0.01% ID/g (van Rooy et al., 2011a)
- 4) in general, only a small proportion of peripherally administered peptides reaches the brain parenchyma; for example, only 0.046% of insulin, following jugular injection, reaches the brain parenchyma (Banks and Kastin, 1998).

Table 6.2 : pDal %ID/gram brain. Values corrected for intravascular content.

Minutes	pDAL/GCPQA brain		pDal Nanofibres brain		Dalargin
	ID%brain	Standard error median	ID%brain	Standard error median	
3	0.166	0.035682359	0.170	0.053882422	0
10	0.046	0.037380151	0.03	0.061015687	0
30	0.030	0.042319616	0.025	0.065341973	0
60	0.003	0.041374916	0.012	0.027003095	0
90	0.022	0.039946013	0.012	0.010008197	0
120	0.001	0.006609626	0.002	0.008567209	0
240	0.000	0.007018821	0.003	0.008108183	0

It is interesting to notice that although the partition of pDal in the liver is very high, also in this organ there is no detection of Dalargin in the groups dosed with both the pDal nanofibre formulations. Liver detection levels showed that a considerable amount of pDal partitions into this tissue, and specifically, after three minutes $22.9 \pm 3.16\%$ ID/g for the pDal nanofibres in formulation with GCPQA and 18.37 ± 5.78 for pDal nanofibres alone, although the levels of pDal measured via LC-MS were not statistically significantly different (Figure 6.14).

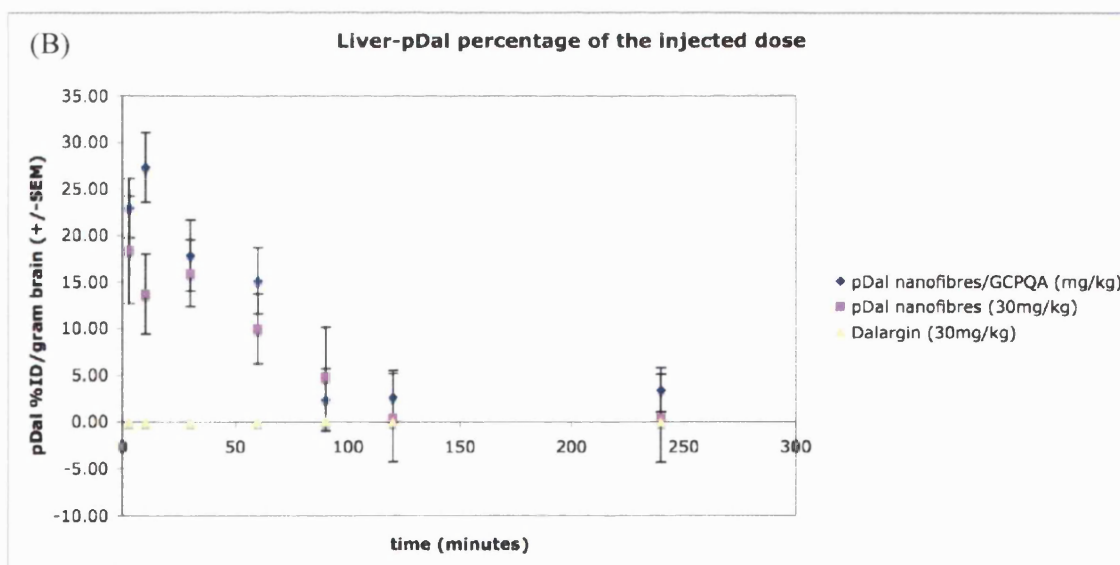
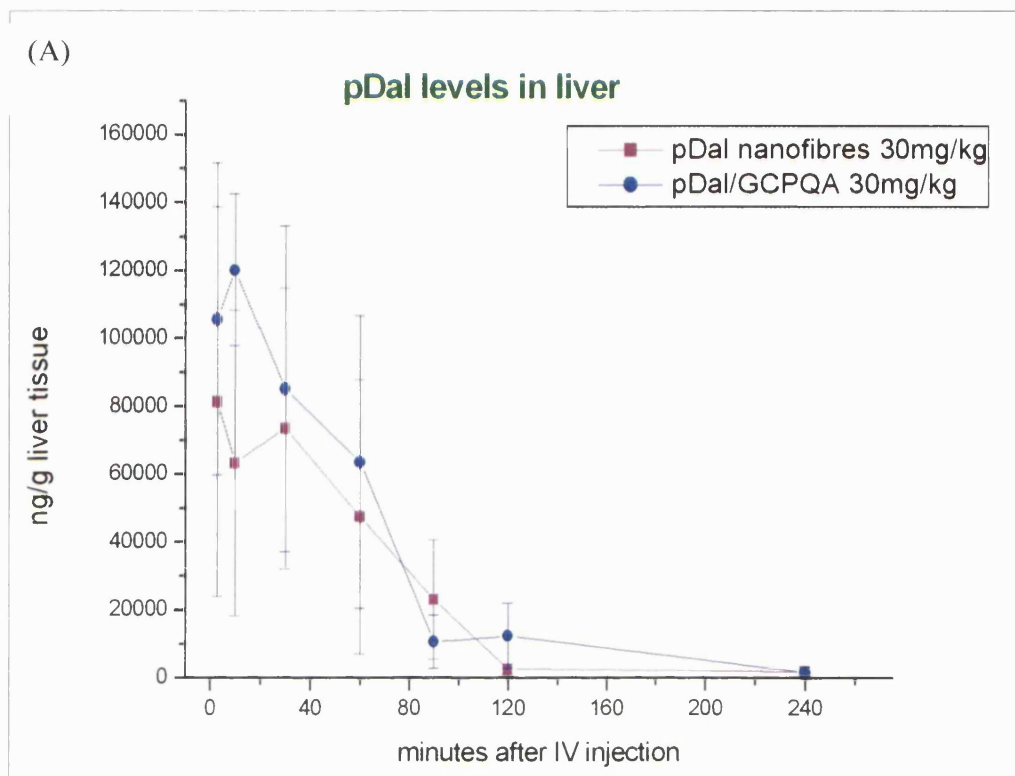


Figure 6.14: (A) pDal levels detected by LC-MS in liver homogenate of animals dosed with pDal nanofibres formulation; (B) percentage of the injected dose / gram of liver recovered in the tissue. One-way ANOVA ($p < 0.05$)

6.3.4 SRS Imaging

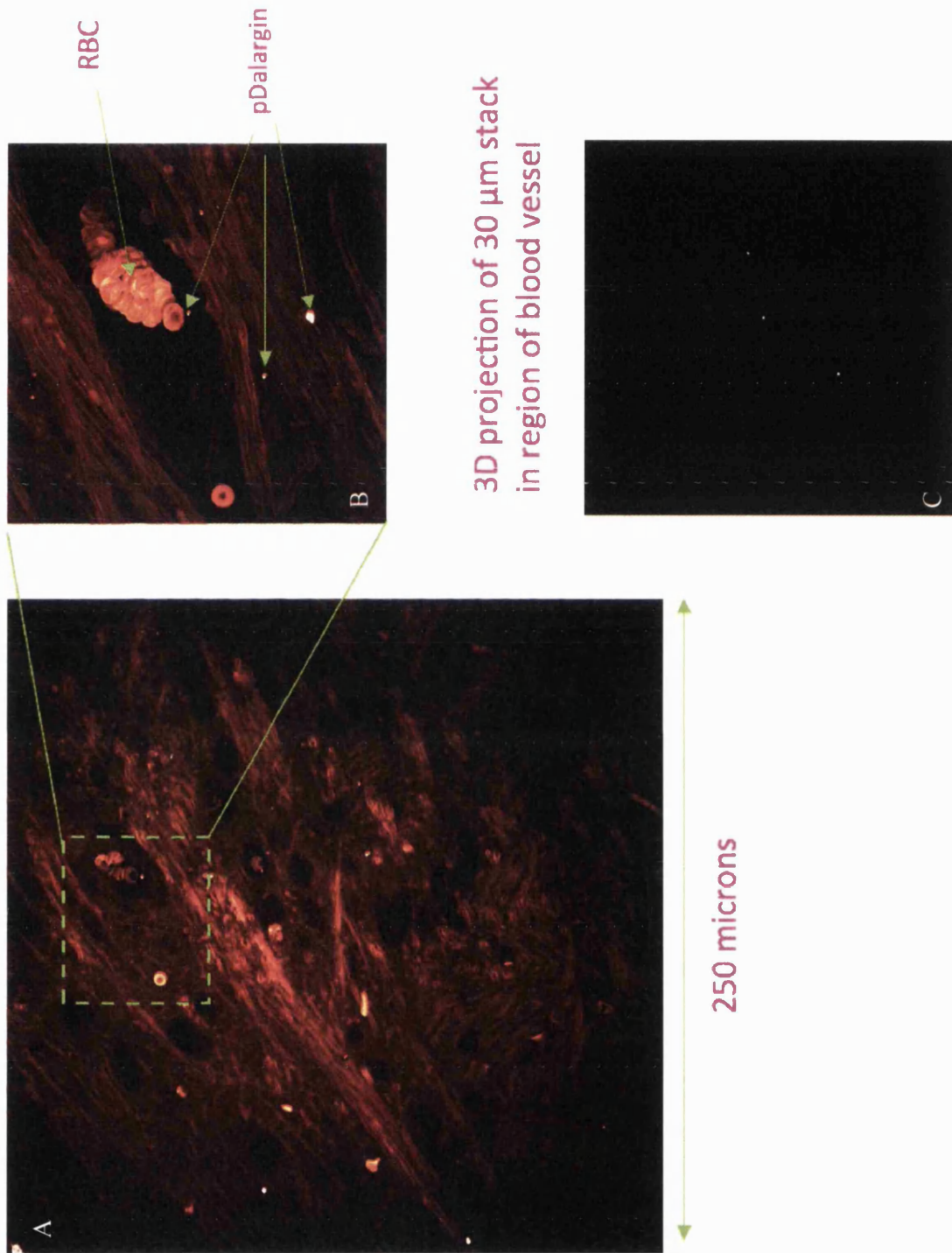


Figure 6.15: *Ex-vivo* CRS images of brain tissue of a male CD-1 mouse 30 minutes following a 30 mg kg^{-1} IV dose of pDal nanofibres fomulation with GCPQA. The large section in figure A represents a $250 \mu\text{m}$ square region of a brain slice. The presence of red blood cells (RBC) in the upper half of the image indicated that the

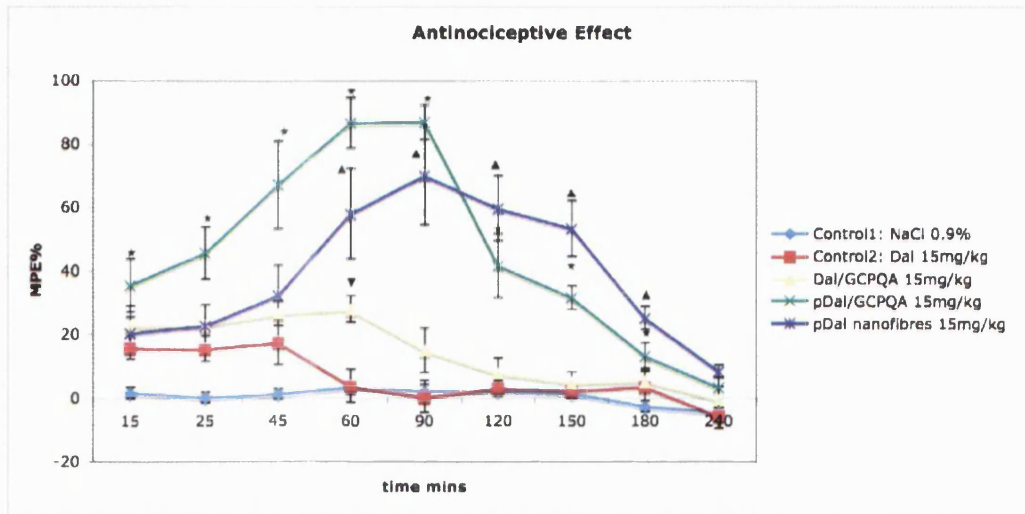
image plain passes through a microvessel (approximately 14 μm in diameter). The smaller section in figure B shows a multiplanar projection three-dimensional reconstruction of a 30 μm deep image stack acquired at a 3x zoom centered on the region containing the blood vessel. The figure C shows a planar projection isolating the pDal signal only.

Stimulated Raman Spectroscopy Imaging allowed the detection of pDal in the brain parenchyma, as shown in Figure 6.15. A strong Stimulated Raman Loss (SRL) signal originates from the CH_2 stretching vibration (2845 cm^{-1}) of lipids in the brain tissue, that is particularly rich in lipids due to the presence of the myelin, thus it was possible to elaborate a section of brain slice of 250 μm of length and 30 μm of depth to re-construct a brain section showing intact blood brain barrier channels with circulating red blood cells (RBCs). pDal penetrated the brain parenchyma, as confirmed by LC-MS and it was imaged both within the blood vessel, as well as in the brain parenchyma (arrows pointing at pDal in Figure 6.15 B) showing an inverted contrast compared to the lipids in the parenchyma.

6.3.5 Pharmacodynamics Studies: warm water bioassay

The ability of the nanofibres system to deliver an active molecule was determined by performing the warm water bioassay and measuring the analgesia as a percentage of the maximum possible effect (MPE), as summarized in Figure 6.16 A and B. Intravenous administration of a dose of 7.5 mgKg^{-1} of peptide formulations did not produce appreciable levels of analgesia in mice. A pronounced analgesia, about 90% of the MPE, was observable when the dose was increased at 15 mgKg^{-1} in the group of animals dosed with pDal nanofibres and GCPQA polymer at 60 and 90 minutes after intravenous injection. In the group of animals dosed with pDal nanofibres alone analgesia was less pronounced compared to the group receiving pDal/GCPQA, but lasted longer over time. Interestingly, it can be observed from the Figure 6.17, that the *brain/plasma ratio* of the pDal quantities measured by LC-MS in brain (ng/g) and plasma (ng/mL) is higher in the brain (pDal in brain > pDal in plasma) only after 90 minutes from the intravenous administration. At this same time point the higher antinociceptive response is also observed in animals receiving pDal nanofibres formulations.

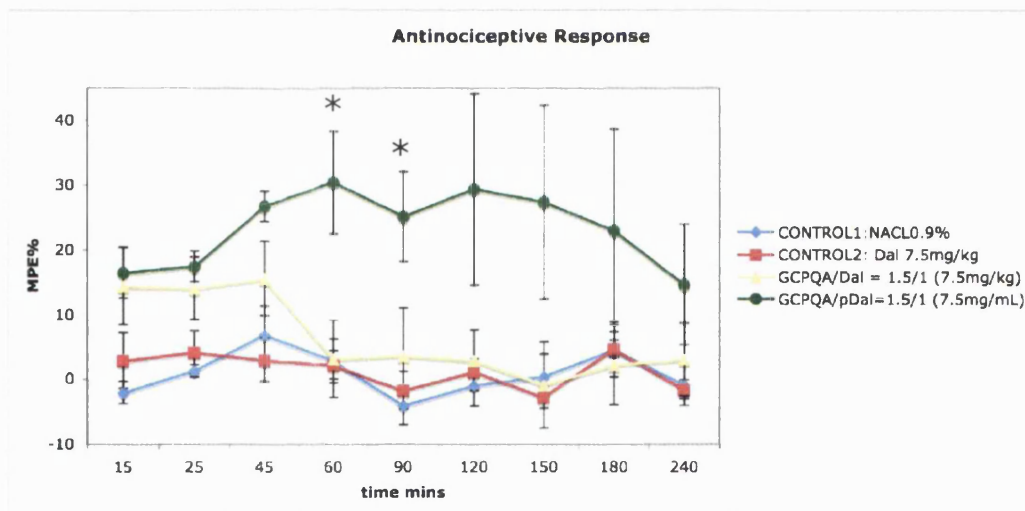
Also, it can be observed that the pDal extent in brain is higher with the formulation of nanofibres alone compared to the formulation of pDal GCPQA.



* = statistically significant difference with control 1, 2 and Dal/GCPQA

▲ = statistically significant difference with control 1, 2 and Dal/GCPQA

▼ = statistically significant difference with control 1, 2



* = statistically significant difference from control 1 and 2;

Figure 6.16: (A) Antinociception response in CD1 mice (n=6) after intravenous injection of pDal nanofibres formulation (15mg/kg); (B) Antinociception response in CD1 mice (n=6) after intravenous injection of pDal nanofibres formulation . Results expressed as percentage of the maximum possible effect (MPE %). Error bars indicate values of standard error median. One-way ANOVA (p <0.05).

We are observing a delay between the brain delivery of the substance and the onset of the pharmacological effect. Kastin and Pan have recently explained that although the pharmacological action of a compound often correlates with its half life, this is less applicable to peptides (Kastin and Pan, 2010). For example, the central action of peptides can persist longer than their half-lives in blood, as it was observed for the luteinizing hormone-releasing factor (Pfaff, 1973).

time (min)	pDal/GCPQA brain/plasma ratio	pDal nanofibres brain/plasma ratio
3	0.029137592	0.049967088
10	0.023409152	0.118913965
30	0.017252814	0.560812148
60	0.096062498	0.695170758
90	1.069269884	1.353466762
120	0.069178945	0.527322153
240	0.076198279	0.488741044

Figure 6.17: *brain/plasma ratio* of the pDal quantities measured by LC-MS in brain (ng/g) and plasma (ng/mL).

Finally, from the Figure 6.17 we can observe that at the same dose (30mgKg^{-1}) the brain/plasma ratio values of pDal for the formulation of pDal nanofibres alone are higher than those of pDal nanofibres in formulation with GCPQA at all the time points measured.

6.4 Discussion

Here we report the use of nanofibres made of self-assembling peptide amphiphiles for brain delivery. Peptide nanofibre formulations have been administered following intravenous injection. The nanofibre formulation enabled the delivery of the amphiphilic peptide pDal to the brain parenchyma.

The assessment of the *in vitro* toxicity was performed using the U87MG human glioblastoma multiforme cell line as a model and selecting the MTT method as quantification of the cell viability. As can be observed in Figure 6.8, the nanofibre formulations have a high compatibility even after a continuous exposure of 24 hours

The IC₅₀ values for pDal nanofibres alone and pDal nanofibres in formulation with GCPQA were of 1.26 mgmL⁻¹ and 2.39 mgmL⁻¹ respectively. These results correlate well with the information extracted from the TEM micrographs of brain endothelial cell line bEnd5 monolayers (Figure 6.9). The cells treated with the pDal nanofibre formulation showed no signs of damage to the monolayer such as membrane disruption or opening of the tight junctions. These data suggest that the nanofibres do not challenge the integrity of the cells and encouraged us to proceed with the evaluation of their efficacy.

The cell-uptake studied by TEM, nevertheless, does not definitively clarify the mechanism involved for the pDal internalization and translocation to the brain parenchyma. Indeed, with respect to internalization it has to be discussed whether it is the supramolecular assembly of pDal nanofibres that are taken up by the endothelial cells or do the single peptide amphiphile units enter the cells by crossing the membrane. With respect to these two possibilities there are few reports in literature pointing in opposite directions.

The uptake of nanofibres has been shown to take place in cells growth on scaffolds made of peptide nanofibre gel. These nanofibres have a diameter ranging between 5 to 8 nm (Beniash et al., 2005). TEM analysis revealed that MC3T3-E1 cells were able to internalize self-assembling peptide nanofibres via endocytosis and to accumulate them in membrane-delineated compartments, most likely lysosomes. Other studies, however, suggest that the internalization may occur for the monomeric peptide amphiphiles through energy-dependent endocytosis and/or through caveolae-independent and clathrin-independent pathways (Missirlis et al., 2009).

Some other possibilities may directly involve the receptor-mediated endocytosis, as in the case of receptors transporters of amyloid beta. The receptor for advanced glycation end products (RAGE) is thought to be a primary transporter of amyloid beta (A β) from the systemic circulation across the BBB and into the brain (Neuwelt et al., 2008), and recently also LRP-1 has been shown to be able to transport A β bi-directionally in and out the brain endothelial cells in a monolayer of BBB in vitro set up experiment (von Einem et al., 2010).

The TEM pictures, in Figure 6.9 and 6.10, show that some of the nanofibres seem to pierce the lipid cell membrane, this same mechanism is used by another class

of fibrillar nanostructures, carbon nanotubes, to access the intracellular environment (Al-Jamal et al., 2011). Other sections of the cells, post-incubation with pDal nanofibres, shows well defined cytoplasmic vesicles and their content (Figures 6.9 D and 6.9 B,D). However, it is hard to confirm that the vesicles content are pDal nanofibres, because their electron density is very low. Hence, the uptake of nanofibres by endothelial brain cells bEND5 by endocytosis remains a hypothesis but it is not fully proven with the present experiments. Furthermore, more than one mechanism, active or passive, could be involved in the translocation of pDal peptide amphiphile or the nanofibre into the brain parenchyma. Lastly, it has to be taken into account that the experiments were performed by incubating the bEND5 cells with a concentration of 0.5 mgmL^{-1} ; this concentration according to the MTT-assay was a safe concentration for the cells to be exposed, in fact tight junctions were expressed and no signs of disruption were present (Figure 6.9 C). TEM Experiments of cell-uptake could be repeated by incubating the cells with higher concentrations of pDal nanofibres and also nanofibres could be marked, i.e. with gold labelling, or with Se-labelling (Porter et al., 2009), in order to have a stronger contrast in TEM and get more insights on the cytoplasmic fate of the nanofibres. These further experiments could help to clarify the mechanism involved in the cell-uptake and translocation of pDal into the brain parenchyma.

Albeit the mechanism by which pDal nanofibres find their access to the CNS is not fully understood, the presence of pDal in the brain parenchyma was confirmed by three sets of *in vivo* studies.

Information about the peptide amphiphiles disposition in biological matrices were obtained by LC-MS analyses.

The first important observation regards dalargin, indeed the hexapeptide it is never detected in the biological matrices. In literature dalargin is reported to have a half life of 23.2 minutes when administered intramuscularly in rats and 21.3 minutes when administered intranasally in rats (Vinogradov et al., 1988), while the half life (of elimination) after intravenous injection in rats was found to be not higher than 5 minutes (Kalenikova EI, 1988). In humans its $t_{1/2}$ (half-elimination) from blood does not exceed 16 minutes and peptide products of its metabolism are not found in blood 85 minutes after injection (Maslov et al., 2002). Surprisingly, in the experiment performed in this work, dalargin was not detected in plasma at any time point, and considering that the earliest time point measured was 3 minutes, we would assume

that the half life is less than 3 minutes in mouse blood. Dalargin is not detected in brain at any time point, thus we can say that it does not cross the blood-brain barrier, as already documented into literature (Kalenikova EI, 1988).

pDal nanofibres were prepared using NaCL 0.9% as vehicle and in combination with GCPQA, a chitosan based polymer of the family of GCPQ, a known bioavailability enhancer used to increase the uptake of central acting therapeutics (Qu et al., 2006). Formulations containing Dalargin/GCPQA nanoparticles, Dalargin and the vehicle on its own were used as control. After intravenous injection via the tail vein we could see that for all the time points dalargin was not detected in the brain, it was possible to detect only its metabolite in plasma; indeed, in the control group of dalargin alone the metabolite was detected only up to 30 minutes after injection, while when dalargin was in formulation with GCPQA it was possible to detect the metabolite up to 90 minutes after injection, thus suggesting that the polymer was able to prolong the resistance to the enzymatic degradation. One explanation for these observations could be that the peptide may adsorb on the surface of the particles formed by GCPQA. Strikingly pDal was detectable in the brain up to 4 hours after intravenous administration and although there was not a statistically significant difference among the groups with or without GCPQA, these results clearly demonstrate that nanofibres have the potential to be used as carriers for peptide delivery to the brain.

Plasma levels of pDal for both the nanofibre formulations show that the nanofibre technology allows long circulating times, indeed the peptide was detected up to four hours since the injection, while the control plasma samples of animals that have received dalargin showed that the peptide was cleared already after three minutes.

Evidence of the presence of pDal in the brain parenchyma was also obtained by employing coherent Raman scattering microscopy. Coherent Raman scattering (CRS) microscopy is a label-free imaging technique that is capable of real-time, imaging of intact tissues with sub-cellular spatial resolution based on molecular vibrational spectroscopy (Freudiger CW, 2008). A coherent non-linear Raman signal is generated by focusing two synchronized ultrafast pulse trains into a sample with a difference in frequency matched to a Raman active mode of a molecular specie of interest.

CRS microscopy was used to visualize pDal nanofibres within the brain parenchyma without the need to modify the fibres with fluorescent labeling.

Fluorescent labeling could cause chemical perturbation, which could influence transport across the BBB. Furthermore, the technique enabled non-destructive visualization of the surrounding brain tissue structures to confirm the location of the fibres in relation to the BBB. The pDal signal, overlaid in white, is present both in the BBB vessel and the brain tissue. Figure 6.15 show that pDal is clearly located in the brain parenchyma, which was confirmed by the LC-MS data.

One of the reasons for the success of this work can be found by looking at the recent literature that focuses on the interaction of elongated micellar particles and blood vessels and their circulation time, as discussed in detail in Chapter 3 of this thesis.

It has been shown that ellipsoidal nanoparticles are phagocytosed more slowly by macrophages compared to spherical particles (Sharma et al., 2010). Interestingly, recent studies on cylindrical micelles have shown persistent blood circulation (up to one week after intravenous injection) (Muro et al., 2008, Geng Y, 2007). Nevertheless, despite these early encouraging studies there is still a lack of understanding of how shape affects the in vivo behavior of these drug delivery systems (Tao et al., 2011), but our data suggest that nanofibres enable peptides to enjoy long circulation times.

Finally, it was important to test the ability of the nanofibres to deliver a compound that would still be active on the site of action. For this purpose, it was chosen to perform a behavioural experiment on animals dosed with the fibrillar nanoparticulate systems.

We observed that antinociception was more pronounced at those time points where the quantity of pDal detected in the brain homogenate was already considerably decreased.

An explanation to this phenomenon could be the fact that by LC-MS it was possible to detect only the original pDal, but no information were obtained with regard to its active product intermediates (APIs) or metabolites. Probably the late effect of the peptide on the analgesia response may be a result of high stability of the peptide-opiate receptor complex. For instance, the half-life period of the dynorphin-opiate receptor complex is 90 minutes, although dynorphin itself is broken up by enzymes in few minutes (Maslov et al., 2002). To be able to identify and quantify the APIs it is necessary to have them as standard and construct a calibration curve. This

was possible to be done for Dalargin, where the metabolite is D-Ala-Leu-Enkephalin, as this is commercially available. Obviously, no APIs bearing a palmitoyl chain were commercially available in the case of pDal, as this was a new molecule synthesised in house. The synthesis of pDal APIs would have been quite time consuming and due to time limitations in accessing the analytical facilities at GSK (Harlow) further investigations could not be performed.

It is known from literature that the dalargin metabolites N-terminus tetrapeptide and pentapeptide (D-Ala-Leu enkephalin) possess opioid activity (Kalenikova EI, 1988), although they do differ in potency, while the N-terminal tripeptide and tyrosine-free fragment of D-Ala-Gly-Phe-Leu possess no opioid properties (Korobov, 1988).

It is also important to observe that up to 4 hours after intravenous injection no dalargin is detected in the groups of animals dosed with pDal nanofibres in the presence or in the absence of the polymer GCPQA. Studies on lipophilic enkephalines bearing an acyl chain on the Tyrosine chain – as it is for dalargin - previously conducted in our group have shown interconversion from the lipophilic peptide to the hydrophilic peptide (Uchegbu IF, 2010). Accordingly, we were able to detect the metabolite D-Ala-Leu enkephalin as a metabolite of pDal, thus proving the hydrolysis of the palmitoyl chain. We can hypothesize that the presence of the palmitoyl chain, the supramolecular assembly and the D-Ala confer more resistance to the enzymatic hydrolysis, thus the carboxypeptidase on the C-terminus may determine formation of the tyrosine N-terminus palmitoyl penta and tetrapeptide.

A variety of peptidases have been detected in the central nervous system tissue, some of these are membrane and tissue bound and others are soluble and exist in the highest concentration in the cytosol (Turner, 1987). Opioid agonists such as the enkephalins are substrates of the endopeptidase-24:11 in the brain, formally called enkephalinase A (Turner, 1987). Peptides that may have been transported across the brain capillary endothelium by a process of transcytosis will be most subject to the enzymatic influences in brain interstitial fluid and on the cell membranes of neurons and glia, and peptides that may have gained access to the central nervous system across the choroids plexus will be more subject to the influences of CSF factors (Segal, 1992). Carboxypeptidase are present in the brain and CSF (Segal, 1992) and are responsible of the enzymatic degradation of peptides starting from the C-terminus. The action of carboxypeptidase on pDal can generate the tyrosine N-terminus palmitoylated tetra and pentapeptides that could still possess opioid activity on the

opioid receptor, as in the case of the N-terminus tetrapeptide and pentapeptide metabolites of dalargin (Kalenikova EI, 1988). These palmitoylated tetra and pentapeptides may contribute to the analgesic response recorded with the warm water bioassay. The presence of tyrosine is important to obtain opioid analgesia (Korobov, 1988) and specifically this is directly dependent on having a free N-terminus on the Tyrosine residue (Beckett and Casy, 1954).

In the pharmacodynamic experiment analgesia was observed only in those groups of animals dosed with the pDal nanofibres formulations with and without GCPQA polymer. The pharmacodynamic experiment was performed previously in this study using a dose of 7.5 mg/kg, as this dose was reported by Kreuters and co-workers to determine analgesia using dalargin loaded nanoparticles (Ramage et al., 1999) and apolipoprotein coated nanoparticles encapsulating dalargin (Kreuter et al., 2002), however this dose did not give rise to pronounced analgesia in the dosed mice that entered the experiment (Figure 6.16 B). The dose was then increased to 15 mg/kg to test the activity and analgesia was observed (Figure 6.16 A).

Lastly, it has to be said, since the warm water bioassay is a behavioural test, that the group of animals that received the formulation of pDal nanofibres in NaCl 0.9% (without GCPQA polymer) showed a pronounced hyperactivity in the first 30 minutes of the experiment after intravenous injection. Hyperactivity was manifested as attempts to escape the capture by the operator and refusal of entering the mouse tube restrainer. This behaviour should be taken into account when analyzing data from a behavioural test, because the outcome may be influenced by other pharmacological effects, nevertheless this does not deny the analgesic response recorded during the experiments.

In conclusion, the present study is the first report on the use of peptide amphiphile nanofibres for the delivery of peptides to the brain, proven by pharmacokinetics and pharmacodynamics studies and supported by in situ detection of the compound in the brain parenchyma using label-free CARS imaging. The peptide amphiphile pDal enjoys longer circulation times compared to the normal peptide dalargin, as the LC-MS analyses have proven, and its surfactant like architecture determines the formation of high axial ratio nanostructures that might better escape macrophage clearance and be responsible for the prolonged release of the bioactive molecule.

CHAPTER 7

Conclusions and Future Perspectives

The incidence of CNS pathologies is increasing with the increase of life expectancy, however the treatment of CNS disorders is still a challenge. The strategies employed in clinics for the treatment of neurological disorders often involve the use of invasive methodologies, such as intrathecal and intraventricular infusion of drugs. The systemic approach to the administration of drugs that are expected to elicit their pharmaceutical action at central level remains limited, and the systemic administration is often unable to achieve central therapeutically active doses. The presence of the BBB plays a key role in the exclusion of molecules from the brain parenchyma, as its physiological function is to prevent the entry of exogenous molecules that may be harmful for the CNS.

Peptides and proteins represent a class of pharmaceuticals of particular interest for the treatment of brain disorders, as they are involved in the pathogenesis and in the regulation of a wide range of neurodegenerative diseases.

In particular, for peptide and proteins technological challenges relating to the crossing of the blood-brain barrier, the instability *in vivo* and the short half-life of these molecules represent some of the key factors that have to be taken into account for the development of new strategies for brain delivery.

The size and the charge of peptide molecules prevent them from crossing the BBB, as these two factors limit the entrance of therapeutics to the CNS. In general, only a small proportion of peripherally administered drugs reaches the brain parenchyma; for example, only the 0.02% of morphine intravenously administered enters the brain parenchyma and only 0.046% of insulin (a peptide sequence of 51 amino acids), following jugular injection, reaches the brain parenchyma (Banks and Kastin, 1998).

The short half-life and the instability *in vivo* are dependent on the action of degrading enzymes present in the blood circulation and in the tissues.

Nanomedicines for peptide delivery have been developed to overcome these limitations relating drug penetration in the brain. Thus, technologies involving the use of monoclonal antibodies for the creation of fusion proteins, or molecular Trojan horses, have been developed (Boado et al., 2010). Fusion proteins can overcome the BBB by targeting specific receptors expressed on the brain endothelial cells. However, conjugation with monoclonal antibodies may determine the loss of the protein active conformation, and/or the release of the active protein involves the intervention of specific enzymes, which then need to be present at the site of interest. Albeit this approach sounds promising, the success of these technologies in a clinical setting still remains to be validated.

Nanoparticles for peptide delivery have also been investigated as potential carrier for brain delivery, as the encapsulation of the peptide in the carrier should prevent enzymatic degradation. However, most nanoparticles exploited for delivery purposes undergo rapid clearance by macrophages (Champion and Mitragotri, 2006). Despite the fact that the influence of shape on macrophage clearance it is still not entirely understood, recent reports suggest that non-spherical particles are more likely to evade macrophage uptake (Decuzzi and Ferrari, 2008, Decuzzi et al., 2010, Sharma et al., 2010), and this opens up a new scenario of investigation in the field of nanomedicine.

In general, nanoparticle strategies for the delivery of drugs to the brain result in values below 0.5% and can be as low as 0.01% ID/g (van Rooy et al., 2011a).

Based on the above-mentioned considerations regarding the inability of peptides to cross the BBB, the instability *in vivo* and the short half-life we have aimed to develop a new nanotechnology platform for the delivery of peptides to the brain. A peptide unable to cross the BBB, dalargin, was specifically chosen in order to test the working hypothesis. We decided to change the physico-chemical characteristics of the molecule by attaching a lipidic moiety in order to obtain a hydrophobic derivative that would have increased passive diffusion. The derivatization created a new chemical entity with amphipatic properties that promoted the formulation of high axial ratio nanostructures. Based also on the consideration that non-spherical nanoparticles may enjoy longer circulation times, we have focused in this work on the characterization of the elongated nanostructures formed by the newly synthesized peptide amphiphiles, thus trying to elucidate the mechanism of self-assembly.

Finally, the ability of the nanofibre technology to deliver therapeutically active doses of peptide to the brain has been assessed, proving the ability of the technology of achieving its goal.

Palmitoyl dalargin, pDal, an amphipatic derivative of dalargin has been synthesized by attachment of a palmitic chain on the lateral phenol group of tyrosin.

The self-assembly of pDa has required an energy input to result in the formation of high axial ratio nanostructures. Indeed, the formulation of nanofibres has been achieved by working out two methods of preparation: probe sonication and electromagnetic radiation heating of a pDal suspension in deionized water. Different environmental conditions, such as addition of surfactants (PF68, Tween 80, PVP), polymers (GCPQA), different media (deionized water, 0.9%NaCL, PBS, Acetate buffer) have also been considered in order to achieve control over the diameter and the length of the nanofibres. However, varying the conditions, the diameter remained constant but the length could not be controlled.

The physicochemical forces driving the self-assembly process have been thoroughly investigated. Self-assembly of peptide amphiphiles is driven by hydrophobic interactions of the alkyl chains as well as H-bonding among the amino acid sequences that give rise to the formation of β -sheet structures. Indeed, the presence of hydrophobic domains within the nanofibre was assessed by encapsulating pyrene into its hydrophobic sites. The peptide sequences formed H-bonds that confer a secondary β -sheet structure to the self-assembled nanostructures. X-ray diffraction showed the presence of a 4.8 \AA structural feature that is the typical distance of hydrogens forming H-bonds in β -sheets. Linear Dichroism fully supported the XRD findings adding further details on the tyrosine orientation: the presence of the two tyrosine peaks at 279 and 286 were found to be shifted higher in wavelength from the position that would have been expected for aqueous media, thus meaning that the tyrosine residues were inside the fiber. A negative signal around 235 nm was also observed, thus meaning that the transition moment along the O-alkyl group of the tyrosine was pointing perpendicular to the fibre long axis, confirming that the palmitoyl chains were hiding inside the fibre. Lastly, two molecular probes specific for the β -sheet conformation, such as Congo Red and Thioflavin-T were used to confirm the presence of the β -sheet conformation. The forces driving the self-assembly showed to

be prevailing on other factors, for example peptide amphiphiles self-assembly was favored also in the presence of surfactants and polymers (GCPQA) that normally encapsulate lipophilic molecules in their hydrophobic core.

Self-assembly of peptide amphiphiles has been previously reported, however the model of peptide nanofibres proposed in literature seems to deviate from reality, under the light of our findings (Hartgerink JD et al., 2003, Hamley, 2011). Peptide nanofibres are believed to result from the radial arrangement of the peptide amphiphile molecules from the fibre long axis. In this work, the peptide-peptide interaction have been investigated also performing a computational study, which shows that the palmitic chains form the hydrophobic core of the fibre and that the peptide sequences align themselves on the nanofibre surface along the long fibre axis, rather than radially, as it has been so far acknowledged.

A full thermal history profile of pDal helped to clarify the thermal properties of the monomeric starting material used for the fabrication of the nanofibres and the influence of these properties on the molecular self-assembly. Thermal analysis clarified the range of temperatures to be used for the preparation of gels made of peptide amphiphiles and experimentally it was demonstrated that by exposing a suspension of pDal in deionized water to a microwave heat equal or above the temperature of melting of the alkyl chain it was possible to form nanofibre gels. These gels might have potential applications as drug delivery system for oral or subcutaneous administration.

The nanofibres were evaluated for biological applications by testing their toxicity *in vitro* on U87MG cells. The values of IC₅₀ obtained for the formulations under investigation were of 1.26 mgmL⁻¹ for pDal nanofibres alone and of 2.39 mgmL⁻¹ for pDal nanofibres in formulation with GCPQA after 24 hours of exposure. These results suggest that nanofibres do not challenge the integrity of the cells.

Finally the ability of the peptide nanofibres to act as peptide delivery systems to the brain was evaluated *in vivo*. Pharmacokinetic studies showed that the peptide amphiphile pDal was able to enter the brain parenchyma and its presence was detected up to 4 hours following intravenous administration, in plasma as well as in

brain, while dalargin peptide was absent in both biological matrices. These data demonstrate that the lipidization of the peptide increased considerably the circulation time of the bioactive molecule, otherwise cleared in less than 3 minutes from the blood. Strikingly, the percentage of the injected doses in brain parenchyma were found to be $0.166\pm 0.035\%$ ID/g for pDal nanofibres formulated with GCPQA and $0.170\pm 0.054\%$ ID/g for pDal nanofibres alone. These results are quite remarkable not only if compared to the results for dalargin, but also considering that intravenously administered drugs have limited brain penetration, for example only 0.02% of injected morphine enters the brain and only 0.046% of insulin, as previously mentioned.

Proof of the brain penetration has been achieved using a label-free imaging technique that combines CARS and SRS: pDal was observed not only in the CNS blood capillary bead but also in the brain parenchyma. The pharmacodynamic studies showed that the nanofibre technology is able to act as a delivery system of peptides to the brain; indeed, animals receiving formulations of pDal nanofibres manifested an antinociceptive response when to a pain stimulus.

In conclusion, the present study is the first report on the use of peptide amphiphile nanofibres for the delivery of peptide to the brain.

Further formulation studies to control the shape and the length of the supramolecular assembly could help to reduce the polydispersity of the system. A chemical approach to this matter could be the addition of acid or basic amino acids, along the sequence of interest, in order to impede the formation of H-bonds, in this way the only driving force would be the hydrophobic interaction of the palmitoyl moieties. For example, in literature is shown that amphipathic peptides with positive charges in proximity of the alkyl chain (i.e. a cholesteric chain) form core shell spherical nanoparticles instead of elongated micelles such as nanofibres (Lihong Liu et al., 2009).

The ability of the nanofibres to encapsulate pyrene suggest also that nanofibres could be exploited as a carrier for hydrophobic molecules that normally do not cross the blood-brain barrier; a good candidate for delivery studies of studies would be paclitaxel, as it is known that this drug is pumped back by the P glycoprotein, thus can not reach the brain parenchyma.

The long-term safety profile of the nanofibre system should be further investigated, despite the fact that peptides can be digested and so metabolized by aminopeptidases and carboxypeptidases into their amino acid components. This is because of the fact that they are morphologically very close to amyloids and abnormal deposits of amyloids in the organs are cause of Amyloidosis (i.e. Alzheimer Disease), a variety of conditions characterized by organ dysfunction, some of which do not have a curative treatment (Merlini et al., 2011, Kolstoe and Wood, 2010).

The mechanism by which pDal molecules or nanofibres are able to cross the BBB has not been fully elucidated by the studies of transmission electron microscopy. Further study would be advisable either using CARS on an in vitro blood-brain barrier monolayer or other transmission electron microscopy studies using Se-labelled nanofibres could be performed.

Peptide nanofibres as a drug delivery carrier to the brain could also have a great potential in the treatment of Alzheimer Disease (AD). They could act as cargoes for small molecules for the treatment of Alzheimer Disease. For AD it is currently conceptualized that there exists a cascade of events to neurotoxicity commencing with protein misfolding and culminating in behavioral symptoms; blocking one of the events at the beginning of the “cascade” such as the protein misfolding of A β should stop and possibly reverse the fate of the disease (Carter et al., 2010b). Thus small hydrophobic molecules, inhibitors of A β aggregation could be used as therapeutic candidates. These include:

- Tramiprosate (Gervais et al., 2007)
- Curcumin (Garcia-Alloza et al., 2007)
- Resveratrol (Rivière C, 2007)

Also nanofibres including β -sheet breaker sequences, such as LVFF, could be evaluated for the treatment of Alzheimer Disease, for instance in vitro cells could be treated with amyloid beta (A β 42) in presence and absence of the LVFF nanofibre formulation treatment and their viability assessed via flow cytometry to measure cell death.

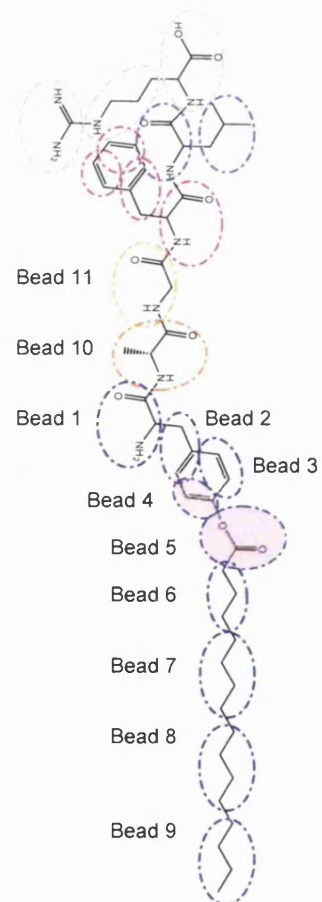
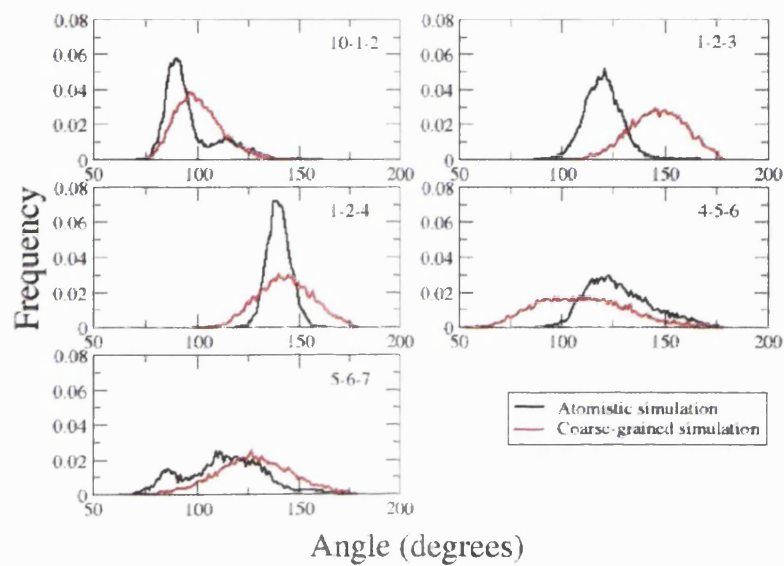
Self-assembling peptide nanostructures have shown a good potential in inducing the cell death of breast epithelial cancer cells in vitro (Standley, Toft et al. 2010).

Treatment options for brain cancer, neurodegenerative diseases and most other CNS conditions are quite limited, although a substantial breakdown of the blood-brain barrier (BBB) occurs during brain tumors at more advanced stage of the disease. This is because of the restricted transport of potential therapeutics, such as paclitaxel, within the brain parenchyma; treatment of tumor cells is likely to remain limited to the immediate vicinity of the leaky barrier. Consequently, more distant tumors or metastases remain essentially impossible to treat, thus rendering the tumor primed for a relapse. This scenario means that the key challenges of successful brain cancer treatment can be directly linked to the lack of delivery strategies able to overcome the BBB. Thus, peptide nanofibres could represent a promising drug delivery system in the treatment of brain cancer, as they could be used (1) as a carrier for small molecules and (2) as a carrier for pro-apoptotic peptide sequences.

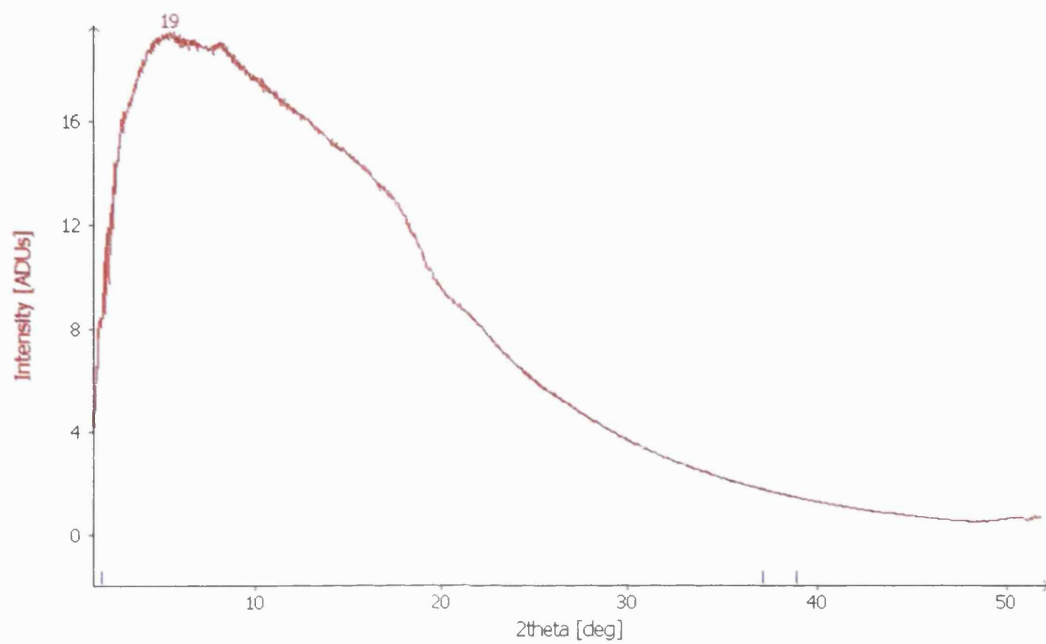
Lastly, further studies on the nanofibre gels network would also be advisable as gels could represent a good candidate for the oral or subcutaneous administration of peptides. Indeed, the peptide bioavailability via oral delivery is still a challenge because of the many barriers in the gastro-intestinal (GI) tract, represented by the proteolytic degradation and the inability of these macromolecules to penetrate the intestinal cell wall (Rekha and Sharma, 2011).

Appendix

- Angle distributions for the pDal molecule



- X-ray diffractogram of pDal gel.



References

- ABBOTT, N. J., PATABENDIGE, A. A., DOLMAN, D. E., YUSOF, S. R. & BEGLEY, D. J. 2010. Structure and function of the blood-brain barrier. *Neurobiol Dis*, 37, 13-25.
- ABRAHAM, M. H. & PLATTS, J. A. 2000. Physicochemical Factors That Influence Brain Uptake. In: BEGLEY, D. J., BRADBURY, M. W. & KREUTER, J. (eds.) *The Blood-Brain Barrier and Drug Delivery to the CNS*. New York: Marcel Dekker, Inc.
- AFERGAN, E., EPSTEIN, H., DAHAN, R., KOROUKHOV, N., ROHEKAR, K., DANENBERG, H. D. & GOLOMB, G. 2008. Delivery of serotonin to the brain by monocytes following phagocytosis of liposomes. *J Control Release*, 132, 84-90.
- AKTAS, Y., YEMISCI, M., ANDRIEUX, K., GURSOY, R. N., ALONSO, M. J., FERNANDEZ-MEGIA, E., NOVOA-CARBALLAL, R., QUINOA, E., RIGUERA, R., SARGON, M. F., CELIK, H. H., DEMIR, A. S., HINCAL, A. A., DALKARA, T., CAPAN, Y. & COUVREUR, P. 2005. Development and brain delivery of chitosan-PEG nanoparticles functionalized with the monoclonal antibody OX26. *Bioconjug Chem*, 16, 1503-11.
- AL-JAMAL, K. T., NERL, H., MULLER, K. H., ALI-BOUCETTA, H., LI, S., HAYNES, P. D., JINSCEK, J. R., PRATO, M., BIANCO, A., KOSTARELOS, K. & PORTER, A. E. 2011. Cellular uptake mechanisms of functionalised multi-walled carbon nanotubes by 3D electron tomography imaging. *Nanoscale*, 3, 2627-35.
- AMBRUOSI, A., GELPERINA, S., KHALANSKY, A., TANSKI, S., THEISEN, A. & KREUTER, J. 2006. Influence of surfactants, polymer and doxorubicin loading on the anti-tumour effect of poly(butyl cyanoacrylate) nanoparticles in a rat glioma model. *J Microencapsul*, 23, 582-92.
- ANDERSEN, C. B., HICKS, M. R., VETRI, V., VANDAHL, B., RAHBEK-NIELSEN, H., THOGERSEN, H., THOGERSEN, I. B., ENGHILD, J. J., SERPELL, L. C., RISCHER, C. & OTZEN, D. E. 2010. Glucagon Fibril Polymorphism Reflects Differences in Protofilament Backbone Structure. *Journal of Molecular Biology*, 397, 932-946.
- ANDERSON, J. M., ANDUKURI, A., LIM, D. J. & JUN, H.-W. 2009. Modulating the gelation properties of self-assembling peptide amphiphiles. *ACS Nano*, 3, 3447-54.
- ANTON, P. & LASCHEWSKY, A. 1994. Solubilization by Polysoaps. *Colloid and Polymer Science*, 272, 1118-1128.
- ASH, W. L., ZLOMISLIC, M. R., OLOO, E. O. & TIELEMAN, D. P. 2004. Computer simulations of membrane proteins. *Biochimica Et Biophysica Acta-Biomembranes*, 1666, 158-189.
- ATTENELLO, F. J., MUKHERJEE, D., DATOO, G., MCGIRT, M. J., BOHAN, E., WEINGART, J. D., OLIVI, A., QUINONES-HINOJOSA, A. & BREM, H. 2008. Use of Gliadel (BCNU) wafer in the surgical treatment of malignant glioma: A 10-year institutional experience. *Annals of Surgical Oncology*, 15, 2887-2893.

- AULISA, L., DONG, H. & HARTGERINK, J. D. 2009a. Self-assembly of multidomain peptides: sequence variation allows control over cross-linking and viscoelasticity. *Biomacromolecules*, 10, 2694-8.
- AULISA, L., FORRAZ, N., MCGUCKIN, C. & HARTGERINK, J. D. 2009b. Inhibition of cancer cell proliferation by designed peptide amphiphiles. *Acta Biomaterialia*, 5, 842-853.
- BANKS, W. A. & KASTIN, A. J. 1998. Differential permeability of the blood-brain barrier to two pancreatic peptides: insulin and amylin. *Peptides*, 19, 883-9.
- BARGONI, A., CAVALLI, R., ZARA, G. P., FUNDARO, A., CAPUTO, O. & GASCO, M. R. 2001. Transmucosal transport of tobramycin incorporated in solid lipid nanoparticles (SLN) after duodenal administration to rats. Part II--tissue distribution. *Pharmacol Res*, 43, 497-502.
- BARLOS, K., CHATZI, O., GATOS, D. & STAVROPOULOS, G. 1991. 2-Chlorotrityl chloride resin. Studies on anchoring of Fmoc-amino acids and peptide cleavage. *Int J Pept Protein Res*, 37, 513-20.
- BARLOS, K., GATOS, D., KAPOLOS, S., PAPAPHOTIU, G., SCHAFER, W. & WENQING, Y. 1989. Veresterung von partiell gesch,tzten peptid-fragmenten mit harzen. Einsatz von 2-chlortritylchlorid zur synthese von Leu15 -gastrin I. *Tetrahedron Letters*, 30, 3947-3950.
- BAUMANN, M. K., TEXTOR, M. & REIMHULT, E. 2008. Understanding self-assembled amphiphilic peptide supramolecular structures from primary structure helix propensity. *Langmuir*, 24, 7645-7647.
- BAUMGARTEN, P. K. 1971. Electrostatic spinning of acrylic microfibers. *J. Colloid Interface Sci.*, 36, 71-79.
- BBCRESEARCH.COM. 2010. *THERAPEUTIC DRUGS FOR CENTRAL NERVOUS SYSTEM (CNS) DISORDERS: TECHNOLOGIES AND GLOBAL MARKETS (PHM068A)* [Online]. Available: <http://www.bccresearch.com/report/PHM068A.html> [Accessed].
- BECKETT, A. H. & CASY, A. F. 1954. Synthetic analgesics: stereochemical considerations. *J Pharm Pharmacol*, 6, 986-1001.
- BENIASH, E., HARTGERINK, J. D., STORRIE, H., STENDAHL, J. C. & STUPP, S. I. 2005. Self-assembling peptide amphiphile nanofiber matrices for cell entrapment. *Acta Biomater*, 1, 387-97.
- BICKEL, U. 1995. Antibody delivery through the blood-brain barrier. *Adv Drug Deliv Rev*, 15, 53-72.
- BICKEL, U. 2005. How to measure drug transport across the blood-brain barrier. *NeuroRX*, 2, 15-26.
- BLASI, P., GIOVAGNOLI, S., SCHOUBBEN, A., RICCI, M. & ROSSI, C. 2007. Solid lipid nanoparticles for targeted brain drug delivery. *Adv Drug Deliv Rev*, 59, 454-77.
- BOADO, R. J. 2007. Blood-brain barrier transport of non-viral gene and RNAi therapeutics. *Pharm Res*, 24, 1772-87.
- BOADO, R. J., ZHOU, Q. H., LU, J. Z., HUI, E. K. & PARDRIDGE, W. M. 2010. Pharmacokinetics and brain uptake of a genetically engineered bifunctional fusion antibody targeting the mouse transferrin receptor. *Mol Pharm*, 7, 237-44.
- BODOR, N. & BUCHWALD, P. 1999. Recent advances in the brain targeting of neuropharmaceuticals by chemical delivery systems. *Advanced Drug Delivery Reviews*, 36, 229-254.

- BOLGEN, N., VARGEL, I., KORKUSUZ, P., MENCELOGLU, Y. Z. & PISKIN, E. 2007. In vivo performance of antibiotic embedded electrospun PCL membranes for prevention of abdominal adhesions. *J Biomed Mater Res B Appl Biomater*, 81, 530-43.
- BOSE, P. P. & BANERJEE, A. 2010. Template-directed nucleation and growth of CdS nanocrystal: the role of helical and nonhelical nanofibers on their shape and size. *Journal of Nanoparticle Research*, 12, 713-718.
- BRASNJEVIC, I., STEINBUSCH, H. W., SCHMITZ, C. & MARTINEZ-MARTINEZ, P. 2009. Delivery of peptide and protein drugs over the blood-brain barrier. *Prog Neurobiol*, 87, 212-51.
- BRENNAN, C. E. 1995. Cavitation and Boiling. In: PRESS, O. U. (ed.) *Cavitation and Bubble Dynamics*.
- BREWER, E. & HENION, J. 1998. Atmospheric pressure ionization LC/MS/MS techniques for drug disposition studies. *Journal of Pharmaceutical Sciences*, 87, 395-402.
- BROOKS, B., BRUCCOLERI, R., OLAFSON, B., STATES, D., SWAMINATHAN, S. & KARPLUS, M. 1983. A program for macromolecular energy, minimization, and dynamics calculations. *Journal of Computational Chemistry*, 1983, 187-217.
- BRUCE CASSEL, R. 2008. High Heating Rate DSC. *TA Technical Notes*, TA 297, 1-11.
- BRUYLANTS, G., WOUTERS, J. & MICHAUX, C. 2005. Differential scanning calorimetry in life science: thermodynamics, stability, molecular recognition and application in drug design. *Curr Med Chem*, 12, 2011-20.
- CALVO, P., GOURITIN, B., CHACUN, H., DESMAELE, D., D'ANGELO, J., NOEL, J. P., GEORGIN, D., FATTAL, E., ANDREUX, J. P. & COUVREUR, P. 2001. Long-circulating PEGylated polycyanoacrylate nanoparticles as new drug carrier for brain delivery. *Pharm Res*, 18, 1157-66.
- CAO, H. Q., LIU, T. & CHEW, S. Y. 2009. The application of nanofibrous scaffolds in neural tissue engineering. *Advanced Drug Delivery Reviews*, 61, 1055-1064.
- CARDOSO, F. L., BRITES, D. & BRITO, M. A. 2010. Looking at the blood-brain barrier: Molecular anatomy and possible investigation approaches. *Brain Research Reviews*, 64, 328-363.
- CARLTON, R. A. 2011a. Polarized Light Microscopy. In: CARLTON, R. A. (ed.) *Pharmaceutical Microscopy*. Springer.
- CARLTON, R. A. 2011b. Thermal Microscopy. In: CARLTON, R. A. (ed.) *Pharmaceutical Microscopy*. Springer.
- CARNALL, J. M., WAUDBY, C. A., BELENGUER, A. M., STUART, M. C., PEYRALANS, J. J. & OTTO, S. 2010. Mechanosensitive self-replication driven by self-organization. *Science*, 327, 1502-6.
- CARPINO L.A, H. S., SALVATORE TRIOLO, EL-SAYED MANSOUR, HOLGER WENSCHUH, FERNANDO ALBERICIO 1993. The 2,2,4,6,7-pentamethyldihydrobenzofuran-5-sulfonyl group (Pbf) as arginine side chain protectant. *Tetrahedron Letters*, 34, 7829-7832.
- CARTER, D. B. & CHOU, K. C. 1998. A model for structure-dependent binding of Congo red to Alzheimer beta-amyloid fibrils. *Neurobiol Aging*, 19, 37-40.
- CARTER, M. D., SIMMS, G. A. & WEAVER, D. F. 2010a. The development of new therapeutics for Alzheimer's disease. *Clin Pharmacol Ther*, 88, 475-86.

- CARTER, M. D., SIMMS, G. A. & WEAVER, D. F. 2010b. The Development of New Therapeutics for Alzheimer's Disease. *Clinical Pharmacology & Therapeutics*, **88**, 475-486.
- CASTELLETTO, V., HAMLEY, I. W., PEREZ, J., ABEZGAUZ, L. & DANINO, D. 2010a. Fibrillar superstructure from extended nanotapes formed by a collagen-stimulating peptide. *Chem Commun (Camb)*, **46**, 9185-7.
- CASTELLETTO, V., NUTT, D. R., HAMLEY, I. W., BUCAK, S., CENKER, C. & OLSSON, U. 2010b. Structure of single-wall peptide nanotubes: in situ flow aligning X-ray diffraction. *Chem Commun (Camb)*, **46**, 6270-2.
- CHAMPION, J. A. & MITRAGOTRI, S. 2006. Role of target geometry in phagocytosis. *Proc Natl Acad Sci U S A*, **103**, 4930-4.
- CHAN W.C, W. P. D. 2000. Fmoc Solid Phase Peptide Synthesis. 28.
- CHE, C., YANG, G., THIOT, C., LACOSTE, M. C., CURRIE, J. C., DEMEULE, M., REGINA, A., BELIVEAU, R. & CASTAIGNE, J. P. 2010. New Angiopep-modified doxorubicin (ANG1007) and etoposide (ANG1009) chemotherapeutics with increased brain penetration. *J Med Chem*, **53**, 2814-24.
- CHENG, W. P., GRAY, A. I., TETLEY, L., HANG TLE, B., SCHATZLEIN, A. G. & UCHEGBU, I. F. 2006. Polyelectrolyte nanoparticles with high drug loading enhance the oral uptake of hydrophobic compounds. *Biomacromolecules*, **7**, 1509-20.
- CHIAPPINI, C., TASCIOTTI, E., FAKHOURY, J. R., FINE, D., PULLAN, L., WANG, Y. C., FU, L., LIU, X. & FERRARI, M. 2010. Tailored porous silicon microparticles: fabrication and properties. *Chemphyschem*, **11**, 1029-35.
- CHOI, J. S. & YOO, H. S. 2010. Nano-inspired fibrous matrix with bi-phasic release of proteins. *J Nanosci Nanotechnol*, **10**, 3038-45.
- CHU-KUNG, A. F., BOZZELLI, K. N., LOCKWOOD, N. A., HASEMAN, J. R., MAYO, K. H. & TIRRELL, M. V. 2004. Promotion of peptide antimicrobial activity by fatty acid conjugation. *Bioconjug Chem*, **15**, 530-5.
- CORNFORD, E. M., HYMAN, S. & SWARTZ, B. E. 1994. The human brain GLUT1 glucose transporter: ultrastructural localization to the blood-brain barrier endothelia. *J Cereb Blood Flow Metab*, **14**, 106-12.
- COSTANTINO, L., TOSI, G., RUOZI, B., BONDIOLI, L., VANDELLI, M. A. & FORNI, F. 2009. Colloidal Systems for CNS drug delivery. In: SHARMA, C. P. (ed.) *Progress in Brain Research* London: Elsevier.
- CUI, H., MURAOKA, T., CHEETHAM, A. G. & STUPP, S. I. 2009. Self-Assembly of Giant Peptide Nanobelts. *Nano Letters*, **9**, 945-951.
- CUI, H., WEBBER, M. J. & STUPP, S. I. 2010. Self-assembly of peptide amphiphiles: from molecules to nanostructures to biomaterials. *Biopolymers*, **94**, 1-18.
- D'EMANUELE, A. & ATTWOOD, D. 2005. Dendrimer-drug interactions. *Adv Drug Deliv Rev*, **57**, 2147-62.
- DAI, H. J., LIU, Z., CAI, W. B., HE, L. N., NAKAYAMA, N., CHEN, K., SUN, X. M. & CHEN, X. Y. 2007. In vivo biodistribution and highly efficient tumour targeting of carbon nanotubes in mice. *Nature Nanotechnology*, **2**, 47-52.
- DAJANI, E. Z., PENIN, V. A., SOKOLOV, L. K., VAHTANGISHVILLI, R., BOGDANOV, A., AFONSKAYA, N., IVANISHVILLI, L., ZHAROVA, Y. & EFREMOVA, I. 1991. Misoprostol and dalargin for the inpatient treatment of duodenal ulcer in the USSR. *J Assoc Acad Minor Phys*, **2**, 18-22.

- DAS, D. & LIN, S. 2005. Double-coated poly (butylcyanoacrylate) nanoparticulate delivery systems for brain targeting of dalargin via oral administration. *J Pharm Sci*, 94, 1343-53.
- DAVIES, P. M. 2005. Opioid Therapy. In: PAPPAGALLO, M. (ed.) *The neurological Basis of Pain*. New York: McGraw-Hill Companies, Inc.
- DE BOER, A. G. & GAILLARD, P. J. 2007. Drug targeting to the brain. *Annual Review of Pharmacology and Toxicology*, 47, 323-355.
- DE LA FUENTE, M., RAVINA, M., PAOLICELLI, P., SANCHEZ, A., SEIJO, B. & ALONSO, M. J. 2010. Chitosan-based nanostructures: a delivery platform for ocular therapeutics. *Adv Drug Deliv Rev*, 62, 100-17.
- DEBINSKI, W. & TATTER, S. B. 2010. Convection-enhanced delivery to achieve widespread distribution of viral vectors: Predicting clinical implementation. *Curr Opin Mol Ther*, 12, 647-53.
- DECUZZI, P. & FERRARI, M. 2008. The receptor-mediated endocytosis of nonspherical particles. *Biophys J*, 94, 3790-7.
- DECUZZI, P., GODIN, B., TANAKA, T., LEE, S. Y., CHIAPPINI, C., LIU, X. & FERRARI, M. 2010. Size and shape effects in the biodistribution of intravascularly injected particles. *J Control Release*, 141, 320-7.
- DENG, M., YU, D., HOU, Y. & WANG, Y. 2009a. Self-assembly of peptide-amphiphile C12-Abeta(11-17) into nanofibrils. *J Phys Chem B*, 113, 8539-44.
- DENG, M. L., YU, D. F., HOU, Y. B. & WANG, Y. L. 2009b. Self-assembly of Peptide-Amphiphile C-12-A beta(11-17) into Nanofibrils. *Journal of Physical Chemistry B*, 113, 8539-8544.
- DERMIETZEL, R., SPRAY, D. C. & NEDERGAARD, M. 2006. *Blood-brain barriers : from ontogeny to artificial interfaces*, Weinheim ; [Chichester], Wiley-VCH.
- DETERMANN, H. 1964. Chromatographic Separations on Porous Gels. *Angewandte Chemie International Edition English*, 3, 608-617.
- DIVRY, P. & FLORKIN, M. 1927. Sur les proprietes optiques de l'amyloide. *C.R. Soc. Biol*, 97, 1808-1810.
- DUFES, C. 2011. Brain Delivery of Peptide and Proteins. In: C, V. D. W. (ed.) *Peptide and Protein Delivery*. London: Elsevier.
- EL-ANEED, A., COHEN, A. & BANOUB, J. 2009. Mass spectrometry, review of the basics: electrospray, MALDI, and commonly used mass analyzers. *Appl. Spectroscop. Rev*, 44, 210-230.
- ELLIS-BEHNKE, R. G., LIANG, Y. X., TAY, D. K., KAU, P. W., SCHNEIDER, G. E., ZHANG, S., WU, W. & SO, K. F. 2006a. Nano hemostat solution: immediate hemostasis at the nanoscale. *Nanomedicine*, 2, 207-15.
- ELLIS-BEHNKE, R. G., LIANG, Y. X., YOU, S. W., TAY, D. K., ZHANG, S., SO, K. F. & SCHNEIDER, G. E. 2006b. Nano neuro knitting: peptide nanofiber scaffold for brain repair and axon regeneration with functional return of vision. *Proc Natl Acad Sci U S A*, 103, 5054-9.
- ELLIS-BEHNKE, R. G. & SCHNEIDER, G. E. 2011. Peptide amphiphiles and porous biodegradable scaffolds for tissue regeneration in the brain and spinal cord. *Methods Mol Biol*, 726, 259-81.
- EPSRC. 2009. *Engineering and Physical Research Council* [Online]. Available: <http://gow.epsrc.ac.uk/ViewPanelROL.aspx?PanelId=4809&RankingListId=6429> [Accessed].
- FANDRICH, M., MEINHARDT, J. & GRIGORIEFF, N. 2009. Structural polymorphism of Alzheimer Abeta and other amyloid fibrils. *Prion*, 3, 89-93.

- FERGUSON, S. D., FOSTER, K. & YAMINI, B. 2007. Convection-enhanced delivery for treatment of brain tumors. *Expert Rev Anticancer Ther*, 7, S79-85.
- FIELDS, G. B. 1997. *Solid-phase peptide synthesis*, San Diego ; London, Academic.
- FISCHER, H., GOTTSCHLICH, R. & SEELIG, A. 1998. Blood-brain barrier permeation: molecular parameters governing passive diffusion. *J Membr Biol*, 165, 201-11.
- FLORENCE, A. T. & ATTWOOD, D. 1998. *Physicochemical principles of pharmacy*, Basingstoke, Macmillan.
- FOLDVARI, M., ATTAH-POKU, S., HU, J., LI, Q., HUGHES, H., BABIUK, L. A. & KRUGER, S. 1998. Palmitoyl derivatives of interferon alpha: potential for cutaneous delivery. *J Pharm Sci*, 87, 1203-8.
- FORMHALS, A. 1938. *Method and apparatus for the production of fibers*. US patent application.
- FORNS, P., LAUER-FIELDS, J. L., GAO, S. & FIELDS, G. B. 2000. Induction of protein-like molecular architecture by monoalkyl hydrocarbon chains. *Biopolymers*, 54, 531-546.
- FRANCIS, M. F., PIREDDA, M. & WINNIK, F. M. 2003. Solubilization of poorly water soluble drugs in micelles of hydrophobically modified hydroxypropylcellulose copolymers. *J Control Release*, 93, 59-68.
- FREITAS, C. & MULLER, R. H. 1999. Correlation between long-term stability of solid lipid nanoparticles (SLN) and crystallinity of the lipid phase. *Eur J Pharm Biopharm*, 47, 125-32.
- FREUDIGER CW, W. M., BRIAN G SAAR, SIJIA LU, GARY R HOLTON, CHENGWEI HE, JASON C. TSAI, JING X KANG, X SUNNEY XIE 2008. Label-free Biomedical Imaging with High Sensitivity by stimulated Raman Scattering Microscopy. *Science*, 322, 1857-1861.
- FRISCH, M. J. T., G. W.; SCHLEGEL, H. B.; SCUSERIA, G. E.; ROBB, M. A.; CHEESEMAN, J. R.; MONTGOMERY, JR., J. A.; VREVEN, T.; KUDIN, K. N.; BURANT, J. C.; MILLAM, J. M.; IYENGAR, S. S.; TOMASI, J.; BARONE, V.; MENNUCCI, B.; COSSI, M.; SCALMANI, G.; REGA, N.; PETERSSON, G. A.; NAKATSUJI, H.; HADA, M.; EHARA, M.; TOYOTA, K.; FUKUDA, R.; HASEGAWA, J.; ISHIDA, M.; NAKAJIMA, T.; HONDA, Y.; KITAO, O.; NAKAI, H.; KLENE, M.; LI, X.; KNOX, J. E.; HRATCHIAN, H. P.; CROSS, J. B.; BAKKEN, V.; ADAMO, C.; JARAMILLO, J.; GOMPERS, R.; STRATMANN, R. E.; YAZYEV, O.; AUSTIN, A. J.; CAMMI, R.; POMELLI, C.; OCHTERSKI, J. W.; AYALA, P. Y.; MOROKUMA, K.; VOTH, G. A.; SALVADOR, P.; DANNENBERG, J. J.; ZAKRZEWSKI, V. G.; DAPPRICH, S.; DANIELS, A. D.; STRAIN, M. C.; FARKAS, O.; MALICK, D. K.; RABUCK, A. D.; RAGHAVACHARI, K.; FORESMAN, J. B.; ORTIZ, J. V.; CUI, Q.; BABOUL, A. G.; CLIFFORD, S.; CIOSLOWSKI, J.; STEFANOV, B. B.; LIU, G.; LIASHENKO, A.; PISKORZ, P.; KOMAROMI, I.; MARTIN, R. L.; FOX, D. J.; KEITH, T.; AL-LAHAM, M. A.; PENG, C. Y.; NANAYAKKARA, A.; CHALLACOMBE, M.; GILL, P. M. W.; JOHNSON, B.; CHEN, W.; WONG, M. W.; GONZALEZ, C.; AND POPLA, J. A 2004. Gaussian 03, Revision C.02. Wallingford CT: Gaussian, Inc.
- FROMM, M. F. 2004. Importance of P-glycoprotein at blood-tissue barriers. *Trends Pharmacol Sci*, 25, 423-9.
- GAILLARD, P. J. & DE BOER, A. G. 2006. A novel opportunity for targeted drug delivery to the brain. *J Control Release*, 116, e60-2.

- GAISFORD, S. 2007. Role of Calorimetry in Preformulation Studies. In: GAISFORD, S. & O'NEILL, M. A. (eds.) *Pharmaceutical Isothermal Calorimetry*. New York: Informa Helathcare, Inc.
- GALLO, J. M., LI, S., GUO, P., REED, K. & MA, J. 2003. The effect of P-glycoprotein on paclitaxel brain and brain tumor distribution in mice. *Cancer Res*, 63, 5114-7.
- GAO, S., CHEN, J., XU, X., DING, Z., YANG, Y. H., HUA, Z. & ZHANG, J. 2003. Galactosylated low molecular weight chitosan as DNA carrier for hepatocyte-targeting. *Int J Pharm*, 255, 57-68.
- GARCIA-ALLOZA, M., BORRELLI, L. A., ROZKALNE, A., HYMAN, B. T. & BACSKAI, B. J. 2007. Curcumin labels amyloid pathology in vivo, disrupts existing plaques, and partially restores distorted neurites in an Alzheimer mouse model. *J Neurochem*, 102, 1095-104.
- GELAIN, F., UNSWORTH, L. D. & ZHANG, S. 2010. Slow and sustained release of active cytokines from self-assembling peptide scaffolds. *J Control Release*.
- GENG, Y., DALHAIMER, P., CAI, S., TSAI, R., TEWARI, M., MINKO, T. & DISCHER, D. E. 2007. Shape effects of filaments versus spherical particles in flow and drug delivery. *Nature Nanotechnology*, 2, 249-55.
- GENG Y, D. P., CAI S, TSAI R, TEWARI M, MINKO T, DISCHER DE 2007. Shape effects of filaments versus spherical particles in flow and drug delivery. *Nature Nanotechnology*, 2, 249-55.
- GERVAIS, F., PAQUETTE, J., MORISSETTE, C., KRZYWKOWSKI, P., YU, M., AZZI, M., LACOMBE, D., KONG, X., AMAN, A., LAURIN, J., SZAREK, W. A. & TREMBLAY, P. 2007. Targeting soluble Abeta peptide with Tramiprosate for the treatment of brain amyloidosis. *Neurobiol Aging*, 28, 537-47.
- GHANAATI, S., WEBBER, M. J., UNGER, R. E., ORTH, C., HULVAT, J. F., KIEHNA, S. E., BARBECK, M., RASIC, A., STUPP, S. I. & KIRKPATRICK, C. J. 2009. Dynamic in vivo biocompatibility of angiogenic peptide amphiphile nanofibers. *Biomaterials*, 30, 6202-12.
- GILL, P., MOGHADAM, T. T. & RANJBAR, B. 2010. Differential scanning calorimetry techniques: applications in biology and nanoscience. *J Biomol Tech*, 21, 167-93.
- GLANGCHAI, L. C., CALDORERA-MOORE, M., SHI, L. & ROY, K. 2008. Nanoimprint lithography based fabrication of shape-specific, enzymatically-triggered smart nanoparticles. *J Control Release*, 125, 263-72.
- GLEESON, M. P. 2008. Generation of a set of simple, interpretable ADMET rules of thumb. *J Med Chem*, 51, 817-34.
- GULER, M. O., CLAUSSEN, R. C. & STUPP, S. I. 2005. Encapsulation of pyrene within self-assembled peptide amphiphile nanofibers. *Journal of Materials Chemistry*, 15, 4507-4512.
- GULER, M. O., HSU, L., SOUKASENE, S., HARRINGTON, D. A., HULVAT, J. F. & STUPP, S. I. 2006. Presentation of RGDS epitopes on self-assembled nanofibers of branched peptide amphiphiles. *Biomacromolecules*, 7, 1855-1863.
- HAINES, P. J. 2002. *Principles of thermal analysis and calorimetry*, Cambridge, Royal Society of Chemistry.
- HAMLEY, I. W. 2011. Self-assembly of amphiphilic peptides. *Soft Matter*, 7, 4122-4138.

- HAMLEY, I. W., CASTELLETTO, V., MOULTON, C. M., RODRIGUEZ-PEREZ, J., SQUIRES, A. M., ERALP, T., HELD, G., HICKS, M. R. & RODGER, A. 2010. Alignment of a model amyloid Peptide fragment in bulk and at a solid surface. *J Phys Chem B*, 114, 8244-54.
- HAMLEY, I. W., KRYSMANN, M. J., KELARAKIS, A., CASTELLETTO, V., NOIREZ, L., HULE, R. A. & Pochan, D. J. 2008. Nematic and columnar ordering of a PEG-peptide conjugate in aqueous solution. *Chemistry*, 14, 11369-75.
- HARTGERINK JD, BENIASH E & SI, S. 2003. Self-assembling and mineralization of peptide amphiphile nanofiber. *Science*, 294, 1684-1688.
- HARTGERINK, J. D., BENIASH, E. & STUPP, S. I. 2001. Self-assembly and mineralization of peptide-amphiphile nanofibers. *Science*, 294, 1684-1688.
- HAYEK, S. M., DEER, T. R., POPE, J. E., PANCHAL, S. J. & PATEL, V. B. 2011. Intrathecal therapy for cancer and non-cancer pain. *Pain Physician*, 14, 219-48.
- HAYNIE, D. T. 2008. *Biological thermodynamics*, Cambridge, Cambridge University Press.
- HEJAZI, R. & AMIJI, M. 2003. Chitosan-based gastrointestinal delivery systems. *J Control Release*, 89, 151-65.
- HENKEL, M., PLEIMLING, M. & SANCTUARY, R. 2007. *Ageing and the glass transition*, Berlin, Springer.
- HERVE, F., GHINEA, N. & SCHERRMANN, J. M. 2008. CNS delivery via adsorptive transcytosis. *AAPS J*, 10, 455-72.
- HESS, B. 2008. P-LINCS: A parallel linear constraint solver for molecular simulation. *Journal of Chem. Theory Comput.*, 4, 116-122.
- HICKS, M. R., KOWALSKI, J. & RODGER, A. 2010. LD spectroscopy of natural and synthetic biomaterials. *Chem Soc Rev*, 39, 3380-93.
- HOKE, S. H., MORAND, K. L., GREIS, K. D., BAKER, T. R., HARBOL, K. L. & DOBSON, R. L. M. 2001. Transformations in pharmaceutical research and development, driven by innovations in multidimensional mass spectrometry-based technologies. *International Journal of Mass Spectrometry*, 212, 135-196.
- HONEYCUTT, L., WANG, J., EKRAMI, H. & SHEN, W. C. 1996. Comparison of pharmacokinetic parameters of a polypeptide, the Bowman-Birk protease inhibitor (BBI), and its palmitic acid conjugate. *Pharm Res*, 13, 1373-7.
- HOOVER, W. G. 1985. Canonical dynamics: Equilibrium phase-space distributions. *Physical Review A*, 31, 1695-1697.
- HOPKINS, A. M., LI, D., MRSNY, R. J., WALSH, S. V. & NUSRAT, A. 2000. Modulation of tight junction function by G protein-coupled events. *Adv Drug Deliv Rev*, 41, 329-40.
- HUANG, R. Q., QU, Y. H., KE, W. L., ZHU, J. H., PEI, Y. Y. & JIANG, C. 2007. Efficient gene delivery targeted to the brain using a transferrin-conjugated polyethyleneglycol-modified polyamidoamine dendrimer. *Faseb Journal*, 21, 1117-1125.
- HUNT, B. J. & HOLDING, S. R. 1989. *Size exclusion chromatography*, Blackie.
- HYUNG PARK, J., KWON, S., LEE, M., CHUNG, H., KIM, J. H., KIM, Y. S., PARK, R. W., KIM, I. S., BONG SEO, S., KWON, I. C. & YOUNG JEONG, S. 2006. Self-assembled nanoparticles based on glycol chitosan bearing hydrophobic moieties as carriers for doxorubicin: in vivo biodistribution and anti-tumor activity. *Biomaterials*, 27, 119-26.

- ILLUM, L. 1998. Chitosan and its use as a pharmaceutical excipient. *Pharm Res*, 15, 1326-31.
- J F DEEKEN, W. L. 2007. The blood brain barrier and cancer: Transporters, treatment, and Trojan horses. *Clinical Cancer Research*, 13.
- JALLOULI, Y., PAILLARD, A., CHANG, J., SEVIN, E. & BETBEDER, D. 2007. Influence of surface charge and inner composition of porous nanoparticles to cross blood-brain barrier in vitro. *Int J Pharm*, 344, 103-9.
- JANG, B. J., CASTANO, O. & KIM, H. W. 2009. Electrospun Materials as Potential Platforms for bone tissue engineering. *Advanced Drug Delivery Reviews*, 61, 1065-1083.
- JIN, L. W., CLABORN, K. A., KURIMOTO, M., GEDAY, M. A., MAEZAWA, I., SOHRABY, F., ESTRADA, M., KAMINKSY, W. & KAHR, B. 2003. Imaging linear birefringence and dichroism in cerebral amyloid pathologies. *Proc Natl Acad Sci U S A*, 100, 15294-8.
- JORGENSEN, W. L., CHANDRASEKHAR, J., MADURE, J., IMPEY, R. & KLEIN, M. 1983. Comparison of simple potential functions for simulating liquid water. *Journal of Chemical Physics*, 79, 926-935.
- KAFKA, A. P., KLEFFMANN, T., RADES, T. & MCDOWELL, A. 2010. The application of MALDI TOF MS in biopharmaceutical research. *Int J Pharm*.
- KAISER, E., COLESCOTT, R. L., BOSSINGER, C. D. & COOK, P. I. 1970. Color test for detection of free terminal amino groups in the solid-phase synthesis of peptides. *Anal Biochem*, 34, 595-8.
- KALENIKOVA EI, D. O., KOROBOV NN, ZHUKOVA SV, TISHENKO VA 1988. Farmakokinetika Dalargina. *Vopr. Med. Khim.*, 34, 75-83.
- KALYANASUNDARAM, K. & THOMAS, J. K. 1977. Environmental Effects on Vibronic Band Intensities in Pyrene Monomer Fluorescence and Their Application in Studies of Micellar Systems. *Journal of the American Chemical Society*, 99, 2039-2044.
- KANAZAWA, T., TAKI, H., TANAKA, K., TAKASHIMA, Y. & OKADA, H. 2011. Cell-Penetrating Peptide-Modified Block Copolymer Micelles Promote Direct Brain Delivery via Intranasal Administration. *Pharm Res*.
- KANE, B. E., SVENSSON, B. & FERGUSON, D. M. 2006. Molecular recognition of opioid receptor ligands. *AAPS J*, 8, E126-37.
- KASTIN, A. J. & PAN, W. 2010. Concepts for biologically active peptides. *Curr Pharm Des*, 16, 3390-400.
- KE, W., SHAO, K., HUANG, R., HAN, L., LIU, Y., LI, J., KUANG, Y., YE, L., LOU, J. & JIANG, C. 2009. Gene delivery targeted to the brain using an Angiopep-conjugated polyethyleneglycol-modified polyamidoamine dendrimer. *Biomaterials*, 30, 6976-85.
- KILEY, P., ZHAO, X., VAUGHN, M., BALDO, M. A., BRUCE, B. D. & ZHANG, S. 2005. Self-assembling peptide detergents stabilize isolated photosystem I on a dry surface for an extended time. *PLoS Biol*, 3, e230.
- KIM, J. H., KIM, Y. S., PARK, K., KANG, E., LEE, S., NAM, H. Y., KIM, K., PARK, J. H., CHI, D. Y., PARK, R. W., KIM, I. S., CHOI, K. & CHAN KWON, I. 2008. Self-assembled glycol chitosan nanoparticles for the sustained and prolonged delivery of antiangiogenic small peptide drugs in cancer therapy. *Biomaterials*, 29, 1920-30.
- KNIGHT, D. K., SHAPKA, S. N. & AMSDEN, B. G. 2007. Structure, depolymerization, and cytocompatibility evaluation of glycol chitosan. *J Biomed Mater Res A*, 83, 787-98.

- KOHLER, K. & ZAHRAOUI, A. 2005. Tight junction: a co-ordinator of cell signalling and membrane trafficking. *Biol Cell*, 97, 659-65.
- KOLSTOE, S. E. & WOOD, S. P. 2010. Drug targets for amyloidosis. *Biochem Soc Trans*, 38, 466-70.
- KOROBOV, N. 1988. Dalargin--an opioid-like peptide with peripheral action. *Farmakol Tokikol*, 51, 35-38.
- KOSTARELOS, K. 2010. Carbon Nanotubes Fibrillar Pharmacology. *Nature Materials*, 9, 793-795.
- KOZIARA, J. M., LOCKMAN, P. R., ALLEN, D. D. & MUMPER, R. J. 2004. Paclitaxel nanoparticles for the potential treatment of brain tumors. *J Control Release*, 99, 259-69.
- KREBS, M. R., MACPHEE, C. E., MILLER, A. F., DUNLOP, I. E., DOBSON, C. M. & DONALD, A. M. 2004. The formation of spherulites by amyloid fibrils of bovine insulin. *Proc Natl Acad Sci U S A*, 101, 14420-4.
- KREBS, M. R. H., BROMLEY, E. H. C. & DONALD, A. M. 2005a. The binding of thioflavin-T to amyloid fibrils: localisation and implications. *Journal of Structural Biology*, 149, 30-37.
- KREBS, M. R. H., BROMLEY, E. H. C. & DONALD, A. M. 2005b. The binding of thioflavin-T to amyloid fibrils: localisation and implications. *Journal of Structural Biology*, 149, 30-37.
- KREUTER, J. 2006a. Nanoparticulate Carriers for Drug Delivery to the brain. In: TORCHILLIN, V. (ed.) *Nanoparticulates as Drug Carriers*. London: Imperial College Press.
- KREUTER, J. 2006b. Nanoparticulate carriers for Drug Delivery to the brain. In: TORCHILLIN, V. (ed.) *Nanoparticulate as Drug Carriers*. London: Imperial College Press.
- KREUTER, J., HEKMATARAA, T., DREISA, S., VOGELB, T., GELPERINAD, S. & LANGER, K. 2007. Covalent attachment of apolipoprotein A-I and apolipoprotein B-100 to albumin nanoparticles enables drug transport into the brain. *Journal of Controlled Release*, 118, 54-58.
- KREUTER, J., RAMGE, P., PETROV, V., HAMM, S., GELPERINA, S. E., ENGELHARDT, B., ALYAUDIN, R., VON BRIESEN, H. & BEGLEY, D. J. 2003. Direct evidence that polysorbate-80-coated poly(butylcyanoacrylate) nanoparticles deliver drugs to the CNS via specific mechanisms requiring prior binding of drug to the nanoparticles. *Pharm Res*, 20, 409-16.
- KREUTER, J., SHAMENKOV, D., PETROV, V., RAMGE, P., CYCHUTEK, K., KOCH-BRANDT, C. & ALYAUDIN, R. 2002. Apolipoprotein-mediated transport of nanoparticle-bound drugs across the blood-brain barrier. *J Drug Target*, 10, 317-25.
- KRIEGER, D. 1983. Brain peptides: What, where, and why? *Science*, 222, 975-985.
- LALATSA, A. 2009. *Carbohydrate nanoparticles for peptide delivery to the CNS*. Doctor of Philosophy, The School of Pharmacy, University of London.
- LE BARS, D., GOZARIU, M. & CADDEN, S. W. 2001. Animal models of nociception. *Pharmacological Reviews*, 53, 597-652.
- LECHUGA-BALLESTEROS, D., ABDUL-FATTAH, A., STEVENSON, C. L. & BENNETT, D. B. 2003. Properties and stability of a liquid crystal form of cyclosporine-the first reported naturally occurring peptide that exists as a thermotropic liquid crystal. *J Pharm Sci*, 92, 1821-31.
- LEE, J. Y., CHOO, J. E., CHOI, Y. S., SUH, J. S., LEE, S. J., CHUNG, C. P. & PARK, Y. J. 2009. Osteoblastic differentiation of human bone marrow stromal

- cells in self-assembled BMP-2 receptor-binding peptide-amphiphiles. *Biomaterials*, 30, 3532-3541.
- LEE, M. N. & MOHRAZ, A. 2010. Bicontinuous macroporous materials from bijel templates. *Adv Mater*, 22, 4836-41.
- LEE, O. S., STUPP, S. I. & SCHATZ, G. C. 2011. Atomistic Molecular Dynamics Simulations of Peptide Amphiphile Self-Assembly into Cylindrical Nanofibers. *Journal of the American Chemical Society*, 133, 3677-3683.
- LEVIN, V. 1980. Relationship of octanol/water partition coefficients and molecular weight to rat brain capillary permeability. *J. Med. Chem.*, 23, 682-684.
- LEVINE, H. 1993. Thioflavin-T interactions with amyloid β -sheet structures. *Amyloid*, 2, 1-6.
- LEWIS, D. F., JACOBS, M. N. & DICKINS, M. 2004. Compound lipophilicity for substrate binding to human P450s in drug metabolism. *Drug Discov Today*, 9, 530-7.
- LIHONG LIU, KAIJIN XU, HUAYING WANG, JEREMY TAN, WEIMIN FAN, SUBBU S. VENKATRAMAN, LANJUAN LI & YANG, Y.-Y. 2009. Self-assembled cationic peptide nanoparticles as an efficient antimicrobial agent. *Nature Nanotechnology*, 4, 457-463.
- LIM, M. S. & ELENOTIBA-JOHNSON, K. S. J. 2004. Proteomics in pathology research. *Laboratory Investigation*, 84, 1227-1244.
- LIM, S. H. & MAO, H. Q. 2009. Electrospun scaffolds for stem cell engineering. *Advanced Drug Delivery Reviews*, 61, 1084-1096.
- LIN, J. H. & LU, A. Y. 1997. Role of pharmacokinetics and metabolism in drug discovery and development. *Pharmacol Rev*, 49, 403-49.
- LIPINSKI, C. A. 2000. Drug-like properties and the causes of poor solubility and poor permeability. *J Pharmacol Toxicol Methods*, 44, 235-49.
- LOCHMAN, P., PLODR, M., PARAL, J. & SMEJKAL, K. 2010. Nanofiber micro-dispersed oxidized cellulose as a carrier for topical antimicrobials: first experience. *Surg Infect (Larchmt)*, 11, 29-32.
- LOCKMAN, P. R., KOZIARA, J. M., MUMPER, R. J. & ALLEN, D. D. 2004. Nanoparticle surface charges alter blood-brain barrier integrity and permeability. *J Drug Target*, 12, 635-41.
- LOCKMAN, P. R., OYEWUMI, M. O., KOZIARA, J. M., RODER, K. E., MUMPER, R. J. & ALLEN, D. D. 2003. Brain uptake of thiamine-coated nanoparticles. *J Control Release*, 93, 271-82.
- LODE, J., FICHTNER, I., KREUTER, J., BERNDT, A., DIEDERICHS, J. E. & RESZKA, R. 2001. Influence of surface-modifying surfactants on the pharmacokinetic behavior of ^{14}C -poly (methylmethacrylate) nanoparticles in experimental tumor models. *Pharm Res*, 18, 1613-9.
- LOSCHER, W. & POTSCHKA, H. 2005. Role of drug efflux transporters in the brain for drug disposition and treatment of brain diseases. *Prog Neurobiol*, 76, 22-76.
- LV, G., HE, F., WANG, X., GAO, F., ZHANG, G., WANG, T., JIANG, H., WU, C., GUO, D., LI, X., CHEN, B. & GU, Z. 2008. Novel nanocomposite of nano Fe_3O_4 and polylactide nanofibers for application in drug uptake and induction of cell death of leukemia cancer cells. *Langmuir*, 24, 2151-6.
- MACKERELL, A., BROOKS, B., BROOKS, C., MILSSON, L., ROUX, B., WON, Y. & KARPLUS, M. 1988. *Encyclopedia of Computational Chemistry*, John Wiley & Sons.

- MADSEN, S. J. & HIRSCHBERG, H. 2010. Site-specific opening of the blood-brain barrier. *J Biophotonics*, 3, 356-67.
- MAKIN, O. S. & SERPELL, L. C. 2005a. X-Ray Diffraction Studies of Amyloid Structure. In: SIGURDSSON, E. M. (ed.) *Amyloid Proteins: Methods and Protocols*. Totowa: Humana Press, Inc.
- MAKIN, O. S. & SERPELL, L. C. 2005b. X-ray diffraction studies of amyloid structure. *Methods Mol Biol*, 299, 67-80.
- MAKOVITZKI, A., BARAM, J. & SHAI, Y. 2008. Antimicrobial lipopolypeptides composed of palmitoyl Di- and tricationic peptides: in vitro and in vivo activities, self-assembly to nanostructures, and a plausible mode of action. *Biochemistry*, 47, 10630-6.
- MANJUNATH, K. & VENKATESWARLU, V. 2005. Pharmacokinetics, tissue distribution and bioavailability of clozapine solid lipid nanoparticles after intravenous and intraduodenal administration. *J Control Release*, 107, 215-28.
- MARINI, D. M., HWANG, W., LAUFFENBURGER, D. A., ZHANG, S. G. & KAMM, R. D. 2002. Left-handed helical ribbon intermediates in the self-assembly of a beta-sheet peptide. *Nano Letters*, 2, 295-299.
- MARRINK, S. J., DE VRIES, A. H. & MARK, A. E. 2004. Coarse grained model for semiquantitative lipid simulations. *Journal of Physical Chemistry B*, 108, 750-760.
- MARRINK, S. J., RISSELADA, H. J., YEFIMOV, S., TIELEMAN, D. P. & DE VRIES, A. H. 2007. The MARTINI force field: Coarse grained model for biomolecular simulations. *Journal of Physical Chemistry B*, 111, 7812-7824.
- MASLOV, L., FEDOROVA, N., DUDKO, V. & KARPOV, R. 2002. Influence of dalargin, a peripheral opiate receptor agonist, on exercise tolerance in patients with coronary and peripheral artery atherosclerosis. *Human Physiology*, 28, 579-584.
- MCDANNOLD, N., VYKHODTSEVA, N. & HYNYNEN, K. 2007. Use of ultrasound pulses combined with definity for targeted blood-brain barrier disruption: A feasibility study. *Ultrasound in Medicine and Biology*, 33, 584-590.
- MERLINI, G., SELDIN, D. C. & GERTZ, M. A. 2011. Amyloidosis: pathogenesis and new therapeutic options. *J Clin Oncol*, 29, 1924-33.
- MERRIFIELD, R. B. & NORD, F. F. 1969. Solid-Phase Peptide Synthesis. *Advances in Enzymology and Related Areas of Molecular Biology*. John Wiley & Sons, Inc.
- MISHRA, V., MAHOR, S., RAWAT, A., GUPTA, P. N., DUBEY, P., KHATRI, K. & VYAS, S. P. 2006. Targeted brain delivery of AZT via transferrin anchored pegylated albumin nanoparticles. *J Drug Target*, 14, 45-53.
- MISRA, A., GANESH, S., SHAHIWALA, A. & SHAH, S. P. 2003. Drug delivery to the central nervous system: a review. *J Pharm Pharm Sci*, 6, 252-73.
- MISSIRLIS, D., KHANT, H. & TIRRELL, M. 2009. Mechanisms of Peptide Amphiphile Internalization by SJS-1 Cells in Vitro. *Biochemistry*, 48, 3304-3314.
- MONTICELLI, L., KANDASAMY, S. K., PERIOLE, X., LARSON, R. G., TIELEMAN, D. P. & MARRINK, S. J. 2008. The MARTINI coarse-grained force field: Extension to proteins. *Journal of Chemical Theory and Computation*, 4, 819-834.

- MOSMANN, T. 1983. Rapid colorimetric assay for cellular growth and survival: application to proliferation and cytotoxicity assays. *J Immunol Methods*, 65, 55-63.
- MULLER, M., KATSOV, K. & SCHICK, M. 2006. Biological and synthetic membranes: What can be learned from a coarse-grained description? *Physics Reports-Review Section of Physics Letters*, 434, 113-176.
- MULLER, R. H. & KECK, C. 2004. Drug delivery to the brain--realization by novel drug carriers. *Journal of Nanoscience and Nanotechnology*, 4, 471-483.
- MURAKAMI, H., TAKANAGA, H., MATSUO, H., OHTANI, H. & SAWADA, Y. 2000. Comparison of blood-brain barrier permeability in mice and rats using in situ brain perfusion technique. *American Journal of Physiology-Heart and Circulatory Physiology*, 279, H1022-H1028.
- MURO, S., GARNACHO, C., CHAMPION, J. A., LEFEROVICH, J., GAJEWSKI, C., SCHUCHMAN, E. H., MITRAGOTRI, S. & MUZYKANTOV, V. R. 2008. Control of endothelial targeting and intracellular delivery of therapeutic enzymes by modulating the size and shape of ICAM-1-targeted carriers. *Mol Ther*, 16, 1450-8.
- NAJLAH, M., FREEMAN, S., ATTWOOD, D. & D'EMANUELE, A. 2006. Synthesis, characterization and stability of dendrimer prodrugs. *Int J Pharm*, 308, 175-82.
- NEUWELT, E., ABBOTT, N., ABREY, L., BANKS, W. A., BLAKLEY, B., DAVIS, T., ENGELHARDT, B., GRAMMAS, P., NEDERGAARD, M., NUTT, J., PARDRIDGE, W., ROSENBERG, G. A., SMITH, Q. & DREWES, L. R. 2008. Strategies to advance translational research into brain barriers. *Lancet Neurology*, 7, 84-96.
- NEUWELT, E. A., BAUER, B., FAHLKE, C., FRICKER, G., IADECOLA, C., JANIGRO, D., LEYBAERT, L., MOLNAR, Z., O'DONNELL, M. E., POVLISHOCK, J. T., SAUNDERS, N. R., SHARP, F., STANIMIROVIC, D., WATTS, R. J. & DREWES, L. R. 2011. Engaging neuroscience to advance translational research in brain barrier biology. *Nat Rev Neurosci*, 12, 169-82.
- NIECE, K. L., CZEISLER, C., SAHNI, V., TYSELING-MATTIACE, V., PASHUCK, E. T., KESSLER, J. A. & STUPP, S. I. 2008. Modification of gelation kinetics in bioactive peptide amphiphiles. *Biomaterials*, 29, 4501-4509.
- NIKANJARN, M., GIBBS, A. R., HUNT, A., BUDINGER, T. F. & FORTE, T. M. 2007. Synthetic nano-LDL with paclitaxel oleate as a targeted drug delivery vehicle for glioblastoma multiforme. *Journal of Controlled Release*, 124, 163-171.
- NISHIYAMA, N. 2007. Nanomedicine - Nanocarriers shape up for long life. *Nature Nanotechnology*, 2, 203-204.
- NITTA, T., HATA, M., GOTOH, S., SEO, Y., SASAKI, H., HASHIMOTO, N., FURUSE, M. & TSUKITA, S. 2003. Size-selective loosening of the blood-brain barrier in claudin-5-deficient mice. *J Cell Biol*, 161, 653-60.
- NORDÉN, B., RODGER, A. & DAFFORN, T. 2010. *Linear dichroism and circular dichroism : a textbook on polarized-light spectroscopy*, Cambridge, Royal Society of Chemistry.
- NOSE, S. A. 1984. Molecular-dynamics method for simulations in the canonical ensemble. *Molecular Physics*, 52, 255-268.
- NOSE, S. A. & KLEIN, M. L. 1983. Constant Pressure Molecular Dynamics for Molecular Systems. *Molecular Physics*, 50.

- OLIVIER, J. C., FENART, L., CHAUVET, R., PARIAT, C., CECHELLI, R. & COUET, W. 1999. Indirect evidence that drug brain targeting using polysorbate 80-coated polybutylcyanoacrylate nanoparticles is related to toxicity. *Pharm Res*, 16, 1836-42.
- OUYANG, H., ANDERSEN, T. E., CHEN, W., NOFSINGER, R., STEFFANSEN, B. & BORCHARDT, R. T. 2009. A comparison of the effects of p-glycoprotein inhibitors on the blood-brain barrier permeation of cyclic prodrugs of an opioid peptide (DADLE). *J Pharm Sci*, 98, 2227-36.
- OWENS, D. E., 3RD & PEPPAS, N. A. 2006. Opsonization, biodistribution, and pharmacokinetics of polymeric nanoparticles. *Int J Pharm*, 307, 93-102.
- PALMER, L. C. & STUPP, S. I. 2008. Molecular Self-Assembly into One-Dimensional Nanostructures. *Accounts of Chemical Research*, 41, 1674-1684.
- PARAMONOV, S. E., JUN, H. W. & HARTGERINK, J. D. 2006. Self-assembly of peptide-amphiphile nanofibers: The roles of hydrogen bonding and amphiphilic packing. *Journal of the American Chemical Society*, 128, 7291-7298.
- PARDRIDGE, W. M. 1998. *Introduction to the blood-brain barrier : methodology, biology and pathology*, Cambridge, Cambridge University Press.
- PARDRIDGE, W. M. 2002. Why is the global CNS pharmaceutical market so underpenetrated? *Drug Discov Today*, 7, 5-7.
- PARDRIDGE, W. M. 2003. Blood-brain barrier drug targeting: the future of brain drug development. *Mol Interv*, 3, 90-105, 51.
- PARDRIDGE, W. M. 2005. The blood-brain barrier: bottleneck in brain drug development. *NeuroRx*, 2, 3-14.
- PARDRIDGE, W. M. 2007. Blood-brain barrier delivery. *Drug Discov Today*, 12, 54-61.
- PARDRIDGE, W. M., BUCIAK, J. L., KANG, Y. S. & BOADO, R. J. 1993. Protamine-mediated transport of albumin into brain and other organs of the rat. Binding and endocytosis of protamine-albumin complex by microvascular endothelium. *J Clin Invest*, 92, 2224-9.
- PARK, K., KIM, J. H., NAM, Y. S., LEE, S., NAM, H. Y., KIM, K., PARK, J. H., KIM, I. S., CHOI, K., KIM, S. Y. & KWON, I. C. 2007. Effect of polymer molecular weight on the tumor targeting characteristics of self-assembled glycol chitosan nanoparticles. *J Control Release*, 122, 305-14.
- PARRINIELLO, M. & RAHMAN, A. 1981. Polymorphic Transitions in Single Crystals: A New Molecular Dynamics Method. *Journal of Applied Physics*, 52, 7182-7190.
- PARTICLES CIC, A. N. 2008. Zeta Potential. Leeds.
- PARTRIDGE, W. M. 2001. Brain Drug Targeting: the future of brain drug development.
- PASHUCK, E. T., CUI, H. & STUPP, S. I. 2010. *Tuning supramolecular rigidity of peptide fibers through molecular structure*. 132.
- PASHUCK, E. T. & STUPP, S. I. 2010a. Direct Observation of Morphological Transformation from Twisted Ribbons into Helical Ribbons. *Journal of the American Chemical Society*, 132, 8819-+.
- PASHUCK, E. T. & STUPP, S. I. 2010b. Direct observation of morphological transformation from twisted ribbons into helical ribbons. *J Am Chem Soc*, 132, 8819-21.

- PAVAN, B., DALPIAZ, A., CILIBERTI, N., BIONDI, C., MANFREDINI, S. & VERTUANI, S. 2008. Progress in drug delivery to the central nervous system by the prodrug approach. *Molecules*, 13, 1035-65.
- PENCHEVA, N., POSPISEK, J., HAUZEROVA, L., BARTH, T. & MILANOV, P. 1999. Activity profiles of dalargin and its analogues in mu-, delta- and kappa-opioid receptor selective bioassays. *Br J Pharmacol*, 128, 569-76.
- PETKOVA, A. T., BUNTKOWSKY, G., DYDA, F., LEAPMAN, R. D., YAU, W. M. & TYCKO, R. 2004. Solid state NMR reveals a pH-dependent antiparallel beta-sheet registry in fibrils formed by a beta-amyloid peptide. *J Mol Biol*, 335, 247-60.
- PETROS, R. A. & DESIMONE, J. M. 2010. Strategies in the design of nanoparticles for therapeutic applications. *Nature Reviews Drug Discovery*, 9, 615-27.
- PFAFF, D. W. 1973. Luteinizing hormone releasing factor potentiates lordosis behavior in hypophysectomized ovariectomized female rats. *Science*, 182, 1148-9.
- PORTER, A. E., KNOWLES, T. P. J., MULLER, K., MEEHAN, S., MCGUIRE, E., SKEPPER, J., WELLAND, M. E. & DOBSON, C. M. 2009. Imaging Amyloid Fibrils within Cells Using a Se-Labeling Strategy. *Journal of Molecular Biology*, 392, 868-871.
- PREGO, C., TORRES, D. & ALONSO, M. J. 2005. The potential of chitosan for the oral administration of peptides. *Expert Opin Drug Deliv*, 2, 843-54.
- PREGO, C., TORRES, D. & ALONSO, M. J. 2006. Chitosan nanocapsules as carriers for oral peptide delivery: effect of chitosan molecular weight and type of salt on the in vitro behaviour and in vivo effectiveness. *J Nanosci Nanotechnol*, 6, 2921-8.
- QU, X., KHUTORYANSKIY, V. V., STEWART, A., RAHMAN, S., PAPAHAJDOPOULOS-STERNBERG, B., DUFES, C., MCCARTHY, D., WILSON, C. G., LYONS, R., CARTER, K. C., SCHATZLEIN, A. & UCHEGBU, I. F. 2006. Carbohydrate-based micelle clusters which enhance hydrophobic drug bioavailability by up to 1 order of magnitude. *Biomacromolecules*, 7, 3452-9.
- RABEL, S. R., JONA, J. A. & MAURIN, M. B. 1999. Applications of modulated differential scanning calorimetry in preformulation studies. *J Pharm Biomed Anal*, 21, 339-45.
- RAINOV, N. G., GORBATYUK, K. & HEIDECKE, V. 2008. Clinical trials with intracerebral convection-enhanced delivery of targeted toxins in malignant glioma. *Rev Recent Clin Trials*, 3, 2-9.
- RAJANGAM, K., BEHANNA, H. A., HUI, M. J., HAN, X. Q., HULVAT, J. F., LOMASNEY, J. W. & STUPP, S. I. 2006. Heparin binding nanostructures to promote growth of blood vessels. *Nano Letters*, 6, 2086-2090.
- RAMGE, P., KREUTER, J. & LEMMER, B. 1999. Circadian phase-dependent antinociceptive reaction in mice determined by the hot-plate test and the tail-flick test after intravenous injection of dalargin-loaded nanoparticles. *Chronobiol Int*, 16, 767-77.
- RAO, K. S., REDDY, M. K., HORNING, J. L. & LABHASETWAR, V. 2008. TAT-conjugated nanoparticles for the CNS delivery of anti-HIV drugs. *Biomaterials*, 29, 4429-38.
- REES, O. J. 2010. *Fourier transform infrared spectroscopy : developments, techniques, and applications*, New York, Nova Science.

- REEVE, W. G. & TODD, J. G. 1990. Intraventricular diamorphine via an Ommaya shunt for intractable cancer pain. *Br J Anaesth*, 65, 544-7.
- REICHEL, A. 2009a. Addressing Central Nervous System (CNS) Penetration in Drug Discovery: Basics and Implications of the Evolving New Concept. *Chemistry & Biodiversity*, 6, 2030-2049.
- REICHEL, A. 2009b. Addressing central nervous system (CNS) penetration in drug discovery: basics and implications of the evolving new concept. *Chem Biodivers*, 6, 2030-49.
- REKHA, M. R. & SHARMA, C. P. 2011. Nanoparticle Mediated Oral Delivery of Peptides and Proteins: Challenges and Perspectives. In: VAN DER WALLE, C. (ed.) *Peptide and Protein Delivery*. Academic Press.
- RIVIÈRE C, T. R., LYSIANE QUENTIN, STÉPHANIE KRISA, JEAN-MICHEL MÉRILLON, JEAN-PIERRE MONTI 2007. Inhibitory activity of stilbenes on alzheimer's disease. *Biorganic and Medicinal Chemistry*, 15, 1160-1167.
- ROBINSON, L. R., FITZGERALD, N. C., DOUGHTY, D. G., DAWES, N. C., BERGE, C. A. & BISSETT, D. L. 2005. Topical palmitoyl pentapeptide provides improvement in photoaged human facial skin. *Int J Cosmet Sci*, 27, 155-60.
- ROUSSELLE, C., CLAIR, P., SMIRNOVA, M., KOLESNIKOV, Y., PASTERNAK, G. W., GAC-BRETON, S., REES, A. R., SCHERRMANN, J. M. & TEMSAMANI, J. 2003. Improved brain uptake and pharmacological activity of dalargin using a peptide-vector-mediated strategy. *J Pharmacol Exp Ther*, 306, 371-6.
- RYU, J. & PARK, B. C. 2009. High Stability of Self-Assembled Peptide Nanowires Against Thermal, Chemical, and Proteolytic Attacks. *Biotechnology and Bioengineering*, 105, 221-230.
- RZEPIELA, A. J., SCHAFFER, L. V., GOGA, N., RISSELADA, H. J., DE VRIES, A. H. & MARRINK, S. J. 2010. Reconstruction of atomistic details from coarse-grained structures. *J Comput Chem*, 31, 1333-43.
- SAAR BG, F. C., REICHMAN J, STANLEY CM, HOLTOM GR, XUNNEY XIE X. 2010. Video-rate Molecular Imaging in vivo with stimulated raman scattering. *Science*, 330, 1368-1370.
- SAAR, B. G., JOHNSTON, R. S., FREUDIGER, C. W., XIE, X. S. & SEIBEL, E. J. 2011. Coherent Raman scanning fiber endoscopy. *Optics Letters*, 36, 2396-8.
- SAHAY, G., ALAKHOVA, D. Y. & KABANOV, A. V. 2010. Endocytosis of nanomedicines. *J Control Release*, 145, 182-95.
- SAHOO, S., ANG, L. T., GOH, J. C. & TOH, S. L. 2010. Growth factor delivery through electrospun nanofibers in scaffolds for tissue engineering applications. *J Biomed Mater Res A*, 93, 1539-50.
- SAITOU, M., FURUSE, M., SASAKI, H., SCHULZKE, J. D., FROMM, M., TAKANO, H., NODA, T. & TSUKITA, S. 2000. Complex phenotype of mice lacking occludin, a component of tight junction strands. *Mol Biol Cell*, 11, 4131-42.
- SANDRA, K., MOSHIR, M., D'HONDT, F., VERLEYSSEN, K., KAS, K. & SANDRA, P. 2008. Highly efficient peptide separations in proteomics Part 1. Unidimensional high performance liquid chromatography. *J Chromatogr B Analyt Technol Biomed Life Sci*, 866, 48-63.
- SANTOSO, S., HWANG, W., HARTMAN, H. & ZHANG, S. G. 2002. Self-assembly of surfactant-like peptides with variable glycine tails to form nanotubes and nanovesicles. *Nano Letters*, 2, 687-691.

- SARGEANT, T. D., GULER, M. O., OPPENHEIMER, S. M., MATA, A., SATCHER, R. L., DUNAND, D. C. & STUPP, S. I. 2008. Hybrid bone implants: Self-assembly of peptide amphiphile nanofibers within porous titanium. *Biomaterials*, 29, 161-171.
- SAXENA, K., DUCLOS, R. I., ZIMMERMANN, P., SCHMIDT, R. R. & SHIPLEY, G. G. 1999. Structure and properties of totally synthetic galacto- and glucocerebrosides. *J Lipid Res*, 40, 839-49.
- SCHAFER, L. & MARRINK, S. J. 2009. GROMACS Coarse-Graining Workshop. CSC, Helsinki, Finland.
- SCHINKEL, A. H. 1997. The physiological function of drug-transporting P-glycoproteins. *Semin Cancer Biol*, 8, 161-70.
- SCHNYDER, A., KRAHENBUHL, S., DREWE, J. & HUWYLER, J. 2005. Targeting of daunomycin using biotinylated immunoliposomes: pharmacokinetics, tissue distribution and in vitro pharmacological effects. *J Drug Target*, 13, 325-35.
- SCHROEDER, U., SCHROEDER, H. & SABEL, B. A. 2000. Body distribution of 3H-labelled dalargin bound to poly(butyl cyanoacrylate) nanoparticles after i.v. injections to mice. *Life Sci*, 66, 495-502.
- SCHROEDER, U., SOMMERFELD, P. & SABEL, B. A. 1998. Efficacy of oral dalargin-loaded nanoparticle delivery across the blood-brain barrier. *Peptides*, 19, 777-80.
- SEDDON, J. M., SQUIRES, A. M., CONN, C. E., CES, O., HERON, A. J., MULET, X., SHEARMAN, G. C. & TEMPLER, R. H. 2006. Pressure-jump X-ray studies of liquid crystal transitions in lipids. *Philosophical Transactions of the Royal Society a-Mathematical Physical and Engineering Sciences*, 364, 2635-2655.
- SEGAL, M. B. 1992. *Barriers and fluids of the eye and brain*, Macmillan.
- SELL, S. A., MCCLURE, M. J., GARG, K., WOLFE, P. S. & BOWLIN, G. L. 2009. Electrospinning of collagen/biopolymers for regenerative medicine and cardiovascular tissue engineering. *Advanced Drug Delivery Reviews*, 61, 1007-1019.
- SENEL, S., KREMER, M. J., KAS, S., WERTZ, P. W., HINCAL, A. A. & SQUIER, C. A. 2000. Enhancing effect of chitosan on peptide drug delivery across buccal mucosa. *Biomaterials*, 21, 2067-71.
- SHAH, S., LIU, Y., HU, W. & GAO, J. 2011. Modeling particle shape-dependent dynamics in nanomedicine. *J Nanosci Nanotechnol*, 11, 919-28.
- SHARMA, G., VALENTA, D. T., ALTMAN, Y., HARVEY, S., XIE, H., MITRAGOTRI, S. & SMITH, J. W. 2010. Polymer particle shape independently influences binding and internalization by macrophages. *J Control Release*, 147, 408-12.
- SHERMAN, P. 1970. Rheology of Dispersed Systems. In: SHERMAN, P. (ed.) *Industrial Rheology*. London: Academic Press Inc.
- SHI, Q., IZVEKOV, S. & VOTH, G. A. 2006. Mixed atomistic and coarse-grained molecular dynamics: Simulation of a membrane-bound ion channel. *Journal of Physical Chemistry B*, 110, 15045-15048.
- SIEW, A. 2009. *Oral Absorption Enhancement of Hydrophobic Drugs by Chitosan Based Amphiphilic Polymers*. Doctor of Philosophy, The School of Pharmacy, University of London.

- SILVA, G. A., CZEISLER, C., NIECE, K. L., BENIASH, E., HARRINGTON, D. A., KESSLER, J. A. & STUPP, S. I. 2004. Selective differentiation of neural progenitor cells by high-epitope density nanofibers. *Science*, 303, 1352-5.
- SIMON, S. L. 2001. Temperature-modulated differential scanning calorimetry: theory and application. *Thermochimica Acta*, 374, 55-71.
- SINGLA, A. K., GARG, A. & AGGARWAL, D. 2002. Paclitaxel and its formulations. *Int J Pharm*, 235, 179-92.
- SMITH, D., SCHMID, E. & JONES, B. 2002. Do drug metabolism and pharmacokinetic departments make any contribution to drug discovery? *Clin Pharmacokinet*, 41, 1005-1010.
- SOUSA, F., MANDAL, S., GARROVO, C., ASTOLFO, A., BONIFACIO, A., LATAWIEC, D., MENK, R. H., ARFELLI, F., HUEWEL, S., LEGNAME, G., GALLA, H. J. & KROL, S. 2010. Functionalized gold nanoparticles: a detailed in vivo multimodal microscopic brain distribution study. *Nanoscale*, 2, 2826-34.
- STANDLEY, S. M., TOFT, D. J., CHENG, H., SOUKASENE, S., CHEN, J., RAJA, S. M., BAND, V., BAND, H., CRYNS, V. L. & STUPP, S. I. 2010. Induction of cancer cell death by self-assembling nanostructures incorporating a cytotoxic peptide. *Cancer Res*, 70, 3020-6.
- STATHOPOULOS, P. B., SCHOLZ, G. A., HWANG, Y. M., RUMFELDT, J. A. O., LEPOCK, J. R. & MEIERING, E. M. 2004. Sonication of proteins causes formation of aggregates that resemble amyloid. *Protein Science*, 13, 3017-3027.
- STENDAHL, J. C., RAO, M. S., GULER, M. O. & STUPP, S. I. 2006. Intermolecular forces in the self-assembly of peptide amphiphile nanofibers. *Advanced Functional Materials*, 16, 499-508.
- TAMAI, I. & TSUJI, A. 2000. Transporter-mediated permeation of drugs across the blood-brain barrier. *J Pharm Sci*, 89, 1371-88.
- TAO, L., HU, W., LIU, Y., HUANG, G., SUMER, B. D. & GAO, J. 2011. Shape-specific polymeric nanomedicine: emerging opportunities and challenges. *Exp Biol Med (Maywood)*, 236, 20-9.
- TAYLOR, G. I. 1969. Electrically driven jets. *Proc. R. Soc. London*, 313A, 453-475.
- THANOU, M., VERHOEF, J. C. & JUNGINGER, H. E. 2001a. Chitosan and its derivatives as intestinal absorption enhancers. *Adv Drug Deliv Rev*, 50 Suppl 1, S91-101.
- THANOU, M., VERHOEF, J. C. & JUNGINGER, H. E. 2001b. Oral drug absorption enhancement by chitosan and its derivatives. *Adv Drug Deliv Rev*, 52, 117-26.
- TOBBB.COM. 2011. Available: <http://www.tobbb.com/index.php?cat=partnering&page=overview> [Accessed].
- TONGA, J., ZIMMERMAN, M., LIC, S., YIA, X., LUXENHOFERD, R., JORDAND, R. & KABANOV, A. 2011. Neuronal uptake and intracellular superoxide scavenging of a fullerene (C60)-poly(2-oxazoline)s nanoformulation. *Biomaterials*, 32, 3654-3665.
- TOSI, G., VERGONI, A. V., RUOZI, B., BONDIOLI, L., BADIALI, L., RIVASI, F., COSTANTINO, L., FORNI, F. & VANDELLI, M. A. 2010. Sialic acid and glycopeptides conjugated PLGA nanoparticles for central nervous system targeting: In vivo pharmacological evidence and biodistribution. *Journal of Controlled Release*, 145, 49-57.
- TOZZINI, V. & MCCAMMON, J. A. 2005. A coarse grained model for the dynamics of flap opening in HIV-1 protease. *Chemical Physics Letters*, 413, 123-128.

- TRAPANI, A., SITTERBERG, J., BAKOWSKY, U. & KISSEL, T. 2009. The potential of glycol chitosan nanoparticles as carrier for low water soluble drugs. *Int J Pharm*, 375, 97-106.
- TROSTER, S. D., MULLER, U. & KREUTER, J. 1990. Modification of the body distribution of poly(methyl methacrylate) nanoparticles in rats by coating with surfactants. 61, 85-100.
- TSONCHEV, S., NIECE, K. L., SCHATZ, G. C., RATNER, M. A. & STUPP, S. I. 2008. Phase diagram for assembly of biologically-active peptide amphiphiles. *Journal of Physical Chemistry B*, 112, 441-447.
- TUMA, P. L. & HUBBARD, A. L. 2003. Transcytosis: crossing cellular barriers. *Physiol Rev*, 83, 871-932.
- TURNER, A. 1987. endopeptidase-24:11 and neuropeptide metabolism. In: TURNER, A. (ed.) *Neuropeptides and their peptidases*. Chichester and Verlagsgesellschaft: Ellis Horwood.
- TYSSELING-MATTIACE, V. M., SAHNI, V., NIECE, K. L., BIRCH, D., CZEISLER, C., FEHLINGS, M. G., STUPP, S. I. & KESSLER, J. A. 2008. Self-assembling nanofibers inhibit glial scar formation and promote axon elongation after spinal cord injury. *J Neurosci*, 28, 3814-23.
- UCHEGBU IF, L. A., SCHATZLEIN AG. 2010. *Delivery of hydrophilic drugs* USA patent application 20100222281.
- UCHEGBU, I. F., SADIQ, L., ARASTOO, M., GRAY, A. I., WANG, W., WAIGH, R. D. & SCHATZLEIN, A. G. 2001. Quaternary ammonium palmitoyl glycol chitosan--a new polysoap for drug delivery. *Int J Pharm*, 224, 185-99.
- UCHEGBU, I. F. & SCHÄTZLEIN, A. G. 2006. *Polymers in drug delivery*, Boca Raton, Fla. ; London, CRC.
- UCHEGBU, I. F., SCHATZLEIN, A. G. & MAZZA, M. 2010. *Delivery of hydrophilic peptides*. GB 1011602.8 patent application GB 1011602.8.
- ULIJN, R. V. & SMITH, A. M. 2008. Designing peptide based nanomaterials. *Chem Soc Rev*, 37, 664-75.
- UPTON, R. N. 2007. Cerebral uptake of drugs in humans. *Clin Exp Pharmacol Physiol*, 34, 695-701.
- USP-NF 1995. Third Supplement, US Pharmacopeia. 2851-3101.
- VAN DEN HEUVEL, M., LOWIK, D. W. & VAN HEST, J. C. 2010. Effect of the diacetylene position on the chromatic properties of polydiacetylenes from self-assembled peptide amphiphiles. *Biomacromolecules*, 11, 1676-83.
- VAN DER WALLE CF & O, O. 2011. An overview of peptide and protein delivery. In: WALLE, C. V. D. (ed.) *Peptide and Protein Delivery*. London: Elsevier.
- VAN ROOY, I., CAKIR-TASCIOGLU, S., HENNINK, W. E., STORM, G., SCHIFFELERS, R. M. & MASTROBATTISTA, E. 2011a. In Vivo Methods to Study Uptake of Nanoparticles into the Brain. *Pharmaceutical Research*, 28, 456-471.
- VAN ROOY, I., MASTROBATTISTA, E., STORM, G., HENNINK, W. E. & SCHIFFELERS, R. M. 2011b. Comparison of five different targeting ligands to enhance accumulation of liposomes into the brain. *J Control Release*, 150, 30-6.
- VELICHKO, Y. S., STUPP, S. I. & DE LA CRUZ, M. O. 2008a. Molecular simulation study of peptide amphiphile self-assembly. *Journal of Physical Chemistry B*, 112, 2326-2334.

- VELICHKO, Y. S., STUPP, S. I. & DE LA CRUZ, M. O. 2008b. Molecular simulation study of peptide amphiphile self-assembly. *J Phys Chem B*, 112, 2326-34.
- VENKATESAN, N., UCHINO, K., AMAGASE, K., ITO, Y., SHIBATA, N. & TAKADA, K. 2006. Gastro-intestinal patch system for the delivery of erythropoietin. *J Control Release*, 111, 19-26.
- VERGONI, A. V., TOSI, G., TACCHI, R., VANDELLI, M. A., BERTOLINI, A. & COSTANTINO, L. 2009. Nanoparticles as drug delivery agents specific for CNS in vivo biodistribution. *Nanomedicine*, 5, 369-77.
- VIGANO, C., MANCIU, L., GOORMAGHTIGH, E. & RUYSSCHAERT, J. M. 2000. attenuated total reflection IR spectroscopy as a tool to investigate the structure, orientation and tertiary structure changes in peptides and membrane proteins. *Biopolymers (Pept. Sci)*, 55, 373-380.
- VINOGRADOV, S. V., BATRAKOVA, E. V. & KABANOV, A. V. 2004. Nanogels for oligonucleotide delivery to the brain. *Bioconjug Chem*, 15, 50-60.
- VINOGRADOV, V., KALENIKOVA, E. & SOKOLOV, A. 1988. Bioavailability of Dalargin and its metabolism during intranasal administration to rats. *Biull Exsp Biol Med*, 106, 48-50.
- VITEZ, I. M. & NEWMAN, A. W. 2007. Thermal Microscopy. In: CRAIG, D. Q. M. & READING, M. (eds.) *Thermal Analysis of Pharmaceuticals*. Boca Raton: CRC Press.
- VON EINEM, B., SCHWANZAR, D., REHN, F., BEYER, A. S., WEBER, P., WAGNER, M., SCHNECKENBURGER, H. & VON ARNIM, C. A. F. 2010. The role of low-density receptor-related protein 1 (LRP1) as a competitive substrate of the amyloid precursor protein (APP) for BACE1. *Experimental Neurology*, 225, 85-93.
- VORBRODT, A. W. 1989. Ultracytochemical characterization of anionic sites in the wall of brain capillaries. *J Neurocytol*, 18, 359-68.
- WANG, J., BYRNE, J. D., NAPIER, M. E. & DE SIMONE, J. M. 2011. More effective nanomedicines through particle design. *Small*, 14, 1919-1931.
- WANG, J., CHOW, D., HEIATI, H. & SHEN, W. C. 2003. Reversible lipidization for the oral delivery of salmon calcitonin. *J Control Release*, 88, 369-80.
- WANG, J., SHEN, D. & SHEN, W. C. 1999. Preparation, purification, and characterization of a reversibly lipidized desmopressin with potentiated anti-diuretic activity. *Pharm Res*, 16, 1674-9.
- WANG, J. X., SUN, X. & ZHANG, Z. R. 2002a. Enhanced brain targeting by synthesis of 3,5-dioctanoyl-5-fluoro-2-deoxyuridine and incorporation into solid lipid nanoparticles. *Eur J Pharm Biopharm*, 54, 285-290.
- WANG, P. P., FRAZIER, J. & BREM, H. 2002b. Local drug delivery to the brain. *Adv Drug Deliv Rev*, 54, 987-1013.
- WANG, W., TETLEY, L. & UCHEGBU, I. F. 2001. The Level of Hydrophobic Substitution and the Molecular Weight of Amphiphilic Poly-L-lysine-Based Polymers Strongly Affects Their Assembly into Polymeric Bilayer Vesicles. *J Colloid Interface Sci*, 237, 200-207.
- WANG, Y. C., WU, Y. C., YEH, C. C. & HWANG, C. C. 2007. Structure-activity relationships of Leu-Enkephalin analog with (4-Carboxamido)phenylalanine substituted for tyrosine: a molecular dynamics study. *Biopolymers*, 86, 231-9.
- WATSON, J. T. & SPARKMAN, O. D. 2007a. MALDI. In: J THROCK WATSON & SPARKMAN, O. D. (eds.) *Introduction to Mass Spectrometry*. New York: Jon Wiley and Sons.

- WATSON, J. T. & SPARKMAN, O. D. 2007b. Mass Spectrometry/Mass Spectrometry. In: J THROCK WATSON & SPARKMAN, O. D. (eds.) *Introduction to Mass Spectrometry*. New York: Jon Wiley and Sons.
- WEBBER, M. J., KESSLER, J. A. & STUPP, S. I. 2010a. Emerging peptide nanomedicine to regenerate tissues and organs. *Journal of Internal Medicine*, 267, 71-88.
- WEBBER, M. J., TONGERS, J., RENAULT, M. A., RONCALLI, J. G., LOSORDO, D. W. & STUPP, S. I. 2010b. Development of bioactive peptide amphiphiles for therapeutic cell delivery. *Acta Biomater*, 6, 3-11.
- WEBBER, M. J., TONGERS, J., RENAULT, M. A., RONCALLI, J. G., LOSORDO, D. W. & STUPP, S. I. 2010c. Development of bioactive peptide amphiphiles for therapeutic cell delivery. *Acta Biomaterialia*, 6, 3-11.
- WHITESIDES, G. M. & BONCHEVA, M. 2002. Beyond molecules: Self-assembly of mesoscopic and macroscopic components. *Proceedings of the National Academy of Sciences of the United States of America*, 99, 4769-4774.
- WILSON, A. P. 2000. Cytotoxicity and viability assays. In: MASTERS, J. R. W. (ed.) *Animal Cell Culture. A Practical Approach*. Oxford University Press.
- WIRADHARMA, N., TONG, Y. W. & YANG, Y. Y. 2009. Self-assembled oligopeptide nanostructures for co-delivery of drug and gene with synergistic therapeutic effect. *Biomaterials*, 30, 3100-9.
- WUNGTANAGORNA, R. & SCHMIDTB, S. J. 2001. Phenomenological study of enthalpy relaxation of amorphous glucose, fructose, and their mixture. *Thermochimica Acta*, 369, 95-116.
- WYATT, P. 1998. *Wyatt: Manual for Optilab DSP Interferometric Refractometer*, Santa Barbara, USA, Wyatt Technology Corporation.
- XIE, Y., YE, L., ZHANG, X., CUI, W., LOU, J., NAGAI, T. & HOU, X. 2005. Transport of nerve growth factor encapsulated into liposomes across the blood-brain barrier: in vitro and in vivo studies. *J Control Release*, 105, 106-19.
- XU, X. D., JIN, Y., LIU, Y., ZHANG, X. Z. & ZHUO, R. X. 2010. Self-assembly behavior of peptide amphiphiles (PAs) with different length of hydrophobic alkyl tails. *Colloids Surf B Biointerfaces*, 81, 329-35.
- YANG, C. Y., SONG, B., AO, Y., NOWAK, A. P., ABELOWITZ, R. B., KORSAK, R. A., HAVTON, L. A., DEMING, T. J. & SOFRONIEW, M. V. 2009. Biocompatibility of amphiphilic diblock copolypeptide hydrogels in the central nervous system. *Biomaterials*, 30, 2881-98.
- YANG, S. J. & ZHANG, S. G. 2006. Self-assembling behavior of designer lipid-like peptides. *Supramolecular Chemistry*, 18, 389-396.
- YANG T, R. K., ABBRUSCATO TJ 2007. Evaluation of bEnd5 Cell Line as an In Vitro Model for the Blood-Brain Barrier under Normal and Hypoxic/Aglycemic Conditions. *JOURNAL OF PHARMACEUTICAL SCIENCES*, 96, 3196-3213.
- YANG, Y. J., FU, X. R., CAO, S. Q., WANG, N. X., ZHANG, S. Z. & WANG, H. 2007. Effect of hydrogen bonding and hydrophobic interaction on the formation of supramolecular hydrogels formed by L-phenylalanine derivative hydrogelator. *Chinese Chemical Letters*, 18, 1001-1004.
- YANG, Z., HUCK, W. T., CLARKE, S. M., TAJBAKSH, A. R. & TERENTJEV, E. M. 2005. Shape-memory nanoparticles from inherently non-spherical polymer colloids. *Nature Materials*, 4, 486-90.

- YU, S. M. & TIRRELL, D. A. 2000. Thermal and structural properties of biologically derived monodisperse hairy-rod polymers. *Biomacromolecules*, 1, 310-2.
- YU, Y. C., TIRRELL, M. & FIELDS, G. B. 1998. Minimal lipidation stabilizes protein-like molecular architecture. *Journal of the American Chemical Society*, 120, 9979-9987.
- YUAN, L., WANG, J. & SHEN, W. C. 2005. Reversible lipidization prolongs the pharmacological effect, plasma duration, and liver retention of octreotide. *Pharm Res*, 22, 220-7.
- YUAN, L., WANG, J. & SHEN, W. C. 2008. Reversible lipidization of somatostatin analogues for the liver targeting. *Eur J Pharm Biopharm*, 70, 615-20.
- ZENSI, A., BEGLEY, D., PONTIKIS, C., LEGROS, C., MIHOREANU, L., BUCHEL, C. & KREUTER, J. 2010. Human serum albumin nanoparticles modified with apolipoprotein A-I cross the blood-brain barrier and enter the rodent brain. *J Drug Target*, 18, 842-8.
- ZETASIZER NANO SERIES TECHNICAL NOTES, M. 2010. Zeta Potential. An introduction in 30 Minutes. *Malvern Instruments*, 1-6.
- ZHANG, S., GELAIN, F. & ZHAO, X. 2005. Designer self-assembling peptide nanofiber scaffolds for 3D tissue cell cultures. *Seminars in Cancer Biology*, 15, 413-420.
- ZHANG, S., GREENFIELD, M. A., MATA, A., PALMER, L. C., BITTON, R., MANTEI, J. R., APARICIO, C., DE LA CRUZ, M. O. & STUPP, S. I. 2010a. A self-assembly pathway to aligned monodomain gels. *Nat Mater*, 9, 594-601.
- ZHANG, S. G., MARINI, D. M., HWANG, W. & SANTOSO, S. 2002. Design of nanostructured biological materials through self-assembly of peptides and proteins. *Current Opinion in Chemical Biology*, 6, 865-871.
- ZHANG, S. M., GREENFIELD, M. A., MATA, A., PALMER, L. C., BITTON, R., MANTEI, J. R., APARICIO, C., DE LA CRUZ, M. O. & STUPP, S. I. 2010b. A self-assembly pathway to aligned monodomain gels. *Nature Materials*, 9, 594-601.
- ZHANG, X., XIE, Y., JIN, Y., HOU, X., YE, L. & LOU, J. 2004. The effect of RMP-7 and its derivative on transporting Evans blue liposomes into the brain. *Drug Deliv*, 11, 301-9.
- ZHOU, M., SMITH, A. M., DAS, A. K., HODSON, N. W., COLLINS, R. F., ULIJN, R. V. & GOUGH, J. E. 2009. Self-assembled peptide-based hydrogels as scaffolds for anchorage-dependent cells. *Biomaterials*, 30, 2523-2530.
- ZUMBUSCH, A. & MULLER, M. 2007. Coherent anti-stokes Raman scattering microscopy. *Chemphyschem*, 8, 2157-2170.